

Structural studies of human cell surface receptors

**On low-density lipoprotein receptor-related protein 1 and
epidermal growth factor receptors 2 and 3**

Camilla De Nardis

A papà

Committee:

Prof.dr. A.M.J.J. Bonvin

Prof.dr. I. Braakman

Prof.dr. T. Logtenberg

Prof.dr. K. Mertens

Dr. S.G.D. Rüdiger

Prof.dr. J. Voorberg

ISBN:978-90-393-6845-9

The research presented in this thesis was performed in the Crystal & Structural Chemistry group at the Bijvoet Center for Biomolecular Research, Utrecht University, The Netherlands.

This research was part of the ManiFold project, a Marie Curie Initial Training Network and Innovative Doctoral Program, funded by the European Union's 7th Framework Program.

Cover illustration: adapted from 'Conoscere' by Giorgio Giardina

Layout and print: ProefschriftMaken | www.proefschriftmaken.nl

Printed on FSC certified recycled paper

© 2017 Camilla De Nardis, all rights reserved.

Structural studies of human cell surface receptors

On low-density lipoprotein receptor-related protein 1 and epidermal growth factor receptors 2 and 3

Onderzoek naar de structuur van de menselijke celoppervlakreceptoren:

'low-density lipoprotein receptor-related protein 1' en

'epidermal growth factor receptor 2 en 3'

(met een samenvatting in het Nederlands)

Proefschrift

ter verkrijging van de graad van doctor aan de Universiteit Utrecht op gezag van de rector magnificus, prof.dr. G.J. van der Zwaan, ingevolge het besluit van het college voor promoties in het openbaar te verdedigen op woensdag 27 september 2017 des middags te 12.45 uur

door

Camilla De Nardis

geboren op 1 januari 1989
te Rome, Italië

Promotor: Prof.dr. P. Gros

This thesis was accomplished with financial support from Merus N.V.

*Curiosity is the faithful companion of the Researcher together with the Doubt.
A Researcher seeks Answers, but there are no Answers without Questions.
Researchers are not only the Scientists, but all the Travelers, the Artists, the Lovers.
All those who are in motion seek something.*

Giorgio Giardina

Table of contents

Chapter 1	General introduction	9
Chapter 2	Recombinant expression of the full-length ectodomain of LDL receptor-related protein 1 (LRP1) unravels pH dependent conformational changes and the stoichiometry of binding with receptor-associated protein (RAP)	29
Chapter 3	Application of unbiased combinatorial screening to generate a bispecific IgG1 that selectively and potently inhibits HER3 signaling via HER2-guided ligand blockade	57
Chapter 4	A new approach for generating bispecific antibodies based on a common light chain format and the stable architecture of human immunoglobulin G1	127
Chapter 5	General discussion	157
Appendix	Summary	178
	Nederlanse samenvatting	181
	List of publications	184
	Curriculum vitae	185
	Acknowledgements	186

CHAPTER 1

General introduction

Protein-ligand interactions

Proteins are the essential building blocks of life. Nearly all cell functions, including important processes such as catalysis, DNA replication and molecular transport depend on them. In order to correctly perform and regulate the tasks they have evolved to fulfil, proteins need to interact selectively with other biomolecules, generally referred to as ligands. (The word ligand comes from the Latin word *ligare*, meaning to bind). Ligands can be nucleic acids, lipids, sugars, ions, or most importantly, other proteins. Ligand-protein or protein-protein interactions are essential for regulating cellular functions such as environmental sensing, signal transduction, enzyme activity homeostasis and cellular organization maintenance (1). Disruption of protein activity causes the cell to malfunction and is at the basis of a wide range of medical conditions. Because of their crucial role in executing and controlling biological functions, protein-ligand interactions are of great interest as therapeutic targets. In pathological conditions, the inhibition, stimulation or restoration of protein activity or protein interactions can help to restore normal cell functions. A deeper understanding of the molecular details of protein-ligand interactions is therefore of crucial importance for the advancement of medicine through rational drug design.

The activity of proteins depends on their three-dimensional structure. Binding to other molecules and changes in conformation can lead to drastic modifications of protein function. The understanding of protein structures is the goal of structural biology. X-ray crystallography, nuclear magnetic resonance (NMR) and cryo-electron microscopy (EM) allow us to investigate the details of protein structure and function at an atomic level. Low resolution structural information can also be derived by numerous other techniques such as small-angle X-ray scattering (SAXS), negative stain EM, native and cross-linking mass spectrometry (MS) and hydrogen-deuterium (H/D) exchange.

Cell surface receptors

To function properly, cells need to be able to adapt to changes in their environment. In multicellular organisms, an important function of cell sensing is the communication with other cells to coordinate growth, migration, survival and differentiation (2). To do so, cells have specialized proteins called cell surface receptors, which have evolved to perform specific tasks. Different cell types express different surface receptors, allowing cells to differentiate their functions. Cell communication happens at multiple scales. Short distance cell-to-cell communication

relies on direct contact. Medium distance cell-to-cell signal transmission can be mediated by a local regulator, e.g. neurotransmitters in synapses. Long distance signals can be directed to multiple cells, e.g. hormones. For all these processes to take place, specific cell surface receptors need to interact with extracellular molecules. By recognizing selected ligands, cell surface receptors perform highly specialized functions such as endocytosis, signal transduction and cell-cell adhesion (3).

Cell surface receptors are generally formed by an extracellular domain which is responsible for ligand binding, a hydrophobic membrane-spanning region and an intracellular domain. The extent of each domain can vary widely depending on the type of receptor. Malfunctioning of cell surface receptors due to mutations or extrinsic factors can lead to disease. Therefore these molecules represent great opportunities for therapeutic intervention at a cellular level and have become the most important class of pharmacological targets.

Types of cell surface receptors

Receptor-mediated endocytosis is the process in which a ligand binds to a specific transmembrane receptor protein and enters the cell as a receptor-ligand complex. The mechanism of receptor-mediated endocytosis was first discovered in patients with a genetic predisposition for atherosclerosis (4). Cholesterol uptake is mostly carried out by hepatocytes via clathrin-coated pits. If this uptake is blocked, cholesterol accumulates in the blood vessels forming atherosclerotic plaques. Cholesterol is mainly transported in the form of cholesterol esters by low-density lipoproteins (LDL), which are recognized and taken up by the low-density lipoprotein receptor (LDLR) and other members of the same family (4,5). LDL-containing vesicles are directed to the endosomes where the LDL is released. Ultimately, the LDL is further transported to the lysosomes for degradation, while the LDLR can recycle back to the plasma membrane (6,7).

Cell signaling is the process that allows signals to be transmitted from the exterior to the interior of the cell to generate a specific response. Cell surface receptors involved in signal transduction can be divided in three main families according to their functions: ion-channel receptors, G-protein coupled receptors and enzyme-linked receptors. Ion-channel receptors or ligand-gated channels convert chemical signals into electrical ones. By binding to a ligand, these receptors undergo a conformational rearrangement that promotes the formation of a channel through the membrane which allows certain ions, mainly Na^+ , Ca^{2+} , K^+ or Cl^- , to go in or out of the cell. G-protein coupled receptors (GPCRs) are seven-transmembrane

domain receptors that can bind ligands that are very different in size, from small molecules to macromolecules, and undergo a conformational change that activates the heterotrimeric G protein (guanine-nucleotide binding protein). GPCRs play many important biological roles in signaling and development and are often involved in cancer. Around 40% of the current therapeutics target GPCRs.

Enzyme-linked receptors contain an enzymatically active domain or recruit enzymes after activation. The catalytic domain is usually localized in the intracellular region and undergoes a conformational change after a ligand binds the extracellular portion of the receptor. The most abundant enzyme-linked receptors are receptor tyrosine kinases (RTKs), which can be divided in 20 subfamilies in humans (8). All the RTKs share a similar architecture, which is highly conserved throughout evolution. They consist of a ligand-binding ectodomain, a single-transmembrane region and a cytoplasmic domain that contains the receptor tyrosine kinase. Since the discovery of their founding member epidermal growth factor receptor (EGFR) in 1982 (9), these receptors have been found involved in various critical cellular processes, such as proliferation, differentiation and survival (8). Mutations or abnormalities in RTKs that alter their function or cellular distribution are associated with several diseases (8).

A highly versatile endocytic receptor: LRP1

Cell surface receptors are usually able to bind a set of related ligands in a highly specific manner, fulfilling one particular function. This is not the case for multi-ligand receptors, which are able to interact specifically with structurally and functionally different classes of ligands (3), carrying out various biological functions. One such receptor is low-density lipoprotein receptor-related protein 1 (LRP1), a member of the LDL receptor family. This family is composed of seven structurally related proteins: LDL receptor, very-low-density lipoprotein (VLDL) receptor, LRP8/apolipoprotein E receptor 2, LRP4/MEGF7, LRP2/megalin, LRP1 and LRP1B (10) (Figure 1). Other, more distantly related members are LRP5, LRP6 and SorLa. While the LDLR is mainly involved in cholesterol homeostasis through receptor-mediated endocytosis of lipoprotein particles, the other members of the family are known to participate in various other physiological processes, including clearance of a variety of plasma components, blood coagulation, signal transduction and neurodevelopment (10). LRP1 is the largest member of the family, together with the highly homologous LRP2 and LRP1B, and it interacts with the largest variety of different ligands. LRP1 is able to bind, with high affinity, more than 30 functionally and structurally different ligands, including protein-

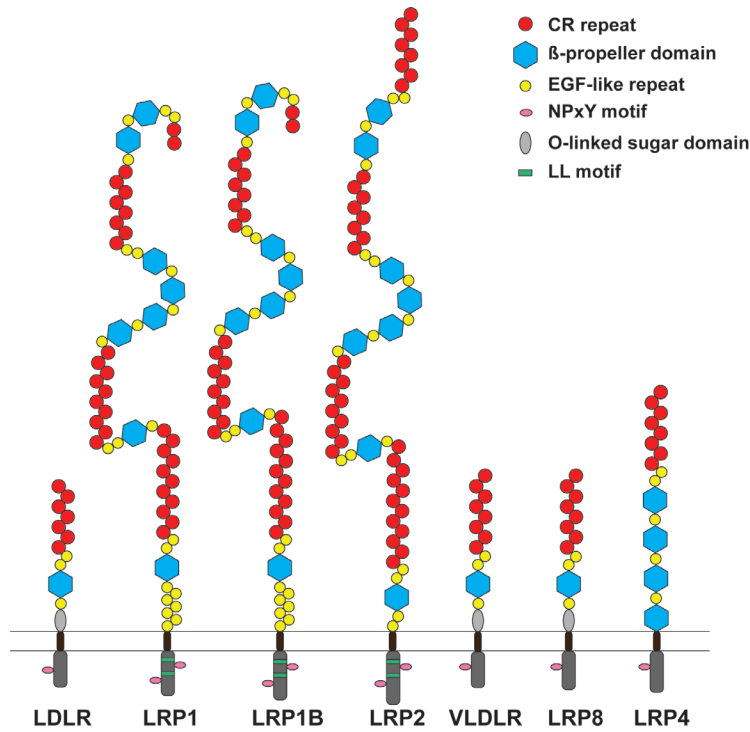


Figure 1. The LDL receptor family in mammals. Members of the LDL receptor family share common structural features including a single membrane anchor, complement-type cysteine-rich (CR) repeats, epidermal growth factor (EGF)-like repeats and YWTD six-bladed β -propellers. NPxY designates the four amino acid motif that can mediate clustering of the receptors into coated pits (23) or their interaction with adaptor and scaffold proteins (24,25). Di-leucine (LL) motifs serve mostly as endocytosis signals (26). O-linked sugar domains are found in some of the receptors. Figure adapted from (12).

ases, proteinase-inhibitor complexes, lipoproteins, extracellular matrix proteins, growth factors, toxins and viral proteins (11–18). LRP1 was first discovered as an endocytic receptor in the 1980's when a protein with an approximate mass of 500 kDa was discovered in complex with α -2-macroglobulin (α -2M) in rat and human liver membranes (19). Later studies found that this α -2M receptor was a member of the LDLR family and could also bind apolipoprotein E (13,20,21). Since then, LRP1 has been found involved in a variety of different biological processes besides endocytosis, such as cell signaling, embryonic development, cell migration and blood-brain barrier integrity (11,12,22).

How one receptor can bind so many different ligands with high specificity is still unclear, but its highly modular nature is likely to be of importance. Similar to the other members of the LDL receptor family, the LRP1 secondary structure consists

of a repetition of complement-type cysteine-rich (CR) repeats, epidermal growth factor (EGF) -like repeats, YWTD six-bladed β -propellers, a single membrane-spanning segment and a cytoplasmic tail that harbors two NPxY motifs (12). The CR repeats are commonly called ligand-binding repeats since they are responsible for binding most of the ligands. These repeats are grouped into four clusters containing up to eleven individual CR repeats. The regions consisting of two EGF-like repeats, a six-bladed YWTD β -propeller and an EGF-like repeat at the end are also referred to as EGF precursor homology regions (11). The importance of these regions has been associated to the uncoupling of the receptor from the ligand once in the endosomal compartments. In fact, when the EGF precursor homology region was deleted from the LDLR and the VLDLR, the receptors were not able to dissociate from their ligand cargo once in the endosomal compartments (4,27). According to the crystal structure of the LDLR at pH 5.3 (28) the two EGF-like repeats and the β -propeller domain interact with the CR repeats involved in ligand binding in a calcium dependent manner, leading to the hypothesis that the β -propeller domain functions as an 'internal ligand' once the receptor is in the low pH environment of the endosome, promoting the uncoupling of the cargo (28).

Structural studies on short fragments of LRP1 and other LDLR family members bound to ligand fragments have elucidated the general mechanism of ligand binding at atomic level, which seems to share similar recognition characteristics (29–36). The binding is based on the formation of salt bridges between aspartic acid residues from the CR repeats and lysine residues from the ligand. The aspartic acid residues are conserved and form a calcium-coordinating binding pocket. This interaction may be further stabilized by an aromatic residue which interacts with the aliphatic portion of the lysine and by other weaker interactions of lysines with acidic residues (37).

LRP1 broad ligand recognition allows for this receptor to function as a sensor of the cellular microenvironment and modulate cellular functions in response. By competitive binding to signaling molecules it can decrease the concentration of these molecules influencing the activity of specific signaling pathways (38). LRP1 has also been found to be involved in modulating signaling pathways through its intracellular domain (24,25,39). The cytoplasmic tail consists of ~100 amino acids and contains two di-leucine motifs that serve mostly as endocytosis signals (26), and two NPxY motifs that can interact with different adaptor and scaffold proteins (24,25). The intracellular domain has also been shown to have a role in transcription modulation (40). After intra-membrane proteolytic cleavage of the LRP1 ectodomain, the intracellular domain is transferred to the cell nucleus where it modulates gene expression (41). Moreover, LRP1 may regulate the activity of signaling pathways by controlling the abundance of certain receptors in

the plasma membrane (42,43). Although it appears that LRP1 can regulate cell signaling in multiple ways, its functional role as signaling molecule has not yet been completely understood.

Receptor tyrosine kinases: the HER family

The human genome contains 58 receptor tyrosine kinases, the vast majority of which is able to bind extracellular ligands called growth factors and promote signal transduction via auto-phosphorylation (44). Among the RTKs, the epidermal growth factor receptor family, also referred to as HER or ErbB family, is one of the most extensively studied for its role in development, physiology and human cancer (45). The EGF receptor family consists of four homologous members: EGFR (HER1 or ErbB1), HER2 (ErbB2), HER3 (ErbB3) and HER4 (ErbB4), which are ubiquitously expressed in epithelial, mesenchymal, cardiac and neuronal cells (46) (Figure 2). By recognizing and binding to a large family of growth factors, these receptors transduce signals into the cell, enabling communication that is crucial for development, growth and homeostasis of multicellular organisms (45). Aberrant signaling due to mutations, overexpression of receptors and self-production of certain growth factors characterizes many forms of cancer, making the HER receptor family an important therapeutic target.

The HER receptors are structurally related, containing a highly glycosylated ectodomain, a single-pass transmembrane domain, a cytosolic part which harbors a tyrosine kinase domain and a C-terminal tail. The extracellular region is composed of a tandem repeat of two leucine-rich domains (domains I and III) and two cysteine-rich domains (domains II and IV). Once a ligand binds to the leucine-rich domains the receptor changes its conformation in order to form homo- and heterodimers with other RTKs. The dimerization triggers the activation of the intracellular tyrosine kinase domain and the subsequent phosphorylation of the C-terminal tail (47). Phosphotyrosine residues then activate, either directly or through adaptor proteins, downstream signaling pathways, of which the mitogen-activated protein kinase (MAPK/ERK) proliferation pathway and the phosphatidylinositol 3-kinase (PI3K)/Akt survival pathway are the main ones (48,49). Numerous extracellular molecules have been described as ligands of the HER receptors. These molecules share a common EGF-like domain and are often synthesized as transmembrane precursors that release a soluble form after proteolytic cleavage (46,50) On the basis of their receptor specificity the EGF-like peptides are grouped in three classes. The first group includes EGF, transforming growth factor (TGF)- α , amphiregulin (AR), and epigen (EPG), which bind spe-

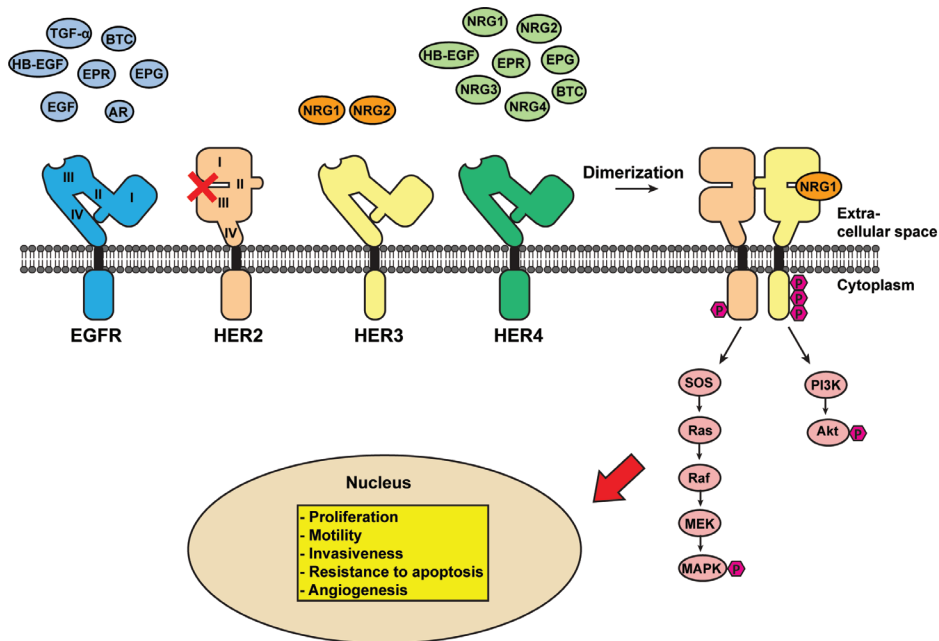


Figure 2. Members of the HER family and downstream signaling pathways. After a ligand binds to EGFR, HER3 or HER4 these receptors change conformation and expose the dimerization arm (domain II) enabling them to form homo- or heterodimers with another member of the family. Receptor dimerization results in phosphorylation of tyrosine residues in the carboxy-terminal domain, recruitment of signaling proteins and activation of several signaling pathways depending on the receptor and ligand combination. These pathways transmit signals to the cell nucleus and trigger gene transcription regulating proliferation and survival processes.

cifically to EGFR; the second group includes betacellulin (BTC), heparin-binding EGF (HB-EGF), and epiregulin (EPR), which bind both EGFR and HER4. The third group, the neuregulins (NRGs), forms two subgroups on the basis of their capacity to bind HER3 and HER4 (NRG-1 or HRG and NRG-2) or only HER4 (NRG-3 and NRG-4) (46,51,52). Interestingly, HER2 is the only member of the family for which no ligand has been found so far.

The mechanism by which the HER receptors transmit signals was firstly discovered for EGFR. The catalytic intracellular domain is activated after the formation of an asymmetric dimer (53) in which one kinase domain, ‘the activator’, allosterically activates the other kinase, ‘the receiver’. HER3 is a pseudokinase, or kinase-dead, because its intracellular kinase domain lacks several key conserved and catalytically important residues. However, although HER3 kinase domain is in an inactivated state, it has low residual kinase activity and can still act as an activator when dimerized with another receptor (54). Structural studies have re-

vealed that the HER receptors undergo major conformational changes connected to their functional role. The 'auto-inhibited' ligand-unbound conformation of EGFR, HER3 and HER4 is characterized by a tether between domain II and IV which buries the dimerization interface (55–57). After ligand binding the receptors acquire an open or un-tethered conformation that exposes the dimerization arm located in domain II (58–60). While two conformations have been described for EGFR, HER3 and HER4, HER2 has been shown to adopt only an open dimer-competent conformation (56). HER2 can activate its tyrosine kinase domain through auto-phosphorylation only after heterodimerization with another HER receptor bound to a ligand (61). Because of its constitutively activated state, HER2 is the preferred partner for ligand-induced heterodimerization, representing a potent signal amplifier (44). High expression levels of HER2 are often found in human canThe preferred dimerization partner for HER2 is HER3. Despite the fact that HER2 and HER3 have been referred to as 'the deaf and the dumb' (64), because of HER2 inability to bind any ligand and HER3 kinase-inactivity, they represent the most potent signaling pair within the HER family (49,65–67). When HER3 has dimerized with HER2, the binding affinity for heregulin (HRG) is several-fold higher than in HER3 monomers (68). High levels of HRG have been associated with higher tumor aggressiveness and drug-resistance due to activation of HER3 autocrine signaling (69,70). Although only discovered later (the HER3 gene was discovered in 1989), HER3 is now considered a key player in tumors where EGFR or HER2 are overexpressed (67,71) due to its ability to directly activate the strong PI3K/Akt survival pathway (72).

Understanding the cross-talk and signal plasticity in these receptors is of crucial importance for the development of better anticancer therapeutics, since if signaling by one receptor is blocked, another one may be able to compensate, resulting in therapeutic unresponsiveness (44,73).

Protein engineering in drug development: bispecific antibodies

Antibodies, or immunoglobulins (Igs), are a class of proteins secreted by plasma cells that play a key role in the immune response by recognizing and neutralizing specific targets called antigens. Antigens are broadly described as any substance that can trigger the immune system, from very simple to highly complex molecules (74). Antibodies protect the host from invading pathogens in different ways. They can directly inactivate their target, e.g. by coating the surface of a virus to prevent the initiation of a productive infection (neutralization). Antibodies can also mark pathogens for destruction by opsonization and recruit phagocytic cells

to ingest them. Moreover, antibodies may activate the complement system to aid the destruction of pathogens.

Antibodies are formed by four polypeptide chains organized around a two-fold symmetry axis: two identical heavy chains (HCs) and two identical smaller light chains (LCs) held together by disulfide bonds, forming a flexible “Y” shaped molecule (75). The N-terminal region of each chain contains a variable domain that binds the antigen, while the C-terminal domains form the constant regions that can assume only five major forms (isotypes), and are responsible of engaging effector mechanisms. The antigen-binding sites consist of six hypervariable loops in the variable domains of the heavy and light chains located at the tip of the two antibody ‘arms’, in a region called the fragment of antigen binding (Fab). These loops, defined as the complementarity-determining regions (CDRs) can harbor an almost infinite variety of sequences, arranged in unique conformations that allow immunoglobulins to recognize an almost equally vast variety of antigens (76).

In the last decades antibodies have been discovered as powerful bio-therapeutics for the treatment of cancer and immunological diseases (77), becoming among the most successful classes of protein therapeutics (78,79). The modes of actions of therapeutic antibodies involve several mechanisms; immune mechanisms consisting of activation of antibody-dependent cell-mediated cytotoxicity, complement-dependent cytotoxicity and T-cell function regulation or mechanisms that interfere directly with tumorigenesis pathways, such as triggering apoptosis, inhibiting or activating signaling cascades and promoting receptor internalization (79,80). This multifaceted approach combined with a high degree of target specificity makes antibodies able to elicit potent anti-tumor effects (81).

A detailed knowledge of antibody structure and activity has allowed the engineering of primary antibodies to improve their anti-tumor properties developing numerous antibody-like molecules (82). One of the most recent advances in therapeutic antibody engineering is the creation of dual-target or bispecific antibodies (bAbs). This technology takes advantage of the natural bivalency of the IgG molecule by producing engineered molecules that can bind two different antigens, yielding potentially better therapeutic efficacy and novel mechanisms of action than inhibition of a single target (83). By recognizing two different targets, bAbs can have a wide range of applications such as redirecting immune cells to tumor cells to enhance killing (84) or simultaneous blocking of two antigens involved in different tumorigenesis mechanisms (85). Moreover, by binding multiple antigens present of the tumor cell surface bAbs allow for increased binding specificity of cancer cells (86), which usually show different protein expression patterns on their surface compared to normal cells. In this way, bispecific antibodies may help reducing drug-related side effects due to off-targeting. For complex multi-

factorial diseases such as cancer and inflammatory disorders, targeting different pathological pathways may result in improved therapeutic efficacy compared to monospecific antibodies (87). Moreover, the development of bispecific antibodies is a promising approach for treating cancers that have developed resistance to targeted mono-therapies (88). Some cancer cells are able to modify their gene expression or signaling pathways in order to bypass the effect of drugs, which might necessitate the use of drugs combinations. Dual-targeting molecules are seen as a preferred alternative to antibody cocktails because of their potentially higher tumor selectivity and enhanced functionality (89). Furthermore, manufacturing and clinical testing must be done with only one molecule instead of two, easing the developmental and regulatory process (87).

Bispecific antibodies can be developed using different approaches. Antibody fragments such as single chain variable-fragment (scFv) or Fab can be attached to the N- or C-terminal (90–94) of the full-length Ig (95) or the binding regions can be modified in order to change their specificity for different antigens in an asymmetric way (73). The first bispecific antibodies were created at the beginning of the 1980's, using chemical cross-linking (96,97) or by somatic fusion of two different hybridoma cell lines (quadroma or hybrid hybridomas) (98). The major limitations were the difficulty of producing large, homogeneous batches (99). In the 1990's innovative DNA-engineering solutions provided the possibility to produce single antibody chains or fragments recombinantly, allowing for higher and more homogeneous production (100).

However, when engineered antibody formats are too different from the natural antibody architecture, problems with stability and pharmacokinetic properties of the molecule may arise (101). Therefore, it is desirable to develop bispecific molecules that are as close as possible to a conventional Ig structure. The assembly of natural antibodies depends on homodimerization of two identical heavy chains and subsequently disulfide linkages between each heavy and light chain. In order to develop asymmetric antibodies the pairing of the two different HCs and of the two LCs with the correct HCs need to be addressed. Co-expression of two different heavy chains may lead to a mixture of equally probable combinations of homo- and heterodimers. Additionally, the light chains can mispair with the incorrect heavy chains. Therefore, many unwanted species may be produced besides the desired bispecific antibody (102). For the "light chain problem" the most common adopted strategy is the use of antibodies with a common light chain identified by phage display libraries or by immunization of transgenic animals (103). To overcome the heavy chain-pairing issue an efficient approach is engineering the heavy chain domains in the constant region of the antibody, called crystallizable fragment (Fc) region, to selectively promote the dimerization

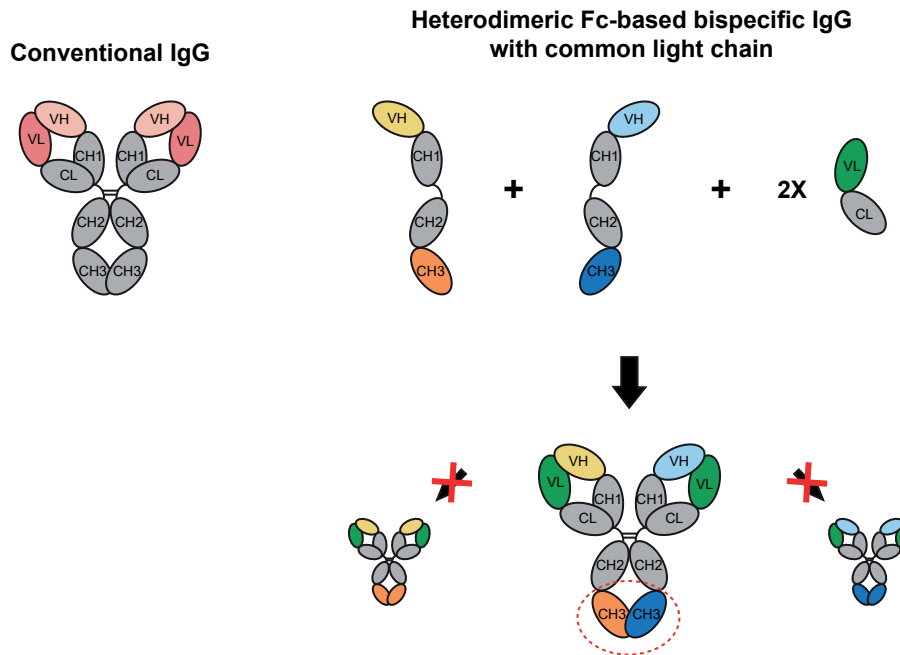


Figure 3. Assembly of a heterodimeric Fc-based bispecific IgG with a common light chain. The CH3 domains of the Fc region of the IgG are engineered to introduce asymmetric mutations, which promote two different heavy chains (HCs) to be assembled together, while disfavoring homodimerization between the same HCs.

of different heavy chains (Figure 3). To do so, various engineering strategies based on the introduction of asymmetric mutations at the two sides of the Fc dimerization interface (104) have been developed.

Scope of the thesis

This thesis aims to investigate the structure and function of a set of human cell surface receptors, using a combination of biological, biochemical and structural techniques.

Chapter 2 focuses on the study of the endocytic receptor LRP1. It describes the production of this unusually large protein and the investigation of its structural features and pH-dependent behavior employing SAXS, surface plasmon resonance (SPR), negative stain EM, native and cross-linking MS.

Chapter 3 illustrates the preclinical development of a novel bispecific antibody (PB4188 or MCLA128) targeting the RTKs HER2 and HER3. The X-ray crystal

structures of the extracellular domains of these receptors in complex with the respective Fabs, together with *in vitro* and *in vivo* experimental assays, shed light on the mechanism of action of this promising anticancer therapeutic, which is currently undergoing clinical trials.

Chapter 4 presents the engineering process that led to the development of MCLA128. A multifaceted approach including computational, biochemical and X-ray crystallography studies contributed to the identification of mutations promoting efficient Fc heterodimerization, which, together with a common light chain approach, resulted in a stable scaffold for bispecific IgG production.

Chapter 5 discusses the implications and the significance of the results presented in this thesis.

References

1. Braun, P., and Gingras, A. C. (2012) History of protein-protein interactions: From egg-white to complex networks. *Proteomics* **12**, 1478–1498
2. Heldin, C.-H., Lu, B., Evans, R., and Gutkind, J. S. (2016) Signals and Receptors. *Cold Spring Harb. Perspect. Biol.* **8**, a005900
3. Krieger, M., and Stern, D. M. (2001) Multiligand receptors and human disease. *J Clin. Invest.* **108**, 645–647
4. Davis, C. G., Goldstein, J. L., Südhof, T. C., Anderson, R. G. W., Russell, D. W., and Brown, M. S. (1987) Acid-dependent ligand dissociation and recycling of LDL receptor mediated by growth factor homology region. *Nature* **326**, 760–765
5. Brown, M. S., and Goldstein, J. L. (1986) Receptor-mediated pathway for cholesterol homeostasis. *Science* **232**, 34–47
6. Goldstein, J. L., Brown, M. S., Anderson, R. G. W., Russell, D. W., and Schneider, W. J. (1985) Receptor-mediated endocytosis: concepts emerging from the LDL receptor system. *Ann. Rev. Cell Biol.* **1**, 1–39
7. Blacklow, S. C. (2007) Versatility in ligand recognition by LDL receptor family proteins: advances and frontiers. *Curr. Opin. Struct. Biol.* **17**, 419–426
8. Lemmon, M. A., and Schlessinger, J. (2010) Cell signaling by receptor tyrosine kinases. *Cell* **141**, 1117–1134
9. Cohen, S., Fava, R. A., and Sawyer, S. T. (1982) Purification and characterization of epidermal growth factor receptor/protein kinase from normal mouse liver. *Proc. Natl. Acad. Sci. USA* **79**, 6237–6241
10. Herz, J., Chen, Y., Masiulis, I., and Zhou, L. (2009) Expanding functions of lipoprotein receptors. *J. Lipid Res.* **50**, S287–S292
11. Herz, J., and Strickland, D. K. (2001) Multiligand receptors LRP : a multifunctional scavenger and signaling receptor. *J. Clin. Invest.* **108**, 779–784
12. Lillis, A. P., van Duyn, L. B., Murphy-Ullrich, J. E., and Strickland, D. K. (2008) LDL receptor-related protein 1: unique tissue-specific functions revealed by selective gene knock-out studies. *Physiol. Rev.* **88**, 887–918
13. Beisiegel, U., Weber, W., Ihrke, G., Herz, J., and Stanley, K. K. (1989) The LDL-receptor-related protein, LRP, is an apolipoprotein E-binding protein. *Nature* **341**, 162–164
14. Strickland, D. K., Ashcom, J. D., Williams, S., Burgess, W. H., Migliorini, M., and Argraves, W. S. (1990) Sequence identity between the alpha-2-macroglobulin receptor and low density lipoprotein receptor-related protein suggests that this molecule is a multifunctional receptor. *J. Biol. Chem.* **265**, 17401–17405
15. Herz, J., Clouthier, D. E., and Hammer, R. E. (1992) LDL receptor-related protein internalizes and degrades uPA-PAI-1 complexes and is essential for embryo implantation. *Cell* **71**, 411–421
16. Scilabra, S. D., Troeberg, L., Yamamoto, K., Emonard, H., Thøgersen, I., Enghild, J. J., Strickland, D. K., and Nagase, H. (2013) Differential regulation of extracellular tissue inhibitor of metalloproteinases-3 levels by cell membrane-bound and shed low density lipoprotein receptor-related protein 1. *J. Biol. Chem.* **288**, 332–342
17. Hofer, F., Gruenberger, M., Kowalski, H., Machat, H., Huettingert, M., Kuechler, E., and Blas, D. (1994) Members of the low density lipoprotein receptor family mediate cell entry of a minor-group common cold virus. *Proc. Natl. Acad. Sci. USA* **91**, 1839–1842
18. Kounnas, M. Z., Morris, R. E., Thompson, M. R., FitzGerald, D. J., and Saelinger, C. B. (1992) The alpha-2-macroglobulin receptor/low density lipoprotein receptor-related protein binds and internalizes Pseudomonas exotoxin A. *J. Biol. Chem.* **267**, 12420–12423

19. Gliemann, J., Davidsen, O., and Moestrup, S. K. (1989) Characterization, size estimation and solubilization of alpha-macroglobulin complex receptors in liver membranes. *Biochim. Biophys. Acta* **980**, 326–332
20. Herz, J., Hamann, U., Rogne, S., Myklebost, O., Gausepohl, H., and Stanley, K. (1988) Surface location and high affinity for calcium of a 500-kd liver membrane protein closely related to the LDL-receptor suggest a physiological role as lipoprotein receptor. *EMBO J.* **7**, 4119–4127
21. Kristensen, T., Moestrup, S. K., Glieman, J., Bendtsen, L., Sand, O., and Sottrup-Jensen, L. (1990) Evidence that the newly cloned low-density-lipoprotein receptor related protein (LRP) is the alpha-2-macroglobulin receptor. *FEBS*. **276**, 151–155
22. Moestrup, S. K., Gliemann, J., and Pallesen, G. (1992) Distribution of the alpha-2-macroglobulin receptor/low density lipoprotein receptor-related protein in human tissues. *Cell Tissue Res.* **269**, 375–382
23. Chen, W.-J., Goldstein, J. L., and Brown, M. S. (1990) NPXY, a sequence often found in cytoplasmic tails, is required for coated pit-mediated internalization of the low density lipoprotein receptor. *J. Biol. Chem.* **265**, 3116–3123
24. Mikhailenko, I., Considine, W., Argraves, K. M., Loukinov, D., Hyman, B. T., and Strickland, D. K. (1999) Functional domains of the very low density lipoprotein receptor: molecular analysis of ligand binding and acid-dependent ligand dissociation mechanisms. *J. Cell Sci.* **3281**, 3269–3281
25. Rudenko, G., Henry, L., Henderson, K., Ichtchenko, K., Brown, M. S., Goldstein, J. L., and Deisenhofer, J. (2002) Structure of the LDL receptor extracellular domain at endosomal pH. *Science* **298**, 2353–2358
26. Dolmer, K., Huang, W., and Gettins, P. G. W. (2000) NMR solution structure of complement-like repeat CR3 from the low density lipoprotein receptor-related protein: evidence for specific binding to the receptor binding domain of human alpha-2-macroglobulin. *J. Biol. Chem.* **275**, 3264–3269
27. Fisher, C., Beglova, N., and Blacklow, S. C. (2006) Structure of an LDLR-RAP complex reveals a general mode for ligand recognition by lipoprotein receptors. *Mol. Cell.* **22**, 277–283
28. Guttman, M., Prieto, J. H., Handel, T. M., Domaille, P. J., and Komives, E. A. (2010) Structure of the minimal interface between ApoE and LRP. *J. Mol. Biol.* **398**, 306–319
29. Jensen, G. A., Andersen, O. M., Bonvin, A. M. J. J., Bjerrum-Bohr, I., Etzerodt, M., Thøgersen, H. C., O’Shea, C., Poulsen, F. M., and Kragelund, B. B. (2006) Binding site structure of one LRP–RAP complex: implications for a common ligand–receptor binding motif. *J. Mol. Biol.* **362**, 700–716
30. Yasui, N., Nogi, T., Kitao, T., Nakano, Y., Hattori, M., and Takagi, J. (2007) Structure of a receptor-binding fragment of reelin and mutational analysis reveal a recognition mechanism similar to endocytic receptors. *Proc. Natl. Acad. Sci. USA* **104**, 9988–9993
31. Verdager, N., Fita, I., Reithmayer, M., Moser, R., and Blaas, D. (2004) X-ray structure of a minor group human rhinovirus bound to a fragment of its cellular receptor protein. *Nat. Struct. Mol. Biol.* **11**, 429–434
32. Lee, C.-J., De Biasio, A., and Beglova, N. (2010) Mode of interaction between beta-2GPI and lipoprotein receptors suggests mutually exclusive binding of beta-2GPI to the receptors and anionic phospholipids. *Structure* **18**, 366–376
33. Dagil, R., O’Shea, C., Nykjær, A., Bonvin, A. M. J. J., and Kragelund, B. B. (2013) Gentamicin binds to the megalin receptor as a competitive inhibitor using the common ligand binding motif of complement type repeats. *J. Biol. Chem.* **288**, 4424–4435
34. Strickland, D. K., Au, D. T., Cunfer, P., and Muratoglu, S. C. (2014) Low-density lipoprotein receptor-related protein-1 role in regulation of vascular integrity. *Arter. Thromb. Vasc. Biol.* **34**, 487–499

35. Gonias, S. L., and Campana, W. M. (2014) LDL receptor-related protein-1 a regulator of inflammation in atherosclerosis, cancer, and injury to the nervous system. *Am. J. Pathol.* **184**, 18–27
36. Gotthardt, M., Trommsdorff, M., Nevitt, M. F., Shelton, J., Richardson, J. A., Stockinger, W., Nimpf, J., and Herz, J. (2000) Interactions of the low density lipoprotein receptor gene family with cytosolic adaptor and scaffold proteins suggest diverse biological functions in cellular communication and signal transduction. *J. Biol. Chem.* **275**, 25616–25624
37. Trommsdorff, M., Borg, J., Margolis, B., and Herz, J. (1998) Interaction of cytosolic adaptor proteins with neuronal apolipoprotein E receptors and the amyloid precursor protein. *J. Biol. Chem.* **273**, 33556–33560
38. Loukinova, E., Ranganathan, S., Kuznetsov, S., Gorlatova, N., Migliorini, M. M., Loukinov, D., Ulery, P. G., Mikhailenko, I., Lawrence, D. A., and Strickland, D. K. (2002) Platelet-derived growth factor (PDGF)-induced tyrosine phosphorylation of the low density lipoprotein receptor-related protein (LRP). *J. Biol. Chem.* **277**, 15499–15506
39. Li, Y., Marzolo, M. P., van Kerkhof, P., Strous, G. J., and Bu, G. (2000) The YXXL motif, but not the two NPXY motifs, serves as the dominant endocytosis signal for low density lipoprotein receptor-related protein. *J. Biol. Chem.* **275**, 17187–17194
40. Kinoshita, A., Shah, T., Tangredi, M. M., Strickland, D. K., and Hyman, B. T. (2003) The intracellular domain of the low density lipoprotein receptor-related protein modulates trans-activation mediated by amyloid precursor protein and Fe65. *J. Biol. Chem.* **278**, 41182–41188
41. Zurhove, K., Nakajima, C., Herz, J., Bock, H. H., and May, P. (2008) Gamma-secretase mediates self-limitation of the inflammatory response by processing LRP1. *Sci. Signal.* **1**, 1–24
42. Gonias, S. L., Wu, L., and Salicioni, A. M. (2004) Low density lipoprotein receptor-related protein: regulation of the plasma membrane proteome. *Thromb. Haemost.* **91**, 1056–1064
43. Gaultier, A., Arandjelovic, S., Li, X., Janes, J., Dragojlovic, N., Zhou, G. P., Dolkas, J., Myers, R. R., Gonias, S. L., and Campana, W. M. (2008) A shed form of LDL receptor-related protein-1 regulates peripheral nerve injury and neuropathic pain in rodents. *J. Clin. Invest.* **118**, 161–172
44. Yarden, Y., and Pines, G. (2012) The ERBB network: at last, cancer therapy meets systems biology. *Nat. Rev.* **12**, 553–563
45. Wieduwilt, M. J., and Moasser, M. M. (2008) The epidermal growth factor receptor family: biology driving targeted therapeutics. *Cell. Mol. Life Sci.* **65**, 1566–1584
46. Hynes, N. E., and Lane, H. A. (2005) ERBB receptors and cancer: the complexity of targeted inhibitors. *Nat. Rev.* **5**, 341–354
47. Linggi, B., and Carpenter, G. (2006) ErbB receptors: new insights on mechanisms and biology. *Trends Cell Biol.* **16**, 649–656
48. Yarden, Y. (2001) The EGFR family and its ligands in human cancer: signalling mechanisms and therapeutic opportunities. *Eur. J. Cancer.* **37**, 3–8
49. Baselga, J., and Swain, S. M. (2009) Novel anticancer targets: revisiting ERBB2 and discovering ERBB3. *Nat. Rev.* **9**, 463–475
50. Massague, J., and Pandiella, A. (1993) Membrane-anchored growth factors. *Annu. Rev. Biochem.* **62**, 515–41
51. Hynes, N. E., and MacDonald, G. (2009) ErbB receptors and signaling pathways in cancer. *Curr. Opin. Cell Biol.* **21**, 177–184
52. Harris, R. C., Chung, E., and Coffey, R. J. (2003) EGF receptor ligands. *Exp. Cell Res.* **284**, 2–13
53. Zhang, X., Gureasko, J., Shen, K., Cole, P. A., and Kuriyan, J. (2006) An allosteric mechanism for activation of the kinase domain of epidermal growth factor receptor. *Cell* **125**, 1137–1149

54. Shi, F., Telesco, S. E., Liu, Y., Radhakrishnan, R., and Lemmon, M. A. (2010) ErbB3/HER3 intracellular domain is competent to bind ATP and catalyze autophosphorylation. *Proc. Natl. Acad. Sci. USA* **107**, 7692–7697
55. Ferguson, K. M., Berger, M. B., Mendrola, J. M., Cho, H., Leahy, D. J., and Lemmon, M. A. (2003) EGF activates its receptor by removing interactions that autoinhibit ectodomain dimerization. *Mol. Cell* **11**, 507–517
56. Cho, H.-S., and Leahy, D. J. (2002) Structure of the extracellular region of HER3 reveals an interdomain tether. *Science* **297**, 1330–1333
57. Bouyain, S., Longo, P. A., Li, S., Ferguson, K. M., and Leahy, D. J. (2005) The extracellular region of ErbB4 adopts a tethered conformation in the absence of ligand. *Proc. Natl. Acad. Sci. USA* **102**, 15024–15029
58. Ogiso, H., Ishitani, R., Nureki, O., Fukai, S., Yamanaka, M., Kim, J.-H., Saito, K., Sakamoto, A., Inoue, M., Shirouzu, M., and Yokoyama, S. (2002) Crystal structure of the complex of human epidermal growth factor and receptor extracellular domains. *Cell* **110**, 775–787
59. Liu, P., Cleveland IV, T. E., Bouyain, S., Byrne, P. O., Longo, P. A., and Leahy, D. J. (2012) A single ligand is sufficient to activate EGFR dimers. *Proc. Natl. Acad. Sci. USA* **109**, 10861–10866
60. Dawson, J. P., Bu, Z., and Lemmon, M. A. (2007) Ligand-induced structural transitions in ErbB receptor extracellular domains. *Structure* **15**, 942–954
61. Karamouzis, M. V., Dalagiorgou, G., Georgopoulou, U., Nonni, A., Kontos, M., and Papavasiliou, A. G. (2016) HER-3 targeting alters the dimerization pattern of ErbB protein family members in breast carcinomas. *Oncotarget* **7**, 5576–5597
62. Slamon, D. J., Clark, G. M., Wong, S. G., Levin, W. J., Ullrich, A., and McGuire, W. L. (1987) Human breast cancer: correlation of relapse and survival with amplification of the HER2/neu oncogene. *Science* **235**, 177–182
63. Arteaga, C. L., and Engelman, J. A. (2014) ERBB receptors: from oncogene discovery to basic science to mechanism-based cancer therapeutics. *Cancer Cell* **25**, 282–303
64. Citri, A., Skaria, K. B., and Yarden, Y. (2003) The deaf and the dumb: the biology of ErbB-2 and ErbB-3. *Exp. Cell Res.* **284**, 54–65
65. Pinkas-Kramarski, R., Eilam, R., Spiegler, O., Lavi, S., Liu, N., Chang, D., Wen, D., Schwartz, M., and Yarden, Y. (1994) Brain neurons and glial cells express Neu differentiation factor/heregulin: a survival factor for astrocytes. *Proc. Natl. Acad. Sci. USA* **91**, 9387–9391
66. Arkhipov, A., Shan, Y., Kim, E. T., Dror, R. O., and Shaw, D. E. (2013) Her2 activation mechanism reflects evolutionary preservation of asymmetric ectodomain dimers in the human EGFR family. *Elife* **2**, e00708
67. Holbro, T., Beerli, R. R., Maurer, F., Koziczak, M., Barbas III, C. F., and Hynes, N. E. (2003) The ErbB2/ErbB3 heterodimer functions as an oncogenic unit : ErbB2 requires ErbB3 to drive breast tumor cell proliferation. *Proc. Natl. Acad. Sci. USA* **100**, 8933–8938
68. Sliwkowski, M. X., Schaefer, G., Akita, R., Lofgren, J. A., Fitzpatrick, V. D., Nuijens, A., Fendly, B. M., Cerione, R. A., Vandlen, R. L., and Carraway III, K. L. (1994) Coexpression of erbB2 and erbB3 protein reconstitutes a high affinity receptor for heregulin. *J. Biol. Chem.* **269**, 14661–14665
69. Lupu, R., Cardillo, M., Cho, C., Harris, L., Hijazi, M., Perez, C., Rosenberg, K., Yang, D., and Tang, C. (1996) The significance of resistance heregulin in breast cancer tumor progression and drug. *Breast Cancer Res. Treat.* **38**, 57–66
70. Ritter, C. A., Perez-Torres, M., Rinehart, C., Guix, M., Dugger, T., Engelman, J. A., and Arteaga, C. L. (2007) Human breast cancer cells selected for resistance to trastuzumab in vivo overexpress epidermal growth factor receptor and ErbB ligands and remain dependent on the ErbB receptor network. *Clin. Cancer Res.* **13**, 4909–4920

71. Soler, M., Mancini, F., Meca-Corted, O., Sanchez-Cid, L., Rubio, N., Lopez-Fernandez, S., Lonzano, J. J., Blanco, J., Fernandez, P. L., and Thomson, T. M. (2009) HER3 is required for the maintenance of neuregulin-dependent and -independent attributes of malignant progression in prostate cancer cells. *Int. J. Cancer* **125**, 2565–2575
72. Amin, D. N., Campbell, M. R., and Moasser, M. M. (2010) The role of HER3, the unpretentious member of the HER family, in cancer biology and cancer therapeutics. *Semin. Cell Dev. Biol.* **21**, 944–950
73. Malm, M., Frejd, F. Y., Ståhl, S., and Löfblom, J. (2016) Targeting HER3 using mono- and bispecific antibodies or alternative scaffolds. *MAbs* **8**, 1195–1209
74. Delves, P. J., and Roitt, I. M. (2000) The immune system. *N. Engl. J. Med.* **343**, 37–49
75. Waxdal, M. J., Konigsberg, W. H., Henley, W. L., and Edelman, G. M. (1968) The covalent structure of a human gamma G-immunoglobulin. II. Isolation and characterization of the cyanogen bromide fragments. *Biochemistry* **7**, 1959–1966
76. Tonegawa, S. (1983) Somatic generation of antibody diversity. *Nature* **302**, 575–581
77. Reichert, J. M. (2008) Monoclonal antibodies as innovative therapeutics. *Curr. Pharm. Biotechnol.* **9**, 423–430
78. Aggarwal, S. (2007) What's fueling the biotech engine? *Nat. Biotechnol.* **25**, 1097–1104
79. Scott, A. M., Allison, J. P., and Wolchok, J. D. (2012) Monoclonal antibodies in cancer therapy. *Cancer Immunol.* **12**, 14–21
80. Ben-Kasus, T., Schechter, B., Sela, M., and Yarden, Y. (2007) Cancer therapeutic antibodies come of age: targeting minimal residual disease. *Mol. Oncol.* **1**, 42–54
81. Shuptrine, C. W., Surana, R., and Weiner, L. M. (2012) Monoclonal antibodies for the treatment of cancer. *Semin. Cancer Biol.* **22**, 3–13
82. Weiner, L. M., Surana, R., and Wang, S. (2010) Monoclonal antibodies: versatile platforms for cancer immunotherapy. *Nat. Rev. Immunol.* **10**, 317–327
83. Spiess, C., Merchant, M., Huang, A., Zheng, Z., Yang, N.-Y., Peng, J., Ellerman, D., Shatz, W., Reilly, D., Yansura, D. G., and Scheer, J. M. (2013) Bispecific antibodies with natural architecture produced by co-culture of bacteria expressing two distinct half-antibodies. *Nat. Biotechnol.* **31**, 753–758
84. Satta, A., Mezzanzanica, D., Turatti, F., Canevari, S., and Figini, M. (2013) Redirection of T-cell effectors functions for cancer therapy: bispecific antibodies and chimeric antigen receptors. *Futur. Oncol.* **9**, 527–539
85. Fan, D., Li, W., Yang, Y., Zhang, X., Zhang, Q., Yan, Y., Yang, M., Wang, J., and Xiong, D. (2015) Redirection of CD4+ and CD8+ T lymphocytes via an anti-CD3 × anti-CD19 bispecific antibody combined with cytosine arabinoside and the efficient lysis of patient-derived B-ALL cells. *J. Hematol. Oncol.* **8**, :108
86. Fan, G., Wang, Z., Hao, M., and Li, J. (2015) Bispecific antibodies and their applications. *J. Hematol. Oncol.* **8**, :130
87. Kontermann, R. (2012) Dual targeting strategies with bispecific antibodies. *MAbs* **4**, 182–197
88. Weidle, U. H., Kontermann, R. E., and Brinkmann, U. (2014) Tumor-antigen-binding bispecific antibodies for cancer treatment. *Semin. Oncol.* **41**, 653–660
89. Chan, A. C., and Carter, P. J. (2010) Therapeutic antibodies for autoimmunity and inflammation. *Nat. Rev. Immunol.* **10**, 301–316
90. Shalaby, M. R., Shepard, H. M., Presta, L., Rodrigues, M. L., Beverley, S. P. C. L., Feldmann, M., and Carter, P. (1992) Development of humanized bispecific antibodies reactive with cytotoxic lymphocytes and tumor cells overexpressing the HER2 protooncogene. *J. Exp. Med.* **175**, 217–225
91. Keler, T., Graziano, R. F., Mandal, A., Wallace, P. K., Fisher, J., Guyre, P. M., Fanger, M. W., and Deo, Y. M. (1997) Bispecific antibody-dependent cellular cytotoxicity of HER2/

- neu-overexpressing tumor cells by Fc γ receptor type I-expressing effector cells. *Cancer Res.* **57**, 4008–4015
92. Shahied, L. S., Tang, Y., Alpaugh, R. K., Somer, R., Greenspon, D., and Weiner, L. M. (2004) Bispecific minibodies targeting HER2/neu and CD16 exhibit improved tumor lysis when placed in a divalent tumor antigen binding format. *J. Biol. Chem.* **279**, 53907–53914
 93. Mølthøj, M., Crommer, S., Brischwein, K., Rau, D., Sriskandarajah, M., Hoffmann, P., Kufer, P., Hofmeister, R., and Baeuerle, P. A. (2007) CD19-/CD3-bispecific antibody of the BiTE class is far superior to tandem diabody with respect to redirected tumor cell lysis. *Mol. Immunol.* **44**, 1935–1943
 94. Robinson, M., Hodge, K., Horak, E., Sundberg, A., Russeva, M., Shaller, C. C., von Mehren, M., Shchaveleva, I., Simmons, H., Marks, J., and Adams, G. (2008) Targeting ErbB2 and ErbB3 with a bispecific single-chain Fv enhances targeting selectivity and induces a therapeutic effect in vitro. *Br. J. Cancer.* **99**, 1415–1425
 95. Weiner, L. M., Holmes, M., Richeson, A., Godwin, A., Adams, G. P., Hsieh-Ma, S. T., Ring, D. B., and Alpaugh, R. K. (1993) Binding and cytotoxicity characteristics of the bispecific murine monoclonal antibody 2B1. *J. Immunol.* **151**, 2877–2886
 96. Brennan, M., Davison, P. F., and Paulus, H. (1985) Preparation of bispecific antibodies by chemical recombination of monoclonal immunoglobulin G1 fragments. *Science* **229**, 81–83
 97. Glennie, M. J., McBride, M., Worth, T., and Stevenson, G. T. (1987) Preparation and performance of bispecific F(ab' γ)₂ antibody containing thioether-linked Fab' γ fragments. *J. Immunol.* **139**, 2367–2375
 98. Milstein, C., and Cuello, A. C. (1983) Hybrid hybridomas and their use in immunohistochemistry. *Nature* **305**, 537–540
 99. Chames, P., and Baty, D. (2009) Bispecific antibodies for cancer therapy: the light at the end of the tunnel? *MAbs* **1**, 539–547
 100. Carter, P., Ridgway, J., and Zhu, Z. (1995) Toward the production of bispecific antibody fragments for clinical applications. *J. Hematother.* **4**, 463–470
 101. Ha, J.-H., Kim, J.-E., and Kim, Y. S. (2016) Immunoglobulin Fc heterodimer platform technology: from design to applications in therapeutic antibodies and proteins. *Front. Immunol.* **7**, 394
 102. Spiess, C., Zhai, Q., and Carter, P. J. (2015) Alternative molecular formats and therapeutic applications for bispecific antibodies. *Mol. Immunol.* **67**, 95–106
 103. Klein, C., Sustmann, C., Thomas, M., Stubenrauch, K., Croasdale, R., Schanzer, J., Brinkmann, U., Kettenberger, H., Regula, J. T., and Schaefer, W. (2012) Progress in overcoming the chain association issue in bispecific heterodimeric IgG antibodies. *MAbs* **4**, 653–663
 104. Von Kreudenstein, T. S., Lario, P. I., and Dixit, S. B. (2014) Protein engineering and the use of molecular modeling and simulation: the case of heterodimeric Fc engineering. *Methods* **65**, 77–94

CHAPTER 2

Recombinant expression of the full-length ectodomain of LDL receptor-related protein 1 (LRP1) unravels pH dependent conformational changes and the stoichiometry of binding with receptor-associated protein (RAP)

Camilla De Nardis¹, Philip Lössl², Maartje van den Biggelaar³, Pramod K. Madoori¹, Nadia Leloup¹, Koen Mertens^{3,4}, Albert J.R. Heck² and Piet Gros¹

¹Crystal & Structural Chemistry, Bijvoet Center for Biomolecular Research, Utrecht University, Utrecht, The Netherlands

²Biomolecular Mass Spectrometry & Proteomics and Netherlands Proteomics Center, Bijvoet Center for Biomolecular Research and Utrecht Institute for Pharmaceutical Sciences, Utrecht University, Utrecht, The Netherlands

³Department of Plasma Proteins, Sanquin Research, Amsterdam, The Netherlands

⁴Department of Pharmaceutics, Utrecht Institute for Pharmaceutical Sciences, Utrecht University, Utrecht, The Netherlands

This chapter has been published in *Journal of Biological Chemistry* (2017) **292**, 912-924

Abstract

LDL receptor-related protein 1 (LRP1) is a highly modular protein and the largest known mammalian endocytic receptor. LRP1 binds and internalizes many plasma components, playing multiple crucial roles as a scavenger and signaling molecule. One major challenge to studying LRP1 has been that it is difficult to express such a large, highly glycosylated, and cysteine-rich protein, limiting structural studies to LRP1 fragments. Here, we report the first recombinant expression of the complete 61 domains of the LRP1 full-length ectodomain. This advance was achieved with a multi-step cloning approach and by using DNA dilutions in order to improve protein yields. We investigated the binding properties of LRP1 using receptor-associated protein (RAP) as a model ligand due to its tight binding interaction. The LRP1 conformation was studied in its bound and unbound state using mass spectrometry, small-angle X-ray scattering and negative-stain electron microscopy at neutral and acidic pH. Our findings revealed a pH-dependent release of the ligand associated with a conformational change of the receptor. In summary, this investigation of the complete LRP1 ectodomain significantly advances our understanding of this important receptor and provides the basis for further elucidating LRP1's mechanism of action in a whole and integrated system.

Introduction

Low-density lipoprotein receptor-related protein-1 (LRP1) is the largest member of the mammalian LDL receptor family, further consisting of LDL receptor (LDLR), very-low-density lipoprotein receptor (VLDLR), apolipoprotein E-receptor-2 (ApoER2), LRP1B, megalin, LRP4, LRP5 and LRP6. LRP1 is ubiquitously expressed in brain endothelium, neurons, astrocytes, smooth-muscle cells, macrophages, fibroblasts and hepatocytes (1). As a scavenger and signalling molecule it is involved in many biological processes ranging from lipoprotein metabolism, proteinase homeostasis, fibrinolysis, vascular signalling, development and maintenance of blood-brain barrier integrity (1–3). LRP1 is able to bind and endocytose an array of structurally and functionally different ligands such as apolipoproteins (4), proteinases and proteinase-inhibitor complexes (5), blood-coagulation factors (2,3), growth factors (3,6), matrix metalloproteinases (7), viruses (8) and bacterial toxins (9). The cellular uptake of ligands, as in the case of other LDL receptor molecules, involves receptor-mediated endocytosis via clathrin-coated pits (10). After uptake, the receptor-ligand complex is delivered to the endosomal compartments, where the ligand dissociates. While the receptor is recycled to the cell surface, the ligand is further degraded in the lysosomal compartments (11,12).

Human LRP1, with 4,525 amino acid residues, is one of the largest glycoproteins known. With at least 159 disulfide bonds and 52 predicted N-glycans LRP1 is a remarkably challenging molecule for expression. It is composed of two non-covalently associated chains, the α -chain (515 kDa) containing the ligand binding regions and the β -chain (85 kDa) composed of the trans-membrane spanning region and intracellular domains (13). The ectodomain of LRP1, which consists of the α -chain and a short extracellular portion of the β -chain, has a highly modular composition resembling that of other LDL receptor molecules. It consists of four clusters, containing in total 31 complement-type cysteine-rich (CR) ligand binding repeats, 22 cysteine-rich epidermal growth factor (EGF)-like repeats and 8 YWTD six-bladed β -propellers. High-resolution structural information is available for CR repeats only (14–18) and low-resolution electron spectroscopic microscopy images of full-length LRP1 purified from human placenta have previously suggested an elongated “zig-zagged” shape spanning 50 to 70 nm length with a globular domain at one end (19). However, detailed structural studies of the full molecule have been hindered by the difficulties in producing recombinant LRP1.

The LRP1 biosynthesis is assisted by the 39 kDa receptor-associated protein (RAP), an endoplasmic reticulum (ER) resident chaperone which contributes to the maturation of different LDL receptors. RAP was initially discovered as a

protein that co-eluted with LRP1 when affinity-purified from placenta (5,20,21). Later studies showed that RAP binds in the early secretory pathway, preventing premature interaction of LRP1 with other ligands (22-24). RAP dissociates from LRP1 in the Golgi, triggered by the lower pH environment (23). Due to its tight binding to LRP1, recombinant RAP has been widely used in biochemical and cellular assays as a universal antagonist for ligand binding studies (22,25). RAP is composed of three domains: D1, D2 and D3. Each domain consists of a three-helical bundle connected by flexible linker regions (26). Domain 3 (RAP-D3) has been shown to be the most important for trafficking and folding of LRP1 (27) and exhibits the highest LRP1 binding affinity (28,29).

RAP and most of the other known LRP1 ligands bind to CR repeats within LRP1 cluster II and IV (30–33), while only RAP is able to bind LRP1 cluster III (31,34). The LRP1 ligand binding model, referred to as “acidic necklace”, involves calcium-coordinating acidic residues on the CR repeats that interact with positively charged residues of the ligand, preferentially lysines (35–37). This mechanism has been proposed to be widely adopted in ligand-receptor interactions for the LDL receptor family (38). The ligand uncoupling mechanism has been linked to the low-pH environment of the endosomal compartments, which is thought to trigger a structural transition of the LDL receptor from an open active conformation at neutral pH to a closed form at acidic pH (39). However, the mechanism by which LRP1 can recognize and bind such a variety of ligands is still not fully understood. So far, the stoichiometry of LRP1 ligand binding remains unknown. Moreover, binding studies on single clusters have reported somewhat inconsistent results regarding the affinities and specificities of cluster-to-ligand binding events. As suggested previously, these ambiguities may be rationalized by the utilization of non-identical, ligand-specific epitopes and the requirement of multiple LRP1 domains for proper endocytosis (32). Thus, the entire arrangement of domains of LRP1 is needed to fully understand its mode of action. This challenge is addressed in the present study, demonstrating for the first time the recombinant expression of the full-length ectodomain of LRP1. Using RAP as a model ligand, we characterize the affinity and the stoichiometry of the binding to LRP1. Furthermore, we present the conformation of the receptor, in its liganded and unliganded state, at neutral and acidic pH.

Results

Functional expression of full-length LRP1

To confirm the proper expression of LRP1 and to investigate its localization we transfected HEK293T cells with full-length LRP1 (residues 20–4544) containing a C-terminal GFP tag. Fig. 1A illustrates the LRP1 cloning strategy. Expression of the receptor was assessed by taking images with a confocal microscope. LRP1-GFP was expressed by a sub-portion of cells and it appeared to be present on the cell surface and in subcellular compartments (Figure 2A), probably endosomes, in agreement with what reported by Laatsch *et al.* (12). To quantify how much LRP1 was expressed on the cell surface we expressed LRP1-GFP in HEK293-Epstein-Barr virus nuclear antigen (EBNA) 1 cells (U-Protein Express) and conducted flow cytometry using a monoclonal antibody against LRP1 ectodomain. We found that approximately 50% of the GFP positive cells are expressing LRP1 on the cell surface (Figure 2B).

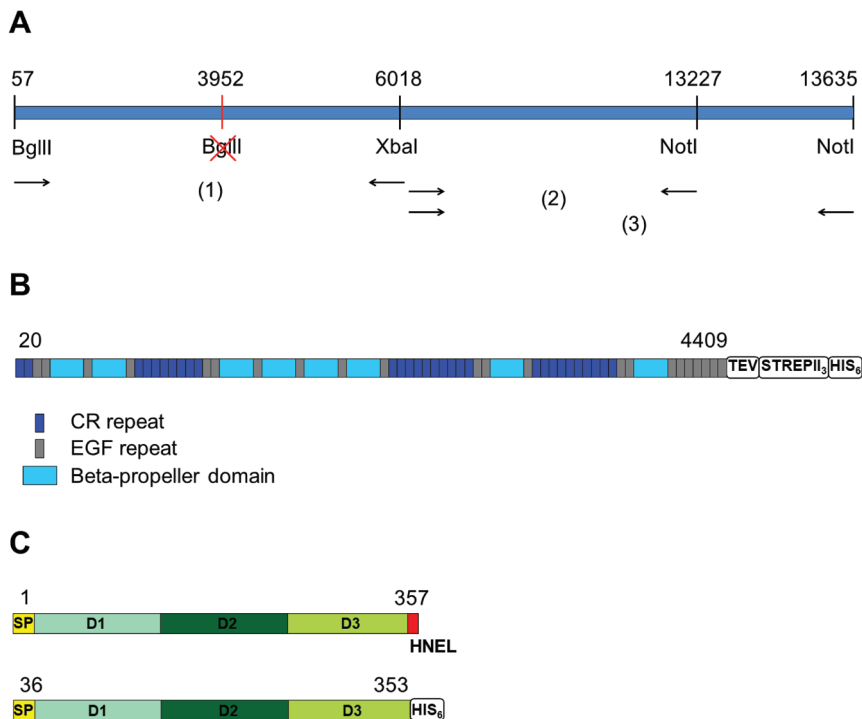


Figure 1. LRP1 cloning strategy and constructs for expression. A, Illustration of the multi-step strategy adopted to clone full-length LRP1. B-C, Schematic representation of the constructs used for expression of full-length LRP1 ectodomain (B) and of full-length RAP (C).

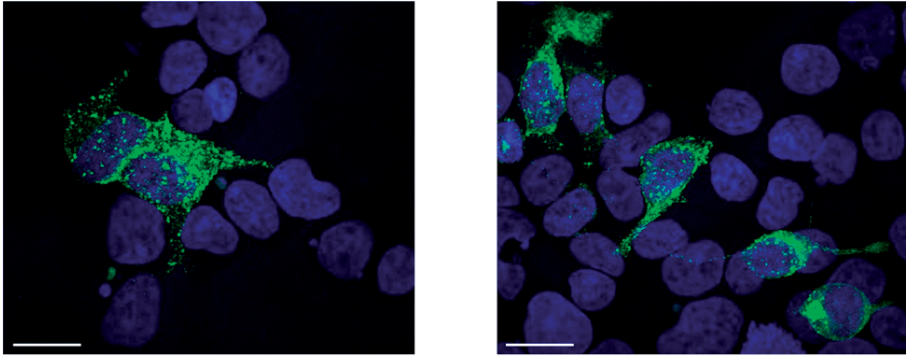
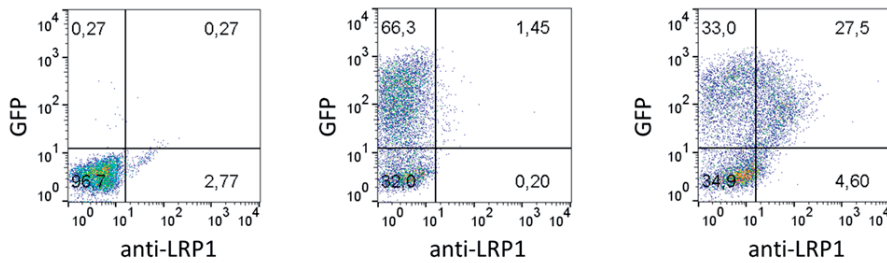
A**B**

Figure 2. Localization of recombinant full-length LRP1 in HEK293 cells. A, Confocal microscopy images of HEK293T cells expressing LRP1-GFP. Nuclei were visualized by DAPI and appear in blue. Bar is 20 μ m. B, FACS analysis of LRP1-GFP in HEK293-EBNA1 cells using a monoclonal antibody against LRP1 ectodomain (8G1). Approximately 50% of the GFP positive cells expressed LRP1 on the cell surface (right panel). Negative controls consisted of cells without any GFP expressed (left panel) and cells expressing LRP1-GFP incubated in absence of the secondary antibody (middle panel).

Expression of full-length LRP1 ectodomain with and without RAP

We tested different vectors for optimal expression of LRP1 full-length ectodomain (residues 20–4409) in HEK293-EBNA1 cells and chose the construct with a C-terminal TEV-StrepII₃-His₆-tag, which was used for all further experiments. Fig. 1, B and C, illustrates the constructs used for expression. This construct contains the whole α -chain and the extracellular part of the β -chain with an expected molecular weight (MW) of 488 kDa without glycans. We did not observe any cleavage of the secreted protein. Expression of LRP1 was performed with and without RAP, demonstrating that RAP is not essential for secretion of LRP1 since yields of about 300 μ g of protein per litre culture were obtained without RAP co-expressed. LRP1 eluted

on size-exclusion chromatography (SEC) as a single peak with some aggregation that migrated with the void volume (Figure 3A). On SDS-PAGE it appeared as a thick band that migrated higher than the 250 kDa MW marker with less prominent bands at slightly lower molecular weights, most probably due to heterogeneity in the N-linked glycosylation (Figure 3). Under non-reducing conditions small amounts of aggregates were observed, which are probably due to improper disulfide bond formation since these higher weight bands were absent under reducing conditions. When LRP1 was co-expressed with RAP an approximately twofold increase in LRP1 production was observed, indicating that co-expression of RAP may facilitate LRP1 secretion (Figure 3B). We observed that RAP was co-secreted and co-purified with LRP1 despite the fact that the RAP construct used for co-expression contained the ER retention signal HNEL at the C-terminus. Possibly, the secretion machinery is overwhelmed at high expression levels, as observed before (40). Another band around 70 kDa also co-eluted with LRP1. Bottom-up proteomics analysis identified this band as human Hsp70.

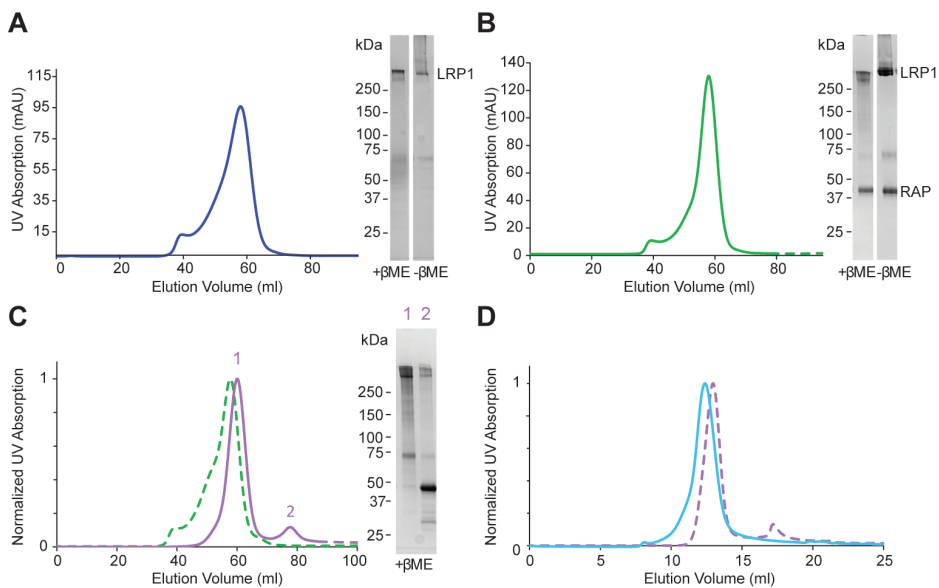


Figure 3. Purification of full-length LRP1 ectodomain and LRP1-RAP complex, and dissociation of RAP at acidic pH. A, SEC profile at pH 7.5 of LRP1 and detection on SDS-PAGE gel. B, SEC profile at pH 7.5 of LRP1-RAP complex after co-expression and detection on SDS-PAGE gel. C, SEC profile at pH 7.5 of LRP1-RAP complex (green dashed line) superposed to the SEC profile at pH 5.5 of LRP1-RAP (violet line) showing dissociation of LRP1 (peak 1) from RAP (peak 2); detection on SDS-PAGE after SEC at pH 5.5 of LRP1-RAP. D, SEC profile at pH 7.5 of LRP1 (blue line) after SEC at pH 5.5 of LRP1-RAP (violet dashed line) and dissociation of RAP (peak 1 from panel C).

LRP1 binds RAP with high affinity at pH 7.4

We used SPR analysis to test the binding of the purified recombinant LRP1 to full-length RAP, RAP-D3 and RAP-D3 K256A/K270A, a variant in which two critical lysine residues were mutated into alanine (41). Initially, we coupled one batch of purified recombinant LRP1 at 3 different densities (1.3, 3.8 and 8.3 fmol/mm² respectively) onto a CM5 chip. As expected, RAP-D3 K256A/K270A showed no appreciable interaction, while full-length RAP and RAP-D3 bound to the chip with high affinity (Figure 4A). The binding kinetics, however, did not fit a 1:1 binding model. To rule out mass transport limitations in the binding data as well as protein batch-dependent artefacts we assessed the binding at 3 different flow rates (30, 60 and 90 µl/min) for 3 different batches of purified recombinant LRP1 coupled onto a CM5 chip at 2.5 fmol/mm². Virtually identical association and dissociation curves were obtained for all analyses, confirming that the LRP1-RAP interaction does not comply with a 1:1 binding model. Therefore, to estimate K_D values, we again coupled three different batches of purified recombinant LRP1 at a ligand density of 2.5 fmol/mm² onto a CM5 chip, repeated the first analysis and fitted the responses at equilibrium by non-linear regression using a standard hyperbola (GraphPad Prism 4 software) (Figure 4B). The combined analysis indicated an affinity of 9 ± 5 nM (n = 27) for full-length RAP and 22 ± 2 nM (n = 6) for RAP-D3. The affinity for the RAP-D3 variant containing the K256A/K270A could not be assessed since binding was virtually absent. To estimate the apparent RAP-LRP1 binding stoichiometry, we calculated the ratio of observed R_{max} to the theoretical R_{max} expected for a 1:1 binding model, assuming a molecular weight of 600 kDa for LRP1, 40 kDa for full-length RAP and 12.8 kDa for RAP-D3. Both full-length RAP and RAP-D3 bound with a ratio of 1.5 ± 0.1 to LRP1, suggesting that more than one RAP molecule can bind LRP1 simultaneously.

LRP1 has two RAP binding sites

To further determine the stoichiometry of RAP binding to LRP1 we applied native MS, which preserves non-covalent interactions and the native-like structure of proteins in the gas phase (42). Native MS analysis of LRP1 is particularly challenging since the presence of numerous N-glycans causes a high degree of protein microheterogeneity. To facilitate native MS experiments, LRP1 and RAP were separately produced in N-acetylglucosaminyltransferase I-deficient (GnT1⁻) HEK293-EBNA1-S cells, which yield shorter and more homogenous N-linked glycan chains (43). The native mass spectrum of LRP1 ectodomain showed a clearly resolved charge-state series, allowing us to calculate its apparent molecular weight to 565.6 ± 0.4 kDa (Figure 5A).

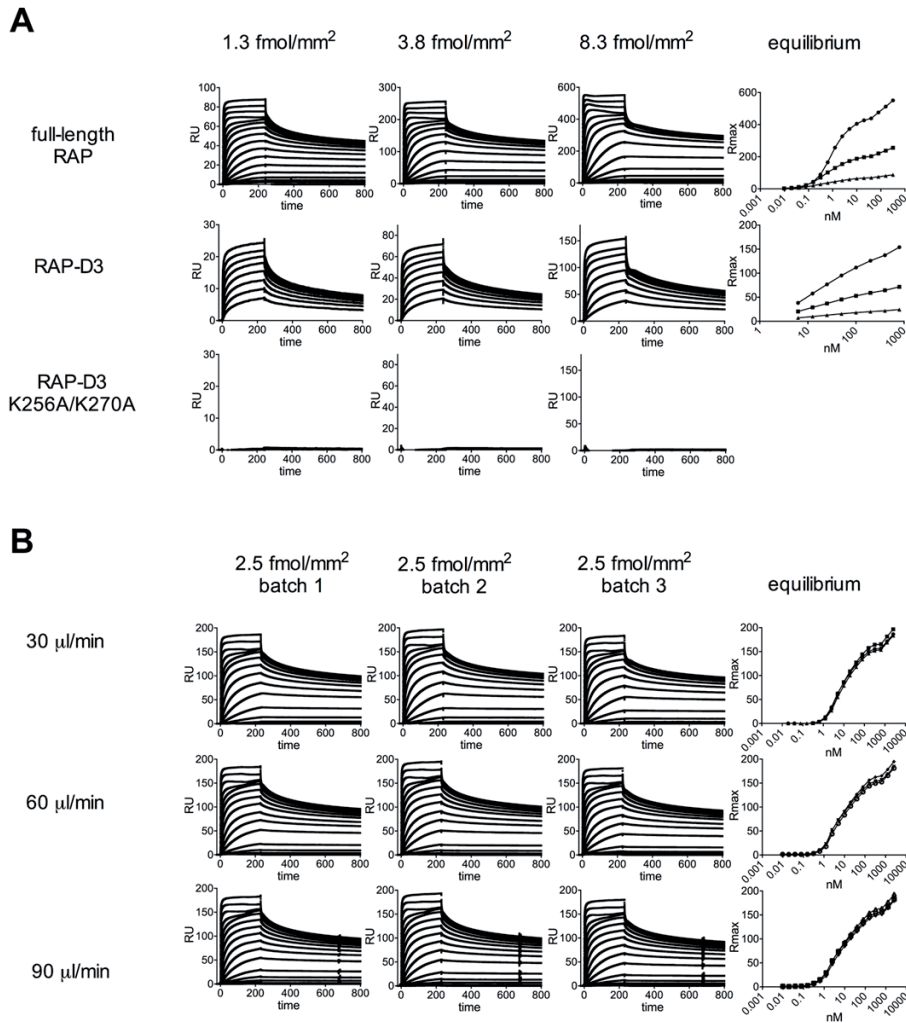


Figure 4. SPR analysis of LRP1-RAP binding interaction. Association and dissociation of RAP, RAP-D3 and RAP-D3 K256A/K270A to recombinant LRP1 was assessed by SPR analysis. Responses at equilibrium were plotted as a function of the analyte concentration. A, One batch of purified recombinant LRP1 was immobilized to a CM5 chip at 3 different ligand densities (1.3, 3.8 and 8.3 fmol/mm² respectively). Subsequently, RAP (0–2560 nM), RAP-D3 (0–800 nM) and RAP-D3 K256A/K270A (0–800 nM) were passed over the immobilized LRP1 at a flow rate of 30 µl/min. Binding to LRP1 was corrected for binding in absence of LRP1. B, Three batches of purified recombinant LRP1 were immobilized to a CM5 chip (2.5 fmol/mm²) as described above. Subsequently, RAP (0–2560 nM) was passed over the immobilized LRP1 as described above with a flow rate of 30, 60 or 90 µl/min.

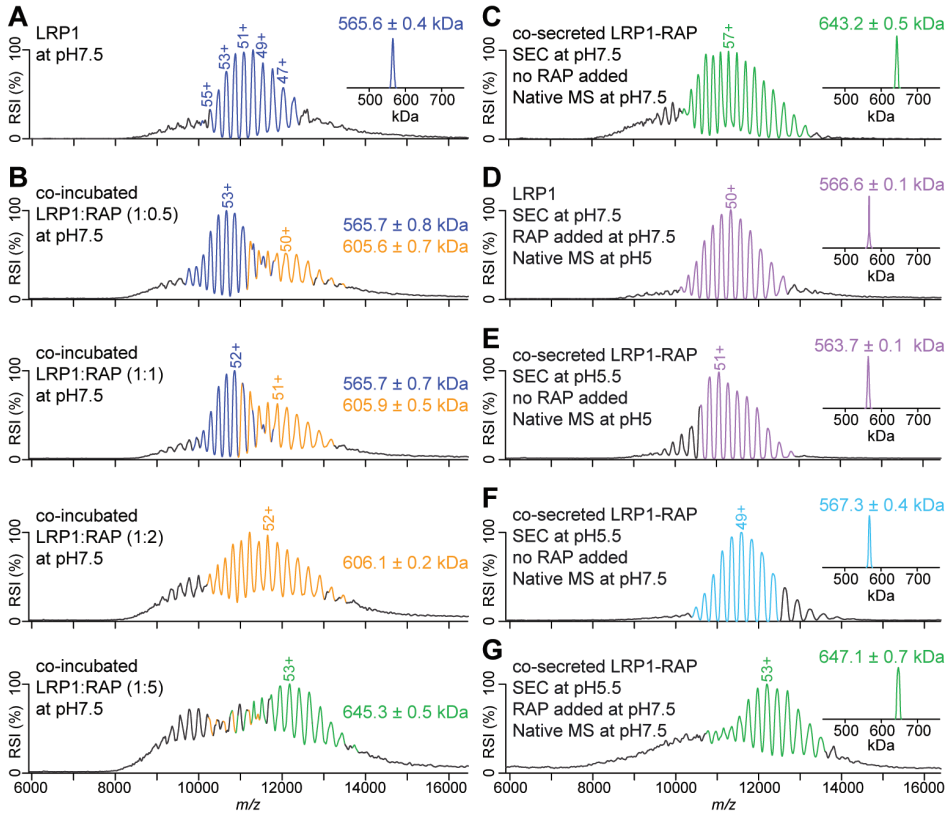


Figure 5. Native MS analysis of LRP1-RAP interaction. Peak labels indicate the charge state of the respective analyte ion. All LRP1 and LRP1-RAP species are represented by series of consecutively charged ions (selected charge states indicated above the peaks), enabling molecular mass determination. These charge state distributions and corresponding molecular masses are color-coded. LRP1 is shown in blue, LRP1-RAP 1:1 complex is shown in orange, and LRP1-RAP 1:2 complex is shown in green. Dissociated LRP1 is shown in violet, when measured at pH 5, and in light blue, when measured at pH 7.5. Peaks shown in black could not be confidently assigned as continuous charge state distributions, suggesting that they represent a mixture of several less abundant species with overlapping charge states. The mass spectra shown as insets have been deconvoluted from m/z to mass domain. A-G, Displayed are native mass spectra of LRP1 (A), LRP1-RAP complex formed *in vitro* after incubating both proteins at different molar ratios (indicated in each mass spectrum) (B), the co-expressed LRP1-RAP complex (C), and pH-shift experiments to study the dissociation and re-association of LRP1 and RAP (D-G). The corresponding experimental conditions are listed in the figure. RSI = relative signal intensity.

Subsequently, native MS was used to monitor *in vitro* LRP1-RAP complex formation after incubating LRP1 with increasing concentrations of RAP (Figure 5B). We observed that sub-stoichiometric amounts of RAP (MW \approx 39 kDa) are sufficient to form a complex with a MW of 605.6 ± 0.7 kDa, which represents a LRP1-RAP 1:1 complex. More than 2-fold molar excess of RAP is required to form LRP1-RAP 1:2 complex with a MW of 645.3 ± 0.5 kDa. Although the three species exhibit extensively overlapping charge state envelopes, the characteristic spacing between the charge states allows for their unambiguous assignment, enabling to determine three distinct molecular weights (Figure 5B). These results

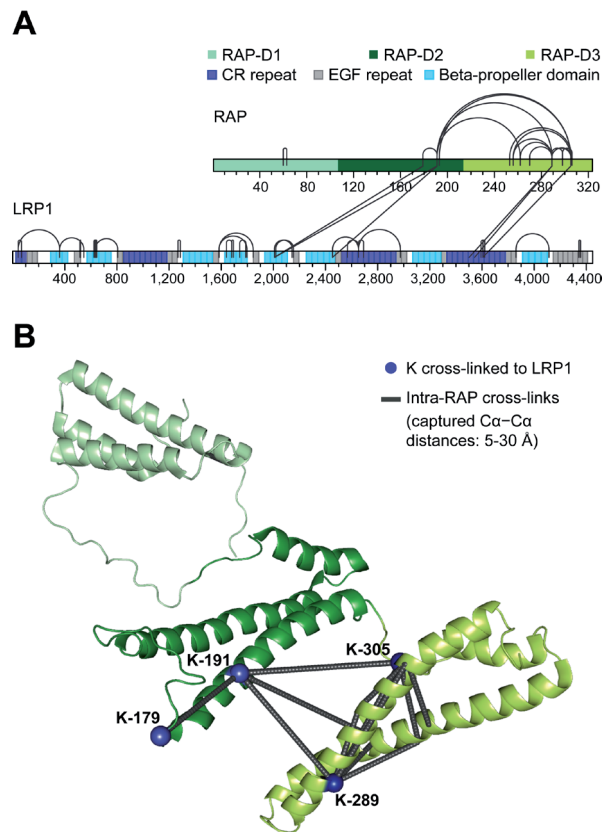


Figure 6. Cross-linking MS analysis of the co-expressed LRP1-RAP complex. A, Sequence bar plot of all identified cross-links. The domain boundaries within RAP and LRP1 are taken from Lee *et al.* (26) and from Uniprot entry Q07954, respectively. B, Structural representation of intramolecular RAP cross-links. The cross-links were mapped onto all structurally characterized RAP conformers (Protein Data Bank (PDB) entry 2P01). Shown here is the RAP conformer structure that agrees best with the cross-linking distance constraints. RAP lysines involved in intermolecular cross-links to LRP1 are depicted as blue spheres.

suggest the presence of two RAP binding sites on LRP1, which seem to exhibit different binding affinities.

Native MS analysis was also performed after co-expressing LRP1 and RAP in HEK293-EBNA1-S cells (Figure 5C). Under these conditions, the LRP1-RAP 1:2 complex with a MW of 643.2 ± 0.5 kDa was clearly the most abundant species. Interestingly, charge states corresponding to the LRP1-RAP 1:1 complex were not observed, suggesting that this species is low abundant or entirely absent when LRP1 and RAP are co-secreted. The LRP1-RAP complex during secretion, thus, forms preferentially with a 1:2 LRP1:RAP binding stoichiometry. Next, we applied cross-linking MS to assess the regions involved in binding (42). In total, we identified 46 unique lysine-lysine connections (Figure 6A, Supplementary Table I). Within LRP1, we observed 25 intramolecular cross-links connecting lysines that are up to eight domains apart. Thus, the cross-linking MS data suggest a certain degree of structural compaction but does not provide evidence for a globular conformation. We also verified 15 intramolecular RAP cross-links, mainly representing contacts within RAP-D3 and between RAP-D3 and -D2 (Figure 6B). Moreover, 6 intermolecular LRP1-RAP cross-links provide insights into the LRP1-RAP binding interfaces. Three intermolecular cross-links connect RAP-D3 with CR25–27 within LRP1 cluster IV. The other three intermolecular cross-links connect RAP-D2 with the LRP1 β -propeller regions between cluster II and III. Interestingly, the involved RAP-D2 lysines are also internally connected to each other and to RAP-D3 (Figure 6B). This raises the possibility that RAP exhibits one LRP1 binding region to which all observed intermolecular cross-links can be mapped. By contrast, there is no evidence for intermolecular interactions between the LRP1 regions that are cross-linked to RAP. Therefore, it is more likely that the two groups of LRP1-RAP cross-links correspond to two distinct RAP binding sites on LRP1.

Acidic pH affects RAP binding and conformation of LRP1

We investigated whether the expressed soluble LRP1 ectodomain releases RAP at pH < 6. SEC analysis at pH 5.5 showed that LRP1-RAP complex dissociates into two peaks corresponding to LRP1 and RAP (Figure 3C). Complementarily, native MS demonstrated that the *in vitro* reconstituted LRP1-RAP complex fully dissociates when analyzed at pH 5 (Figure 5D). The LRP1 charge state distribution at pH 5 and pH 7.5, however, are highly similar (compare Figures 5A and 5D), suggesting that LRP1 retains a folded conformation at acidic pH.

Next, we probed the reversibility of the pH-induced RAP release. To this end, the co-secreted LRP1-RAP complex was subjected to SEC at pH 5.5, leading to full dissociation of the complex as evidenced by native MS analysis at pH 5 and

pH 7.5 (Figure 5E and 5D). Raising the sample pH to 7.5 and incubating it with a molar excess of RAP, however, restored the LRP1-RAP 1:2 complex (Figure 5F), showing that LRP1-RAP association/dissociation is a reversible, pH-dependent process.

To investigate the effect of the pH on LRP1 conformation, we conducted SAXS measurements with on-line SEC on soluble LRP1 and on the LRP1-RAP complex at pH 7.5 and pH 5.5. At neutral pH, LRP1 and LRP1-RAP complex behave very similarly as shown by the almost overlapping scattering curves (Figure 7A). Guinier and distance distribution function analysis showed similar R_g values and a D_{max} of ~ 39 nm for LRP1 and of ~ 38 nm for LRP1-RAP (Figure 7B-C, Table

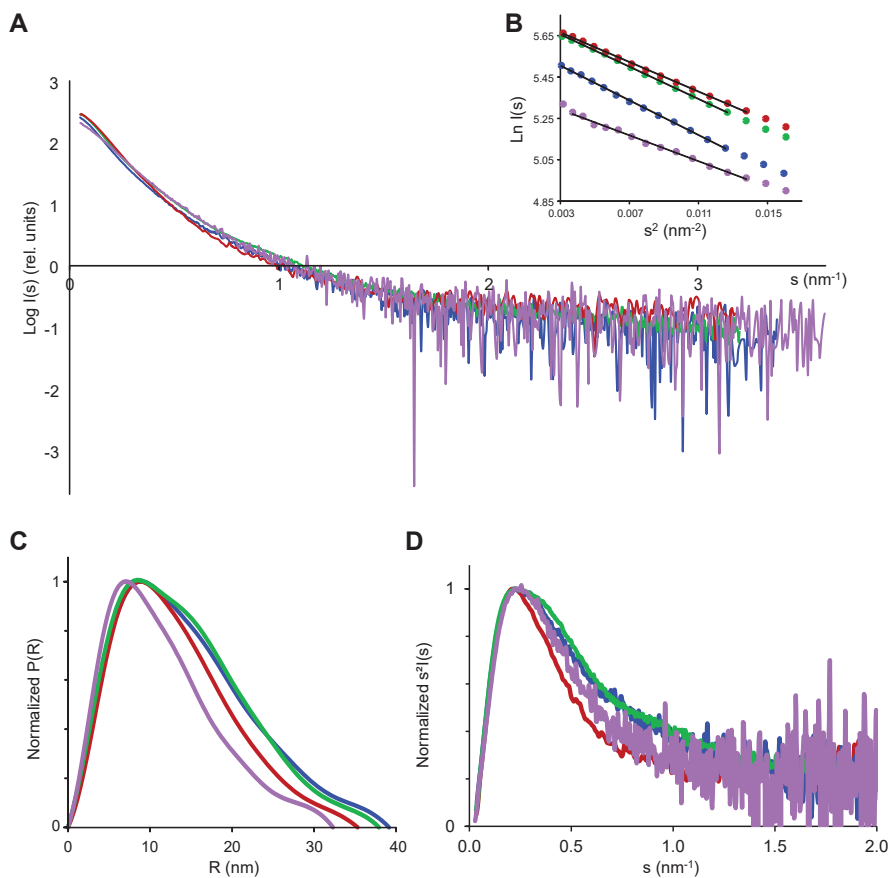


Figure 7. SAXS analysis of LRP1 and LRP1-RAP complex at pH 7.5 and pH 5.5. LRP1 at pH 7.5 is shown in blue, LRP1-RAP at pH 7.5 is shown in green, LRP1 at pH 5.5 is shown in red and LRP1-RAP at pH 5.5 is shown in violet. A, Superposition of scattering curves scaled for comparison. B, Guinier plot. C, Normalized distance distribution function. D, Normalized Kratky plot.

Table 1. SAXS parameters.

	LRP1 pH 7.5	LRP1-RAP pH 7.5	LRP1 pH 5.5	LRP1(-RAP) pH 5.5
R_g from Guinier (nm)	11.2	10.8	10.3	9.6
R_g from $P(r)$ (nm)	11.6	11.3	10.4	9.4
D_{max} from $P(r)$ (nm)	39.1	37.9	35.3	32.3

I). Moreover, the Kratky plot of LRP1-RAP shows a small shoulder appearing at higher s ranges, which is also observed for free LRP1, although the curve is noisier in this region (Figure 7D). This feature hints at a conformation with a globular part and an elongated flexible extremity. A plateau is reached at $s = 1.5 - 2.0 \text{ nm}^{-1}$ indicating partial flexibility for both species. At acidic pH (i.e., conditions where RAP is released) both LRP1 and LRP1-RAP exhibited a different behavior, showing decreased values of R_g and a D_{max} of $\sim 35 \text{ nm}$ for LRP1 only and $\sim 32 \text{ nm}$ for LRP1 after RAP dissociation (Table 1). The Kratky plot for LRP1 at pH 5.5 adopts a more bell-like shape, which converges to a plateau around 1.0 nm^{-1} (Figure 7D). Also for LRP1 after RAP release the Kratky plot indicates a more compact shape compared to the curves at neutral pH values, even though it is noisier. Overall, the SAXS data suggest that, at low pH, LRP1 undergoes a conformational change acquiring a more compact shape. Based on the values of R_g and D_{max} , the pH-dependent conformational change appears more enhanced when there is concomitant release of RAP.

Additional SEC studies showed that, after dissociation from RAP at acidic pH, the LRP1 elution peak shifts back to its usual elution volume at higher apparent molecular weights if the pH is brought back to 7.5 (Figure 3D). This indicates that the LRP1 conformational change is reversible, which is in good agreement with the observed restorability of the LRP1-RAP interaction (Figure 5D–F).

LRP1 is structurally highly flexible

To obtain structural information complementary to that provided by SAXS, we performed negative-stain EM studies on LRP1 and LRP1-RAP complex after SEC at neutral and at acidic pH. EM of negatively stained particles revealed for all conditions a very heterogeneous population. Such variety in the particle shape points towards a high degree of flexibility, where some particles have a more compact-kinked conformation while others are more elongated. Reference-free alignment and classification yielded multiple orientations of particles with a maximum length of $\sim 35 \text{ nm}$. In Figure 8, the most 10 populated 2D-averaged classes with the highest signal-to-noise ratio are shown. No significant difference in conformation and size was observed between LRP1 and LRP1-RAP, also when

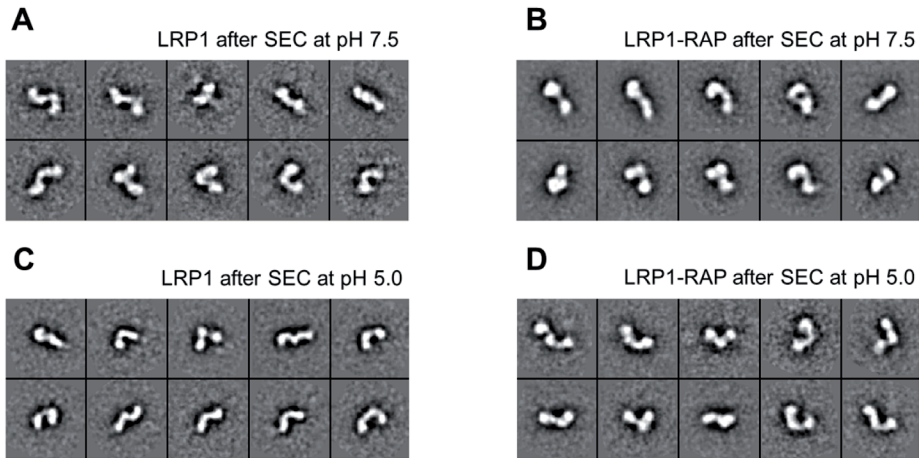


Figure 8. Negative-stain EM 2D class averages of LRP1 and LRP1-RAP complex. The averaged 10 most populated classes with the highest signal-to-noise ratio of a total of ~2,000 particles manually picked for each sample preparation are shown. The box size is 62 nm². A, LRP1 after gel filtration at pH 7.5. B, Co-expressed LRP1-RAP complex after gel filtration at pH 7.5. C, LRP1 after gel filtration at pH 5.5. D, Co-expressed LRP1-RAP after gel filtration at pH 5.5 and dissociation of RAP.

samples were prepared after SEC at pH 5. Possibly, the pH of the negative-stain affected the sample preparation, compromising the analysis of pH-dependent conformational effects and RAP binding.

Discussion

LRP1 is a challenging protein to express recombinantly due to its size, high number of glycans and disulfide bridges. We were able for the first time to express the entire ectodomain of LRP1 and characterize its conformation, binding properties and pH dependence, using RAP as a model ligand. In our experimental setup, RAP was not essential for proper LRP1 secretion, but the presence of co-expressed RAP resulted in higher protein production. This supportive effect is likely caused by stable interactions between RAP and LRP1 since SEC and native MS have shown that they are co-secreted as a stable complex, likely with a 1:2 LRP1:RAP binding stoichiometry (Figure 3B, 5C). SPR showed apparent affinity constants in the low nanomolar range, which are in agreement with previous studies (35,41) (Figure 4B). Native MS-based titration experiments showed that LRP1 harbors two RAP binding sites (Figure 5B). These sites probably exhibit different binding affinities since sub-stoichiometric amounts of RAP were sufficient to form the

LRP1-RAP 1:1 complex whereas a more than 2-fold molar excess of RAP was needed to observe the LRP1-RAP 1:2 complex. The corresponding LRP1-RAP binding interfaces were probed with cross-linking MS (Figure 6A). Although cross-linking MS, as such, cannot directly elucidate binding stoichiometries, it is likely that the verified intermolecular connections represent more than one LRP1-RAP interface. In line with previous reports (27,33), the data show that CR25-CR27 is the most effective RAP binding region within cluster IV and that RAP-D3 is an important LRP1 binding site. A second binding site is probably captured by three intermolecular cross-links connecting the LRP1 β -propeller domains 5 and 6 at the boundary between cluster II and III with RAP-D2.

The presence of two RAP binding sites is consistent with Williams *et al.* (55) and with the findings that cluster II and IV are the most effective ligand binding regions of LRP1 (31–33,40,44). However, it is important to point out that direct cross-links to the CR repeats region of cluster II are absent. A possible explanation is that the cross-linker did not penetrate the immediate cluster II binding site because the cluster II lysines were either spatially not accessible, involved in non-covalent interactions or generally less reactive (e.g., due to the local pKa) (45). This hypothesis is supported by the fact that also intramolecular crosslinks among the cluster II lysines are lacking. Instead, the cross-linker may have reacted with lysines that are located in neighboring regions, such as the β -propellers, that might be proximal to the binding interface. Notably, the location of the cross-links between the CR repeats regions of cluster II and III also supports alternative explanations. We cannot exclude that RAP is binding to cluster III, which is known to contain a lower affinity RAP binding site (31,34). Likewise, the involvement of a yet uncharacterized binding site cannot be ruled out. The previously suggested existence of more than two RAP binding sites, however, is not in agreement with our native MS results.

The overall conformation of LRP1 remains largely unchanged upon RAP binding, as shown by the similarity of the SAXS curves and by the negative-stain EM class averages (Figure 7A, 8A-B). Conformational transitions upon RAP binding might be happening at a local level, influencing perhaps the relations of the neighboring domains without producing large structural rearrangements visible at low resolution, as hypothesized by Migliorini *et al.* (35). SAXS analysis showed a maximum particle diameter of 39 nm for LRP1 at neutral pH (Table I) while from negative-stain EM we could measure a maximum particle dimension of 35 nm. This difference is probably due to the hydration shell and the flexibility of the system leading to an apparent bigger dimension for SAXS. Averaged EM classes showed, in fact, that the particles are highly flexible. Unfortunately, the inhomogeneity of the particles hinders any high-resolution 3D structure determination.

However, a maximum diameter of less than 40 nm precludes a model where LRP1 is completely elongated since, based on the LDLR X-ray structure (39), it would be spanning almost 100 nm. Therefore, it is reasonable to assume that there is a certain degree of compaction in LRP1 conformation, which is also in agreement with our cross-linking MS data.

According to the proposed ligand-internalization mechanism, LRP1 should release its cargo at $\text{pH} < 6$ in order to recycle to the cell surface. SEC studies at $\text{pH} 5.5$ showed complete dissociation of RAP from LRP1 (Figure 3C). This finding was confirmed by native MS analysis, which moreover indicated that LRP1 remains folded at $\text{pH} 5$ (Figure 5D). Using negative-stain EM, SAXS and SEC we compared the behavior of LRP1 and LRP1-RAP complex at $\text{pH} < 6$. Size analysis from SAXS data showed that after RAP release at $\text{pH} 5.5$, LRP1 D_{max} decreases from 38 to 32 nm, while for unbound LRP1 it shifts from 39 to 35 nm (Figure 7, Table I). SEC studies showed a shift of LRP1 elution volume towards lower molecular weight when the pH was acidified (Figure 3C). Interestingly, when the pH was brought back to neutral values, LRP1 migrated as a higher molecular weight species again, indicating that the conformational change is reversible (Figure 3D). Correspondingly, the RAP binding capabilities of LRP1 could be restored by shifting the pH from 5 to 7.5 (Figure 5E-G). These results suggest that LRP1 switches between a RAP binding competent conformation at neutral pH and a binding incompetent conformation at acidic pH . The 'acidic' LRP1 conformation appears to be somewhat more compact, similarly to what has been shown for LDLR (39). Therefore, the release of the LRP1 cargo at acidic pH is probably due to a conformational change of the receptor, possibly with intramolecular interactions competing for the RAP binding sites and promoting its release. Intriguingly, according to the SAXS data, the extent of LRP1 conformational change at acidic pH seems to be influenced by the presence of RAP. This could be due to the existence of two RAP binding sites with different binding kinetics. When the pH is lowered, one RAP molecule could be released firstly, while the second more tightly bound RAP molecule remains bound to LRP1 for a slightly longer time, promoting the conformational change of the receptor. Then, after interacting with both sites and causing compaction of the receptor, also the second RAP molecule is released. This hypothesis also provides an explanation for the previously made observation that RAP can bind more than one LRP1 site at the same time (31). Altogether, this initial structural and functional investigation of the complete LRP1 ectodomain significantly advances our understanding of this complex and important receptor and forms the basis to further characterize its binding properties using the full-length molecule.

Experimental Procedures

Constructs for recombinant expression of full-length LRP1

Human LRP1 (isoform 1) cDNA pcDNA 3.1(-) Neo vector with NotI and XhoI restriction sites (kindly given by Dr. Joachim Herz, University of Texas, Dallas) was used in a multistep cloning approach to clone LRP1 full-length and LRP1 soluble ectodomain into the in-house mammalian expression system. First, the two DNA fragments with nucleotide sequences 57(BglII)-3952 and 3952-6018(XbaI) were obtained in two separate PCR reactions using primers designed to mutate the native BglII site at position 3952. PCR products from both reactions were mixed in equimolar ratio and an overlap extension PCR reaction was performed using *PFU Turbo Hotstart DNA Polymerase* (Agilent Technologies) to obtain the mutated insert 57-6018 (insert 1 in Figure 1). Insert 1 was further cloned into a gateway recombinational cloning entry vector (pCR8/GW/TOPO, Invitrogen). The DNA sequence of the whole mutated area was confirmed by DNA sequencing. Further, in another two separate PCR reactions DNA fragments with nucleotide sequence 6018-13635 and 6018-13227 (insert 2 and 3 in Figure 1) were obtained using primers that introduced a NotI site at the 3' end. Insert 2 and 3 were subsequently cloned into gateway recombinational cloning entry vectors (pCR8/GW/TOPO, Invitrogen) and their DNA sequence was confirmed by DNA sequencing. As a final step insert 1 containing XbaI at 3' end (obtained by restriction digestion using BglII and XbaI) and insert 2 containing XbaI at 5' end (obtained by restriction digestion with XbaI and NotI) were combined in equimolar ratio in a ligation reaction to obtain the full-length receptor (nt 57-13635); in another ligation reaction insert 1 was combined with insert 3 to obtain the complete ectodomain (nt 57-13227). Both constructs had Bgl2 site at 5' and NotI site at 3' for further cloning into mammalian expression vectors. DNA sequencing pointed out that our LRP1 clone is a natural variant with P instead of Q in amino acid position 2900 (Uniprot Q07954). Full-length LRP1 was subcloned in expression vector pUPE7.21 with N-terminal cystatin secretion signal and C-terminal eGFPm His tag for confocal microscopy experiments. LRP1 ectodomain was subcloned in several mammalian expression vectors including pUPE107.55 (N-terminal cystatin secretion signal and C-terminal TEV- His₆), pUPE7.50 (N-terminal cystatin secretion signal and C-terminal TEV-StrepII₃-His₆) and pUPE3478 (cystatin C-term TEV-eGFPm-StrepII₃) which were used for expression tests. The construct in vector pUPE7.50 (N-terminal cystatin secretion signal and C-terminal TEV-StrepII₃-His₆) showed the best expression yield.

Constructs for recombinant expression of RAP

For co-expression with LRP1 a construct of full-length human RAP (pcDNA kindly given by Dr. Madelon Maurice, UMC, Utrecht) including native signal peptide (residues 1–357) was subcloned using BamHI/NotI sites in pUPE1.02 (tagless vector for intracellular expression). For extracellular expression of human RAP the construct without native signal peptide and ER retention signal (residues 36–353) was subcloned into pUPE107.03 (N-terminal cystatin secretion signal and C-terminal His₆).

Confocal microscopy

To visualize the cellular localization of LRP1, HEK293T human embryonic kidney cells (kindly provided by W. de Lau, Hubrecht Institute, Utrecht) were transfected with full-length LRP1 with a C-terminal eGFP-His tag. Cells were grown at 37°C and 5% CO₂ in a 75 cm² flask in Dulbecco's Modified Eagle Medium (ATCC) supplemented with 10% fetal bovine serum (FBS) and Penicillin/Streptomycin. At 3 days after transfection, cells were passaged (TripLE Express) onto poly-D-lysine-precoated Menzel glasses in a 12-well plate. At 6 days after transfection, cells were washed with phosphate buffered saline (PBS) and fixed with 4% paraformaldehyde (PFA) (Merck) in PBS. Coverslips were mounted on slides using Hard Set Mounting Medium with 4', 6-diamidino-2-phenylindole (DAPI) (Vectashield, H-1500) and imaged using a Zeiss LSM700 Confocal Microscope (Carl Zeiss). Images were taken using a Plan Apochromat 63x/1.4 objective lense. Images shown in Figure 2A are maximum intensity projections generated with ZEN software (Carl Zeiss).

Flow cytometry

The percentage of LRP1-GFP expressed on the cell surface of HEK293-EBNA 1 cells (U-Protein Express) was determined by flow cytometry. Cells (5 x 10⁶ cells/ml) were incubated with 5 µl/ml anti-LRP1 mouse mAb (8G1, Calbiochem) for 30 minutes on ice. Samples were washed twice with 1% (w/v) bovine serum albumin (BSA) (Merck) in PBS and incubated with an Alexa Fluor 546-conjugated goat anti-mouse secondary antibody (ThermoFisher) for 30 minutes on ice. The cells were then fixed with 150 µl 1% PFA (Merck) and analysed with a BD FACSCalibur flow cytometer (BD Biosciences). Negative controls consisted of cells without any GFP expressed and cells expressing LRP1-GFP incubated in absence of the secondary antibody. The acquired data were analyzed with FlowJo (Tree Star).

Expression and purification of full-length LRP1 ectodomain

Soluble ectodomain of human LRP1 in pUPE7.50 was transiently expressed in HEK293-EBNA1 cells (U-Protein Express). Expression was optimized for protein

yield by plasmid titration (46), which indicated that transfections with 10-fold dilutions of expression plasmid in non-expressing dummy plasmid improved LRP1 production approximately two- to threefold. Protein yield was further improved (approximately twofold) when co-expressed with RAP in ratio LRP1:RAP 10:1. Six days after transient expression medium was harvested and 6-fold concentrated using a 10-kDa molecular mass cut-off membrane. LRP1 ectodomain was purified by Strep affinity chromatography followed by SEC on a Superose6 column (GE Healthcare) equilibrated with 150 mM NaCl, 4 mM CaCl₂ and 25 mM HEPES pH 7.5.

Expression and purification of RAP

RAP construct for extracellular expression was expressed in HEK293-EBNA1-S cells (43) and purified by nickel-nitrilotriacetic acid affinity chromatography followed by SEC on a Superdex75 column equilibrated with 150 mM NaCl and 25 mM HEPES pH 7.0. RAP-D3 and RAP-D3 K256A/K270A were produced and purified as described (41).

SDS-PAGE

10 µl of purified protein was diluted with 5 µl of SDS loading dye with or without 6% (v/v) β-mercaptoethanol for reducing and non-reducing SDS-PAGE, respectively. Samples were run on Mini-PROTEAN TGX precast 4–15% gradient gel (Biorad). Gel was stained with Coomassie Blue.

Native mass spectrometry (MS)

LRP1, RAP and the LRP1-RAP complex were produced recombinantly in HEK293-EBNA1-S cells (43) and subsequently transferred to 150 mM ammonium acetate pH 7.5 using Vivaspin centrifugal filter units with a 10 kDa or 100 kDa molecular weight cut-off (Sartorius). Prior to native MS analysis, LRP1 and the co-secreted LRP1-RAP complex were diluted to a final concentration of 0.5–1 µM. The RAP concentration was varied according to the molar ratios indicated in Figure 5B. To assess the protein behavior at pH < 6, the protein stock solutions were 6–8-fold diluted with 150 mM ammonium acetate pH 5. The samples were loaded into gold-coated borosilicate capillaries and analyzed by native nano-electrospray ionization MS on a modified Orbitrap Exactive Plus EMR mass spectrometer (Thermo Fisher Scientific) (47). The instrument was externally calibrated using CsI clusters, and operated in positive ion mode with the following settings: capillary voltage = 1.4–1.5 kV, source fragmentation voltage = 10 eV, ion injection time = 100 ms, higher-energy collision (HCD) dissociation energy = 200 eV, N₂ gas pressure in HCD cell = 8–9 × 10⁻¹⁰ bar,

mass resolution at m/z 200 = 2,000. The analyte transmission was optimized by manually tuning the ion transfer settings. The mass spectra were analyzed with Xcalibur v2.2 (Thermo Fisher Scientific) and Databridge in combination with MassLynx v4.1 (both Waters).

Cross-linking MS

The co-expressed LRP1-RAP complex was cross-linked at a concentration of 1 mg/ml using 1 mM bis(sulfosuccinimidyl)suberate (BS3, Thermo Fisher Scientific). The cross-linking reaction proceeded for 45 min at room temperature and was quenched by adding 20 mM Tris-HCl pH 7.6. The cross-linked samples were denatured with 2 M urea, reduced with 4 mM DTT (30 min at 56 °C), alkylated with 8 mM iodoacetamide (30 min in the dark), and again treated with 4 mM DTT. Next, the samples were deglycosylated by over-night shaking incubation with 0.2 U/ μ g PNGase F (Roche) and subsequently digested by a 6-hour incubation with trypsin (Promega) at a 1:60 (*w/w*) protease:substrate ratio. Both reactions were carried out at 37 °C. The resulting peptide mixture was desalted using Sep-Pak C18 cartridges (Waters), dried under vacuum, dissolved in 10% (*v/v*) HCOOH and analyzed by reversed-phase nano-high performance liquid chromatography (column material: Poroshell 120 EC-C18, 2.7 μ m (Agilent Technologies))/tandem mass spectrometry. The experiments were conducted using a Proxeon EASY-nLC 1000 coupled to an Orbitrap Elite mass spectrometer (both Thermo Fisher Scientific) or an ultra-HPLC Agilent 1200 (Agilent Technologies) coupled to an Orbitrap Fusion mass spectrometer (Thermo Fisher Scientific). All precursor ions were mass analyzed in the Orbitrap using a mass resolution setting of 60,000 at m/z 200. The most abundant and at least triply charged precursor ions were selected for MS2 experiments, using a top-5 data-dependent acquisition approach (Orbitrap Elite) or the top-speed data dependent mode with 2 s cycle time (Orbitrap Fusion). The precursor ions were fragmented by sequentially applying collision-induced dissociation (CID) and electron transfer dissociation (ETD). The corresponding CID- and ETD-MS2 scans were acquired in the Orbitrap mass analyzer with 15,000 mass resolution at m/z 200.

Cross-linked peptides were identified using the XlinkX software in enumeration mode and validated based on a target-decoy database search strategy, as described previously (48,49). Cross-link identifications were verified based on the individual XlinkX N scores of the linked peptides. Cross-links were accepted when the more confidently identified linked peptide was verified at 1% false-discovery rate and the less confidently identified linked peptide was verified at 5% false-discovery rate.

Surface plasmon resonance (SPR)

Association and dissociation of RAP, RAP-D3 and RAP-D3 K256A/K270A to recombinant LRP1 was assessed by SPR analysis employing a BIAcore T200 biosensor (Biacore AB). Different batches of purified recombinant LRP1 were immobilized at varying ligand densities onto a CM5-sensor chip using the amine-coupling method according to the manufacturer's instructions. Subsequently, RAP (0–2560 nM), RAP-D3 (0–800 nM) and RAP-D3 K256A/K270A (0–800 nM) were passed over the immobilized LRP1 in running buffer containing 150 mM NaCl, 5 mM CaCl₂, 0.05% (v/v) Tween 20 and 20 mM HEPES pH 7.4 at 25°C with a flow rate of 30, 60 or 90 µL/min. The sensor chip surface was regenerated three times after each concentration of analyte with a buffer containing 150 mM NaCl, 20 mM EDTA, 0.05% (v/v) Tween 20 and 20 mM HEPES pH 7.4 followed by equilibration using running buffer. Binding to LRP1 was corrected for binding in absence of LRP1. Responses at equilibrium were plotted as a function of the analyte concentration. To estimate K_D values the responses at equilibrium were fitted by non-linear regression using a standard hyperbola (GraphPad Prism 4 software).

Small-angle X-ray scattering (SAXS)

SAXS data were collected at the European Synchrotron Radiation Facility (ESRF Grenoble, France) BioSAXS beamline at 12.5 keV (0.9919 Å) with a 2D Pilatus 1M detector (DECTRIS). For online purification we used the high-performance liquid chromatography (HPLC) system consisting of an in-line degasser (DGU-20A5R, Shimadzu), binary pump (LC-20ADXR, Shimadzu), valve for buffer selection and gradients, autosampler (SIL-20ACXR, Shimadzu), UV-VIS array photospectrometer (SPD-M20A, Shimadzu) and a conductimeter (CDD-10AVP, Shimadzu). LRP1 and LRP1-RAP from HEK293-EBNA1 cells were analyzed in different buffer conditions. Protein samples were loaded into vials and automatically injected onto the Superose6 5/150 analytical column pre-equilibrated with 150 mM NaCl, 4 mM CaCl₂ and 25 mM HEPES pH 7.5, or alternatively with 150 mM NaCl, 4 mM CaCl₂, and 25 mM MES pH 5.5. All data were collected using a sample-to-detector distance of 2.81 m corresponding to a scattering vector s ($s = 4\pi \sin \theta/\lambda$) range of 0.03–5.0 nm⁻¹. Approximately 1500 frames (1 frame s⁻¹) were collected per 30 minutes sample run. Initial data processing was performed automatically using *EDNA* pipeline (50), generating azimuthally integrated, calibrated and normalized one-dimensional profiles for each frame. All frames were compared with the initial frame and matching frames were merged to create the reference buffer. About 15 to 30 frames for each run with a consistent radius of gyration (R_g) and corresponding to the highest protein concentration

based on forward scattering intensity $I(0)$ values were merged to yield a single averaged frame corresponding to the scattering of an individual SEC purified species. The curves obtained were used for further data processing using PRIMUS of the ATSAS suite (51,52). R_g values were evaluated within the range of Guinier approximation $sR_g < 1.3$ according to the equation:

$$I(s) = I(0) \exp(-1/3(sR_g)^2)$$

The R_g was also computed from the entire scattering patterns using Porod's law by the calculation of the distance distribution function $P(r)$ using the program GNOM (53), also giving the maximum particle diameter D_{max} . SAXS measurements were repeated with different protein batches three times for each sample condition.

Negative-stain electron microscopy (EM)

5 μ l of purified protein (5–10 μ g/ml) was applied after SEC to a glow discharged carbon coated copper grid (Electron Microscopy Sciences, CF200-Cu) and stained with freshly prepared 0.75% uranyl formate solution. Image acquisition was done using a Tecnai12 (FEI) operating at 120 kV. Images were recorded with a BM-Eagle CCD camera (FEI) 2,048x2,048 at x30,000 magnification. Around 2,000 particles for each sample were manually selected and projections were subjected to reference-free alignment and classification using the EMAN2 software package (54).

Acknowledgments

We thank Dr. Joachim Herz for providing us with LRP1 pcDNA. Dr. Madelon Maurice for RAP pcDNA. W. de Lau for the provision of HEK293T cells. Joke C. M. Granneman and Dimpna H. Meijer for assistance in expressing LRP1-GFP in HEK293T cells and acquiring images with the confocal microscope. Kok P. M. van Kessel for assistance with FACS experiments. U-Protein Express BV for the provision of protein expression facilities. Fan Liu for assistance in designing the MS acquisition methods. The European Synchrotron Radiation Facility (ESRF) for the provision of synchrotron radiation facilities and beamline scientists of the ESRF and the European Molecular Biology Laboratory for assistance, in particular Adam Round and Martha E. Brennich. E.G. Huizinga for the fruitful discussions. Financial support was provided by the ManiFold project (grant no. 317371) and the BioStruct-X (grant no. 283570) embedded in the European Union's Seventh

Framework Programme (FP7/2007–2013), the Roadmap Initiative Proteins@Work (project no. 184.032.201) funded by The Netherlands Organisation for Scientific Research (NWO) and The Landsteiner Foundation for Blood Transfusion Research (LSBR fellowship 1517 to M.v.d.B).

Author contributions

C.D.N. performed cloning, expression and purification of LRP1, SAXS and negative-stain EM experiments and analysis. P.L. performed native and cross-linking MS experiments and analysis. M.v.d.B performed RAP D3 and RAP D3 K256A/K270A expression and purification, SPR experiments and analysis. P.K.M. designed the LRP1 cloning strategy and supervised initial expression tests. N.L. purified RAP full-length and helped in expressing LRP1-GFP in HEK293T cells for confocal microscopy. K.M. provided guidance and helped in designing the research. C.D.N., P.L., M.v.d.B., A.J.R.H. and P.G. discussed results and wrote the paper. P.G. supervised the project. All authors approved the final version of the manuscript.

References

1. Moestrup, S. K., Gliemann, J., and Pallesen, G. (1992) Distribution of the alpha 2-macroglobulin receptor/low density lipoprotein receptor-related protein in human tissues. *Cell Tissue Res.* **269**, 375–382
2. Herz, J. and Strickland, D. K. (2001) LRP: a multifunctional scavenger and signaling receptor. *J. Clin. Invest.* **108**, 779–784
3. Lillis, A. P., Van Duyn, L. B., Murphy-Ullrich, J. E., and Strickland, D. K. (2008) LDL receptor-related protein 1: unique tissue-specific functions revealed by selective gene knockout studies. *Physiol. Rev.* **88**, 887–918
4. Beisiegel, U., Weber, W., Ihrke, G., Herz, J., and Stanley, K. K. (1989) The LDL-receptor-related protein, LRP, is an apolipoprotein E-binding protein. *Nature* **341**, 162–164
5. Strickland, D. K., Ashcom, J. D., Williams, S., Burgess, W. H., Migliorini, M., and Argraves, W. S. (1990) Sequence identity between the alpha 2-macroglobulin receptor and low density lipoprotein receptor-related protein suggests that this molecule is a multifunctional receptor. *J. Biol. Chem.* **265**, 17401–17404
6. Herz, J., Clouthier, D. E., and Hammer, R. E. (1992) LDL receptor-related protein internalizes and degrades uPA-PAI-1 complexes and is essential for embryo implantation. *Cell* **71**, 411–421
7. Scilabra, S. D., Troeberg, L., Yamamoto, K., Emonard, H., Thogersen, I., Enghild, J. J., Strickland, D. K., and Nagase, H. (2013) Differential regulation of extracellular tissue inhibitor of metalloproteinases-3 levels by cell membrane-bound and shed low density lipoprotein receptor-related protein 1. *J. Biol. Chem.* **288**, 332–342
8. Hofer, F., Gruenberger, M., Kowalski, H., Machat, H., Huettinger, M., Kuechler, E., Blaas, D. (1994) Members of the low density lipoprotein receptor family mediate cell entry of a minor-group common cold virus. *Proc. Natl. Acad. Sci. U. S. A.* **91**, 1839–1842
9. Kounnas, M.Z., Morris, R.E., Thompson, M.R., FitzGerald, D.J., Strickland, D.K., Saelinger, C.B. (1992) The alpha 2-macroglobulin receptor/low density lipoprotein receptor-related protein binds and internalizes Pseudomonas exotoxin A. *J. Biol. Chem.* **267**, 12420–12423
10. Chen, W. J., Goldstein, J. L., and Brown, M. S. (1990) NPXY, a sequence often found in cytoplasmic tails, is required for coated pit-mediated internalization of the low density lipoprotein receptor. *J. Biol. Chem.* **265**, 3116–3123
11. Czekay, R. P., Orlando, R. A., Woodward, L., Lundstrom, M., and Farquhar, M. G. (1997) Endocytic trafficking of megalin/RAP complexes: dissociation of the complexes in late endosomes. *Mol. Biol. Cell* **8**, 517–532
12. Laatsch, A., Panteli, M., Sornsakrin, M., Hoffzimmer, B., Grewal, T., and Heeren, J. (2012) Low density lipoprotein receptor-related protein 1 dependent endosomal trapping and recycling of apolipoprotein E. *PLoS One* **7**, e29385
13. Herz, J., Kowal, R. C., Goldstein, J. L., and Brown, M. S. (1990) Proteolytic processing of the 600 kd low density lipoprotein receptor-related protein (LRP) occurs in a trans-Golgi compartment. *EMBO J.* **9**, 1769–1776
14. Huang, W., Dolmer, K., and Gettins, P. G. (1999) NMR Solution structure of complement-like repeat CR8 from the low density lipoprotein receptor-related protein. *J. Biol. Chem.* **274**, 14130–14136
15. Dolmer, K., Huang, W., and Gettins, P. G. (2000) NMR solution structure of complement-like repeat CR3 from the low density lipoprotein receptor-related protein. Evidence for specific binding to the receptor binding domain of human alpha(2)-macroglobulin. *J. Biol. Chem.* **275**, 3264–3269
16. Simonovic, M., Dolmer, K., Huang, W., Strickland, D.K., Volz, K., and Gettins, P. G. (2001) Calcium coordination and pH dependence of the calcium affinity of ligand-binding repeat

- CR7 from the LRP. Comparison with related domains from the LRP and the LDL receptor. *Biochemistry* **40**, 15127–15134
17. Jensen, G. A., Andersen, O. M., Bonvin, A. M., Bjerrum-Bohr, I., Etzerodt, M., Thøgersen, H. C., O’Shea, C., Poulsen, F. M., and Kragelund, B. B. (2006) Binding site structure of one LRP-RAP complex: implications for a common ligand-receptor binding motif. *J. Mol. Biol.* **362**, 700–716
 18. Guttman, M., Prieto, J. H., Handel, T. M., Domaille, P. J., and Komives, E. A. (2010) Structure of the minimal interface between ApoE and LRP. *J. Mol. Biol.* **398**, 306–319
 19. Delain, E., Barray, M., Pochon, F., Gliemann, J., and Moestrup, S. K. (1994) Electron microscopic visualization of the human alpha 2-macroglobulin receptor and its interaction with alpha 2-macroglobulin/chymotrypsin complex. *Ann. N. Y. Acad. Sci.* **737**, 202–211
 20. Ashcom, J. D., Tiller, S. E., Dickerson, K., Cravens, J. L., Argraves, W. S., and Strickland, D. K. (1990) The human alpha 2-macroglobulin receptor: identification of a 420-kD cell surface glycoprotein specific for the activated conformation of alpha 2-macroglobulin. *J. Cell Biol.* **110**, 1041–1048
 21. Kristensen, T., Moestrup, S. K., Gliemann, J., Bendtsen, L., Sand, O., and Sottrup-Jensen, L. (1990) Evidence that the newly cloned low-density-lipoprotein receptor related protein (LRP) is the alpha 2-macroglobulin receptor. *FEBS Lett.* **276**, 151–155
 22. Herz, J., Goldstein, J. L., Strickland, D. K., Ho, Y. K., and Brown, M. S. (1991) 39-kDa protein modulates binding of ligands to low density lipoprotein receptor-related protein/alpha 2-macroglobulin receptor. *J. Biol. Chem.* **266**, 21232–21238
 23. Bu, G., Geuze, H. J., Strous, G. J., and Schwartz, A. L. (1995) 39 kDa receptor-associated protein is an ER resident protein and molecular chaperone for LDL receptor-related protein. *EMBO J.* **14**, 2269–2280
 24. Willnow, T. E., Rohlmann, A., Horton, J., Otani, H., Braun, J. R., Hammer, R. E., and Herz, J. (1996) RAP, a specialized chaperone, prevents ligand-induced ER retention and degradation of LDL receptor-related endocytic receptors. *EMBO J.* **15**, 2632–2639
 25. Iadonato, S. P., Bu, G., Maksymovitch, E. A., and Schwartz, A. L. (1993) Interaction of a 39 kDa protein with the low-density-lipoprotein-receptor-related protein (LRP) on rat hepatoma cells. *Biochem. J.* **296**, 867–875
 26. Lee, D., Walsh, J. D., Migliorini, M., Ping, Y., Cai, T., Schweiters, C. D., Krueger, S., Strickland, D.K., and Wang, Y.X. (2007) The structure of receptor-associated protein (RAP). *Protein Sci.* **16**, 1628–1640
 27. Obermoeller, L. M., Warshawsky, I., Wardell, M. R., and Bu, G. (1997) Differential functions of triplicated repeats suggest two independent roles for the receptor-associated protein as a molecular chaperone. *J. Biol. Chem.* **272**, 10761–10768
 28. Andersen, O. M., Schwarz, F. P., Eisenstein, E., Jacobsen, C., Moestrup, S. K., Etzerodt, M., and Thøgersen, H. C. (2001) Dominant thermodynamic role of the third independent receptor binding site in the receptor-associated protein RAP. *Biochemistry* **40**, 15408–15417
 29. Lasic, A., Dolmer, K., Strickland, D. K., and Gettins, P. G. (2006) Dissection of RAP-LRP interactions: binding of RAP and RAP fragments to complement-like repeats 7 and 8 from ligand binding cluster II of LRP. *Arch. Biochem. Biophys.* **450**, 167–175
 30. Horn, I. R., van den Berg, B. M., van der Meijden, P. Z., Pannekoek, H., and van Zonneveld, A. J. (1997) Molecular analysis of ligand binding to the second cluster of complement-type repeats of the low density lipoprotein receptor-related protein. Evidence for an allosteric component in receptor-associated protein-mediated inhibition of ligand binding. *J. Biol. Chem.* **272**, 13608–13613
 31. Neels, J. G., van Den Berg, B. M., Lookene, A., Olivecrona, G., Pannekoek, H., and van Zonneveld, A. J. (1999) The second and fourth cluster of class A cysteine-rich repeats of

- the low density lipoprotein receptor-related protein share ligand-binding properties. *J. Biol. Chem.* **274**, 31305–31311
32. Obermoeller-McCormick, L. M., Li, Y., Osaka, H., FitzGerald, D. J., Schwartz, A. L., and Bu, G. (2001) Dissection of receptor folding and ligand-binding property with functional minireceptors of LDL receptor-related protein. *J. Cell Sci.* **114**, 899–908
 33. Meijer, A. B., Rohlena, J., van der Zwaan, C., van Zonneveld, A. J., Boertjes, R. C., Lenting, P. J., and Mertens, K. (2007) Functional duplication of ligand-binding domains within low-density lipoprotein receptor-related protein for interaction with receptor associated protein, alpha2-macroglobulin, factor IXa and factor VIII. *Biochim. Biophys. Acta* **1774**, 714–722
 34. Bu, G. and Rennke, S. (1996) Receptor-associated protein is a folding chaperone for low density lipoprotein receptor-related protein. *J. Biol. Chem.* **271**, 22218–22224
 35. Migliorini, M. M., Behre, E. H., Brew, S., Ingham, K. C., and Strickland, D. K. (2003) Allosteric modulation of the ligand binding properties of LRP by the receptor associated protein (RAP) requires critical lysine residues within its carboxyl-terminal domain. *J. Biol. Chem.* **278**, 17986–17992
 36. Fisher, C., Beglova, N., and Blacklow, S. C. (2006) Structure of an LDLR-RAP complex reveals a general mode for ligand recognition by lipoprotein receptors. *Mol. Cell* **22**, 277–283
 37. van den Biggelaar, M., Madsen, J. J., Faber, J. H., Zuurveld, M. G., van der Zwaan, C., Olsen, O. H., Stennicke, H. R., Mertens, K., and Meijer, A. B. (2015) Factor VIII Interacts with the endocytic receptor low-density lipoprotein receptor-related protein 1 via an extended surface comprising “hot-spot” lysine residues. *J. Biol. Chem.* **290**, 16463–16476
 38. Strickland, D. K., Au, D. T., Cunfer, P., and Muratoglu, S. C. (2014) Low-density lipoprotein receptor-related protein-1: role in the regulation of vascular integrity. *Arterioscler. Thromb. Vasc. Biol.* **34**, 487–98
 39. Rudenko, G., Henry, L., Henderson, K., Ichtchenko, K., Brown, M. S., Goldstein, J. L., and Deisenhofer, J. (2002) Structure of the LDL receptor extracellular domain at endosomal pH. *Science* **298**, 2353–2358
 40. Willnow, T. E., Orth, K., and Herz, J. (1994) Molecular dissection of ligand binding sites on the low density lipoprotein receptor-related protein. *J. Biol. Chem.* **269**, 15827–15832
 41. van den Biggelaar, M., Sellink, E., Klein Gebbinck, J. W., Mertens, K., and Meijer, A. B. (2011) A single lysine of the two-lysine recognition motif of the D3 domain of receptor-associated protein is sufficient to mediate endocytosis by low-density lipoprotein receptor-related protein. *Int. J. Biochem. Cell Biol.* **43**, 431–440
 42. Lössl, P., van de Waterbeemd, M., and Heck, A. J. (October 26, 2016) The diverse and expanding role of mass spectrometry in structural and molecular biology. *EMBO J.* 10.15252/embj.201694818
 43. Peng, W. C., de Lau, W., Madoori, P. K., Forneris F., Granneman, J. C., Clevers, H., Gros, P. (2013) Structures of Wnt-antagonist ZNRF3 and its complex with R-spondin 1 and implications for signaling. *PLoS One.* **8**, e83110
 44. Bloem, E., Ebberink, E. H., van den Biggelaar, M., van der Zwaan, C., Mertens, K., and Meijer, A. B. (2015) A novel chemical footprinting approach identifies critical lysine residues involved in the binding of receptor-associated protein to cluster II of LDL receptor-related protein. *Biochem. J.* **468**, 65–72
 45. Guo, X., Bandyopadhyay, P., Schilling, B., Young, M. M., Fujii, N., Aynechi, T., Guy, R. K., Kuntz, I. D., and Gibson B. W. (2008) Partial acetylation of lysine residues improves intraprotein cross-linking. *Anal. Chem.* **80**, 951–960
 46. Half, E. F., Versteeg, M., Brondijk, T. H., and Huizinga, E. G. (2014) When less becomes more: optimization of protein expression in HEK293-EBNA1 cells using plasmid titration - a case study for NLRs. *Protein Expr. Purif.* **99**, 27–34

47. Snijder, J., van de Waterbeemd, M., Damoc, E., Denisov, E., Grinfeld, D., Bennett, A., Agbandje-McKenna, M., Makarov, A., and Heck A. J. (2014) Defining the stoichiometry and cargo load of viral and bacterial nanoparticles by orbitrap mass spectrometry. *J. Am. Chem. Soc.* **136**, 7295–7299
48. Liu, F., Rijkers, D. T., Post, H., and Heck, A. J. (2015) Proteome-wide profiling of protein assemblies by cross-linking mass spectrometry. *Nat. Methods* **12**, 1179–1184
49. Lössl, P., Brunner, A. M., Liu, F., Leney, A. C., Yamashita, M., Scheltema, R. A., and Heck, A. J. (2016) Deciphering the interplay among multisite phosphorylation, interaction dynamics, and conformational transitions in a tripartite protein system. *ACS Cent. Sci.* **2**, 445–455
50. Brennich, M. E., Kieffer, J., Bonamis, G., De Maria Antolinos, A., Hutin, S., Pernot, P., and Round, A. (2016) Online data analysis at the ESRF BioSAXS beamline. *J. Appl. Cryst.* **49**, 203–212
51. Konarev, P. V., Volkov, V. V., Sokolova, A. V., Koch, M. H. J., and Svergun, D. I. (2003) PRIMUS - a Windows-PC based system for small-angle scattering data analysis. *J. Appl. Cryst.* **36**, 1277–1282
52. Petoukhov, M. V., Franke, D., Shkumatov, A. V., Tria, G., Kikhney, A. G., Gajda, M., Gorba, C., Mertens, H. D. T., Konarev, P. V. and Svergun, D. I. (2012) New developments in the ATSAS program package for small-angle scattering data analysis. *J. Appl. Cryst.* **45**, 342–350
53. Svergun, D. I. (1992) Determination of the regularization parameter in indirect-transform methods using perceptual criteria. *J. Appl. Cryst* **25**, 495–503
54. Tang, G., Peng, L., Baldwin, P. R., Mann, D. S., Jiang, W., Rees, I., and Ludtke, S. J. (2007) EMAN2: an extensible image processing suite for electron microscopy. *J. Struct. Biol.* **157**, 38–46
55. Williams, S. E., Ashcom, J. D., Argraves, W. S., and Strickland, D. K. (1992) A novel mechanism for controlling the activity of α 2-macroglobulin receptor/low density lipoprotein receptor-related protein 1. *J. Biol. Chem.* **267**, 9035–9040D

CHAPTER 3

Application of unbiased combinatorial screening to generate a bispecific IgG1 that selectively and potently inhibits HER3 signaling via HER2-guided ligand blockade

Cecile Geuijen¹, Camilla De Nardis², David Maussang¹, Eric Rovers¹,
Tristan Gallenne¹, Linda J.A. Hendriks¹, Therese Visser¹, Roy Nijhuis¹, Ton
Logtenberg¹, John de Kruif¹, Piet Gros² and Mark Throsby¹

¹Merus N.V., Utrecht, The Netherlands

²Crystal & Structural Chemistry, Bijvoet Center for Biomolecular Research, Utrecht University,
Utrecht, The Netherlands

An adapted version of this chapter has been submitted for publication

Abstract

HER2-targeting agents have demonstrated efficacy and provided meaningful clinical benefit to patients with HER2-amplified breast and gastric cancer. However, not all patients respond to the current drugs and some eventually progress on treatment. Sustained inhibition of tumor growth and survival signaling pathways, particularly the PI3K/Akt pathway, is a key determinant of therapeutic benefit from HER2 targeted agents. (Re)-activation of the PI3K/Akt pathway can occur through heregulin (HRG) -driven stimulation of the HER2/HER3 heterodimer. We describe here the identification of a bispecific full-length human IgG1 antibody (PB4188) that selectively targets the HER2/HER3 heterodimer and potently inhibits ligand-driven tumor growth and survival *in vitro* and *in vivo*. PB4188, in contrast to HER2 and HER3 targeting monoclonal antibodies or their combinations, is capable of inhibiting HRG signaling at supramaximal concentrations that may occur via autocrine receptor activation in tumors harboring ligand-translocations or as a result of transcriptional upregulation. Experimental data, structural studies and statistical modeling suggest that PB4188 employs a novel mode of action involving the docking of the HER2 Fab to domain I of the receptor, optimally positioning a second high affinity HER3 binding arm to effectively block HRG interaction with domain III of the receptor. The high selectivity and potency of PB4188 demonstrated here in preclinical studies suggest it could provide benefit to patients with inherent or acquired resistance to current HER2 targeted drugs either as a single agent or in combination. Furthermore, the mode of action of PB4188 and the approach used to identify the bispecific IgG1 could be applied more broadly to precisely target other signaling pathways and mechanisms important to the growth and survival of tumors.

Introduction

The HER (ErbB) family of transmembrane receptor tyrosine kinases (RTKs) includes the epidermal growth factor receptor (EGFR), also known as HER1 (or ErbB1), and the homologous receptors HER2 (ErbB2), HER3 (ErbB3) and HER4 (ErbB4). These receptors are widely expressed on epithelial cells and generally heterodimerize to transduce external signals that differently regulate proliferation and survival programs, depending on the receptor and ligand combination (1). The dysregulation of HER signaling is a frequent occurrence in human cancer. Genetic events such as amplification of HER2 copy number or activating mutations in the signaling domains of EGFR are common in breast and non-small cell lung (NSCL) cancer respectively, and are associated with tumor invasion, metastasis, resistance to chemotherapy, and poor prognosis (1–3). Several different therapeutic interventions have been developed to target these oncogenic driving events, such as monoclonal antibodies that extracellularly disrupt overexpressed receptor signaling or small molecule inhibitors that intracellularly target the kinase domain.

In contrast to HER2 and EGFR, amplification or mutation of HER3 is less frequently detected in tumors, and mutated HER3 is unable to transform cells lines on its own (4). Instead, the oncogenic activity of HER3 is primarily driven by overexpression of its ligand, neuregulin (also referred to as heregulin, HRG) (5). This can occur in an autocrine manner through translocation of the HRG gene, which has been reported in NSCL and ovarian cancers (6,7), or transcriptional activation in tumors as a bypass mechanism of pathway inhibition (8–13). Treatment of HER2-overexpressing breast cancer cells with trastuzumab *in vitro* induces autocrine HRG expression and secretion, a resistance mechanism that could be clinically relevant in patients that progress on trastuzumab (14,15). Alternatively, HRG can act in a paracrine setting as a result of transcriptional upregulation in stroma of the tumor microenvironment (16,17) or in sequestered locations where HRG serves other physiological functions, such as the brain, where it can potentiate the formation of metastatic nodes (18,19).

HER2 is the preferred dimerization partner for HER3 resulting in the most potent HER family dimer (20). In the HER2-amplified setting, the abundance of HER2, present in a constitutively active form, drives the formation of HER2/HER3 dimers without the requirement for a ligand; however, this conformation is distinct from the ligand dependent conformation in terms of stability of the complex and oncogenic signaling potential (21). The HER2/HER3 dimer reconstitutes a high-affinity binding site for HRG that is > 10-fold higher than HER3 in its non-dimerized state (22). Although HER3 lacks a functional kinase

domain (23,24), once a ligand-stabilized heterodimer is formed it strongly induces downstream signaling via six direct docking sites for p85-PI3K on its cytoplasmic domain resulting in tumor cell proliferation and cell migration (25).

Therapeutic approaches to effectively block HRG/HER3 pathway activation have focused on more powerful and sustained blockade of HER intracellular kinase activity (26), blockade of HER2 dimerization (27) or blockade of ligand binding to HER3 itself (28–30). Studies have shown that many HER2-amplified breast cancer cells become insensitive to tyrosine kinase inhibitors (TKIs) when HRG concentrations are increased (31). A PI3K/Akt-driven inhibitory feedback loop also results in upregulation of active HER3 at the cell membrane through cell surface re-localization and reduced HER3 dephosphorylation (32,33). Ligand-driven activation of HER3 has been shown to restore PI3K signaling upon treatment of HER2-overexpressing breast cancer cells with first generation TKIs (31,34). To address the inability of these agents to suppress long-term HER3 signaling, irreversible inhibitors of HER2 kinase activity have been developed (35). These not only potently inhibit HER2 kinase activity but also that of EGFR, which could be therapeutically advantageous in certain settings (26), but have the unwanted consequence of increasing the severity of gastrointestinal (GI) and skin toxicities (36).

Antibody mediated blockade of HER2 dimerization with therapeutic agents such as pertuzumab is more specific, but also inhibits dimerization with any other HER family member, including homodimerization. It also has a different toxicity profile with more significant GI adverse events than trastuzumab, which only blocks HER2 signaling (37). Pertuzumab as a single agent has not shown significant activity in the indications investigated to date. However, the combination of pertuzumab and trastuzumab provides meaningful clinical benefit with an acceptable safety profile, while the combination of pertuzumab and cetuximab leads to unacceptable overlapping toxicity (38). Several monoclonal antibodies that target HER3 are in development and offer the most direct approach to blocking HRG/HER3 pathway activation. Many of these demonstrated good preclinical activity, however, although still in the early phases of clinical development, these results have not been translated into meaningful clinical activity. To address the shortcomings of current therapeutic strategies, we undertook an unbiased in-format screening approach to generate a bispecific antibody (bAb) targeting the extracellular domain (ECD) of HER2 and HER3 that specifically and potently blocks HRG-driven signaling of the HER2/HER3 heterodimer.

Results

Unbiased screening leads to identification of bispecific antibodies that potently inhibit tumor cell growth under normal and HRG stress conditions

To develop a therapeutic agent that effectively and specifically inhibits ligand dependent activation of the HER2/HER3 heterodimer, we performed an unbiased screen of more than 500 bispecific antibodies targeting HER2 and HER3. The full-length IgG1 bAbs were generated by combining common light chain (LC) Fab domains with heavy chain (HC) domains engineered to favor heterodimerization over homodimerization (74). These asymmetric IgG1 bAbs were assembled from combinations of Fabs with different characteristics (e.g. affinity, epitope specificity) that bound to either the HER2 (n = 22) or HER3 (n = 25) ectodomains (Table S1 and S2). A number of analogs of HER2 and HER3 monoclonal antibodies, as well as the bispecific antibody MM-111, were produced (based on patent literature) as functional comparators, and demonstrated specific binding to their targets (Figure S1). Initial functional screening was performed on the BxPC3 cell line due to its balanced levels of HER2 and HER3 expression and because the cell growth is HRG-dependent *in vivo*. To model a compensatory signaling loop that frequently occurs in the tumor microenvironment (39), BxPC3 cells were also stimulated with exogenous HRG in starvation medium, rendering the cells dependent on ligand for growth (Figure 1A). From the panel of 545 bAbs, 192 inhibited autonomous cell proliferation and 236 inhibited growth of ligand-stimulated cells; 82 were significantly more potent than trastuzumab in one or both assay settings (n = 2). Proliferation inhibition assays with a selection of the antibody panel were carried out on the MCF-7 cell line at submaximal HRG-driven growth conditions (EC90 = 0.34 nM) to increase assay sensitivity (Figure S3A). Titration of the HER2 antibodies trastuzumab or pertuzumab alone demonstrated significant inhibition of growth in a dose dependent manner, but they were not as effective as the equimolar combination of the two antibodies or of the HER3 targeting antibody MM-121 (Figure 1B). The most active bAbs identified in the BxPC3 screening assays were titrated under the same assay conditions. Several showed significantly greater potency than the combination of trastuzumab and pertuzumab (T+P) analogs (Figure 1C). To screen bAbs for tumor inhibitory activity *in vivo*, BxPC3 cells transduced with a luciferase reporter gene were implanted orthotopically in mice. Tumor growth was measured by bioluminescence and growth inhibition was confirmed using a cocktail of HER2 and HER3 monospecific antibodies (mAbs) (Figure S2A). The 12 best growth-inhibiting anti-HER2xHER3 bAbs (under both independent and ligand-dependent growth conditions) were evaluated in two separate experiments. Four bispecific antibod-

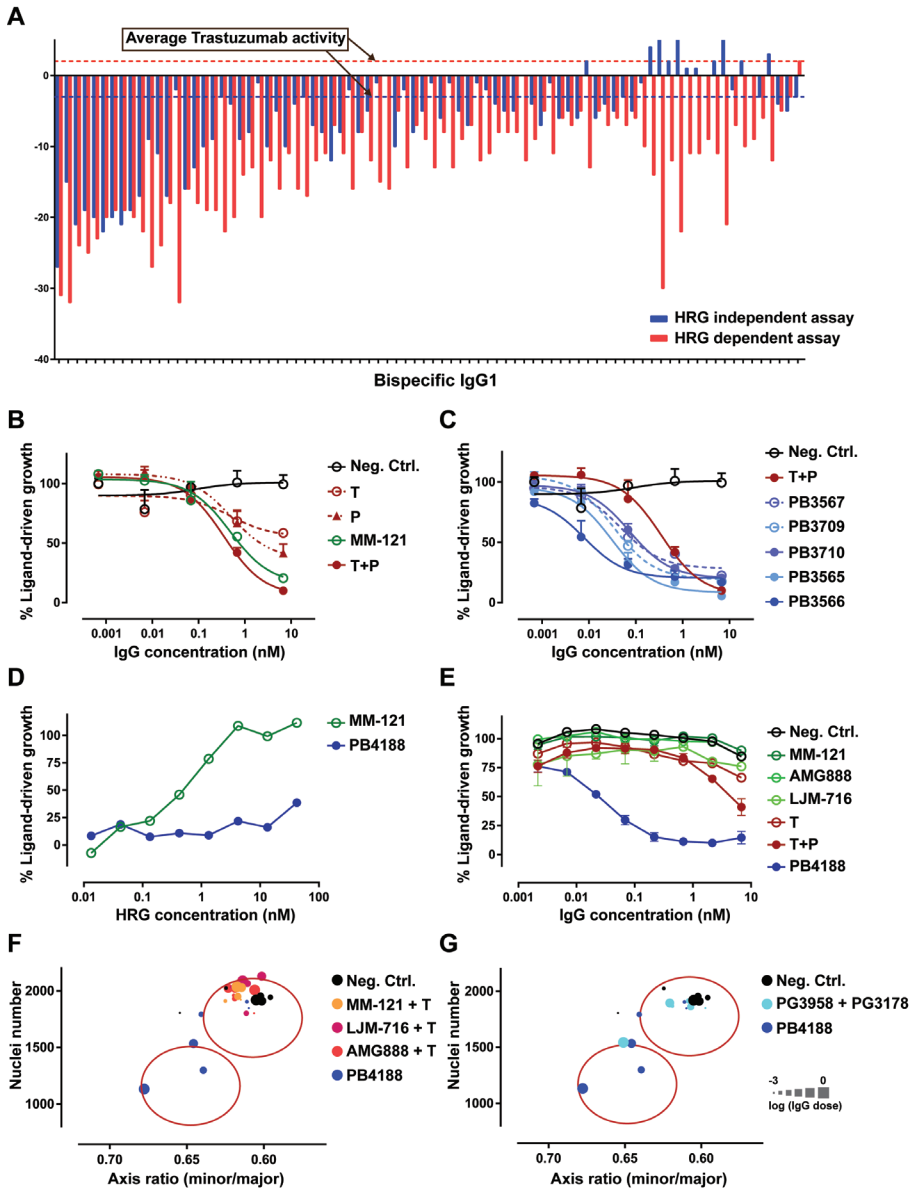


Figure 1. PB4188 potently inhibits HRG-induced proliferation. A, Functional activity of the top 82 HER2xHER3 bAbs (based on combined inhibition) at 1 $\mu\text{g/ml}$ on BxPC3 cells with or without ligand stimulation. Dotted lines represent activity of trastuzumab. Proliferation was measured with Alamar Blue readout and data were normalized against growth without HRG. Trastuzumab was used as a control in all assays. B-C, Titration curves in MCF-7 cells at submaximal HRG concentration (0.125 nM). B, Comparison of negative control (Neg. Ctrl.) antibody, analogs of anti-HER2 mAbs trastuzumab (T), pertuzumab (P) and combination thereof (T+P), and of anti-HER3 mAb MM-121. C, The best anti-HER2xHER3 bAbs were compared to negative control (Neg. Ctrl.) antibody and the combination of

trastuzumab + pertuzumab (T+P). D, N87 cells were stimulated with a titration of HRG and a single concentration of PB4188 or anti-HER3 mAb analog MM-121 (68 nM). E, N87 cells were stimulated with 12.5 nM HRG and a titration of PB4188 or anti-HER3 mAb analogs (MM-121, AMG888, LJM-716), trastuzumab (T), combination of trastuzumab + pertuzumab (T+P), or negative control (Neg. Ctrl.) antibody. 3 days later, proliferation was measured by Alamar Blue. F-G, SKBR-3 cells were cultured in Matrigel in regular growth medium supplemented with 12.5 nM HRG. The effect of equimolar mixtures of trastuzumab (T) and anti-HER3 mAb analogs (F) or of the HER2 and HER3 parental Fabs formatted as bivalent IgG (G) and of negative control (Neg. Ctrl.) antibody were assessed. Cell proliferation was measured by number of nuclei per well. Cell invasion was quantified by measuring cellular shape, dividing the shortest cell axis (minor) by the longest axis (major) of the SKBR-3 cell cluster. An axis ratio of 1 describes a sphere, while decreasing ratios are associated with more invasive structures.

ies demonstrated significantly greater inhibition of tumor growth compared to trastuzumab (Figure S2B-C). Clone PB3566, composed of Fab arms MF3004 and MF3178 was the most potent *in vitro* and *in vivo*. The EC₅₀ of PB3566 on MCF-7 cells (7.9 pM; n = 2) was 50-fold more potent than T+P and 20-fold more potent than the bivalent HER3 mAb PG3178 (which shares the same HER3 Fab as PB3566) (Table S3). The HER2 Fab of PB3566 was humanized and subsequent rounds of sequence optimization were performed to improve developability and manufacturability characteristics, resulting in the variant bAb PB4188 used in further experiments.

Cancer cells can activate secondary signaling pathways to overcome tyrosine kinase inhibitors. In particular, high expression levels of growth factors such as HRG can bypass inhibition of primary oncogenic kinases (31,34). Addition of HRG to HER2-amplified tumor cell lines *in vitro* increases proliferation and invasive properties until they reach a plateau (Figure S3A-B). HRG was titrated into cultures of the HER2-amplified cell line N87 containing a fixed concentration of IgG (68 nM). Like previous observations using the TKI lapatanib (31), the inhibitory activity of HER3 mAb analog MM-121 was reduced in a dose dependent manner as HRG concentration was elevated above the EC₉₀ (0.11 nM) in culture. Remarkably, PB4188 was able to suppress growth even at the highest ligand concentration tested (Figure 1D). At these “stress conditions” (> 10 nM HRG) which are ~100-fold greater than the EC₉₀ for HRG stimulated growth in N87 cells (Figure S3B), analogs of HER2 and HER3 targeting antibodies failed to inhibit ligand-driven growth (Figure 1E). Similarly, an analog of the previously described HER2/HER3 bispecific antibody MM-111 (40) was unable to inhibit ligand-driven growth of N87 cells (Figure S3C), although it was active at submaximal HRG-driven growth conditions (Figure S3D). In contrast, PB4188 was capable of completely suppressing ligand-driven growth at IgG concentrations of > 1 nM (EC₅₀ = 35 pM) (Figure 1C). To confirm these results with an

alternative method, phenotypic profiling of additional HER2-amplified cell lines under HRG stress conditions was carried out using high content imaging to measure growth and invasive morphology. PB4188 was capable of suppressing both morphological parameters (number of nuclei as well as invasion) associated with HRG stimulation of SKBR-3 cells (Figure S4A) in a dose dependent manner (Figure 1F-G). Monospecific antibodies targeting HER3 (Figure S4B) or equimolar mixtures of the HER2 mAb trastuzumab and different HER3 mAbs (Figure 1F), or equimolar mixtures of the HER2 and HER3 parental Fab formatted as bivalent IgG (Figure 1G), were not equally effective. Similar results were observed with a third HER2-amplified cell line BT-474 (data not shown). Consistent with its ability to block *in vitro* cellular proliferation, PB4188 was significantly more potent than T+P in blocking cell cycle progression induced by both submaximal HRG stimulation (Figure S5A-C) and ligand stress conditions (Figure S5D-F). PB4188 inhibited HRG-induced proliferation in cell lines with different levels of HER2 expression, and activity was highest in the HER2-amplified cell lines JIMT-1 and SKBR-3 compared to MCF-7 (Figure S5). Collectively these data demonstrate that the bispecific antibody PB4188 potently blocks HRG-driven proliferation of cancer cell lines regardless of HER2 expression level. In HER2-amplified cell lines cultured under ligand stress conditions PB4188 retained the ability to block HRG-driven proliferation in contrast to monoclonal antibodies, individually or in combination, targeting HER2 and HER3.

PB4188 selectively inhibits ligand mediated HER2/HER3 heterodimerization and downstream signaling

All HER family members can heterodimerize with each other to transduce intracellular signals that vary in both the type of pathway activated and the signal strength (1). The specificity of PB4188 inhibition was investigated using reporter cell lines overexpressing pairs of HER family members that heterodimerize in response to ligand stimulation. In the group of HER2 containing dimers, pertuzumab was capable of inhibiting ligand-dependent heterodimerization of EGFR/HER2 induced by EGF as well as heterodimerization of HER2/HER3 or HER2/HER4 induced by HRG. In contrast, PB4188 selectively inhibited the HER2/HER3 heterodimer and was more potent than anti-HER3 comparator antibody AMG888 (Figure 2A-C). Activity on the EGFR/HER3 dimers was reversed with the AMG888 analog being significantly more potent than PB4188 (Figure 2D). The modest inhibitory activity measured for PB4188 is presumably a consequence of monovalent HER3 interaction. Pertuzumab could not inhibit EGFR/HER3 dimers and, as shown previously, trastuzumab was unable to block any ligand-induced heterodimerization (21). Consistent with its heterodimer specific-

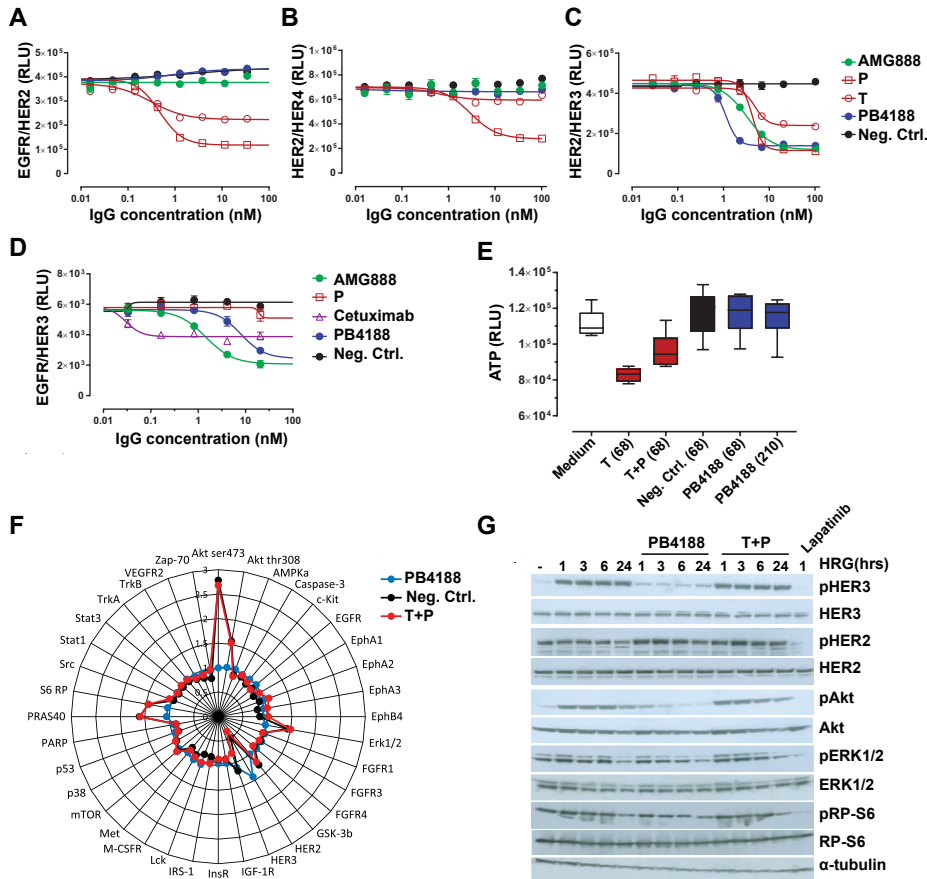


Figure 2. Specificity of PB4188 for HER2/HER3 signaling. A-D, PathHunter assays were used to determine the specificity of PB4188 towards ligand-induced EGFR/HER2 (A), HER2/HER4 (B), HER2/HER3 (C) and EGFR/HER3 (D) dimerization. Cells were stimulated with an EC80 concentration of EGF (A) or HRG (B, C, D) and titrations of PB4188, trastuzumab (T), pertuzumab (P), AMG888 or cetuximab analogs, or negative control (Neg. Ctrl.) antibody. E, Human stem cell-derived cardiomyocytes were incubated with mAb analogs trastuzumab (T), the combination of trastuzumab + pertuzumab (T+P), negative control (Neg. Ctrl.) antibody or PB4188 for 5 days. Cell viability was determined by measuring the cellular ATP levels with a CellTiter-Glo assay. Antibodies were used at a concentration of 68 nM and PB4188 was used in addition at 210 nM. F, SKBR-3 cells were cultured in serum-free medium supplemented with 12.5 nM HRG and either negative control (Neg. Ctrl.) antibody, the combination of trastuzumab + pertuzumab (T+P) analogs or PB4188. 24 hours later, protein lysates were analyzed with PathScan array to measure signaling protein phosphorylation status. Data were normalized against signals measured in cells that were not stimulated with HRG. G, Phosphorylated and total levels of signaling proteins at 24 hours after HRG stimulation (12.5 nM) in N87 cells analyzed with Western blot.

ity, PB4188 displayed no additive toxicity with the anthracycline doxorubicin on adult cardiomyocytes, which depend on the HER2/HER4 heterodimer for growth signaling (Figure 2E). This is in contrast to the additive toxicity observed for trastuzumab alone or combined with pertuzumab in the assay (Figure 2E), and which is clinically manifested in breast cancer patients (41).

HER2/HER3 heterodimerization leads to cellular proliferation via phosphorylation of specific downstream signaling pathways. SKBR-3 cells incubated for 24 hours under HRG stress conditions displayed enhanced activation of the PI3K signaling pathway, including a 3-fold increase in phosphorylation of Akt and increased S6 RP, PRAS40 and Erk1/2 phosphorylation, as demonstrated by antibody array (Figure 2F). PB4188 effectively blocked changes in cellular phosphorylation events caused by HRG incubation in contrast to T+P treated cells. In particular, the large increase in Akt phosphorylation at Ser⁴⁷³ was similar between T+P and negative control treated cells, but was completely inhibited by PB4188. Western blot analysis of N87 cells confirmed the differential effect of PB4188 on HRG induced intracellular signaling at 24 hours (Figure 2G). PB4188 fully inhibited the HRG-induced phosphorylation of HER3 and Akt, and in the case of Akt this inhibition was time-dependent. Similar to its anti-proliferative activity, the combination T+P could not inhibit Akt phosphorylation induced by HRG stress conditions. However, T+P treatment did inhibit HER2 phosphorylation in contrast to PB4188. Collectively these data show that PB4188 is capable of selectively inhibiting downstream signaling events induced by HRG binding to the HER2/HER3 heterodimer in contrast to the HER2 targeting agents trastuzumab and/or pertuzumab, which show a broader spectrum of activity across HER family members.

The HER2 binding arm of PB4188 is the main determinant of its binding avidity and facilitates tumor targeting

PB4188 binding as determined by FACS was higher than that of trastuzumab on all cell lines tested, regardless of their level of HER2 expression (Figure S6). The binding pattern of the bispecific PB4188 is similar to that of a monovalent bispecific control IgG that combines the HER2 Fab arm of PB4188 with a Fab arm binding the irrelevant target tetanus toxoid (HER2xTT) (Figure 3A-C). These data suggest that monovalent interaction with HER2, rather than avidity associated with the binding of both HER2 and HER3 on the cell surface, confers a binding advantage over HER2 bivalent interaction, increasing the absolute number of IgG molecules bound to the cell surface. Genetic aberrations such as amplified copy number frequently result in much higher surface expression of HER2 than HER3 on cancer cell lines (42). Expression of HER2 in HER2-amplified cells

can become as high as 1.2 million copies, whereas HER3 is expressed in numbers below 100,000 copies. Consistent with this, the binding of anti-HER3 mAbs was lower than that of trastuzumab, except in MCF-7 cells that are classified as HER2 0–1⁺ (43) and have relatively low surface expression of HER2 (Figure 3A).

Affinity constants were determined by Scatchard analysis based on measurements with radiolabeled antibodies on HER2-amplified cell lines. This approach has the advantage that monovalent and bivalent affinities are measured on natively expressed cell surface proteins, avoiding the requirement of recombinant proteins necessary for surface plasmon resonance (SPR) measurements. The affinity of trastuzumab measured with this approach was similar to that previously reported ($K_D = 5$ nM; trastuzumab product information sheet). In the BT-474 cell line, binding of the monovalent HER2xTT bAb was almost identical to that of PB4188, while the binding affinity of the monovalent HER3xTT bispecific was more than 10-fold higher (Table 1). A similar pattern was observed in the SKBR-3

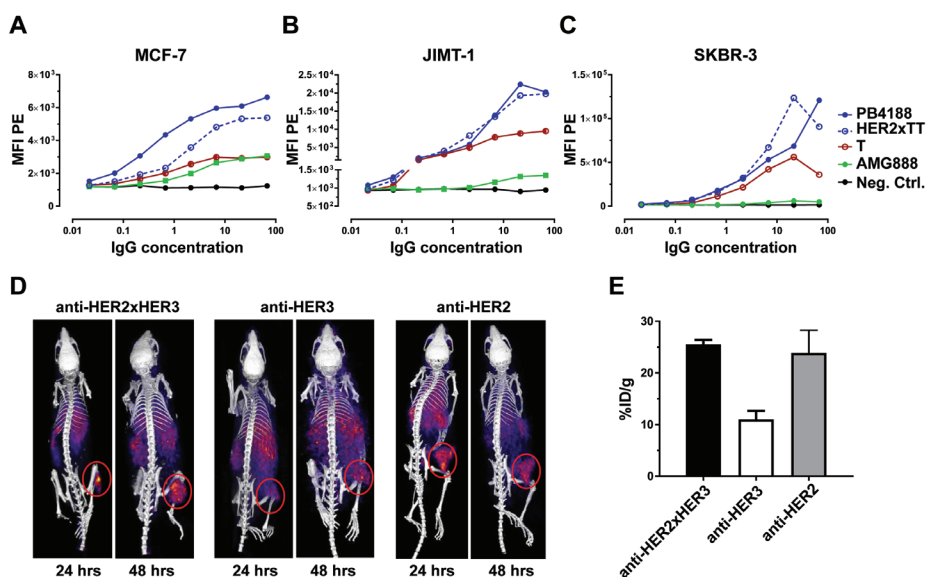


Figure 3. Increased targeting specificity of PB4188. A–C, Breast cancer cell lines expressing low (A), intermediate (B) and high (C) HER2 protein expression levels were assessed for binding of PB4188, a monovalent bAb that combines the HER2 parental Fab arm with a Fab against the irrelevant target tetanus toxoid (HER2xTT), mAb analogs trastuzumab (T) and AMG888, or negative control (Neg. Ctrl.) antibody. All antibodies were detected with PE-labeled anti-human IgG and analyzed by flow cytometry. D, An anti-HER2xHER3 PB4188 antibody analog and bivalent monospecific anti-HER2 or anti-HER3 antibodies with identical Fab arms were radiolabeled with ⁶⁴Cu and injected i.v. in mice xenografted with JIMT-1 tumors. MicroPET-CT imaging showed accumulation of antibodies in tumor xenografts. E, Accumulation of radiolabeled antibodies in the tumors was quantified in gamma counters.

Table 1. Binding affinities. Binding affinities of trastuzumab, PB4188 and its parental HER2 and HER3 Fab arms formatted as monovalent bispecific IgGs with one arm against tetanus toxoid (TT) in HER2-amplified breast cancer cell lines.

Antibody	BT-474	SKBR-3
Trastuzumab analog	3.7 ± 0.5 nM	1.3 ± 0.1 nM
HER2xTT	3.9 ± 0.6 nM	2.3 ± 0.7 nM
HER3xTT	0.23 ± 0.08 nM	0.99 ± 0.4 nM
PB4188	3.2 ± 0.5 nM	2.0 ± 0.4 nM

cell line. These data suggest that the overall avidity of PB4188 binding is driven by HER2 expression and interaction.

The targeting of HER2 with therapeutic agents *in vivo* has been well studied in both humans and animals (44). Radiolabeled antibodies targeting HER2 consistently show excellent tumor contrast because of HER2 overexpression on tumor cells. However, in comparison to HER2, surface expression of HER3 on tumors is considerably lower and closer to expression levels found on normal epithelium. As a result, bAbs such as PB4188 may have an advantage over anti-HER3 monoclonal antibodies in targeting HER2/HER3 heterodimers. To address this question *in vivo*, an imaging experiment was performed comparing surrogates of bAb PB4188 and mAb PG3178, which were fully cross-reactive for human and murine HER3. After labelling with ⁶⁴Cu, antibodies were injected intravenously in mouse xenografted with JIMT-1 cells, which harbor HER2 gene amplification. Micro-PET imaging demonstrated that the PB4188 surrogate more effectively accumulated in tumors compared to the HER2 and HER3 monoclonal Abs with identical Fab binding arm (Figure 3D). Gamma-counter quantification of radioactivity present in tumors confirmed that levels of PB4188 variant in the tumors were 2.5-fold higher than for the parental anti-HER3 antibody, and similar to monoclonal antibody targeting HER2 (Figure 3E). Overall, *in vitro* and *in vivo* data demonstrate that HER2 interaction is responsible for enhanced binding of PB4188 on tumor cells, resulting in more effective targeting of HER2/HER3 heterodimers.

Several lines of evidence suggest that recruitment of immune effector cells may be an important complementary mechanism for the anti-tumor activity of trastuzumab and other RTK-targeting mAbs (45,46). To exploit this mechanism and leverage the enhanced binding observed on HER2 expressing tumor cell lines *in vitro* and its HER2 targeting *in vivo*, PB4188 was engineered to maximize its antibody dependent cellular cytotoxicity (ADCC) activity (Figure S7). The resulting ADCC-enhanced antibody variant PB4188* was tested for ADCC activity in two

assay settings and showed more potent ADCC in comparison to trastuzumab or to its non-engineered version (Figure S7A-D).

PB4188* inhibits HRG-driven tumor growth *in vivo* in a dose-dependent manner

PB4188* was evaluated in several *in vivo* xenograft models where tumors were dependent on HRG for growth. In the HER2-amplified JIMT-1 model that is resistant to trastuzumab and T-DM1, PB4188* was over 100-fold more potent than T+P in inhibiting JIMT-1 growth *in vitro* (Figure 4A) and significantly more potent than T+P *in vivo* (Figure 4B), and this activity was dose dependent (Figure 4C). Pharmacodynamic analysis of tumors harvested 24 hours after last treatment showed significant reductions in HER2/HER3 heterodimers and HER3/p85-PI3K complexes as measured by VeraTag assay (Figure 4D). Consistent with the downstream suppression of PI3K signaling observed *in vitro*, PB4188* induced an almost complete suppression of Akt phosphorylation in tumor lysates taken during (after 2 doses) or at the end (after 4 doses) of the treatment period (Figure 4E). The *in vivo* therapeutic activity of PB4188* was further explored in an HRG-driven brain metastasis patient-derived xenograft (PDX) model resistant to trastuzumab. ST1360B tumor cells derived from an HER2-amplified breast cancer patient were implanted into mice brains, where HRG is widely expressed (47). Mice were treated weekly for four weeks and animals were followed for survival. Tumor size was measured periodically by MRI and animals were monitored for signs of health deterioration. Systemic treatment with PB4188* led to a 100% survival during the treatment period, and animals survived twice as long when treated with PB4188* than with vehicle (Figure 4F). PB4188* was tested in the ovarian cancer model OV-10-0050 PDX, which contains a HRG gene fusion. This genetic aberration leads to high expression levels of HRG protein containing the EGF-like domain, which in turn can activate HER2/HER3 signaling in an autocrine manner. Animals implanted subcutaneously with OV-10-0050 tumors were treated with PB4188* once weekly over 28 days and displayed complete tumor regression, in contrast with the vehicle treated group that showed exponential tumor growth (Figure 4G). PB4188* was also investigated in xenograft models lacking HRG secretion (either autocrine or paracrine). In this setting, no significant reduction in tumor growth was observed (Table S4). Consistently with *in vitro* studies, PB4188 suppresses the growth of four HRG-dependent tumor models, which are resistant to trastuzumab treatment, by inhibiting the HER3/PI3K signaling pathway.

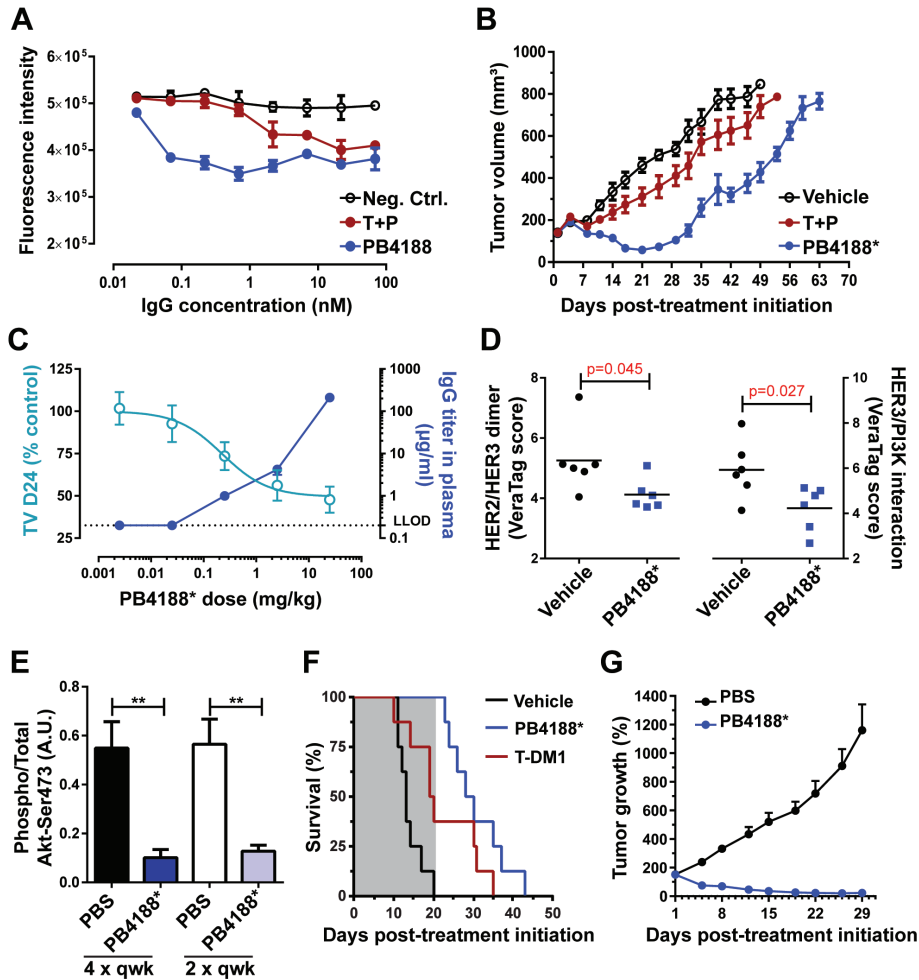


Figure 4. Superior in vivo anti-tumor activity of PB4188*. A, JIMT-1 cells cultured in soft agar were incubated with titrations of PB4188*, the combination of trastuzumab and pertuzumab (T+P) or negative control (Neg. Ctrl.) antibody. Cellular metabolic activity was measured 8 days later with Alamar Blue readout. B, CB17.SCID mice bearing subcutaneous (s.c.) 150 mm³ JIMT-1 xenografts were injected i.p. on day 1, 8, 15 and 22 with vehicle, or 2.5 mg/kg PB4188* or 2.5 mg/kg of the combination of trastuzumab and pertuzumab (T+P). C, CB17.SCID mice bearing JIMT-1 xenografts were injected i.p. on day 1, 8, 15 and 22 with vehicle or different doses of PB4188* (25, 2.5, 0.25, 0.025 and 0.0025 mg/kg). Tumor volume in the treated animals was normalized against vehicle-treated animals on day 24. Serum was obtained 24 hrs after the last dose and analyzed for human IgG titers. Serum samples from mice treated with 0.0025 or 0.025 mg/kg PB4188* were below lower limit of detection (LLOD). D, CB17.SCID mice bearing 400 mm³ JIMT-1 xenografts were injected i.p. on day 1 and 8 with vehicle or 25 mg/kg PB4188*. Four hours after the last dose, tumors were harvested and quantified for the levels of HER2/HER3 dimers and HER3/PI3K complexes by VeraTag assay. E, Levels of phosphorylated Akt were quantified by Luminex in JIMT-1 tumors harvested from mice treated with

2 or 4 weekly doses of PB4188* (25 mg/kg) or vehicle. F, Nude mice were intracranially injected with cell suspension extracted from the patient-derived xenograft ST1360B. Tumor growth was monitored by magnetic resonance imaging (MRI) prior to initiating 3-week treatment (grey shade) with vehicle or PB4188* (25 mg/kg, i.v.). Mice were sacrificed when the scoring of clinical signs (behavior, appearance) reached pre-set criteria. G, BALB/c nude mice bearing s.c. OV-10-0050 PDX tumors were treated once per week during 28 days with PBS or PB4188* (25 mg/kg). Tumor growth was monitored by caliper measurements.

The activity of PB4188 under ligand stress conditions is dependent on a specific combination of HER2 and HER3 epitopes

PB4188 was selected from a large panel of bispecifics combining Fab's binding to different epitopes of HER2 and HER3. In reviewing the characteristics of PB4188 we noted that it contained, along with many of the most active bispecifics, Fab arms that bound domain I of HER2. To determine if this was an important attribute for potency of PB4188 we compared the two best Fabs targeting each of the four HER2 domains combined with an active HER3-targeting arm (MF3178). Antibodies were tested in HER2-amplified SKBR-3 cells and HER2 low MCF-7 cells stimulated with submaximal (Figure 5A-B) and high concentrations of HRG (Figure 5C-D), that have been shown to bypass inhibition of primary oncogenic kinases. In all cases the bAbs that contained HER2 Fabs binding domain I were more potent in reducing cell proliferation than bAbs targeting other HER2 domains (Figure 5). In the cell lines incubated with submaximal (90% ligand-driven growth stimulation) HRG concentrations, bAbs targeting domain II, III or IV of HER2 showed some level of efficacy but were not as potent as the domain I targeting bAbs (Figure 5A-B). In this set of experiments, the level of HER2 on the cell surface also had an impact on proliferation inhibition. At submaximal concentrations of HRG, MCF-7 cells were similarly inhibited by all the bAbs. In contrast, in SKBR-3 cells the HER2 domain I-targeting bAbs showed a higher potency and stronger efficacy than bAbs binding to other HER2 domains. Importantly, under 'ligand stress' conditions, only bAbs binding domain I of HER2 were able to reduce proliferation compared to negative control mAb and bAbs binding other HER2 domains.

The potent blocking activity of HER3/HRG signaling by PB4188 is due to its mode of binding

Our *in vitro* functional data suggested that the anti-tumor activity of PB4188 is related to its interaction with a specific combination of HER2 and HER3 domains. To gain further molecular insights, the epitopes of both the HER2 and HER3 Fabs were investigated by X-ray crystallography. The crystal structure of

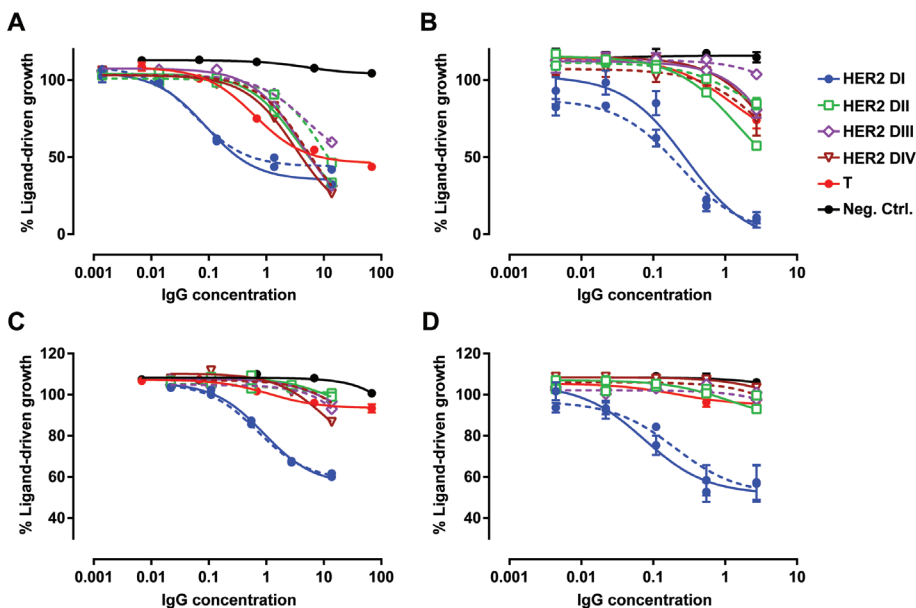


Figure 5. Importance of HER2 epitope location for the activity of PB4188. N87 (A, C) and MCF-7 cells (B, D) were stimulated with low (0.125 nM) (A-B) or high (12.5 nM) (C-D) HRG concentration. A titration of bAbs containing anti-HER3 Fab MF3178 and an anti-HER2 Fab binding one of the four domains of HER2, mAb analog trastuzumab (T) or negative control (Neg. Ctrl.) antibody was added. Proliferation was measured using Alamar Blue readout.

HER2 ectodomain (residues T23-T652, Uniprot numbering) in complex with MF3958 (Figure 6A) was solved at 3.0-Å resolution (see Table S5 for X-ray crystallography statistics). The domain organization of HER2 is very similar to previous structures (48–52) with root-mean-square deviation (rmsd) for the C α -backbone atoms ranging from 0.4 to 0.8 Å. MF3958 binds to HER2 at the C-terminal part of domain I through a shallow interaction surface that buries 683 Å², mediated almost entirely by the three complementarity-determining regions (CDRs) of the Fab HC (Table S6 and Figure S8A-B). The epitope is composed of two peptide stretches, residues 143–147 and 160–181, of HER2 (Figure 6B). The details of the interaction analysis are listed in Table S7 and S8. These observations are in agreement with the findings of the alanine scanning that identified the functional importance of HER2 residues T144, R166, R181, P172 and G179 (Figure S9A). The region recognized by MF3958 differs from that of pertuzumab and trastuzumab Fabs, which bind residues located in the center of domain II and in domain IV, respectively (Figure S10A-B). It partly overlaps with the scFv A21 (53), which binds three patches with residues 100–105, 135–144 and 163–187

at the C-terminus of domain I (Figure S10C). Consistently with these structural observations, binding studies showed that trastuzumab and PB4188 can bind simultaneously to HER2 (Figure S11).

The crystal structures of the HER3 ectodomain (residues S20-T643) in complex with MF3178 solved at 4.5- and 3.4-Å resolution show the same HER3-Fab binding conformation with HER3 in its tethered state (Figure 6C). All four extracellular domains (I-IV) of HER3 are observed in the electron density of the 4.5-Å resolution data set, while in the structure at 3.4 Å almost the whole domain I (residues M1- P260, K279-C301) of HER3 has a poorly defined electron density (Figure S12). Structural analysis was based on the structure determined at 3.4-Å resolution. The overall conformation of HER3 is very similar to previously solved structures (28–30,54), with an rmsd ranging from 0.8 to 2.0 Å for the C α -backbone atoms, reflecting minor domains reorientations. The epitope is localized on domain III of HER3. The protruding loop containing residues Y424, N425 and R426 is embedded in a pocket formed by CDR-L1, CDR-L3 and CDR-H3 of the Fab (Figure 6D and Table S6). The MF3178 interface buries only 426 Å² on the HER3 side with the heavy and the light chain contributing almost equally (238 Å² for HC and 188 Å² for the LC) (Figure S8C-D). These results confirm the importance of residue R426 that was previously identified by alanine shotgun scanning (Figure S9B). Although the HER2 and HER3 Fabs of PB4188 share a single light chain in germline configuration, the LC appears to significantly contribute to the recognition of the HER3 epitope, while it is scarcely involved in binding HER2. Interestingly, Y32 from CDR-L1 is contributing to the binding of both HER2 and HER3 (Table S6). The MF3178 epitope is different from all other published HER3-Fab structures. The epitope of the DL11 Fab (28), also localized in domain III, shows a different conformational arrangement with different residues involved (Figure S13A). Based on the published structure of EGFR-EGF dimeric complex (55) we could predict that the binding site of MF3178 is incompatible with the untethered (active) conformation of HER3 because it would sterically clash with domain I. More importantly, the MF3178 binding site on HER3 overlaps with the putative HRG binding site. Thus, these observations suggest a mechanism of action in which MF3178 binds HER3 in its inactive monomeric conformation and prevents HRG from binding.

Additionally, we performed small-angle X-ray scattering (SAXS) on the HER2-ECD:HER3-ECD:PB4188 complex, investigating the binding of PB4188 when both receptor ectodomains are present in solution. By fitting the crystal structures of the HER2-ECD:MF3958 and HER3-ECD:MF3178 complexes and a representative Fc region with the SAXS *ab initio* models (Figure 6E) we could confirm that PB4188 IgG is able to bind to both HER2 and HER3 ectodomains in solution at the same time. Moreover, we noted that the epitopes on the soluble forms of HER2

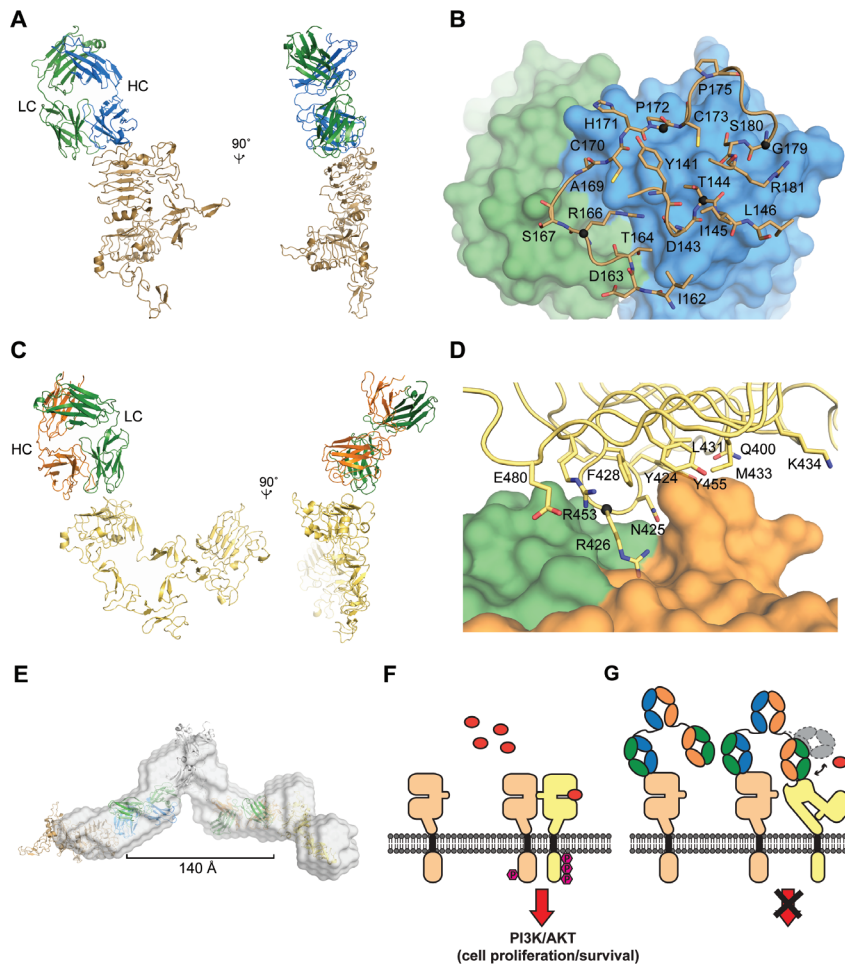


Figure 6. Structural investigation of PB4188 mode of binding. A, Structure of HER2-ECD:MF3958 complex in two orthogonal views. HER2 is colored sand, MF3958 HC is blue and LC is green. B, Bottom-view of HER2-ECD:MF3958 interaction with HER2 residues shown as sticks and MF3958 shown as surface (color scheme as in A). Residues identified as critical for binding by the alanine shotgun mutagenesis are marked with spheres; 'primary residues' are colored black, 'secondary residues' are grey. C, Structure of HER3-ECD:MF3178 complex in two orthogonal views (4.5-Å resolution structure). HER3 is colored yellow, MF3178 HC is orange and LC is green. D, Side-view of HER3-ECD:MF3178 interaction with HER3 residues shown as sticks and MF3178 shown as surface (color scheme as in C). Residues identified as critical for binding by the alanine shotgun mutagenesis are marked with a black sphere. E, Superposition of a representative SAXS ab initio beads model of HER2-ECD:HER3-ECD:PB4188 complex (shown as grey surface) on the crystal structures of HER2-ECD:MF3958, HER3-ECD:MF3178 (color scheme as in A and C) and the Fc region (dark grey). The Fc region is taken from a full IgG structure with PDB ID 1HZH. The paratope-to-paratope reach is indicated with a black line. F-G, Cartoon models illustrating HRG-mediated signaling in absence (F) and in presence of PB4188 (G). HRG is shown in red, HER2 is orange, HER3 is yellow.

and HER3 are separated by ~ 140 Å in the SAXS model, whereas the distance between the epitopes in the putative heterodimer of HER2 and HER3 is predicted to be ~ 90 Å based on published EGFR homodimer structure (55). Thus, based on the orientation of the epitopes, the distance between them, and in the case of HER3, steric hindrance, it is unlikely that PB4188 would be capable of binding a single HER2/HER3 heterodimer simultaneously with both HER2 and HER3 Fab arms.

We used the statistical thermodynamic theory of the grand canonical formalism (see Supplementary Experimental Procedures) to model the binding of the bAb PB4188 compared to a bivalent monospecific anti-HER3 based on PG3178. We considered two hypothetical cell lines with low (modeled on MCF-7, $\sim 30,000$ copies) and high (modeled on SKBR-3, $\sim 3,000,000$) HER2 expression levels, at low HRG concentration (HRG = 0.1 nM) and at HRG stress conditions (HRG = 10 nM). In this model, we took into account the binding constants from Table 1 and a dissociation constant for HER3-HRG binding of 0.2 nM according to previous reports (22). We could confirm the experimental observation that in cell types with low expression levels of HER2, PB4188 does not perform better than PG3178 mAb (Figure S15A-C). However, in cell types where HER2 is overexpressed PB4188 is much more effective in competing for the HRG binding both at low and high HRG concentrations (Figure S15B-D). In this way, we could model the action of PB4188, which, as shown experimentally, has a more potent activity than anti-HER3 mAb in HER2-amplified conditions (Figure S16).

Discussion

The HER2 targeted agent trastuzumab in combination with chemotherapy is the standard of care for patients with HER2-positive breast cancer (56). Other HER2-targeting agents such as pertuzumab, T-DM1, lapatinib and neratinib are being developed, or have been approved in certain settings, to provide additional benefit to this patient population. However, *de novo* or acquired resistance to these HER2-targeting agents eventually develops, leading to clinical progression. HER2-amplified tumors have a strong dependence on PI3K/Akt signaling, as sustained blockade of this pathway appears to be required for the anti-tumor effect of HER2 antagonists (33,57). Several lines of evidence show that (re)activation of the HRG/HER3 pathway can bypass HER2 inhibition and result in treatment resistance. The preferred dimerization partner of HER3 is HER2, and this heterodimer is the most potent oncogenic signaling unit of the HER family (1). In HER2-amplified tumors, evidence suggests that ligand activated HER3 will

always be associated with HER2 (58). Thus, there is a clear rationale to target HER2 and HER3 simultaneously (13,42).

We have used a bispecific full-length human IgG1 format to target ligand-driven signaling through the HER2/HER3 heterodimer. Because little is known about the optimal mechanism to achieve pharmacologically relevant inhibition with bispecific antibodies, we pursued an unbiased in-format screening approach with a downstream readout (cell growth inhibition). This allowed us to operate without making assumptions concerning affinity, epitope specificity of the bispecific IgG binding arms or the specific mechanistic outcome of the targeting. Using this approach we identified several potent inhibitors of ligand-dependent proliferation that shared a number of common attributes. First, they were capable of sustaining blockade of ligand signaling even in the presence of supramaximal concentrations of HRG. In contrast, a panel of HER2 and HER3 mAb analogs, which were active at submaximal concentrations, were unable to inhibit proliferation at supramaximal levels of ligand. This was also true when HER2 and HER3 targeting antibodies were combined in equimolar concentrations or when the parental binding arms of the most potent bispecific IgG1, PB4188, were reformatted as conventional bivalent monoclonal IgG1 and combined. Second, they all shared a domain I binding HER2 Fab. This is in contrast to active HER2 targeting antibodies such as trastuzumab that binds in domain IV and pertuzumab that binds in domain II of HER2. Given the potent inhibition of HER2 signaling by trastuzumab, bispecific antibodies containing domain IV binding Fabs combined with HER3 inhibiting Fabs might have been expected to have synergistic inhibitory activity. Indeed one of the most potent bispecifics identified in the initial *in vitro* and *in vivo* screens was PB3448 that contained a domain IV binding HER2 Fab. However, although it was as effective as PB4188 in tumor reduction of BxPC3 cells, this bispecific antibody failed to inhibit cell line proliferation at supramaximal ligand concentrations. This activity was restricted to the group of bispecific antibodies that contain domain I binding HER2 Fabs combined with HER3 Fabs binding domain III. FACS binding studies clearly showed that PB4188, or a monovalent version with only the HER2 Fab arm, bind more efficiently to tumor cell lines with varying levels of HER2 than trastuzumab. In addition, a surrogate of PB4188 effectively targeted HER2 *in vivo*. This is unrelated to a greater affinity for HER2 since both trastuzumab and MF3958 have equal monovalent affinities. The more efficient binding observed could be a result of less competition for a particular epitope in contrast to bivalency, which leads to higher avidity for the target but with the potential for epitope competition, particularly when the target may be clustered such as in amplified conditions (59). Consequently, PB4188 is more efficient than other HER2-targeting antibodies at opsonizing tumor cells and has a low rate of

internalization. Based on these features PB4188* (ADCC enhanced variant) was generated to leverage immune cell-mediated tumor cell killing as a complementary mechanism to the potent cytostatic activity of PB4188.

The potency and mechanism of action demonstrated *in vitro* by PB4188* was experimentally verified in three different and pathophysiologically relevant xenograft models driven by HRG. In the JIMT-1 trastuzumab resistant breast cancer model, where HRG transcription has been upregulated, PB4188 was significantly more potent than the combination of trastuzumab and pertuzumab, and the activity was dose dependent. In a second autocrine ovarian cancer PDX model, driven by HRG gene translocation, administration of PB4188 led to complete tumor regression during treatment. Finally, in an orthotopic BC PDX model from a patient with trastuzumab resistant brain metastasis, PB4188 protected 100% of mice from outgrowth during the treatment. The brain is an anatomical site where HRG is present in high abundance and this may partly explain why brain metastasis of breast cancer is difficult to treat with HER2 inhibitors. All these studies were carried out with PB4188*, an ADCC enhanced version of PB4188, and immune mediated tumor killing cannot be excluded from contributing to the therapeutic effects observed. However, the studies were carried out in immunodeficient mice where the number and functional competence of immune effector cells is diminished. Moreover, in the JIMT-1 model we were able to correlate tumor reduction with relevant pharmacodynamic factors such as a decrease in Akt phosphorylation, HER2/HER3 and HER3/p85-PI3K dimer formation, confirming the mechanism of action *in vitro*. Finally, in models where tumor growth was not ligand-driven PB4188 was not effective.

PB4188 represents a highly selective inhibitor of HER2/HER3 signaling that shows potent activity *in vitro* and *in vivo* in settings where HRG is driving tumor growth. In a panel of HER dimer pairs, PB4188 was only effective in completely blocking HER2/HER3 dimer signaling. PB4188 only inhibited HRG-driven phosphorylation events and had no impact, for example, on HER2 phosphorylation. Other HER targeting agents disrupting HER2/HER3 signaling such as pertuzumab or HER3 monoclonals have broader spectrums of activity which can be manifested in unwanted toxicities and a reduced therapeutic index. Indeed, in both modalities GI toxicities have been observed, and this has reduced the possibilities for combinations of these agents, in particular with drugs targeting the MAPK pathway. In the case of HER3 monoclonal antibodies, lack of effective targeting has led to high dosing to achieve evidence of pharmacodynamic activity at the tumor site. In contrast, the specific targeting and inhibitory activity of PB4188 is expected to result in a good safety profile in patients. Evidence from the early clinical evaluation of PB4188 (also known as MCLA-128) is consistent

with the preclinical evidence (60). In particular, to date there has been no evidence of cardiovascular toxicity, a known complication of HER2 targeting agents. This is consistent with our data on adult cardiomyocyte cultures and with lack of blocking activity on HER2/HER4 signaling dimers, which are important in adult cardiomyocyte physiology.

To gain a structural understanding of the mechanism by which PB4188 exerts its potent anti-HER3 signaling activity we pursued the crystal structures of both Fabs in complex with their targets. The epitope of the HER3 binding Fab MF3178 is in close proximity to the ligand-binding pocket of HER3. Based on the data generated, MF3178 is predicted to preferentially bind to HER3 in its inactive tethered conformation and sterically hinder binding of HRG to HER3. This is consistent with the ability of the parental monoclonal antibody PG3178 to inhibit ligand-driven proliferation. The epitope of the HER2 Fab of PB4188 was localized at the top of domain I, the most distal location from the membrane surface. With the HER2 Fab of PB4188 bound at this location, we hypothesize that the HER3 Fab (MF3178) has the maximum freedom to interact with HER3, block ligand binding and inhibit dimer formation, resulting in the observed enhancement of PB4188 activity over the single HER3 targeting mAb PG3178. Early work demonstrated that heterodimerization of HER3 with HER2 creates a high affinity binding site for heregulin (22). The affinity of HRG for HER3 alone is already significantly higher than measured for EGF binding to EGFR, and this is greatly increased upon heterodimerization with HER2 (60). Our experimental data is consistent with these observations. At supramaximal concentrations heregulin is able to reverse HER3 monoclonal antibody inhibition of proliferation and cell cycle arrest, and this can be modeled based on the relative avidities of the ligand and antibodies for the receptor. Importantly, our model predicts that HER2 amplification increases resistance to ligand-driven proliferation inhibition of the HER3 mAb (PG3178) but not of the bAb (PB4188). At submaximal levels of HRG the model predicts that PG3178 and PB4188 will be equally efficient at inhibiting ligand-driven proliferation. Of note, our experimental data suggest that PB4188 retains a potency advantage over the PG3178 in the HER2-low situation, indicating that modeling affinity does not capture the full biological complexity of the interactions. The model correctly predicts that under HER2-amplified conditions PG1378 is unable to inhibit supramaximal concentrations of ligand-driven growth in contrast to PB4188.

A previous study reported the design of a HER2/HER3 bispecific scFv construct, MM-111 (40,42). In contrast to the unbiased screen approach that identified PB4188, a systems biology approach was applied, resulting in the use of a HER2-targeting arm with higher affinity than the HER3 arm to drive better

targeting to HER2-amplified tumors. We demonstrate that specific targeting *in vitro* and *in vivo* is unaffected by the presence of a high affinity HER3 binding arm, presumably due to the relatively low expression level of HER3 compared to HER2. However, because of this design choice, the 16 nM HER3 arm of MM-111 is presumably disadvantaged in overcoming the high affinity interaction of HRG with the HER2/HER3 dimer. Indeed, the analog of MM-111 that we generated was not able to inhibit supramaximal ligand-driven proliferation of HER2-amplified cell lines, in spite of the fact that it was able to bind with high avidity to these cells.

Based on our experimental data, structural analysis and modeling we propose that PB4188 uses a ‘dock and block’ mechanism to inhibit HRG-driven proliferation of HER2-amplified cells lines. In this model, the HER2-targeting Fab is able to saturate the available binding sites on tumor cells and optimally position the HER3-targeting arm to inhibit HRG interaction with HER3 (Figure 6F-G). Importantly, as HRG concentration is increased, there is no competition for binding of the HER2 Fab, so the HER3 Fab arm always remains in close proximity, increasing its relative affinity for HER3 (61). We believe that this ‘cis’ mode of action may be broadly applicable to bispecific antibody targeting. It opens up a new avenue of application for the bispecific antibody class of therapeutics which to date have focused on ‘trans’ based activities, as exemplified by the T cell engager antibodies. Indeed, we have recently reported on a novel human full-length IgG1 bispecific antibody targeting Lrg5 and EGFR that leverages a ‘cis’ binding mechanism resulting in superior potency (62). The development candidate of PB4188* (MCLA-128) is now in Phase I/II clinical evaluation in breast, gastric, ovarian, endometrial and lung cancer. Based on our preclinical results it is expected to provide benefit in settings where current HER2 targeting agents are not effective.

Experimental Procedures

Cell line proliferation assays

SKBR-3 cells were cultured in DMEM F/12 medium (Life Technologies) supplemented with L-glutamine and 10% heat inactivated FBS. BxPC-3-luc2 and N87 cells were cultured in RPMI1640 (Life Technologies) supplemented with 10% heat inactivated FBS. MCF-7 cells were cultured in RPMI1640 supplemented with 100 μ M NEAA, 1 mM sodium pyruvate, 4 μ g/ml insulin and 10% heat inactivated FBS. JIMT-1 cells were cultured in DMEM and 10% heat inactivated FBS. Proliferation assay media for the different cell lines were: RPMI-1640, 0.05% BSA, 10 μ g/ml Holo-transferrin, 1 mM sodium pyruvate, MEM NEAA

for MCF-7; DMEM, 0.05% BSA for JIMT-1; DMEM/F-12, 2 mM L-glutamine, 0.05% BSA, 10 µg/ml Holo-transferrin for SKBR-3; RPMI-1640, 0.05% BSA, 10 µg/ml Holo-transferrin for N87 cells.

Conventional plate-based proliferation assays. Subconfluent cell cultures were harvested in assay medium containing recombinant Human NRG1-beta 1/HRG1-beta 1 EGF domain protein. Dilution series of antibodies were added to the cells in a volume of 100 µl in 96-well black bottom plates (ABgene AB-0932). Cells were cultivated for 3–5 days at 37°C, 5% CO₂, before Alamar Blue™ (Invitrogen) was added according to the manufacturer's instructions and incubated for a further 6 or 24 hours. Fluorescence was measured at 550 nm excitation and 590 nm emission wavelengths.

Suspension proliferation assays in agar plates. 100 µL of the soft agar bottom layer (0.6% final concentration in complete medium) was added per well of 96-well plate and left to solidify. 50 µL of the soft agar top layer (0.4% final concentration) containing 10,000 JIMT-1 cells were then added per well and incubated at 37°C, 5% CO₂. 24 hours later, titration of antibodies in DMEM medium were added and incubated for 8 days. Wells were then incubated with Alamar Blue for 3–5 hours at 37°C and fluorescence intensity was determined (excitation 560 nm; emission 590 nm).

Matrigel based phenotypic assays. SKBR-3 (2000) or BT-474 (2250) cells were seeded in 15µl matrigel per well of a 384-well plate (Greiner 781091). 24 hours later, antibodies diluted in culture medium were added in quadruplicate in the absence or presence of HRG. Cells were incubated for 7 days at 37°C, 5% CO₂. Cells were then fixed and stained with phalloidin and Hoechst dye to image the actin cytoskeleton and nuclei, respectively. Fluorescent images were taken at different levels through the gel (Z-stack) using confocal microscopy and the images were superimposed. A variety of morphological features were measured (800 in total). Only features that differed between medium and HRG treatments were selected for analysis. Single parameter analyses were performed and t-tests were used to compare treatments to medium.

Cell cycle analysis in HRG-stimulated cell lines

MCF-7, JIMT-1 and SKBR-3 cells were seeded into 24-well plates in 1 ml assay medium and incubated overnight at 37°C, 5% CO₂. 24 hours later antibodies were added in the presence of HRG (1 or 100 ng/ml) and incubated for 24 (for JIMT-1 or SKBR-3 cells) or 48 hours (for MCF-7 cells). Cells were then harvested and stained with the Click-iT EdU AlexaFluor488 kit (Life Technologies) according to the manufacturer instructions. 30 minutes prior to analysis by flow cytometry, cells were incubated with 200 nM FxCycle far red dye (Life Technologies) and

100 µg/ml RNase A (Life Technologies). Data were analyzed by gating single cells on an FSC-width vs FSC-height scatter plot, and subgating the G0/G1, S and G2M phases of the cell cycle on an APC vs AlexaFluor488 scatter plot, as EdU^{neg}APC^{low}, EdU^{pos} and EdU^{neg}APC^{high} populations, respectively. Data were represented as the proliferation index, calculated by dividing the percentage of cells in the S and G2/M phases by the percentage of cells in the G0/G1 phase.

Dimerization assay

PathHunter. Heterodimerization assays for EGFR/HER2, HER2/HER3 and HER2/HER4 were performed with PB4188, surrogates of AMG888, trastuzumab and pertuzumab. Heterodimerization assay for EGFR/HER3 was performed with PB4188, surrogates of AMG888, pertuzumab and cetuximab. The anti-tetanus toxoid mAb was included as negative control in all the assays. Antibodies were assayed in quadruplicates at a maximum concentration of 100 nM. Antibodies were pre-incubated for 3 hours prior to stimulation with the agonistic ligands EGF (10 ng/ml) to EGFR/HER2, HRG (30 ng/ml) to HER2/HER3 and HER2/HER4, and HRG (230 ng/ml) (Prospec Bio) to EGFR/HER3 reporter cells, respectively. Heterodimerization was determined by measuring β-galactosidase-based fluorescence 16 hr later.

In vitro cardiomyocyte viability assay

Human stem cell-derived cardiomyocytes (Plurionics BV) were seeded at a density of 20,000/well in white flat-bottom assay plates (Corning 655098). On day 5 of culture, the medium was replaced with glucose- and galactose-free culture medium supplemented with 12.5 nM HRG. On day 7, test antibodies were added at the concentrations indicated in combination with doxorubicin (3 µM). Cell viability was assayed on day 9 using the Promega CellTiter-Glo assay.

Phosphorylation assays

PathScan array analysis. Cells in logarithmic growth phase were harvested and seeded in 6-well plates (1.5x10⁶ cells for SKBR-3) in starvation medium and incubated overnight. The next day, antibodies were added to a final concentration of 5 nM, incubated for one hour at 37°C, and after that HRG was added to a final concentration of 12.5 nM (100 ng/ml). After 24 hr incubation, plates were placed on ice and cells were washed twice with cold PBS. Subsequently, cells were washed and lysed (Cell signaling RTK # 9803 or IC # 7018) for a minimum of 30 minutes on ice. Protein concentrations were measured using the BCA method (Pierce #23235) and adjusted to 2 mg/ml with lysis buffer. PathScan RTK Signaling Antibody Arrays (Cell Signaling #7949) or PathScan Intracellular Signaling

Antibody Arrays were used according to manufacturer guidelines using 800 µg/ml protein lysate. Slides were allowed to dry before imaging on an Odyssey®Clx. Spot fluorescence intensity was calculated using Image Studio software.

Western blot analysis. 20x10⁶ N87 cells were seeded in 10 cm dishes in starvation medium. The next day, antibodies were added to a final concentration of 5 nM (PB4188 or trastuzumab + pertuzumab) or 10 µM (lapatinib) and cells were incubated for one hour. HRG was then added to a final concentration of 12.5 nM. After 1, 3, 6 or 24 hours, dishes were placed on ice, washed twice with cold PBS and cells were lysed in RIPA lysis buffer (Cell Signaling Technology) containing protease and phosphatase inhibitors. 30 µg of protein lysate was analyzed by Western blot using the following primary antibodies (Cell Signaling Technology): Phospho-Akt (ser 473), Total Akt, Phospho-HER2 (Tyr 1221/1222), Total HER2, Phospho-HER3 (Tyr 1289), Total HER3, Phospho-ERK1/2 (Thr 202/Tyr 204), Total ERK1/2, Phospho-S6 RP (Ser 235/236), Total S6 RP. Protein expression levels were detected with HRP-conjugated goat anti-rabbit in combination with enhanced chemoluminescence with X-ray films (Amersham).

Affinity determination

Antibodies were radiolabeled with ¹²⁵I using IODO-GEN® Precoated Iodination Tubes (Pierce) according to the manufacturer's instructions. Radiolabeled IgGs were diluted to an activity of ~1–2 x 10⁸ cpm/ml in 25 mM Tris-HCl, 0.4 M NaCl, 0.25% bovine serum albumin, 5 mM EDTA, 0.05% NaN₃. Flow cytometry analysis of the labeled and non-labeled IgG using BT-474 and SKBR-3 cells showed no or only minor signs of reduction in binding after radiolabeling. Steady state cell affinity measurements were performed by seeding SKBR-3 or BT-474 cells in 96-well plates. The next day, various concentrations of antibodies were incubated at 4°C for 4 hours. Unbound radioactivity was removed and cell-bound radioactivity was measured using a gamma well counter. Non-specific binding was measured by adding a receptor-blocking concentration (100-fold excess) of unlabeled antibody. Each condition was tested in triplicate and three independent experiments were performed per antibody. K_D values were calculated based on a non-linear regression model that compensates for non-specific binding (Prism 6.0, GraphPad).

Xenograft studies

JIMT-1 model. 8-week old female CB.17 SCID mice (Charles River) were injected subcutaneously in the right flank with 5 x10⁶ JIMT-1 tumor cells (0.2 ml cell suspension harvested from exponentially growing cultures). The tumors were measured twice per week with a caliper in two dimensions to monitor size. Once

tumor size had reached 100–150 mm³, animals were enrolled in the efficacy study and randomly distributed into groups of 10 mice. Mice received four weekly injections of antibody and tumor sizes were measured biweekly by caliper.

Biodistribution study. Variants of bAb PB4188, anti-HER3 PG3178 and anti-HER2 PG3958 were conjugated to a bifunctional chelator (63). Binding characteristics of the conjugated products to the target were confirmed using flow cytometry-based binding assays. Proteins were then labeled with ⁶⁴Cu and mice bearing JIMT-1 breast xenografts were administered the radiolabeled antibodies via tail vein. MicroPET/CT images were acquired 48 hours post-injection, after which tumors were excised and radioactivity was measured in a gamma counter. Results were expressed as percentage injected dose per gram tissue.

ST1360B intracranial model. Subcutaneous ST1630B PDX tumors grown subcutaneously in NMRI nude mice were harvested, washed with PBS and residual connective tissues at the surface of the tumor were trimmed. Tumors were cut into small pieces and digested with accutase and collagenase IV to generate a suspension of single cells. Digestion was stopped by addition of media containing fetal bovine serum and the cell suspension filtered through a 100 µm filter, washed and resuspended in PBS to a final concentration of 18 million viable cells/ml. NMRI nude mice were anaesthetized by hypnorm/midazolam (1 ml/100 g body weight) and placed in a stereotactic frame. A longitudinal incision was made in the scalp exposing the calvarium. A hole was drilled in the skull 1.5 mm right of the sutura saggitalis and 0.5 mm posterior to the bregma using a micro-drill. 10 µl of the cell suspension (180,000 cells) were injected at a depth of 2–2.5 mm at a rate of 60 nl/sec using a 100 µl syringe with a 25-gauge needle placed in a micro infusion pump. Lidocain (1 mg/100 g body weight) was administrated in the incision site for local anesthetic and the skin was closed with a suture. Mice were monitored until fully recovered from the anesthesia and at least twice per week (weight and clinical signs) after tumor inoculation and more often if clinical signs or weight loss were present. Mice were enrolled into study based on two pathological MR scans showing tumor growth and a tumor volume of about 10–20 mm³. Each time mice met the enrolment criteria, animals were randomized into one of two groups so that all groups presented the same mean tumor volume at treatment initiation. Mice were treated weekly i.v. with either vehicle or PB4188* (25 mg/kg). Tumor volume was measured on the images by drawing region of interests (ROIs) on the individual slices and calculating volume of the ROIs. Image analysis was performed using Horos (www.horosproject.com). Animals were observed for clinical signs and scored for changes in body weight, behavior or physical appearance. Animals with deteriorating health (clinical score superior to a pre-defined threshold) were euthanized by cervical dislocation.

HER expression and downstream phosphorylation in tumor samples

VeraTag assay. Mice bearing JIMT-1 tumor xenografts (300–400 mm³) were treated with 2 weekly doses of antibody (25 mg/kg). 4 hours post-last dose, tumor were removed and fixed in 10% neutral buffered formalin. Samples were then paraffin-embedded and processed for HER2-HER3 heterodimers (H23D) and HER3-PI3 kinase (H3PI3K) VeraTag analyses (Monogram). Analysis was performed as previously described (64).

Phosphorylated protein measurement (Luminex). Mice bearing JIMT-1 tumor xenografts (100–150 mm³) were treated with 2 or 4 weekly doses of antibody (25 mg/kg). 24 hours post-last dose, tumors were flash-frozen and processed to powder. Tumor lysates were prepared to a concentration of 50 mg tumor/ml by adding cold BioRad Lysis Buffer to the frozen powder samples. Samples were then incubated at 4°C on a rocker for 60 minutes to ensure complete lysis. The samples were centrifuged at 4°C for 10 minutes at 16,000 x g and aliquoted. Total protein was determined using the BCA method. Total AKT, phospho Akt Ser473 and Thr308 were detected using commercial Luminex kits (Millipore 48–618MAG, 46–645MAG and 46645M-1K, respectively) in each sample in duplicate. Dilutions were prepared in sample diluent to load a target of approximately 25 µg protein per well for all total and phosphorylated analyte determinations. The Millipore kits were used according to the manufacturer's specifications.

X-ray crystallography

His-tagged monomeric human HER2 and HER3 ectodomains were produced in HEK293-EBNA (Epstein-Barr virus nuclear antigen) cells deficient in N-acetylglucosaminyltransferase I (GnTI; U-Protein Express), which yield shorter and more homogenous N-linked glycan chains suitable for crystallization of glycosylated proteins. Fab regions MF3958 and MF3178 were expressed in HEK293-F cells. His-tagged proteins were purified by IMAC column followed by gel filtration on a Superdex 200 16/600, whereas the Fabs were purified by Capto-L affinity resin (GE Healthcare) followed by gel filtration on a Superdex 75 16/600. Purified HER2 and HER3 ECDs were mixed with MF3958 and MF3178 respectively, in a 1:2 receptor:Fab ratio and incubated overnight at 4°C. The complexes were separated from the excess of Fab by size-exclusion chromatography on a Superdex-200 10/30 column equilibrated with buffer containing 25 mM Tris pH 7.5 and 150 mM NaCl. The purified complexes were concentrated to 10 mg/ml. Crystals of the HER2-ECD:MF3958 complex were grown by hanging drop vapor diffusion technique equilibrating the protein mixture with a reservoir solution containing 0.1 M MES pH 6.0 and 15% w/v PEG 6,000 in a 1:1 protein:mother liquor ratio at 18°C. Crystals of the HER3-ECD:MF3178 complex were grown

at 18°C by sitting drop vapor diffusion equilibrated in a 1:1 ratio with reservoir solutions containing 0.1 M Bis-Tris propane pH 8.5, 0.2 M KSCN and 20% w/v PEG 3350, and 0.1 M Bis-Tris propane pH 7.5, 0.15 M sodium citrate and 20% w/v PEG 3350, for the 3.4 Å and 4.5 Å datasets respectively. The crystals were transferred to cryo-protectant solutions with mother liquor and 20% v/v glycerol (HER2:MF3958) or 25% v/v ethylene glycol (HER3:MF3178) and flash frozen in liquid nitrogen. Data collection for HER2-ECD:MF3958 was performed at the Swiss Light Source (SLS) and for HER3-ECD:MF3178 at the European Synchrotron Radiation Facility (ESRF). Diffraction data were integrated by IMOSFLM (65) and scaled and merged by the AIMLESS pipeline (66). The structures were solved by molecular replacement (MR) using PHASER MR (67). For the MR of HER2-ECD:MF3958 the extracellular domain of rat HER2 (PDB code 1N8Y (48)) was used as a first search model and in a second MR cycle the LC from the Fab with PDB code 3SKJ (68) and the HC from Fab with PDB code 2EH7 (69) were used due to their high sequence homology. For HER3-ECD:MF3178 iterative cycles of MR were required using single domains of the extracellular portion of human HER3 (PDB code 1M6B (70)), followed by the LC of Fab with PDB code 3SKJ (68) and the HC of Fab with PDB 4HCR. Iterative manual model building and refinement were carried out using COOT (71) and PHENIX (72). Validation of the final models was done using MOLPROBITY (73). The structures figures were generated by PYMOL (<http://pymol.org>).

Acknowledgements

We gratefully thank the European Synchrotron Radiation Facility (ESRF) and the Swiss Light Source (SLS) for the provision of synchrotron radiation facilities and beamline scientists of the ESRF, SLS, and the European Molecular Biology Laboratory for assistance. We gratefully thank Willem Kegel for instructive and stimulating discussions. Financial support was provided by the BioStruct-X (grant no. 283570) embedded in the European Union's Seventh Framework Programme (FP7/2007–2013).

Author contributions

CDN performed the structural investigation. TV, RN, LJAH contributed to the antibody isolation and characterization experiments. DM, ER, TG performed the *in vitro* experiments. CG, DM, ER, TG, JdK, MT contributed to the *in vitro* and

in vivo experiments. CG, CDN, DM, ER, TG, LJAH, JdK, PG, MT conducted data analysis. CG, DM, TL, JdK, PG, MT conceived the study. MT, CG, DM, CDN, PG wrote the manuscript.

Accession numbers

The atomic coordinates and structures have been deposited in the Protein Data Bank (<http://www.pdb.org>) with PDB ID 5O4G, 5O4O and 5O7P.

References

1. Yarden, Y., and Pines, G. (2012) The ERBB network: at last, cancer therapy meets systems biology. *Nat Rev Cancer*. **12**, 553–563
2. Arteaga, C. L., and Engelman, J. A. (2014) ERBB Receptors: from oncogene discovery to basic science to mechanism-based cancer therapeutics. *Cancer Cell*. **25**, 282–303
3. Hynes, N. E., and Lane, H. A. (2005) ERBB receptors and cancer: the complexity of targeted inhibitors. *Nat Rev Cancer*. **5**, 341–354
4. Jaiswal, B. S., Kljavin, N. M., Stawiski, E. W., Chan, E., Parikh, C., Durinck, S., *et al.* (2012) Oncogenic ERBB3 mutations in human cancers. *Cancer Cell*. **23**, 603–617
5. Montero, J. C., Rodriguez-Barrueco, R., Ocana, A., Diaz-Rodriguez, E., Esparis-Ogando, A., and Pandiella, A. (2008) Neuregulins and cancer. *Clin Cancer Res*. **14**, 3237–3241
6. Fernandez-Cuesta, L., Plenker, D., Osada, H., Sun, R., Menon, R., Leenders, F., *et al.* (2014) CD74-NRG1 fusions in lung adenocarcinoma. *Cancer Discov*. **4**, 415–422
7. Jung, Y., Yong, S., Kim, P., Lee, H. Y., Jung, Y., Keum, J., *et al.* (2015) VAMP2-NRG1 fusion gene is a novel oncogenic driver of non-small-cell lung adenocarcinoma. *J Thorac Oncol*. **10**, 1107–1111
8. Lupu, R., Cardillo, M., Cho, C., Harris, L., Hijazi, M., Perez, C., *et al.* (1996) The significance of heregulin in breast cancer tumor progression and drug resistance. *Breast Cancer Res Treat*. **38**, 57–66
9. Peles, E., Bacus, S. S., Koski, R. A., Lu, H. S., Wen, D., Ogden, S. G., *et al.* (1992) Isolation of the neu/HER-2 stimulatory ligand: a 44 kd glycoprotein that induces differentiation of mammary tumor cells. *Cell*. **69**, 205–216
10. Koninki, K., Barok, M., Tanner, M., Staff, S., Pitkanen, J., Hemmila, P., *et al.* (2010) Multiple molecular mechanisms underlying trastuzumab and lapatinib resistance in JIMT-1 breast cancer cells. *Cancer letters*. **294**, 211–219
11. Hegde, G. V., de la Cruz, C. C., Chiu, C., Alag, N., Schaefer, G., Crocker, L., *et al.* (2013) Blocking NRG1 and other ligand-mediated Her4 signaling enhances the magnitude and duration of the chemotherapeutic response of non-small cell lung cancer. *Sci Transl Med*. **5**, 171ra18
12. Lee, C. Y., Lin, Y., Bratman, S., Feng, W., Kuo, A., Scheeren, F., *et al.* (2014) Neuregulin autocrine signaling promotes self-renewal of breast tumor-initiating cells by triggering HER2/HER3 activation. *Cancer Res*. **74**, 341–352
13. Wilson, T. R., Lee, D. Y., Berry, L., Shames, D. S., and Settleman, J. (2011) Neuregulin-1-mediated autocrine signaling underlies sensitivity to HER2 kinase inhibitors in a subset of human cancers. *Cancer Cell*. **20**, 158–172
14. Gijsen, M., King, P., Perera, T., Parker, P. J., Harris, A. L., Larijani, B., *et al.* (2010) HER2 phosphorylation is maintained by a PKB negative feedback loop in response to anti-HER2 herceptin in breast cancer. *PLoS Biol* **8**, e1000563
15. Ritter, C. A., Perez-Torres, M., Rinehart, C., Guix, M., Dugger, T., Engelman, J. A., *et al.* (2007) Human breast cancer cells selected for resistance to trastuzumab in vivo overexpress epidermal growth factor receptor and ErbB ligands and remain dependent on the ErbB receptor network. *Clin Cancer Res*. **13**, 4909–4919
16. Visscher, D. W., Sarkar, F. H., Kasunic, T. C., and Reddy, K. B. (1997) Clinicopathologic analysis of amphiregulin and heregulin immunostaining in breast neoplasia. *Breast Cancer Res Treat*. **45**, 75–80
17. De Boeck, A., Pauwels, P., Hensen, K., Rummens, J. L., Westbroek, W., Hendrix, A., *et al.* (2013) Bone marrow-derived mesenchymal stem cells promote colorectal cancer progression through paracrine neuregulin 1/HER3 signalling. *Gut*. **62**, 550–560

18. Meyer, D., Yamaai, T., Garratt, A., Riethmacher-Sonnenberg, E., Kane, D., Theill, L. E., *et al.* (1997) Isoform-specific expression and function of neuregulin. *Development*. **124**, 3575–3586
19. Marchionni, M. A., Goodearl, A. D., Chen, M. S., Bermingham-McDonogh, O., Kirk, C., Hendricks, M., *et al.* (1993) Glial growth factors are alternatively spliced erbB2 ligands expressed in the nervous system. *Nature*. **362**, 312–318
20. Holbro, T., Beerli, R. R., Maurer, F., Koziczak, M., Barbas, C. F. 3rd, Hynes, N. E. (2003) The ErbB2/ErbB3 heterodimer functions as an oncogenic unit: ErbB2 requires ErbB3 to drive breast tumor cell proliferation. *Proc Natl Acad Sci U S A*. **100**, 8933–8938
21. Junttila, T. T., Akita, R. W., Parsons, K., Fields, C., Lewis Phillips, G. D., Friedman, L. S., *et al.* (2009) Ligand-independent HER2/HER3/PI3K complex is disrupted by trastuzumab and is effectively inhibited by the PI3K inhibitor GDC-0941. *Cancer Cell*. **15**, 429–440
22. Sliwkowski, M. X., Schaefer, G., Akita, R. W., Lofgren, J. A., Fitzpatrick, V. D., Nuijens, A., *et al.* (1994) Coexpression of erbB2 and erbB3 proteins reconstitutes a high affinity receptor for heregulin. *J Biol Chem*. **269**, 14661–14665
23. Coker, K. J., Staros, J. V., and Guyer, C. A. (1994) A kinase-negative epidermal growth factor receptor that retains the capacity to stimulate DNA synthesis. *Proc Natl Acad Sci U S A*. **91**, 6967–6971
24. Guy, P. M., Platko, J. V., Cantley, L. C., Cerione, R. A., and Carraway, K. L. 3rd. (1994) Insect cell-expressed p180erbB3 possesses an impaired tyrosine kinase activity. *Proc Natl Acad Sci U S A*. **91**, 8132–8136
25. Campbell, M. R., Amin, D., and Moasser, M. M. (2010) HER3 comes of age: new insights into its functions and role in signaling, tumor biology, and cancer therapy. *Clin Cancer Res*. **16**, 1373–1383
26. Leto, S. M., Sassi, F., Catalano, I., Torri, V., Migliardi, G., Zanella, E. R., *et al.* (2015) Sustained inhibition of HER3 and EGFR is necessary to induce regression of HER2-amplified gastrointestinal carcinomas. *Clin Cancer Res*. **21**, 5519–5531
27. Lee-Hoeflich, S. T., Crocker, L., Yao, E., Pham, T., Munroe, X., Hoeflich, K. P., *et al.* (2008) A central role for HER3 in HER2-amplified breast cancer: implications for targeted therapy. *Cancer Res*. **68**, 5878–5887
28. Schaefer, G., Haber, L., Crocker, L. M., Shia, S., Shao, L., Dowbenko, D., *et al.* (2011) A two-in-one antibody against HER3 and EGFR has superior inhibitory activity compared with monospecific antibodies. *Cancer Cell*. **20**, 472–486
29. Garner, A. P., Bialucha, C. U., Sprague, E. R., Garrett, J. T., Sheng, Q., Li, S., *et al.* (2013) An antibody that locks HER3 in the inactive conformation inhibits tumor growth driven by HER2 or neuregulin. *Cancer Res*. **73**, 6024–6035
30. Mirschberger, C., Schiller, C. B., Schröml, M., Dimoudis, N., Friess, T., Gerdes, C. A., *et al.* (2013) RG7116, a therapeutic antibody that binds the inactive HER3 receptor and is optimized for immune effector activation. *Cancer Res*. **73**, 5183–5194
31. Wilson, T. R., Fridlyand, J., Yan, Y., Penuel, E., Burton, L., Chan, E., *et al.* (2012) Widespread potential for growth-factor-driven resistance to anticancer kinase inhibitors. *Nature*. **487**, 505–509
32. Garrett, J. T., and Arteaga, C. L. (2011) Resistance to HER2-directed antibodies and tyrosine kinase inhibitors: mechanisms and clinical implications. *Cancer Biol Ther*. **11**, 793–800
33. Chandarlapaty, S., and Modi, S. (2011) Targeted therapy for human epidermal growth factor receptor 2-positive breast cancer: can there be too many active drugs? *J Clin Oncol*. **29**, 3111–3113
34. Sergina, N. V., Rausch, M., Wang, D., Blair, J., Hann, B., Shokat, K. M., *et al.* (2007) Escape from HER-family tyrosine kinase inhibitor therapy by the kinase-inactive HER3. *Nature*. **445**, 437–441

35. Ocana, A., and Amir, E. (2009) Irreversible pan-ErbB tyrosine kinase inhibitors and breast cancer: current status and future directions. *Cancer Treat Rev.* **35**, 685–691
36. Barron, F., de la Torre-Vallejo, M., Luna-Palencia, R. L., Cardona, A. F., and Arrieta, O. (2016) The safety of afatinib for the treatment of non-small cell lung cancer. *Expert Opin Drug Saf.* **15**, 1563–1572
37. Swain, S. M., Schneeweiss, A., Gianni, L., Gao, J. J., Stein, A., Waldron-Lynch, M., *et al.* (2017) Incidence and management of diarrhea in patients with HER2-positive breast cancer treated with pertuzumab. *Ann Oncol.* **28**, 761–768
38. Rubinson, D. A., Hochster, H. S., Ryan, D. P., Wolpin, B. M., McCleary, N. J., Abrams, T. A., *et al.* (2014) Multi-drug inhibition of the HER pathway in metastatic colorectal cancer: results of a phase I study of pertuzumab plus cetuximab in cetuximab-refractory patients. *Invest New Drugs.* **32**, 113–122
39. Mueller, M. M., and Fusenig, N. E. (2004) Friends or foes - bipolar effects of the tumour stroma in cancer. *Nat Rev Cancer.* **4**, 839–849
40. McDonagh, C. F., Huhlov, A., Harms, B. D., Adams, S., Paragas, V., Oyama, S., *et al.* (2012) Antitumor activity of a novel bispecific antibody that targets the ErbB2/ErbB3 oncogenic unit and inhibits heregulin-induced activation of ErbB3. *Mol Cancer Ther.* **11**, 582–593
41. Ewer, M. S., and Ewer, S. M. (2010) Cardiotoxicity of anticancer treatments: what the cardiologist needs to know. *Nat Rev Cardiol.* **7**, 564–575
42. Schoeberl, B., Pace, E. A., Fitzgerald, J. B., Harms, B. D., Xu, L., Nie, L., *et al.* (2009) Therapeutically targeting ErbB3: a key node in ligand-induced activation of the ErbB receptor-PI3K axis. *Sci signal.* **2**, ra31
43. Subik, K., Lee, J. -F., Baxter, L., Strzepak, T., Costello, D., Crowley, P., *et al.* (2010) The expression patterns of ER, PR, HER2, CK5/6, EGFR, Ki-67 and AR by immunohistochemical analysis in breast cancer cell lines. *Breast Cancer.* **4**, 35–41
44. Corcoran, E. B., and Hanson, R. N. (2014) Imaging EGFR and HER2 by PET and SPECT: a review. *Med Res Rev.* **34**, 596–643
45. Musolino, A., Naldi, N., Bortesi, B., Pezzuolo, D., Capelletti, M., Missale, G., *et al.* (2008) Immunoglobulin G fragment C receptor polymorphisms and clinical efficacy of trastuzumab-based therapy in patients with HER-2/neu-positive metastatic breast cancer. *J Clin Oncol.* **26**, 1789–1796
46. Bibeau, F., Lopez-Crapez, E., Di Fiore, F., Thezenas, S., Ychou, M., Blanchard, F., *et al.* (2009) Impact of FcγRIIIa-FcγRIIIa polymorphisms and KRAS mutations on the clinical outcome of patients with metastatic colorectal cancer treated with cetuximab plus irinotecan. *J Clin Oncol.* **27**, 1122–1129
47. Long, L. E., Anderson, P., Frank, E., Shaw, A., Liu, S., Huang, X. F., *et al.* (2015) Neuregulin 1 expression and electrophysiological abnormalities in the Neuregulin 1 transmembrane domain heterozygous mutant mouse. *PLoS One.* **10**, e0124114
48. Cho, H. S., Mason, K., Ramyar, K. X., Stanley, A. M., Gabelli, S. B., Denney, D. W. Jr., *et al.* (2003) Structure of the extracellular region of HER2 alone and in complex with the Herceptin Fab. *Nature.* **421**, 756–760
49. Franklin, M. C., Carey, K. D., Vajdos, F. F., Leahy, D. J., de Vos, A. M., and Sliwkowski, M. X. (2004) Insights into ErbB signaling from the structure of the ErbB2-pertuzumab complex. *Cancer Cell.* **5**, 317–328
50. Bostrom, J., Yu, S. F., Kan, D., Appleton, B. A., Lee, C. V., Billeci, K., *et al.* (2009) Variants of the antibody herceptin that interact with HER2 and VEGF at the antigen binding site. *Science.* **323**, 1610–1614
51. Eigenbrot, C., Ultsch, M., Dubnovitsky, A., Abrahmsen, L., and Hard, T. (2010) Structural basis for high-affinity HER2 receptor binding by an engineered protein. *Proc Natl Acad Sci U S A.* **107**, 15039–15044

52. Fisher, R. D., Ultsch, M., Lingel, A., Schaefer, G., Shao, L., Birtalan, S., *et al.* (2010) Structure of the complex between HER2 and an antibody paratope formed by side chains from tryptophan and serine. *J Mol Biol.* **402**, 217–229
53. Zhou, H., Zha, Z., Liu, Y., Zhang, H., Zhu, J., Hu, S., *et al.* (2011) Structural insights into the down-regulation of overexpressed p185her2/neu protein of transformed cells by the antibody chA21. *J Biol Chem.* **286**, 31676–3183
54. Lee, S., Greenlee, E. B., Amick, J. R., Ligon, G. F., Lillquist, J. S., Natoli, E. J. Jr., *et al.* (2015) Inhibition of ErbB3 by a monoclonal antibody that locks the extracellular domain in an inactive configuration. *Proc Natl Acad Sci U S A.* **112**, 13225–13230
55. Ogiso, H., Ishitani, R., Nureki, O., Fukai, S., Yamanaka, M., Kim, J. H., *et al.* (2002) Crystal structure of the complex of human epidermal growth factor and receptor extracellular domains. *Cell.* **110**, 775–787
56. Arteaga, C. L., Sliwkowski, M. X., Osborne, C. K., Perez, E. A., Puglisi, F., and Gianni, L. (2012) Treatment of HER2-positive breast cancer: current status and future perspectives. *Nat Rev Clin Oncol.* **9**, 16–32
57. Yakes, F. M., Chinratanalab, W., Ritter, C. A., King, W., Seelig, S., and Arteaga, C. L. (2002) Herceptin-induced inhibition of phosphatidylinositol-3 kinase and Akt is required for antibody-mediated effects on p27, cyclin D1, and antitumor action. *Cancer Res.* **62**, 4132–4141
58. Sithanandam, G., and Anderson, L. M. (2008) The ERBB3 receptor in cancer and cancer gene therapy. *Cancer Gene Ther.* **15**, 413–448
59. Chung, I., and Mellman, I. (2015) Single-molecule optical methods analyzing receptor tyrosine kinase activation in living cells. *Methods Mol Biol.* **1233**, 35–44
60. Calvo, E., Alsina, M., Schellens, J. H., Huitema, A. D., Tabernero, J., de Vries-Schultink, A., *et al.* (2016) Abstract CT050: a phase I/II study of MCLA-128, a full-length IgG1 bispecific antibody targeting HER2 and HER3, in patients with solid tumors. *Cancer Res.* **76**, CT050
61. Neri, D., Momo, M., Prospero, T., and Winter, G. (1995) High-affinity antigen binding by chelating recombinant antibodies (CRABs). *J Mol Biol.* **246**, 367–373
62. Roovers, R., Herpers, B., James, M., Eppink, B., Cortina, C., Maussang, D., *et al.* (2017) Identification and characterisation of MCLA-158 as an anti-EGFRxLGR5 bispecific antibody that potently inhibits patient-derived CRC organoid growth. Paper presented at: AACR Annual Conference; 2017 Apr 1–5; Washington, D.C., USA
63. Paterson, B. M., Roselt, P., Denoyer, D., Cullinane, C., Binns, D., Noonan, W., *et al.* (2014) PET imaging of tumours with a ⁶⁴Cu labeled macrobicyclic cage amine ligand tethered to Tyr3-octreotate. *Dalton Trans.* **43**, 1386–1396
64. Mukherjee, A., Badal, Y., Nguyen, X. T., Miller, J., Chenna, A., Tahir, H., *et al.* (2011) Profiling the HER3/PI3K pathway in breast tumors using proximity-directed assays identifies correlations between protein complexes and phosphoproteins. *PLoS One.* **6**, e16443
65. Battye, T. G., Kontogiannis, L., Johnson, O., Powell, H. R., and Leslie, A. G. (2011) iMOSFLM: a new graphical interface for diffraction-image processing with MOSFLM. *Acta Crystallogr D Biol Crystallogr.* **67**, 271–281
66. Evans, P. R., and Murshudov, G. N. (2013) How good are my data and what is the resolution? *Acta Crystallogr D Biol Crystallogr.* **69**, 1204–1214
67. McCoy, A. J., Grosse-Kunstleve, R. W., Adams, P. D., Winn, M. D., Storoni, L. C., and Read, R. J. (2007) Phaser crystallographic software. *J Appl Crystallogr.* **40**, 658–674
68. Peng, L., Oganessian, V., Damschroder, M. M., Wu, H., and Dall'Acqua, W. F. (2011) Structural and functional characterization of an agonistic anti-human EphA2 monoclonal antibody. *J Mol Biol.* **413**, 390–40569. Chi, S. W., Maeng, C. Y., Kim, S. J., Oh, M. S., Ryu, C. J., Kim, S. J., *et al.* (2007) Broadly neutralizing anti-hepatitis B virus antibody reveals

- a complementarity determining region H3 lid-opening mechanism. *Proc Natl Acad Sci U S A*. **104**, 9230–9235
70. Cho, H. S., and Leahy, D. J. Structure of the extracellular region of HER3 reveals an interdomain tether. *Science*. **297**, 1330–1333
 71. Emsley, P., Lohkamp, B., Scott, W. G., and Cowtan, K. (2010) Features and development of Coot. *Acta Crystallogr D Biol Crystallogr*. **66**, 486–501
 72. Adams, P. D., Afonine, P. V., Bunkoczi, G., Chen, V. B., Davis, I. W., Echols, N., *et al.* (2010) PHENIX: a comprehensive Python-based system for macromolecular structure solution. *Acta Crystallogr D Biol Crystallogr*. **66**, 213–221
 73. Chen, V. B., Arendall, W. B. 3rd, Headd, J. J., Keedy, D. A., Immormino, R. M., Kapral, G. J., *et al.* MolProbity: all-atom structure validation for macromolecular crystallography. *Acta Crystallogr D Biol Crystallogr*. **66**, 12–21
 74. De Nardis, C., Hendriks, L. J. A., Poirier, E., Arvinte, T., Gros, P., Bakker, A. B. H., and de Kruif, J. (2017). A new approach for generating bispecific antibodies based on a common light chain format and the stable architecture of human immunoglobulin G1. *J Biol Chem*. First published on June 27, 2017, doi: 10.1074/jbc.M117.793497

Supplementary Experimental Procedures

Recombinant proteins and constructs

Fc-tagged EGFR, HER2, HER3 and HER4 and Human NRG1-beta 1/HRG1-beta 1 EGF domain protein were purchased from R&D Systems. HER2 recombinant protein was provided by Bender Med Systems. Constructs expressing human, cynomolgus, rat or mouse HER2 and HER3 (ECDs) were generated in pVAX1 vector (Invitrogen) for DNA immunizations and pDisplay vector (Invitrogen) for cell line transfections. For crystallography studies HER2 and HER3 ECDs were cloned upstream of a C-terminal histidine tag (6x). Chimeric swapped domain constructs for HER2 and HER3 were generated by swapping human domains I to IV with the chicken and rat orthologues, respectively. All constructs were sequence verified. VH and VL sequences from reference antibodies were copied from patents and recloned in the IgG1 backbone vector. MF3958 and MF3718 were recloned to generate Fab material according to procedures described by Griffiths et al. (1) and de Haard et al. (2).

Mouse immunizations, phage library generation and phage selection

C57/BL6 mice were immunized every 2 weeks with the following material: L292-HER2 or L292-HER3 cells (2×10^6 cells), Fc-HER2 or Fc-HER3 (20 mg/mouse in Titermax Gold) or DNA vaccination with pVax-HER2 or pVax-HER3. Sera were screened for binding to transfected HEK293T-HER2 or -HER3 cells and on recombinant HER2 and HER3 proteins in ELISA. Phage libraries were constructed from immunized mouse material as previously described (3). From each individual mouse, RNA was isolated and cDNA was synthesized and VH-family specific PCRs were performed. Subsequently all VH family PCR products per mouse were purified, digested and ligated in a phage-display vector containing the common-light chain to generate a mouse-human chimeric phage library. All phage libraries contained $> 10^6$ clones with an insert frequency of $> 85\%$. Antibody fragments were selected using antibody phage display libraries. Immunized libraries and synthetic libraries (as described in (4)) were used for selections. Phage libraries were rescued with VCS-M13 helper phage (Stratagene) and selected for two rounds in immunotubes (Nunc) coated with recombinant protein. Positive phage clones binding HER2 or HER3 were then identified in FACS for binding to the breast cancer cell line BT-474. The VH genes of all HER2 and HER3 specific clones were sequenced. VH gene rearrangements were established with VBASE2 software to identify unique clones. All HER2 unique clones were then tested in phage format for binding in FACS to HEK293T cells (negative control), HEK293T cells transiently transfected with HER2 and BT-

474 cells. HER3-specific phage clones were selected on K562 cells, K562 cells stably overexpressing HER3 and BT-474 cells. VH genes of unique antibodies, as judged by VH gene sequence and some sequence variants thereof, derived from the (immunized mouse) phage libraries were cloned in the backbone IgG1 vector as described (3). IgGs were produced in transiently transfected 293F Freestyle (Invitrogen) cells according to manufacturer's instructions. Bispecific antibodies were generated using CH3 technology to ensure efficient hetero-dimerization and formation of a bispecific antibody. The CH3 technology uses charge-based point mutations in the CH3 region to allow efficient pairing of two different heavy chain molecules as previously described (24). Antibodies were purified using protein A batch purification (Pierce) and characterized based on their affinity in antigen titration ELISA (5). The panel of anti-HER2 and HER3 antibodies was binned based on their binding onto CHO-K1 cells transiently transfected with HER2 or HER3 ECD derived from various species (human, cynomolgus, mouse, rat, chicken) or with HER2 or HER3 domain swap chimeric constructs.

Humanization

Anti-HER2 mouse Fab MF2971 was humanized by CDR grafting technology and the immunogenicity potential was further reduced by T cell epitope elimination *in silico* (Lonza). A total of seven humanized/de-immunized variant sequences of MF2971 were expressed, validated and characterized *in vitro* as monoclonal and in bispecific format with anti-HER3 human Fab MF3178. Based on production, integrity, stability and functionality, a variant of MF2971 (2971-var2) was chosen as the optimal humanized variant of the VH to be used in a bispecific format with MF3178. This 2971-var2 was renamed MF3958. The bispecific HER2xHER3 combination MF3958xMF3178 resulted in PB4188.

Cell surface binding measured by FACS

Cell lines with varying levels of surface HER2 expression, MCF-7 (HER2+), MDA-MB-468 (HER2+), MDA-MB-175 (HER2+), MDA-MB-453 (HER2++), MDA-MB-361(HER2++), ZR-75-1 (HER2++), JIMT-1 (HER2+++), BT-474 (HER2+++), SKBR-3 (HER2+++), in exponential growth were harvested and resuspended in FACS buffer (10^6 cells/ml in PBS, 0.5% BSA, 0.5 mM EDTA). $1-2 \times 10^5$ cells were stained for 1 hour on ice with 50 μ l of primary antibody. After washing, bound antibodies were detected with PE-labeled mouse anti-human IgG (Invitrogen). Cells were analyzed by FACS for median fluorescence intensity in the PE channel.

Antibody dependent cytotoxicity assays

Chromium release assays. SKBR-3 and MCF-7 target cells expressing high and low HER2 levels, respectively, were loaded with ^{51}Cr (Amersham) and opsonized with the indicated concentrations of antibody. PBMC fractions isolated from healthy donors were used as effector cells in a 200 μl reaction in RPMI 1640 + 10% heat-inactivated FCS. Cells were incubated for 4 hours, and lysis was estimated by measuring radioactivity in the supernatant using a gamma scintillator. Percentage of specific lysis was calculated as follows: $(\text{experimental cpm} - \text{basal cpm}) / (\text{maximal cpm} - \text{basal cpm}) \times 100$, with maximal lysis being determined in the presence of 5% Triton X-100 and basal lysis in the absence of antibody and effectors.

Reporter assays. The ADCC reporter gene assay from Promega was used and adapted to 384-well plate format. Briefly, SKBR-3 target cells were seeded at a density of 1,000 cells/well in 30 μl assay medium (RPMI with 4% low IgG serum) 20–24 hours before the bioassay. Culture medium was then removed and 10 μl of serially diluted antibodies were added to the wells in duplicate and combined with 5 μl of either the V158 or F158 Fc γ RIIIa variant Jurkat reporter cell lines. Cells were incubated for 6 hours at 37°C then 15 μl Bio-Glo luciferase substrate was added per well, incubated for 5 minutes and luminescence was detected on a Biotek plate reader.

Internalization assay

Purified antibodies were labeled with a pH sensor dye with a succinimidyl ester reactive group (Promega, CS1783A01) according to the manufacturer's instructions. SKBR-3 and N87 cells in an exponential growth phase were harvested and seeded in 96-well plates (1.5×10^4 cells per well) in 100 μl assay medium containing 0.125 nM (1 ng/ml) HRG. After overnight incubation, 20 μl of pH-sensitive dye-labeled antibodies were added to reach a final concentration of 100 nM. After overnight incubation, cells were harvested by collecting non-adherent cells and by trypsinizing adherent cells. Cells were washed with FACS buffer (PBS with 0.5% BSA, 0.1% sodium azide) and analyzed by flow cytometry on a FACSCanto (BD Biosciences). Median fluorescence intensities (MFI) of the PE channel were used to determine the extent of internalization.

Xenograft studies

BxPC-3 model. 8–10 weeks old CB17.SCID female mice were anesthetized and laid on the right side to expose the left side. A 0.5 cm incision was made on the left flank region and the pancreas and spleen were exteriorized. 1×10^6 BxPC-3-Luc2 tumor cells were injected in a volume of 20 μl into the sub-capsular space of the pancreas tail. One week after implantation, bioluminescence imaging (BLI)

data were generated. 15 minutes prior to imaging, all of the mice received i.p. injections of 150 mg/kg luciferin (D-Luciferin-EF Potassium Salt, Cat. #E6552, Promega). BLI was performed once or twice weekly using the left side view. Outlier animals – based on BLI/tumor volume – were removed and the mice were randomly distributed into groups of 7 mice. On experimental day 8, the treatment was started. The animals in the antibody treatment group were dosed weekly for 3 consecutive weeks (days 0, 7, 14 and 21) with 30 mg/kg of antibody. At day 0 of treatment, the animals received twice the loading dose, i.e. 60 mg/kg of antibody. The final imaging was carried out at day 31 (Supplementary Figure S2).

Epitope mapping

Alanine scanning mutagenesis was used to map the epitopes of anti-HER2 PG3958 and anti-HER3 PG3178. Clones were generated by substituting each amino acid residue of the HER2/HER3 extracellular domain (ECD) for alanine. DNA of each clone was transfected into HEK293T cells. 24 hours later, the reactivity of antibodies was measured by immunofluorescent staining leading to binding maps and identification of critical residues for antibody binding. In parallel, expression levels of the HER2 and HER3 ECD constructs were verified by FACS analysis using commercially available monoclonal antibodies (R&D Systems mAb 1129 (HER2) and 66223 (HER3)). Binding of anti-HER2 and anti-HER3 antibodies was tested at a concentration of 0.25 $\mu\text{g/ml}$. The critical residues involved in binding were confirmed by introducing the specific point mutations in the HER2 or HER3 ECD constructs prior to FACS binding.

SAXS

The SAXS data were collected at the European Synchrotron Radiation Facility (ESRF) BioSAXS beamline at 12.5 keV (0.9919 Å) with a 2D Pilatus 1M detector (DECTRIS). PB4188 was mixed with HER2 and HER3 ectodomains in a 1:1:1 ratio and let it incubate overnight at 4°C. For online size-exclusion chromatography (SEC) the protein sample was automatically injected onto a Superdex 200 5/150 analytical column previously equilibrated with buffer containing 25 mM Tris pH 7.5, 150 mM NaCl and connected to a high-performance liquid chromatography (HPLC) Shimadzu system (France). Data were collected using a sample-to-detector distance of 2.81 m corresponding to a scattering vector s ($s = 4\pi \sin \theta/\lambda$) range of 0.03 – 5.0 nm^{-1} . Approximately 1,500 frames were collected per 30 minutes sample run (1 frame s^{-1}). Data processing was performed automatically using EDNA pipeline (6), generating azimuthally integrated, calibrated and normalized one-dimensional profiles for each frame. Frames with a consistent

radius of gyration (R_g) and corresponding to the highest protein concentration based on $I(0)$ values were merged to yield a single averaged frame corresponding to the scattering of an individual SEC purified species. The curves obtained were used for further data processing using PRIMUS of the ATSAS suite (7). Radius of gyration (R_g) was evaluated within the range of Guinier approximation $sR_g < 1.3$ according to the equation $I(s) = I(0) \exp(-1/3(sR_g)^2)$. The R_g was also computed from the entire scattering pattern using Porod's law by the calculation of the distance distribution function $P(r)$ using the program GNOM (8) which gave also the maximum particle dimension D_{max} . A set of low resolution *ab initio* models was generated using the program DAMMIF (9).

The use of grand canonical ensemble for modeling the binding of PB4188

Under the approximation of the grand canonical ensemble the chemical potential (μ), the volume (V) and the temperature (T) of the system are kept constant while the number of molecules can vary. This approach has been widely used in surface science (10). Hereby we applied it to obtain a model of the binding of PB4188 compared to monospecific bivalent anti-HER3 (PG3178). The basis of the method is to simulate a series of states where the ligand and the antibody are in solution and their concentration can vary, while the receptors are fixed on a one-dimensional lattice. The receptors, the ligand and the antibody are considered as rigid models (11) and binding of the antibody and the ligand to the antigens sites is uncorrelated. Moreover, this model assumes random mixing (each state is equally probable). The grand canonical ensemble accounts only for essential variables such as number of receptors on the surface, ligand/antibody concentrations (L and A) and binding affinities.

The states considered in the model approximate the interactions of ligand/antibody with the receptors on the cell surface as pairs: 2 copies of HER2, 2 copies of HER3 or 1 copy of HER2 and 1 copy of HER3. The interactions taken into account are: binding of HRG to HER3 with $K_D = 0.2$ nM, binding of bivalent monospecific anti-HER3 PG3178 with $K_D = 0.2$ nM for each Fab arm and binding of a bispecific antibody with anti-HER2 Fab MF3958 with $K_D = 2$ nM and anti-HER3 Fab MF3178 with $K_D = 0.2$ nM. The values of the dissociation constants correspond to the energy contribution of each interaction. The states taken into account to generate the grand canonical partition function (Ξ), which describes the statistical properties of the system, represent all the possible ways in which the antibody (either monospecific or bispecific) and the ligand can bind to the three paired situations, as shown in the illustrations below. The output of the model is the average amount of ligand (P) bound to HER3 on the lattice at determinate conditions of antibody (bispecific or monospecific), concentration of

antibody, ligand concentration and HER2/HER3 copy number ratio (cell type). Supplementary Figure S15 illustrates the behavior of P_l at increasing concentrations of antibody. We modeled this relation for three different concentrations of ligand: low HRG (0.1 nM), stress conditions (10 nM) and extremely high HRG (10,000 nM), and for two different cell lines where HER3 copy number is always 30,000 while HER2 copy number is either 30,000 (~ MCF7 cell line) or 3,000,000 (~ SKBR-3 cell line).

Main equations in the grand canonical model

$$P_l = \frac{\langle N_l \rangle}{N_{tot}} = \lambda_l \left(\frac{d \ln \Xi}{d \lambda_l} \right)_{\lambda_i}$$

$$\Xi = p_{22} \Xi_{22} + p_{33} \Xi_{33} + p_{23} \Xi_{23}$$

$$e^{-2\beta \epsilon_i} = (e^{-\beta \epsilon_i})^2 = K_{Ai}^2 = \frac{1}{K_{Di}^2}$$

$$p_{22} = \frac{N_2^2}{N_{tot}^2}$$

$$p_{33} = \frac{N_3^2}{N_{tot}^2}$$

$$p_{23} = 2 \frac{N_2 N_3}{N_{tot}^2}$$

Ξ = grand partition function

ϵ_i = binding energy

λ_i = fugacity ~ concentration

p_{ii} = probability associated to that state

$N_{tot} = N_2 + N_3$

$N_3 = 30,000$

$N_2 = 30,000 / 3,000,000$

State equations for monoclonal anti-HER3 antibody

$$\Xi_{33} = 1 + 2 \frac{\lambda_a}{K_{D3}} + \frac{\lambda_a}{K_{D3}^2} + 2 \frac{\lambda_a \lambda_l}{K_{D3} K_{Dl}} + \frac{\lambda_l^2}{K_{Dl}^2} + 2 \frac{\lambda_a^2}{K_{D3}^2}$$

$$\Xi_{23} = 1 + \frac{\lambda_a}{K_{D3}} + \frac{\lambda_l}{K_{Dl}}$$

State equations for bispecific anti-HER2/HER3 antibody

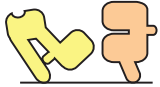
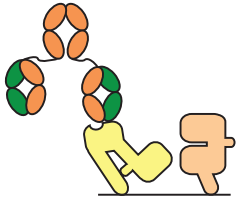
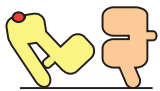
$$\Xi_{22} = 1$$

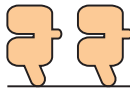
$$\Xi_{22} = 1 + 2 \frac{\lambda_a}{K_{D2}} + \frac{\lambda_a^2}{K_{D2}^2}$$


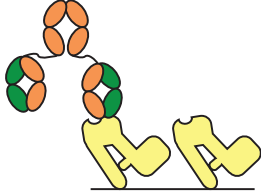
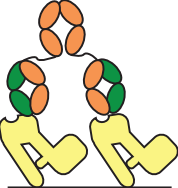
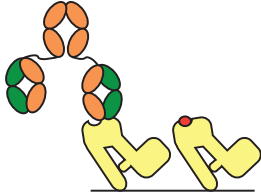
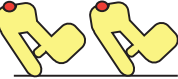
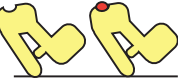
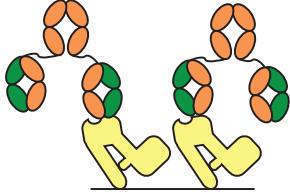
$$\Xi_{33} = 1 + 2 \frac{\lambda_a}{K_{D3}} + 2 \frac{\lambda_a \lambda_l}{K_{D3} K_{Dl}} + \frac{\lambda_l^2}{K_{Dl}^2} + 2 \frac{\lambda_l}{K_{Dl}} + \frac{\lambda_a^2}{K_{D3}^2}$$

$$\Xi_{23} = 1 + \frac{\lambda_a}{K_{D3}} + \frac{\lambda_a}{K_{D2}} + \frac{\lambda_a}{K_{D2} K_{D3}} + \frac{\lambda_l}{K_{Dl}} + \frac{\lambda_a \lambda_l}{K_{D2} K_{Dl}} + \frac{\lambda_a^2}{K_{D2} K_{D3}}$$

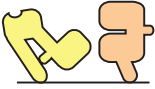
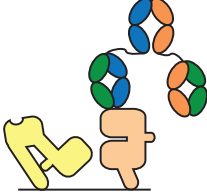
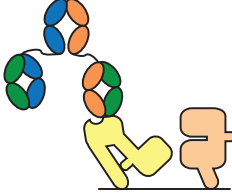

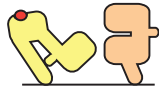
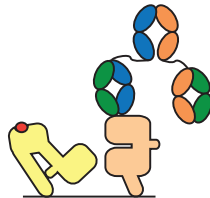
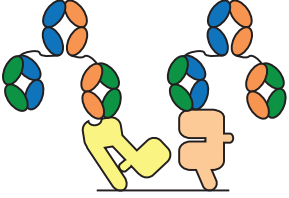
States modeled for the binding of monospecific anti-HER3 Ab



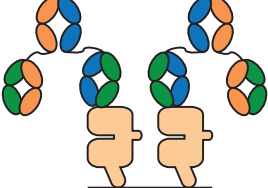
HER2-HER3	
States	Weights
	1
	$\lambda_a e^{-\beta \epsilon_3}$
	$\lambda_i e^{-\beta \epsilon_l}$


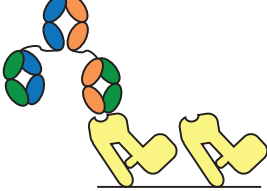
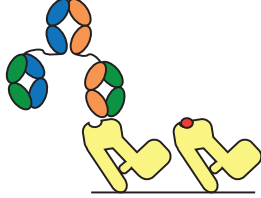


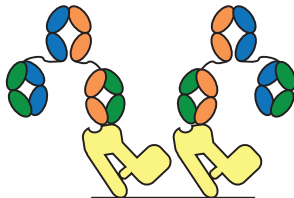
HER2-HER2	
States	Weights
	1

HER3-HER3	
States	Weights
	1
	$2\lambda_a e^{-\beta \varepsilon_3}$
	$\lambda_a e^{-2\beta \varepsilon_3}$
	$2\lambda_a \lambda_l e^{-\beta(\varepsilon_3 + \varepsilon_l)}$
	$\lambda_l^2 e^{-2\beta \varepsilon_l}$
	$2\lambda_l e^{-\beta \varepsilon_l}$
	$\lambda_a^2 e^{-2\beta \varepsilon_3}$

States modeled for the binding of bispecific anti-HER2xHER3 Ab

HER2-HER3	
States	Weights
	1
	$\lambda_a e^{-\beta \epsilon_2}$
	$\lambda_a e^{-\beta \epsilon_3}$
	$\lambda_a e^{-\beta(\epsilon_3 + \epsilon_2)}$
	$\lambda_l e^{-\beta \epsilon_l}$
	$\lambda_l \lambda_a e^{-\beta(\epsilon_l + \epsilon_2)}$
	$\lambda_a^2 e^{-\beta(\epsilon_3 + \epsilon_2)}$

HER2-HER2	
States	Weights
	1
	$\lambda_a e^{-\beta \epsilon_2}$
	$\lambda_a^2 e^{-2\beta \epsilon_2}$

HER3-HER3	
States	Weights
	1
	$2\lambda_a e^{-\beta \epsilon_3}$
	$2\lambda_a \lambda_l e^{-\beta(\epsilon_3 + \epsilon_l)}$
	$\lambda_l^2 e^{-2\beta \epsilon_l}$
	$2\lambda_l e^{-\beta \epsilon_l}$
	$\lambda_a^2 e^{-2\beta \epsilon_3}$

Supplementary Tables

Table S1. Overview of binning of HER2 and HER3 antibodies. Binning of HER2 antibodies was established based on the antibodies reactivity with chicken-human-HER2 chimeras. Binning of HER3 antibodies was performed with rat-human-HER3 chimeras and with full-length HER3 ectodomains of human and non-human origin. “Number” indicates the number of unique antibodies in each group.

Bin	Domain reactivity	Number
HER2		
1	Domain I specific	25
2	Domain II specific	2
3	Domain III specific	23
4	Domain IV specific	7
5	Domain IV specific and murine cross-reactive	2
6	Reactive to all constructs	2
7	Human WT reactive only	4
HER3		
1	High domain III reactivity, rat and mouse reactive and minor reactivity to domain IV	8
2	High domain III reactivity, rat, human and cynomolgus reactive, minor reactivity to domain IV	8
3	Reactive to rat, cynomolgus and human HER3	43
4	Reactive to human HER3	32
5	Reactive to all constructs	33

Table S2. Binning of HER2 antibodies.

Antibodies of the HER2 panel were binned based on the intensity of staining to chicken-human HER2 chimeras and the comparison of staining between chicken-human HER2 chimeras and human HER2. Numbers on the left indicate the identity of the IgG, the CDR3 of the heavy chain shows the diversity in the antibody panel.

Bin	ID	HCDR3	Chicken	Domain I	Domain II	Domain III	Domain IV	Human	Mouse
1a	3003	GQLGLEAWFAY	403	4342	218	319	226	6307	239
1b	2977	GPNYDYDGPWFVY	124	9409	133	135	134	5328	131
1c	3031	GVYDYDGAWFA	236	8887	205	346	228	8221	225
1d	3025	PHYGYDDWYFAV	222	7518	219	574	288	5896	219
2	2889	GDYDYKYAMD	225	250	6152	244	280	5161	257
3a	2908	RHDGYYGGMDY	472	550	329	2012	532	651	368
3b	2935	KFSSGYDWYGM DY	118	129	130	3428	131	4333	129
3c	1847	GWWHPLLSGFDY	184	217	223	5977	202	5396	195
3d	2890	NGVYSSNYERYFAMDY	303	346	230	5448	201	5125	211
3e	2930	SNPLYFAMDY	327	235	234	3234	500	1250	336
4a	1898	DGFRRTTSLSGFDY	131	137	136	146	4006	5925	137
4b	2026	GYFPRTLLAGFDY	122	147	135	140	4350	4415	135
4c	2732	SSPGYSYAFDP	139	155	162	166	3501	2767	571
5	1848	GDYGSYHSYAFDY	131	154	151	154	4277	3421	3289
6a	1868	GRYNYFYGFED	509	4364	457	797	706	2678	2638
6b	1871	GRYDLWYGFEDY	1578	5881	1223	2534	2088	4533	2592
7	2926	RGDWSFDV	131	139	147	177	180	4506	127

Table S3. EC50 values calculated from the titration of MCF-7 cells with bispecific (PB codes), mono-specific anti-HER3 (PG3178), anti-HER2 (PG2916) and analogs of anti-HER2 and anti-HER3 monospecific antibodies (n = 2).

Sample	VH arms	EC50	
		ng/ml	pM
PB3566	3178:3004	1.15	7.9
PB3565	3178:2973	4.52	30.9
PB3709	3178:3025	5.05	34.5
PB3567	3178:2971	6.80	46.5
PB3710	3178:2916	10.85	74.2
PG3178		20.46	139.4
PG2916		136.92	939.3
MM-121		72.99	504.4
Trastuzumab+Pertuzumab		51.22	351.9
Trastuzumab		72.90	500.8
Pertuzumab		75.24	516.9

Table S4. PB4188* activity in different xenograft models.

s.c. = subcutaneous engraftment; o.t. = orthotopic engraftment.

Single agent				
Cell line	Tissue	Autocrine HRG	PB4188* single agent efficacy	Model
BxPC-3	Pancreas HER2 2+	Yes	Yes	s.c.
JIMT-1	Breast HER 2+	Yes	Yes	s.c.
NCI-N87	Gastric HER2 3+	No	No	s.c.
OVCAR-3	Ovary HER2 1+	No	No	s.c.
MCF-7	Breast HER2 1+	No	No	s.c.
MDA-MB-231	Breast HER2 0	No	No	s.c.

PDX	Tissue	Autocrine HRG	PB4188* single agent efficacy	Model
GA0055	Gastric HER2 3+	No	No	s.c.
GA6215	Gastric HER2 1+	No	No	s.c.
GXF251	Gastric HER2 2+	No	No	s.c.
GXA3039	Gastric HER2 3+	No	No	s.c.
ST1360B	Breast (HER2 3+ HER3 3+)	No	Yes	o.t.
OV-10-0050	Ovarian	Yes	Yes	s.c.
MDA-MB-175-VII	Breast (HER2 1+)	Yes	Yes	s.c.

Table S5. Crystallographic data collection and refinement statistics. Values in parentheses are for reflections in the highest resolution shell.

ASU is asymmetric unit; CC is correlation coefficient; R.M.S.D. is root mean square deviation. Rfree values are calculated based on 5% randomly selected reflections.

Data collection	HER2-MF3958	HER3-MF3178	HER3-MF3178
Space group	P 1 21 1	I 1 2 1	P 64 2 2
Unit cell (Å, °)	a = 62.8 b = 113.5 c = 113.5 $\alpha = 90.0 \beta = 101.9$ $\gamma = 90.0$	a = 64.4 b = 144.0 c = 218.8 $\alpha = 90.0 \beta = 97.9$ $\gamma = 90.0$	a = 141.1 b = 141.1 c = 320.8 $\alpha = 90.0 \beta = 90.0$ $\gamma = 120.0$
X-ray source	SLS-PXI	ESRF-ID30A-3	ESRF-ID23-1
Wavelength (Å)	1.00002	0.96771	0.97626
Resolution (Å)	35.8–3.0 (3.2–3.0)	60.0–3.4 (3.5–3.4)	49.0–4.5(5.0–4.5)
No. copies per ASU	1	1	1
Total no. of reflections	10,7273	89,247	129,605
Multiplicity	3.5	3.2	10.9
Mean I/ σ (I)	8.6 (2.5)	17.7 (2.3)	9.6(2.2)
Completeness (%)	98.9 (99.6)	99.2 (99.5)	99.2(100.0)
CC _{1/2} (%)	98.0 (47.9)	94.2 (69.1)	99.8 (83.1)
R _{merge} (%)	14.4 (78.6)	20.7 (55.7)	20.2 (143.6)
Refinement			
R _{work} /R _{free} (%)	22.9/27.1	21.5/26.1	24.7/29.6
Unique reflections	30,435 (3,066)	27,028 (2,699)	11,886 (1,148)
R.M.S.D. bonds (Å)	0.016	0.002	0.010
R.M.S.D. angles (°)	0.58	0.51	0.73
All-atom clashscore	5.4	3.7	7.1
Ramachandran favoured (%)	94.0	93.2	92.1
Ramachandran outliers (%)	0.2	0.6	0.5
Rotamer outliers (%)	0.4	0.9	0.7
Mean B-factor (Å ²)	81 (14–206)	54 (10–158)	248 (124–440)
Protein Data Bank code	5O4G	5O4O	5O7P

Table S6. Sequences of the Fab variable regions of PB4188 with the residues forming the paratopes highlighted in yellow (CDR1 in blue, CDR2 in green, CDR3 in red) as identified by the X-ray structures of HER2-ECD:MF3958 and HER3-ECD:MF3178.

MF3958	VH	QVQLVQSGAEVKKPGASVKLSCKASGYTFTAYYINWVRQA- PGQGLEWIGRIYPGSGYTSYAQKFQGRATLTAD ^{EST} - STAYMELSSLRSED ^{TAVYFCARPPVYYDSAWFAY} WGQGLVT
	VL	DIQMTQSPSSLSASVGD ^{RVTTITCRASQSISSYLN} WYQQKPGKAP- KLLIYAASSLQSGVPSRFSGSGSGTDFLT ^{LTIS} LQPEDFATYYCQQ- SYSTPPTFGQGTKVEIK
MF3178	VH	QVQLVQSGAEVKKPGASVKVCKASGYTFTGYMHVWRQAP- GQGLEWMGW ^{INPNSGGTNYAQKFQGRVTMTRDTSISTAYMEL-} SRLRSDDTAVYYCAR ^{DHGSRHFWSYWGFDY} WGQGLVT
	VL	DIQMTQSPSSLSASVGD ^{RVTTITCRASQSISSYLN} WYQQKPGKAP- KLLIYAASSLQSGVPSRFSGSGSGTDFLT ^{LTIS} LQPEDFATYYCQQ- SYSTPPTFGQGTKVEIK

Table S7. Hydrogen bonds and salt bridges at the HER2-ECD:FabMF3958 interface (calculated by PISA, EMBL (12)).

	MF3958	HER2 ECD
HC	Tyr33[OH]	Asp143[OD2]
	Tyr52[OH]	Ser180[O]
	Gly54[O]	Arg181[NH1]
	Ser55[OG]	Asp143[O]
	Tyr57[OH]	Ile162[O], Thr164[OG1]
	Glu74[OE1, OE2]	Arg181[NH1], Arg181[NH2]
	Tyr103[OH]	Tyr141[N], Asp143[OD1], Arg166[NH2], Cys170[O]
LC	Asp104[OD1, OD2]	Cys170[N], Arg166[NH1]
	Tyr32[OH]	Ser167[O]

Table S8. Residues buried at the HER2-ECD:FabMF3958 interaction surface.

The vertical bars indicate the degree of buried surface area: one bar corresponds to 10% of the total solvent-accessible surface area buried (calculated by PISA, EMBL (12)).

MF3958	HC	Thr28 II
		Thr30 IIIIIII
		Ala31 IIIIIIIII
		Tyr32 III
		Arg50 III
		Ser59 I
		Val101 II
	Tyr102 IIIIIII	
	Ser105 III	
	Trp107 I	
	LC	Tyr92 I
		Thr94 I
	HER2	Thr144 IIIIIIIIIII
		Ile145 IIIIIII
Leu146 III		
Trp147 I		
Thr160 I		
Asp163 I		
Asn165 I		
Arg166 I		
Arg168 I		
Ala169 IIIIIII		
His171 III		
Pro172 IIIIIIIII		
Cys173 IIIIIII		
Pro175 I		
Gly179 IIIIIII		

Table S9. Hydrogen bonds at the HER3-ECD:FabMF3178 interface (calculated by PISA, EMBL (12)).

	MF3178	HER3
HC	Phe105[O]	Arg426 [NH1]
	Ser107[O]	Arg426 [NH2]
	Trp106[NE1]	Tyr424 [OH]
LC	Tyr32[OH]	Asn425 [OD1], Arg426 [N]
	Ser91[O]	Arg426 [NE]

Table S10. List of residues buried at the HER3-ECD:FabMF3178 interaction surface. The vertical bars indicate the degree of buried surface area: one bar corresponds to 10% of the total solvent-accessible surface area buried (calculated by PISA, EMBL (12)).

MF3178	HC	His104 I
		Tyr108 I
		Trp109 III
	LC	Tyr92 IIIIIII
		Ser93 I
		Thr94 I
HER3	Gln400 IIIII	
	Phe428 IIIII	
	Leu423 II	
	Gly427 IIIIIIIII	
	Leu431 IIIIIIIII	
	Met433 IIIII	
	Arg453 IIII	
	Tyr455 IIIII	
	Glu480 I	
	Asp483 I	

Table S7. SAXS parameters. R_g is radius of gyration. D_{max} is maximum diameter. $P(r)$ is the paired distribution function.

HER2-ECD:HER3-ECD:PB4188	
R_g from Guinier (nm)	7.5
R_g from $P(r)$ (nm)	8.0
D_{max} from $P(r)$ (nm)	26.2
Porod volume (nm ³)	431.0

Supplementary Figures

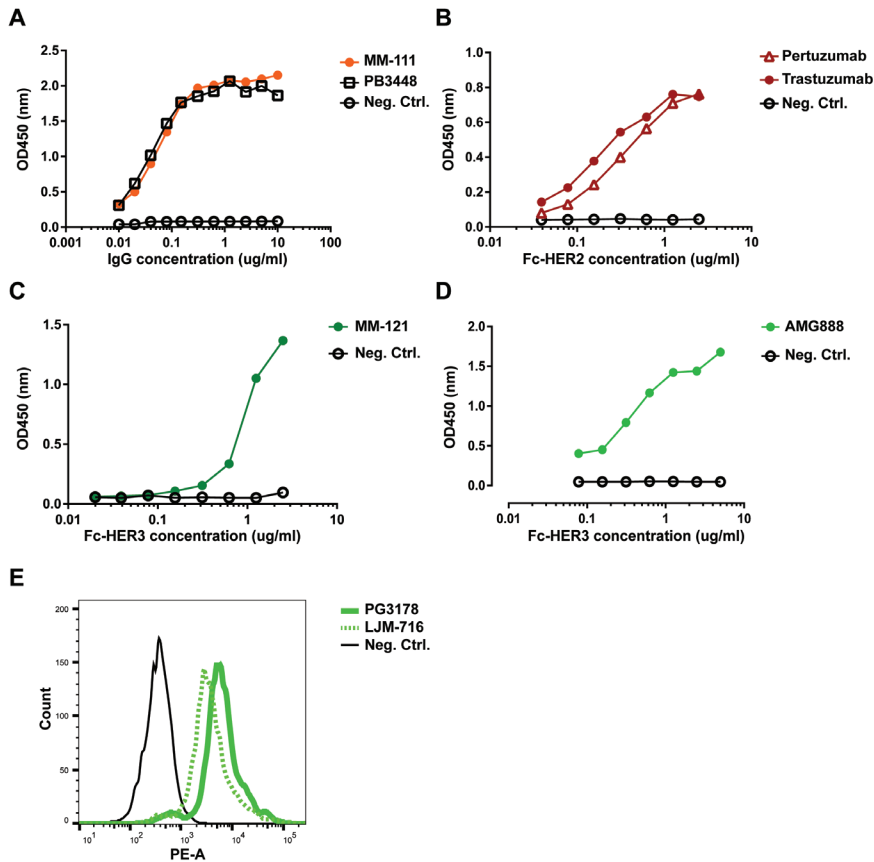


Figure S1. Binding of produced antibodies to their targets. A, Serial titrations of bispecific Abs MM-111 and PB3448 were added to ELISA plates coated with Fc-HER2 recombinant protein. HER3-FITC recombinant protein was added and detection was done with anti-FITC Fab HRP. B-D, ELISA plates were coated with a serial titration of Fc-HER2 or Fc-HER3 recombinant proteins. HER2 or HER3 specific antibodies were tested for binding using 10 μ g/ml. Antibodies bound to the coated proteins were detected with HRP-conjugated goat anti-human IgG. Binding of anti-HER2 mAbs trastuzumab and pertuzumab to Fc-HER2 (B). Binding of anti-HER3 mAbs MM-121 (C) and AMG888 (D) to Fc-HER3. E, FACS-based staining of HER3-overexpressing K562 cells with anti-HER3 mAb LJM-716. PG3178 was used as positive control.

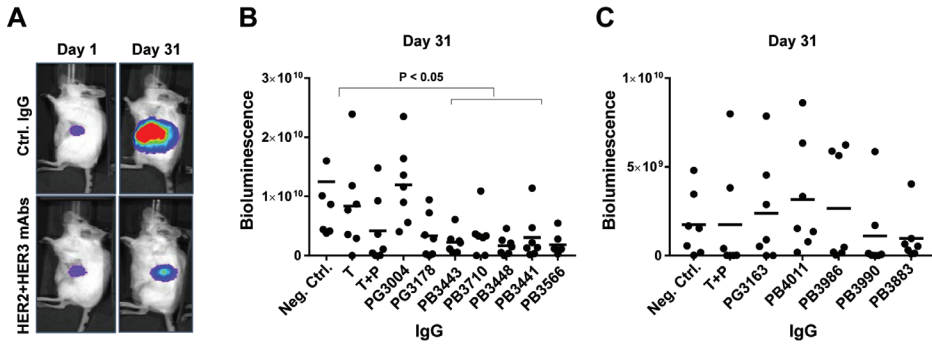


Figure S2. Orthotopic BxPC-3 luc2 xenograft model. A, Tumor growth was measured by bioluminescence after using a cocktail of HER2 and HER3 monospecific antibodies (mAbs) or negative control antibody (Ctrl. IgG). B-C, Tumor growth inhibition activity of trastuzumab and trastuzumab + pertuzumab (T+P) was compared to anti-HER2 (PG3004) and anti-HER3 (PG3178, PG3163) monospecific antibodies, and bispecific antibodies (PB code) derived from a lead panel. PG3004 and PG3178 are the Fab arms of PB3566.

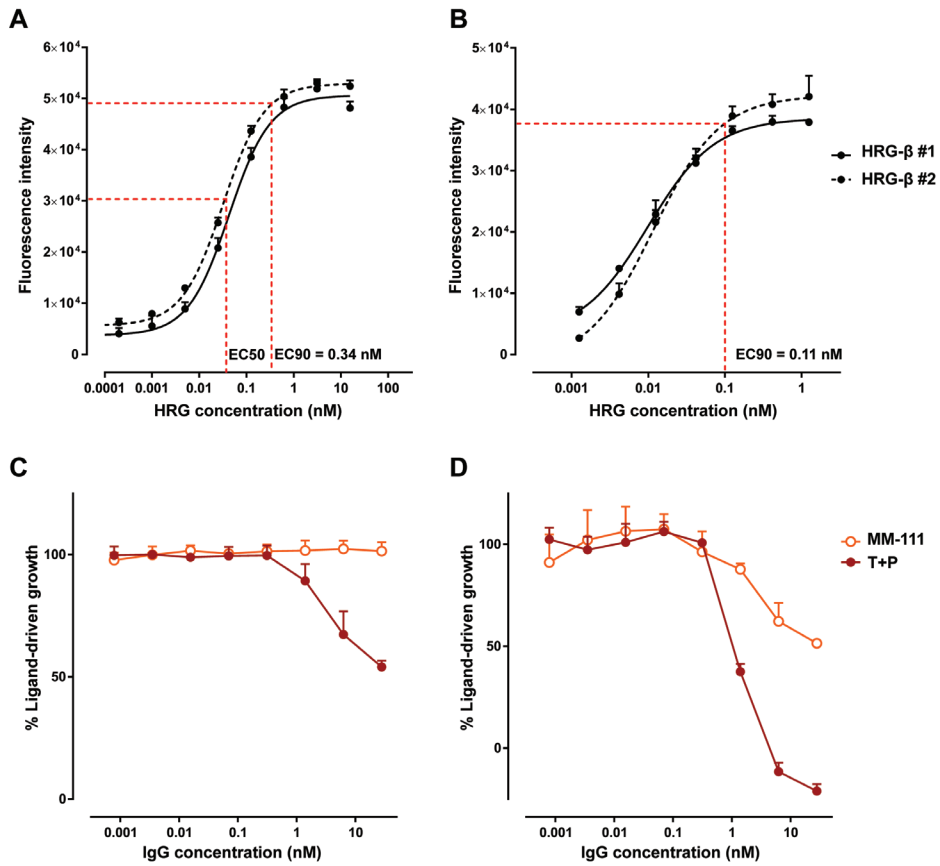


Figure S3. A-B, Titration of HRG in cancer cell lines MCF-7 (A) and N87 (B). C-D, Titration of an analog of the bispecific antibody MM-111 compared to the combination of trastuzumab + pertuzumab (T+P) in MCF-7 cells at HRG “stress conditions” (12.5 nM) (C) and at submaximal HRG levels (0.125 nM) (D).

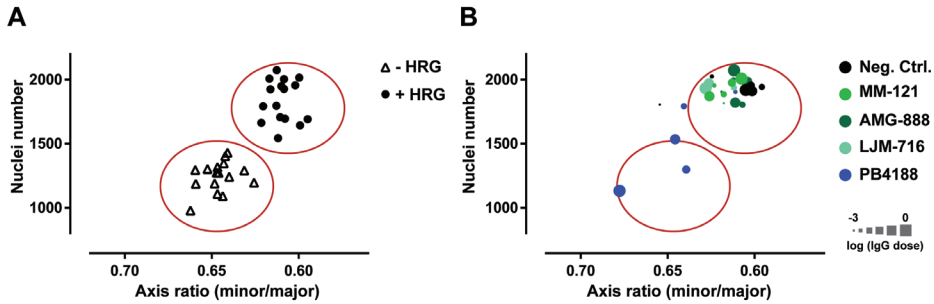


Figure S4. SKBR-3 cells were cultured in Matrigel in regular growth medium supplemented or not with 12.5 nM HRG (A). The effect of anti-HER3 antibody analogs and PB4188 was assessed in the presence of 12.5 nM HRG (B). Cell proliferation was measured by number of nuclei per well. Cell invasion was quantified by measuring cellular shape, dividing the shortest cell axis (minor) by the longest axis (major) of the SKBR-3 cell cluster. An axis ratio of 1 describes a sphere, while decreasing ratios are associated with more invasive structures.

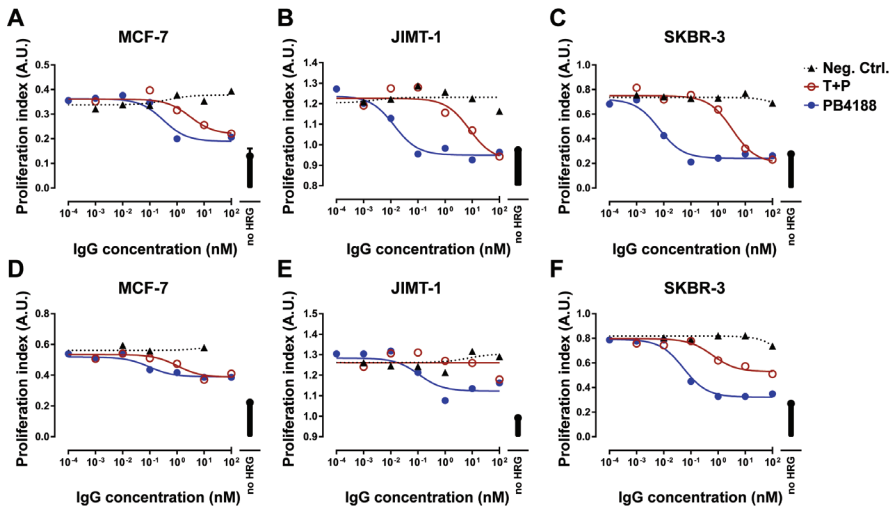


Figure S5. Cell cycle analysis was performed on breast cancer cell lines expressing low (MCF-7, A,D), intermediate (JIMT-1, B,E) and high (SKBR-3, C,F) HER2 protein expression levels. All cells were stimulated with low (0.125 nM, A-C) and high HRG concentration (12.5 nM, D-F) and titrations of negative control (Neg. Ctrl.) antibody, PB4188 or the combination of trastuzumab and pertuzumab (T+P). The proliferation index was calculated by dividing the percentage of cells in the G0/G1 and S phase by the percentage of cells in the G2/M phase.

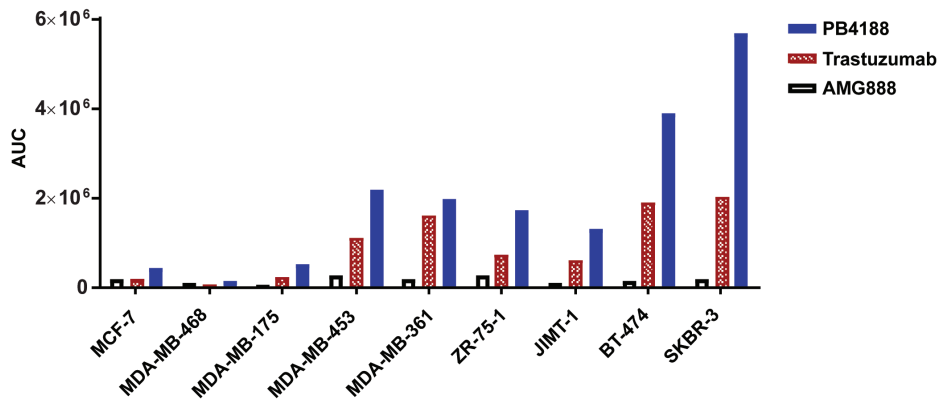


Figure S6. Area under the curve (AUC) measurements of FACS median fluorescence intensity (MFI). PB4188 was dose-titrated for binding to breast cancer cell lines expressing different levels of HER2 and was compared to trastuzumab and AMG888. Bound antibodies were detected using PE-labelled anti-human IgG and the median fluorescence intensity values were used to calculate the AUC for all antibodies (Prism 6.0, GraphPad).

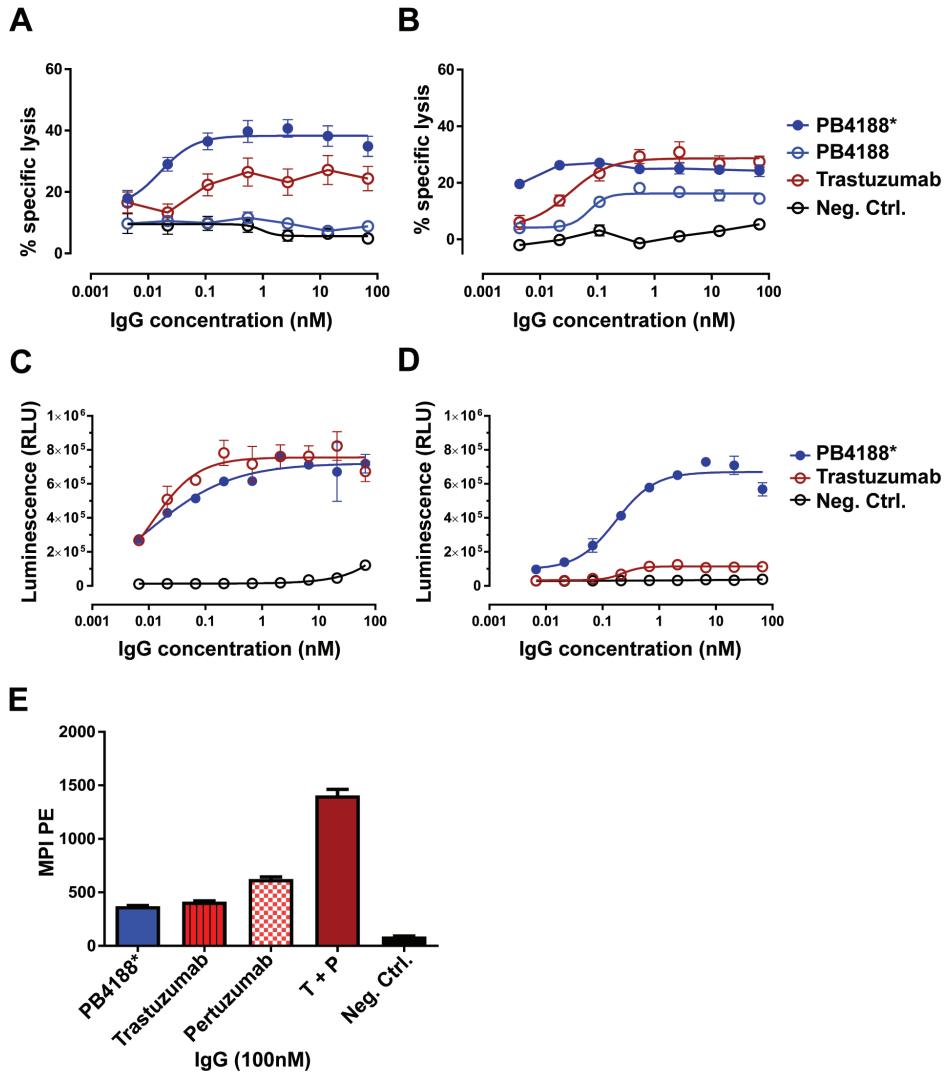


Figure S7. ADCC activity measurement of engineered PB4188. PB4188* was produced in cells co-transfected with the prokaryotic enzyme GDP-6-deoxy-D-lyxo-4-hexulose reductase, which leads to the removal of fucose moieties and enhances binding of the Fc chain to CD16 (13). A-B, Breast cancer cells expressing high (SKBR-3, A) or low (MCF-7, B) levels of HER2 protein were labeled with ⁵¹Cr and incubated with titration of antibodies in the presence of human PBMC. PB4188* was compared with its non-defucosylated parent antibody PB4188, trastuzumab and negative control (Neg. Ctrl.) antibody. The mean EC₂₀ value for ADCC activity of PB4188* on SKBR-3 cells was 0.06 ng/ml compared to 0.84 ng/ml for trastuzumab. C-D, HER2-amplified SKBR-3 cells were used in the ADCC reporter assays using V158 (high affinity, C) and F158 (low affinity, D) variants of FcγRIIIa. Luciferase activity was measured after 6 hours incubation. ADCC activity of trastuzumab and PB4188* is equal when binding the V158 CD16 variant (C). With F158 CD16 variant cells (D) PB4188* is still able

to induce a strong ADCC response while trastuzumab has only a minor effect. E, To compare the internalization profiles antibodies were labeled with a pH-sensitive dye (14) and incubated for 24 hours on SKBR-3 cells. Fluorescence intensity was measured by flow cytometry. All single agent antibodies presented similar internalization signals after 24 hours incubation, with pertuzumab showing a slightly stronger signal, while the combination of trastuzumab and pertuzumab showed a much stronger internalization signal than single agent antibodies.

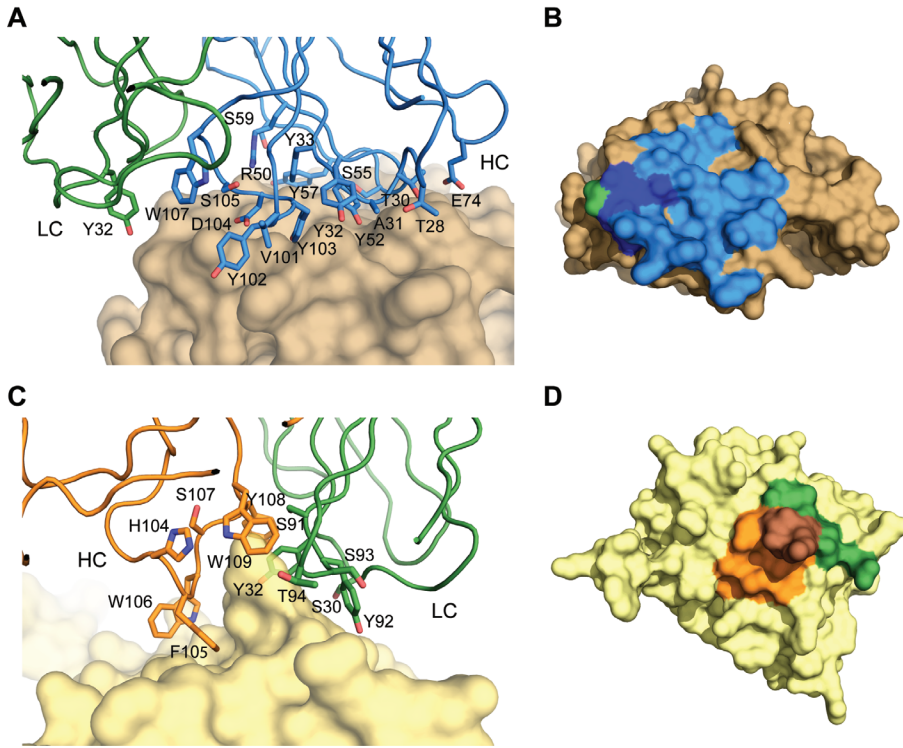


Figure S8. A, Detailed view of MF3958 residues (shown as sticks) interacting with HER2 domain I (shown as surface). B, Top-view of the interaction surface of MF3958 on HER2 domain 1–2 shown as surface. HER2 residues interacting with the MF3958 HC are colored blue, LC green, both HC and LC dark blue. C, Detailed view of MF3178 residues (shown as sticks) interacting with HER3 domain 3 (shown as surface). D, Top-view of the interaction surface of MF3178 on HER3 domain 3 shown as surface. HER3 residues interacting with MF3178 HC are colored orange, LC green, both HC and LC brown.

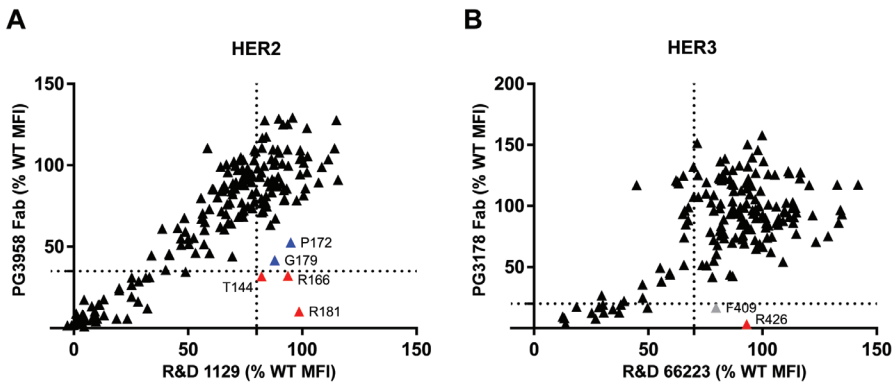


Figure S9. Shotgun mutagenesis epitope mapping of PG3958 (A) and PG3178 (B). Critical residues are shown in red. Secondary critical residues are shown in blue.

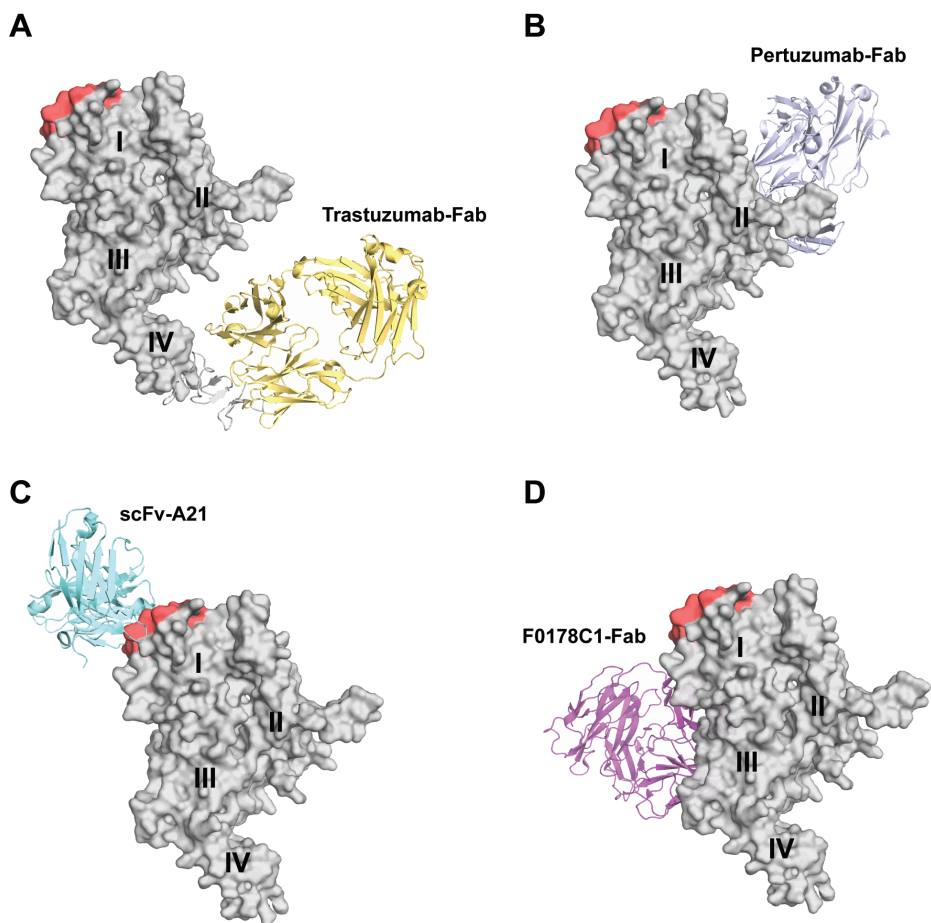


Figure S10. Summary of published HER2-ECD:Fab structures. A, HER2-ECD:Trastuzumab-Fab (PDB ID 1N8Z (15)). B, HER2-ECD:Pertuzumab-Fab (PDB ID 1S78 (16)). C, HER2-ECD:scFvA21 (PDB ID 3H3B (17)). D, HER2-ECD:F0178C1-Fab (PDB ID 3WSQ (18)).

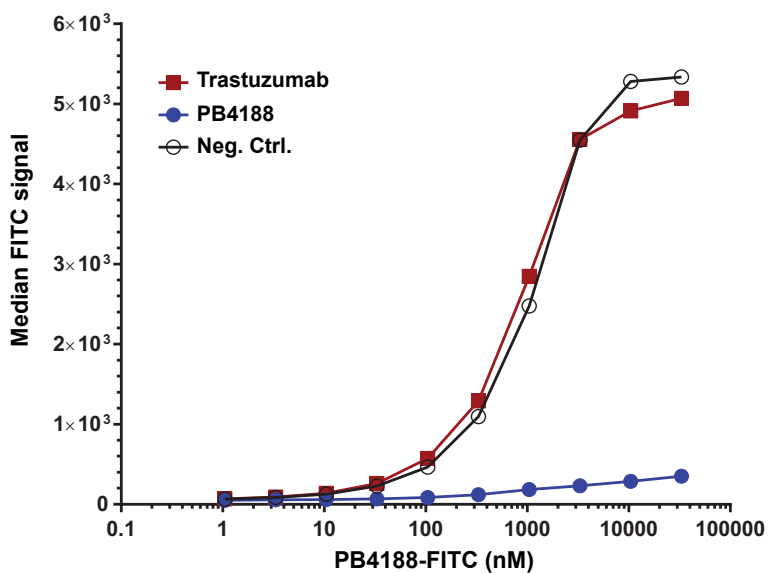


Figure S11. Binding of a serial titration of FITC-labeled PB4188 to SKBR-3 cells pre-incubated with a saturated concentration of PB4188, trastuzumab or a negative control (Neg. Ctrl.) antibody. FITC-labeled PB4188 binds as effectively to SKBR-3 cells in the presence of trastuzumab or control antibody.

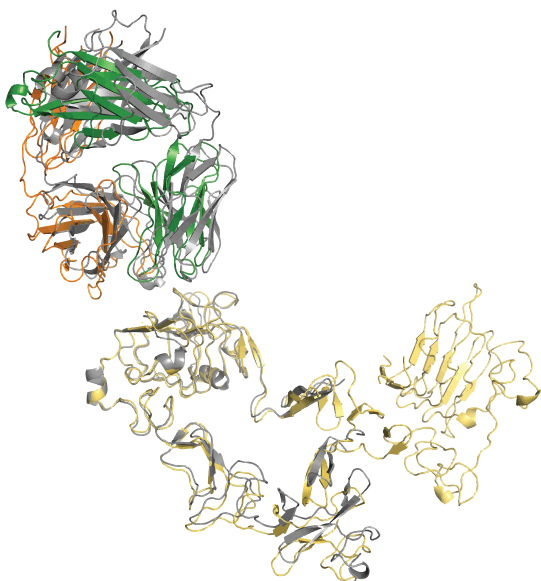


Figure S12. Superposition of the two crystal structures of HER3-ECD:MF3178 complex at 3.4- (grey) and 4.5-Å resolution (color scheme as in Figure 6).

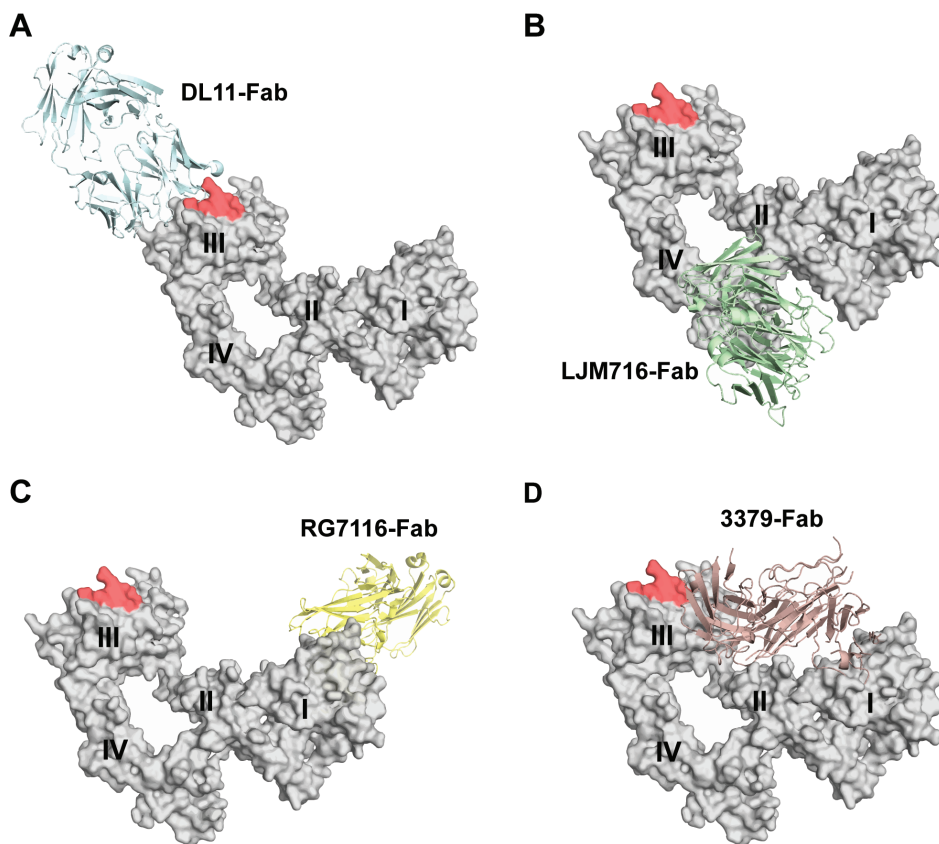


Figure S13. Summary of published Fab:HER3-ECD structures. A, HER3-ECD: DL11-Fab (PDB ID 3P11 (19)). B, HER3-ECD:LJM16-Fab (PDB ID 4P59 (20)). C, HER3-ECD: RG7116-Fab (PDB ID 4LEO (21)). D, HER3-ECD:3379-Fab (PDB ID 5CUS (22)).

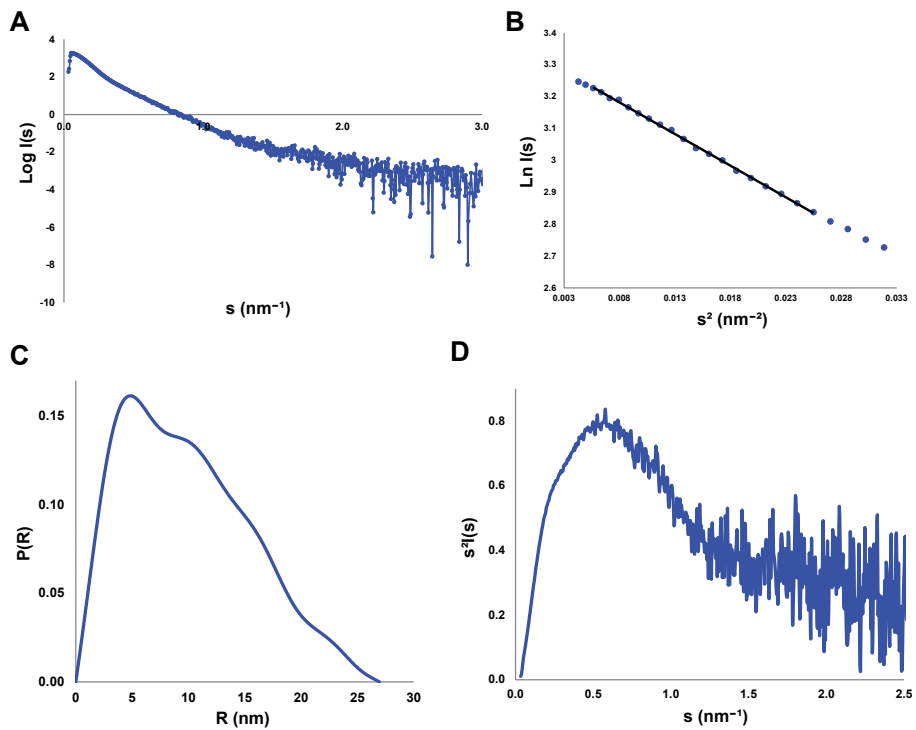


Figure S14. SAXS analysis of PB4188 in complex with HER2-ECD and HER3-ECD. A, Scattering curve. B, Guinier analysis. C, Paired distance distribution function. D, Kratky analysis.

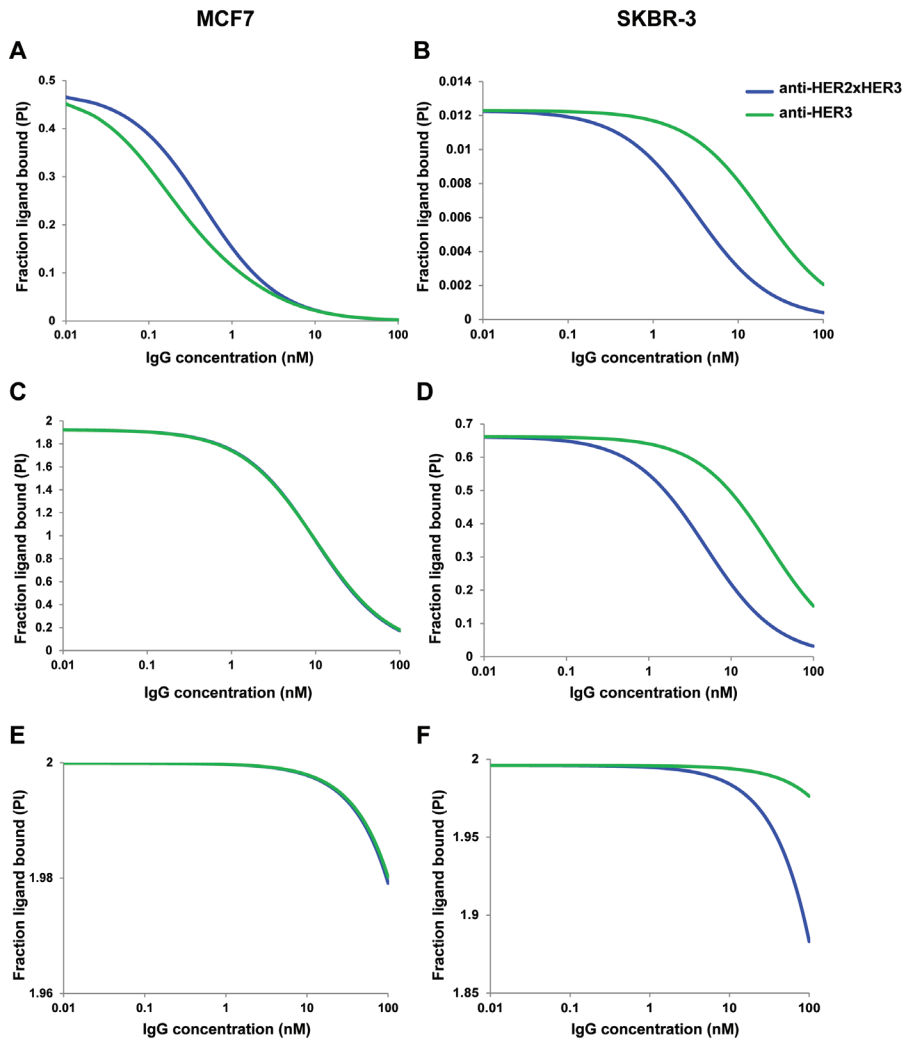


Figure S15. Grand canonical model of the binding of a bispecific anti-HER2xHER3 antibody compared to a monospecific anti-HER3 antibody. A-B, MCF7 (A) and SKBR-3 (B) cell lines at low HRG concentration (0.1 nM). C-D, MCF7 (C) and SKBR-3 (D) cell lines at high HRG concentration (10 nM). E-F, MCF7 (E) and SKBR-3 (F) cell lines at extremely high HRG concentration (10,000 nM).

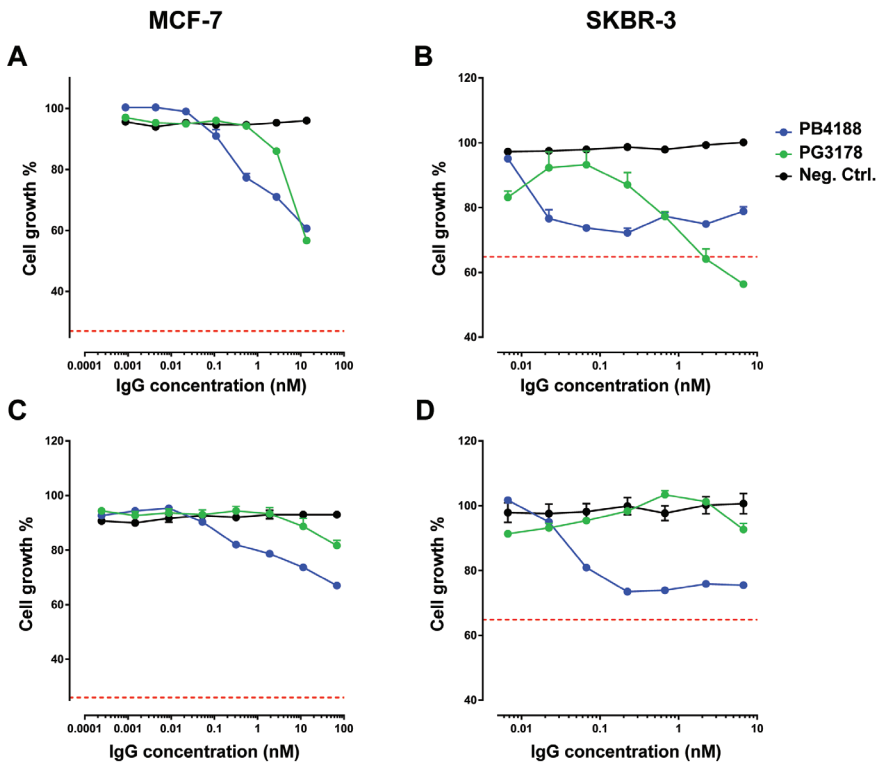


Figure S16. Potency of PB4188 and PG3178 antibodies in the inhibition of HRG mediated proliferation in MCF-7 (A,C) and SKBR-3 (B,D) cells at low (0.125 nM, A-B) or high (12.5 nM, C-D) HRG concentration.

Supplementary References

1. Griffiths, A. D., Malmqvist, M., Marks, J. D., Byel, J. M., Embleton, M. J., McCafferty, J., Baier, M., Holliger, K. P., Gorick, B. D., Hughes-Jones, N. C., Hoogenboom, H. R., and Winter, G. (1993) Human anti-self antibodies with high specificity from phage display libraries. *EMBO J.* **12**, 725–734
2. de Haard, H. J., van Neer, N., Reurs, A., Hufton, S. E., Roovers, R. C., Henderikx, P., de Bruine, A. P., Arends, J.-W., and Hoogenboom, H. R. (1999) A large non-immunized human Fab fragment phage library that permits rapid isolation and kinetic analysis of high affinity antibodies. *J. Biol. Chem.* **274**, 18218–18230
3. de Kruijf, J., Kramer, A., Visser, T., Clements, C., Nijhuis, R., Cox, F., van der Zande, V., Smit, R., Pinto, D., Throsby, M., and Logtenberg, T. (2009) Human immunoglobulin repertoires against tetanus toxoid contain a large and diverse fraction of high-affinity promiscuous VH genes. *J. Mol. Biol.* **387**, 548–558
4. de Kruijf, J. D., Boel, E., and Logtenberg, T. (1995) Selection and application of human single chain Fv antibody fragments from a semi-synthetic phage antibody display library with designed CDR3 regions. *J. Mol.* **248**, 97–105
5. Devash, Y., Calvelli, T. A., Wood, D. G., Reagan, K. J., and Rubinstein, A. (1990) Vertical transmission of human immunodeficiency virus is correlated with the absence of high-affinity/avidity maternal antibodies to the gp120 principal neutralizing domain. *Proc. Natl. Acad. Sci. USA.* **87**, 3445–3449
6. Brennich, M. E., Kieffer, J., Bonamis, G., De Maria Antolinos, A., Hutin, S., Pernot, P., and Round, A. (2016) Online data analysis at the ESRF bioSAXS beamline, BM29. *J. Appl. Crystallogr.* **49**, 203–212
7. Petoukhov, M. V., Franke, D., Shkumatov, A. V., Tria, G., Kikhney, A. G., Gajda, M., Gorba, C., Mertens, H. D. T., Konarev, P. V., and Svergun, D. I. (2012) New developments in the ATSAS program package for small-angle scattering data analysis. *J. Appl. Crystallogr.* **45**, 342–350
8. Svergun, D. I. (1992) Determination of the regularization parameter in indirect-transform methods using perceptual criteria. *J. Appl. Crystallogr.* **25**, 495–503
9. Franke, D., and Svergun, D. I. (2009) DAMMIF, a program for rapid ab-initio shape determination in small-angle scattering. *J. Appl. Crystallogr.* **42**, 342–346
10. Clark, M., Guarnieri, F., Shkurko, I., and Wiseman, J. (2006) Grand canonical Monte Carlo simulation of ligand-protein binding. *J. Chem. Inf. Model.* **46**, 231–242
11. Weinert, F. M., Brewster, R. C., Rydenfelt, M., Phillips, R., and Kegel, W. K. (2014) Scaling of gene expression with transcription-factor fugacity. *Phys. Rev. Lett.* **113**, 258101
12. Krissinel, E., and Henrick, K. (2007) Inference of macromolecular assemblies from crystalline state. *J. Mol. Biol.* **372**, 774–797
13. von Horsten, H. H., Ogorek, C., Blanchard, V., Demmler, C., Giese, C., Winkler, K., Kaup, M., Berger, M., Jordan, I., and Sandig, V. (2010) Production of non-fucosylated antibodies by co-expression of heterologous GDP-6-deoxy-D-lyxo-4-hexulose reductase. *Glycobiology.* **20**, 1607–1618
14. Nath, N., Godat, B., Zimprich, C., Dwight, S. J., Corona, C., McDougall, M., and Urh, M. (2016) Homogeneous plate based antibody internalization assay using pH sensor fluorescent dye. *J. Immunol. Methods.* **431**, 11–21
15. Cho, H.-S., Mason, K., Ramyar, K. X., Stanley, A. M., Gabelli, S. B., Dennery Jr, D. W., and Leahy, D. (2003) Structure of the extracellular region of HER2 alone and in complex with the Herceptin Fab. *Nature.* **421**, 756–759

16. Franklin, M. C., Carey, K. D., Vajdos, F. F., Leahy, D. J., de Vos, A. M., and Sliwkowski, M. X. (2004) Insights into ErbB signaling from the structure of the ErbB2-pertuzumab complex. *Cancer Cell*. **5**, 317–328
17. Zhou, H., Zha, Z., Liu, Y., Zhang, H., Zhu, J., Hu, S., Shen, G., Cheng, L., Niu, L., Greene, M. I., Teng, M., and Liu, J. (2011) Structural insights into the down-regulation of overexpressed p185 her2/neu protein of transformed cells by the antibody chA21. *J. Biol. Chem.* **286**, 31676–31683
18. Fu, W., Wang, Y., Zhang, Y., Xiong, L., Takeda, H., Ding, L., Xu, Q., He, L., Tan, W., Bethune, A. N., Zhou, L., Fu, W., Wang, Y., Zhang, Y., Xiong, L., Takeda, H., Ding, L., Xu, Q., and He, L. (2014) Insights into HER2 signaling from step-by-step optimization of anti-HER2 antibodies. *MAbs*. **6**, 978–990
19. Schaefer, G., Haber, L., Crocker, L. M., Shia, S., Shao, L., Dowbenko, D., Totpal, K., Wong, A., Lee, C. V., Stawicki, S., Clark, R., Fields, C., Phillips, G. D. L., Prell, R. A., Danilenko, D. M., Franke, Y., Stephan, J.-P., Hwang, J., Wu, Y., Bostrom, J., Sliwkowski, M. X., Fuh, G., and Eigenbrot, C. (2011) Article A two-in-one antibody against HER3 and EGFR has superior inhibitory activity compared with monospecific antibodies. *Cancer Cell*. **20**, 472–486
20. Garner, A. P., Bialucha, C. U., Sprague, E. R., Garrett, J. T., Sheng, Q., Li, S., Sineshchekova, O., Saxena, P., Sutton, C. R., Chen, D., Chen, Y., Wang, H., Liang, J., Das, R., Mosher, R., Gu, J., Huang, A., Haubst, N., Zehetmeier, C., Haberl, M., Elis, W., Kunz, C., Heidt, A. B., Herlihy, K., Murtie, J., Schuller, A., Arteaga, C. L., Sellers, W. R., and Ettenberg, S. A. (2013) An antibody that locks HER3 in the inactive conformation inhibits tumor growth driven by HER2 or neuregulin. *Cancer Res.* **73**, 6024–6036
21. Mirschberger, C., Schiller, C. B., Schraml, M., Dimoudis, N., Friess, T., Gerdes, C. A., Reiff, U., Lifke, V., Hoelzlwimmer, G., Kolm, I., Hopfner, K.-P., Niederfellner, G., and Bossenmaier, B. (2013) RG7116, a therapeutic antibody that binds the inactive HER3 receptor and is optimized for immune effector activation. *Cancer Res.* **73**, 5183–5195
22. Lee, S., Greenlee, E. B., Amick, J. R., Ligon, G. F., Lillquist, J. S., Natoli, E. J., Hadari, Y., Alvarado, D., and Schlessinger, J. (2015) Inhibition of ErbB3 by a monoclonal antibody that locks the extracellular domain in an inactive configuration. *Proc. Natl. Acad. Sci. USA.* **112**, 13225–13230
23. Ogiso, H., Ishitani, R., Nureki, O., Fukai, S., Yamanaka, M., Kim, J.-H., Saito, K., Sakamoto, A., Inoue, M., Shirouzu, M., and Yokoyama, S. (2002) Crystal structure of the complex of human epidermal growth factor and receptor extracellular domains. *Cell*. **110**, 775–787
24. De Nardis, C., Hendriks, L. J. A., Poirier, E., Arvinte, T., Gros, P., Bakker, A. B. H., and de Kruif, J. (2017) A new approach for generating bispecific antibodies based on a common light chain format and the stable architecture of human immunoglobulin G1. *J Biol Chem*. First published on June 27, 2017, doi: 10.1074/jbc.M117.793497

CHAPTER 4

A new approach for generating bispecific antibodies based on a common light chain format and the stable architecture of human immunoglobulin G1

Camilla De Nardis^{1,*}, Linda J.A. Hendriks^{2,*}, Emilie Poirier³, Tudor Arvinte^{3,4},
Piet Gros¹, Alexander B.H. Bakker² and John de Kruijf²

*These authors contributed equally

¹Crystal & Structural Chemistry, Bijvoet Center for Biomolecular Research, Utrecht University, Utrecht, The Netherlands

²Merus N.V., Utrecht, The Netherlands

³Therapeomic Inc., Basel, Switzerland

⁴School of Pharmaceutical Science, University of Geneva, Geneva, Switzerland

This chapter has been published in *Journal of Biological Chemistry* (2017),
doi:10.1074/jbc.M117.793497

Abstract

Bispecific antibodies combine two different antigen binding sites in a single molecule, enabling more specific targeting, novel mechanisms of action and higher clinical efficacies. Although they have the potential to outperform conventional monoclonal antibodies, many bispecific antibodies have issues regarding production, stability and pharmacokinetic properties. Here we describe a new approach for generating bispecific antibodies using a common light chain format and exploiting the stable architecture of human immunoglobulin G₁. We used iterative experimental validation and computational modeling to identify multiple Fc variant pairs that drive efficient heterodimerization of the antibody heavy chains. Accelerated stability studies led to the selection of one Fc variant pair dubbed “DEKK” consisting of substitutions L351D and L368E in one heavy chain combined with L351K and T366K in the other. Solving of the crystal structure of the DEKK Fc region at a resolution of 2.3 Å enabled detailed analysis of the interactions inducing CH3 interface heterodimerization. Local shifts in the IgG backbone accommodate the introduction of lysine side chains that form stabilizing salt-bridge interactions with substituted and native residues in the opposite chain. Overall, the CH3 domain adapted to these shifts at the interface, yielding a stable Fc conformation, very similar to that in wild-type IgG. Using the DEKK format we generated the bispecific antibody MCLA-128, targeting human EGFRs 2 and 3. MCLA-128 could be readily produced and purified at industrial scale with a standard mammalian cell culture platform and a routine purification protocol. Long-term accelerated stability assays confirmed that MCLA-128 is highly stable and has excellent biophysical characteristics.

Introduction

Bispecific antibodies (bsAbs) combine two different antigen binding sites in a single molecule. Bispecific antibodies can address multiple antigens resulting in more specific targeting, novel mechanisms of action and higher clinical efficacies (1). Numerous technical solutions are available for linking the two different antibody specificities (2). Extensive engineering of therapeutic proteins may however generate molecules whose drug-like properties - such as production yields, stability and half-life - are less favorable. Bispecific molecules that remain faithful to the natural IgG format use a structure shaped by million years of evolution. Drugs based on such molecules are therefore more likely to have pharmacokinetic properties similar to the natural antibody.

Conventional IgG antibodies are bivalent and monospecific, and their assembly depends upon the homodimerization of the so-called crystallizable fragment (Fc). The process is mediated by the association of two identical heavy chains (HCs) followed by the assembly of two identical light chains (LCs). The Fc portion of an IgG is composed of a hinge region, a CH2 domain, and a CH3 domain, with the CH3 domain forming the dimerization interface. In the production of bispecific IgGs, heterodimer formation can thus be induced by engineering the CH3 domains such that homodimer-favoring interactions are replaced by asymmetric interactions. Most bispecific formats based on native IgG benefit from the use of a common light chain (cLC) (3,4), which has the advantage of preventing mispairing of heavy and light chains without the need for engineering. Different structure-based design strategies have so far been adopted for the production of heterodimeric CH3 variant pairs, and these have recently been reviewed by Ha *et al.* (4). Annealing-based approaches for producing bispecific antibodies by mixing two different antibody components are also being pursued (5). Other native formats are rat-mouse hybrids or IgG₁-IgG₃ hybrids (6), in which there is no preferential pairing between heavy chains. Purification of these bsAbs relies on their differential binding affinity for purification matrices.

Challenges encountered during bispecific IgG generation using CH3 engineering include loss of stability relative to the natural Fc and the presence of homodimer contaminations. In this study we therefore aimed to identify Fc variant pairs that enable efficient formation of IgG heterodimers while maintaining the stability of the natural Fc region. Taking a novel charge-introduction approach, we first identified residues within the CH3 interface that impaired the formation of IgG homodimers. Based on this information, variant pairs were designed and analyzed for their efficiency of heterodimer formation. The charge pair that had the most favorable heterodimer/homodimer ratio was used in a computational

approach called HADDOCK (High Ambiguity Driven protein-protein Docking) (7,8), an information-driven docking tool for modeling biomolecular complexes. This generated several candidates for further experimental analysis. The screening resulted in the selection of the Fc variant pair DEKK, which contained the substitutions L351D,L368E in one heavy chain and L351K,T366K in the other. The crystal structure of the Fc region of DEKK was determined at a resolution of 2.3 Å, which revealed the molecular interactions at the dimerization interface. Finally, the DEKK Fc variant pair was used to construct MCLA-128, a bispecific humanized full-length IgG₁ antibody. This bsAb specifically targets the human epidermal growth factor receptors (HER) 2 and 3 and is currently undergoing clinical Phase I/II evaluation in patients with solid tumors (NCT02912949). MCLA-128 was produced and purified at industrial scale and a liquid formulation was identified in which the protein was shown to have excellent long-term stability.

Results

Charged residues were introduced at different positions within the CH3 interface to identify those substitutions that interfere with IgG homodimer formation (Table 1). The constructs were expressed and analyzed using non-reducing SDS-PAGE. Constructs containing CH3 interfaces that allowed homodimer formation are visible as bands at 144 kDa while interference with dimer formation is demonstrated by the presence of 74 kDa bands. The data are summarized in Table 1 and an example of the SDS-PAGE analysis is presented in Figure 1. This analysis demonstrated that the six charge-introduction substitutions Y349K, L351K, S354K, T366K, T394K, and V397K strongly interfered with homodimer formation.

Charged pairs containing these residues were constructed based on rational design (Table 2). Interacting residues were identified based on published data (9,10,11) and opposite charges were engineered into the complementary CH3 regions. The combinations were expressed, purified, and analyzed using native mass spectrometry (nMS). The data in Table 2 show that one pair, T366K/L351D, resulted in significant levels of bispecific antibody formation but only low levels of contaminating homodimers.

Table 1. Substitutions constructed in the CH3 region of full-length IgG and interpretation of SDS-PAGE data.

SDS-PAGE gels were analyzed for the presence of a band at ~ 74kDa, indicative of a substitution that impairs homodimer formation; see Figure 1 for examples. Effect on homodimer formation was scored from +++ (strong) to - (absent). nd is not determined.

Substitutions	Effect on homodimer formation
Q347K	-
Y349D	+/-
Y349K	+/-
T350K	-
T350K, S354K	+/-
L351K, S354K	+/-
L351K, T366K	++
L351K, P352K	+/-
L351K, P353K	++
S354K, Y349K	++
D356K	-
E357K	-
S364K	++
T366K, L351K	++
T366K, Y407K	+++
L368K	nd
L368K, S364K	++
N390K, S400K	+/-
T394K, V397K	+
T394K, F405K	+++
T394K, Y407K	+++
P395K, V397K	+/-
S400K	-
F405K	+++
Y407K	++
Q347K, V397K, T394K	++
Y349D, P395K, V397K	++
T350K, T394K, V397K	nd
L351K, S354K, S400K	++
S354K, Y349K, Y407K	++
T350K, N390K, S400K	+
L368K, F405K	++

Table 1. Substitutions constructed in the CH3 region of full-length IgG and interpretation of SDS-PAGE data.

SDS-PAGE gels were analyzed for the presence of a band at ~74kDa, indicative of a substitution that impairs homodimer formation; see Figure 1 for examples. Effect on homodimer formation was scored from +++ (strong) to - (absent). nd is not determined. (continued).

Substitutions	Effect on homodimer formation
D356K, T366K, L351K	+++
Q347K, S364K	++
L368D, Y407F	++
T366K	++
L351K, S354K, T366K	+++
Y349D, Y407D	++
Y349D, S364K, Y407D	++
Y349D, S364K, S400K, T407D	++

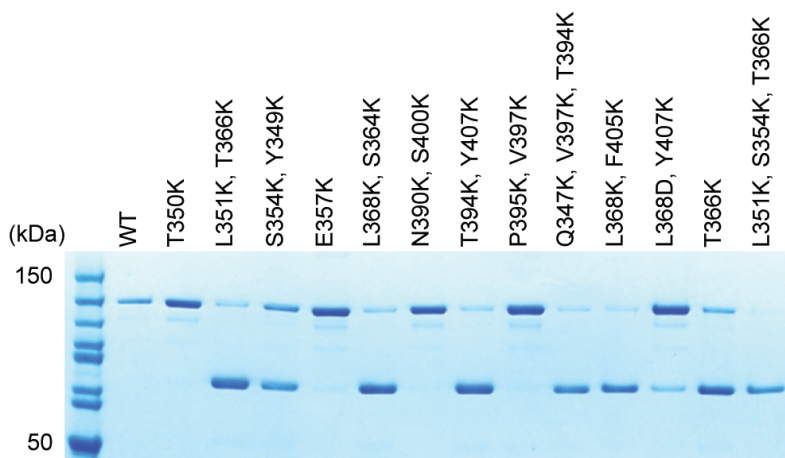


Figure 1. Identification of CH3 residues that block IgG homodimer formation. Constructs contain CH3 substitutions as indicated. Constructs containing CH3 interfaces that allow homodimer formation are visible as bands at 144 kD while interference with dimer formation is demonstrated by the presence of 74 kD bands. WT denotes wild-type IgG₁.

The HADDOCK docking tool and internal analysis were employed to predict the contribution of additional charge interactions across a dimer interface that already contained charged substitutions at positions T366 and L351. HADDOCK scores for the heterodimers (AB) and homodimer combinations (AA and BB) were calculated for each variant pair as listed in Table 3. HADDOCK scores for the charged pair substitutions (AB) ranged from -207.5 to -255.2 while scores for the

Table 2. Overview of nMS results showing relative quantification of homo- and heterodimers and half-IgG molecules for four combinations of modified heavy chains.

The total amount of all bivalent IgG species (heterodimers and homodimers) was set at 100%, while the amount of monovalent species, or half-IgGs, was calculated as a percentage relative to the amount of bivalent IgG species. AA, AB and BB denote dimers resulting from interactions of the A and B chains; A and B denote half-IgG.

Chain A	Chain B	AA	AB	BB	A	B
T366K	L351D	0.0	91.2	8.8	31.2	0.0
L351K	T366D	31.9	55.0	13.2	0.0	0.0
S354K, Y349K	S354D, Y349D	4.0	58.2	37.8	2.5	1.3
T394K	V397D	27.5	57.5	15.0	0.0	1.3

homodimers ranged from -179.5 to -228.4. Variants that had low HADDOCK scores for the Fc heterodimeric (AB) pairs, and those that had large differences between the scores of the heterodimeric (AB) and the homodimeric pairs (AA, BB) were inserted into an expression cassette and expressed. The resulting IgG proteins were analyzed by nMS for the presence of heterodimers (AB), homodimers (AA, BB), and monomers (A, B). The data in Table 3 show that bispecific (AB) antibody levels ranged from 87% to 100%. Varying levels of homodimers and monomers, i.e. half-IgG molecules, were observed in these samples.

The six Fc variant pairs that had the highest levels of bispecific IgG were further characterized by subjecting them to stress conditions and analyzing the aggregation and unfolding of the bispecific IgG molecules. The variants showed very few aggregates, neither before the application of stress, nor after five freeze-thaw cycles, as detected by Nile Red microscopy and 90° light scattering (Table 4). The variants were very stable when subjected to thermal-induced aggregation. The antibodies were incubated for 2 days at 50°C, an aggressive stress which few antibodies are known to survive¹. Indeed, following these stress conditions, we saw aggregation or unfolding of the IgG protein for most of the Fc variant pairs. However, for one variant pair (L351D,L368E/T366K,L351K) the levels of aggregation and unfolding were similar to those detected for natural human IgG₁. The β half-life of this variant pair in mice was also similar to that of native human IgG₁ (Table 4). For this variant pair, which we referred to as DEKK, the CH3 melting temperature was 69.5°C.

DNA encoding the DEKK Fc variant pair was transfected in skewed ratios to study the effect of such skewing on hetero- and homodimer formation. When the

¹ Therapeutic, unpublished data

Table 3. HADDOCK scores and nMS data.

HADDOCK scores are the weighted calculated energy values used to rank the Fc variant pairs, with higher scores indicating lower affinities between the interacting surfaces. In the nMS columns, AA, BB, and AB denote homo- and heterodimers resulting from expression of the Fc variant pairs. A and B denote half-IgGs. The total amount of all bivalent IgG species (heterodimers and homodimers) was set at 100% while the amount of the monovalent species, or half-IgGs, was calculated as a percentage relative to the amount of bivalent IgG species.

A	B	HADDOCK			nMS				
		AB	AA	BB	AA	AB	BB	A	B
WT	WT	-208.2	-208.2	-208.2					
T366K	L351D	-210.6	-191.7	-212.5	0.0	97.2	2.8	0.1	0.0
T366K	L351D, Y349D	-218.7	-191.7	-204.9					
T366K	L351D, Y349E	-215.9	-191.7	-190	1.5	97.7	0.8	4.4	0.3
T366K	L351D, L368D	-220.3	-191.7	-204.3					
T366K	L351D, L368E	-223.3	-191.7	-198.9	0.0	100.0	0.0	13.4	0.0
T366K	L351E, Y349E	-214.5	-191.7	-187.5	2.1	97.9	0.0	12.2	0.0
T366K	L351E, L368E	-214.2	-191.7	-211					
T366K	L351D, Y349E, L368E	-207.5	-191.7	-179.5	1.6	97.7	0.7	4.6	0.0
T366K	L351D, R355D	-213.3	-191.7	-211.9					
T366K	L351D, S354A, R355D	-215.5	-191.7	-209.6					
T366D	L351K, Y349K	-214.9	-198.1	-221.3					
T366D	L351K, L368K	-237.9	-198.1	-228.4	3.0	94.7	2.4	2.4	0.0
T366K, L351K	L351D	-233.2	-205.0	-212.5	0.0	86.9	13.1	11.8	0.8
T366K, L351K	L351E	-227.4	-205	-217.9					
T366K, L351K	L351D, Y349D	-255.2	-205	-204.3	1.1	98.3	0.7	3.8	0.4
T366K, L351K	L351D, Y349E	-227.2	-205	-190	0.4	98.0	1.6	3.8	0.9
T366K, L351K	L351D, L368E	-243.9	-205	-198.9	0.0	100.0	0.0	8.9	0.0
T366K, L351K	L351E, L368E	-228.9	-205	-211					
T366K, L351K	L351D, R355D	-233.6	-205	-211.9	0.0	90.7	9.3	11.4	1.6
T366K, L351K	L351D, Y349D, R355D	-242.8	-205	-183.5	1.1	97.7	1.2	3.3	0.9
T366K, L368K	L351D	-220.9	-220.7	-212.5					
T366E, L351E	L351K	-233.6	-203	-224.4					

levels of DNA encoding the two Fc variant genes were identical, the expression of the bispecific DEKK IgG species was consistently found to be 99% (Figure 2B). Overexpression of one or the other Fc variants resulted in only ~70% of correctly assembled DEKK IgG in the purified IgG samples. Samples resulting from overexpression of the Fc variant containing the L351D,L368E substitutions contained

Table 4. Biophysical analysis following accelerated stress conditions of six Fc variant pairs and wild-type human IgG₁. Combinations of the Fc variant pairs are indicated. Two days at 50°C or five freeze-thaw (5xFT) cycles were used to stress the proteins and compare the result with protein stored at 4°C. The formation of subvisible aggregates was detected by Nile Red fluorescence microscopy, 90° light scatter and 1,8-ANS fluorescence spectroscopy. Melting temperatures of CH3 regions were measured using differential scanning calorimetry (DSC) and the β half-life (β_{HL} in h) was determined in mice. cps is counts per second; * after stress many small particles formed; ** measured in two groups of twelve mice. nd is not determined.

A	B	Stress	Nile Red (particles/ μ l)	90° light scatter ($\times 10^7$ cps)	1,8-ANS fluorescence			β_{HL} (h)	
					1,8-ANS intensity ($\times 10^6$ cps)	λ_{Max} (nm)	Shift (nm) to 4°		
WT	WT	4°C	10–20	1.1	5.1	521	0	82.5	204/421**
		5xFT	30–50	2	5.1	521			
		2d 50°C	10–20	0.7	5.1	521			
T366K	L351D, Y349E	4°C	20–30	1	5.6	515		nd	nd
		5xFT	> 2000*	1.2					
		2d 50°C	> 2000*	0.9	6.2	513	-2		
T366K	L351E, Y349E	4°C	20–30	1	7.5	505		66.6	92
		5xFT	> 2000*	1.2					
		2d 50°C	> 3000*	1	7.5	505	0		
T366K, L351K	L351D, Y349D	4°C	30–50	1	7.0	505		63.4	111
		5xFT	20–30	1.1					
		2d 50°C	150–200	1.1	8.7	499	-6		
T366K, L351K	L351D, Y349E	4°C	20–30	0.9	7.6	506		64.3	128
		5xFT	> 2000*	1.2					
		2d 50°C	30–50	0.9	7.7	502	-4		
T366K, L351K	L351D, L368E	4°C	10–20	0.8	6.2	511		69.5	390
		5xFT	30–50	0.7					
		2d 50°C	10–20	0.7	6.5	508	-3		
T366K, L351K	L351D, Y349D, R355D	4°C	30–50	1	7.5	507		nd	nd
		5xFT	> 2000*	1.4					
		2d 50°C	50–100	1	8.1	500	-7		

up to 25% of the homodimer dubbed DEDE (Figure 2A), while samples resulting from overexpression of the Fc variant containing the T366K,L351K substitutions also contained ‘KK’ half-IgG molecules (Figure 2C).

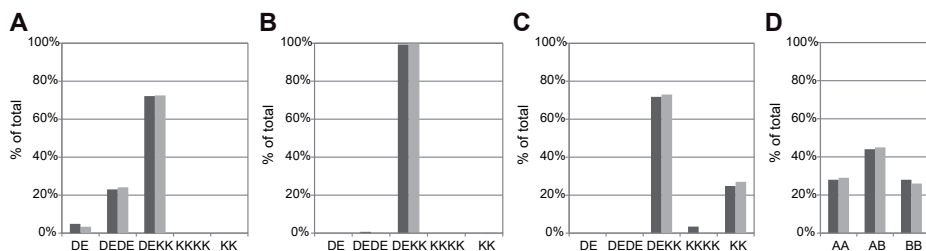


Figure 2. Efficiency of bispecific formation by DEKK. Transient transfections were performed using skewed DNA ratios of two vectors each expressing one arm of the DEKK Fc variant pair, followed by nMS analysis to determine the relative amounts of the IgG species (A-C). As a control, transfections were performed using two different IgG₁ heavy chains containing WT Fc regions (D). Black and gray bars represent duplicate experiments using different VH gene combinations in the context of the DEKK Fc variant pair or WT Fc regions. The VH gene combinations used were MF1337x-MF1122 and MF1337xMF2729. A, DE:KK DNA transfection ratio 5:1; B, DE:KK DNA transfection ratio 1:1; C, DE:KK DNA transfection ratio 1:5. DE indicates L351D,L368E; KK indicates T366K,L351K. DEDE, KKKK, DEKK, DE, KK denote the homo- and heterodimers and ‘half-IgGs’ of the L351D,L368E and T366K,L351K arms. D, WT Fc regions, DNA transfection ratio 1:1. A and B denote heavy chains containing different VH regions. AB indicates bispecific molecules while AA and BB indicate monospecific antibodies.

To obtain detailed structural information of the interactions that promote heterodimer formation, we solved the crystal structures of the DEKK Fc region and of the homodimeric Fc byproduct that had mutations L351D,L368E in both chains (referred to as DEDE). To resolve the asymmetry at the dimerization interface, Fc DEKK was crystallized with the Fc-III peptide (12) bound as recently described by Leaver-Fay *et al.* (13). The crystal structure of DEKK with the Fc-III peptide bound was determined at 2.3-Å resolution and that of DEDE at 2.2-Å resolution. A summary of data collection and refinement statistics is listed in Table 5. We compared these structures with a set of wild-type Fc structures (PDB # 1L6X, 3V7M, 3AVE, 2DTS, 1HZH (14,15,16,17)). The buried surface area (BSA) of the CH3 interface in DEKK was found to be ~2,100 Å², which is in the same range as that of natural IgG structures — measured at 2,100 to 2,400 Å² (as calculated by PISA (18) using the set of wild-type Fc structures with PDB codes mentioned above). The root-mean-square deviation (r.m.s.d.) for the C α -backbone atoms of DEKK compared to Fc wild-type ranged from 0.31 to 0.41 Å when the CH3 domain was superimposed separately, and from 0.45 to 0.88 Å for

the CH2 domain. For whole Fc fragments, the r.m.s.d. increased by 0.64 to 2.50 Å, mostly due to variations in the orientation between CH3 and CH2 domains. For DEDE, the r.m.s.d. for the C α -backbone atoms for superimposed CH3 and CH2 domains ranged from 0.25 to 0.57 Å, while that for the whole molecule ranged from 0.40 to 1.90 Å. The r.m.s.d. for the C α positions between DEKK and DEDE was 0.90 Å for the whole molecule, 0.22 Å for the CH3 domain, and 0.40 Å for the CH2 domain, indicating a difference in the CH3-CH2 hinge region between these two Fc crystal structures.

Figure 3A shows a superposition based on the CH3 domains of Fc DEKK and a wild-type (WT) Fc structure (PDB # 1L6X (14)). In the crystal structure of DEKK, the mutated residues L351K,T366K in chain A and L351D,L368E in chain B are clearly resolved (Figure 3B). K366(A) is engaged in electrostatic interactions with the mutated residues D351(B) and E368(B) from the opposite chain (Figure 3C), as predicted by the HADDOCK model. K351(A), however, is observed to interact with P352(B), S354(B) and E357(B), in contrast to the HADDOCK-predicted interaction of K351(A) with D351(B) (Figure 3E). The C α -backbone has adjusted in the crystal structure to accommodate the mutations, yielding a modified arrangement. The central region of the interface widens in a vertical direction from 12.3 to 14 Å between P353(A) and P353(B), whereas across the interface region the distance between K351(A) and D351(B) is unchanged at 7.0 Å (Figure 3D). The changes are propagated into the helix containing residues 354–359, which shifts by ~1.5 Å, consistent with similar variations previously seen in this helix (13). It should be noted that this conformational variation does not affect the overall orientations and native interactions of the residues on the β -sheets of the CH3 interface core.

Figure 4A shows the superposition of the Fc DEDE and a WT Fc structure (PDB # 1L6X (14)), based on the CH3 domains. In the structure of Fc DEDE, the distance from P353(A) to P353(B) is 13.2 Å, which is in between the values for DEKK and Fc WT. However, the distance from D351(A) to D351(B) between the β -sheets forming the core of the dimerization interface is 7.6 Å, therefore 0.6 Å larger than in DEKK and natural IgG (Figure 4B).

The DEKK design was used to construct and produce a human bispecific IgG₁, named MCLA-128, at industrial scale for clinical use. Bispecific protein was expressed and purified with yields ranging from 1.0 to 1.5 g/l and downstream processing (DSP) yields ranging from 60 to 75%. A cation exchange chromatography (CEX) step was used to remove minor residual homodimer and half-IgG contamination (Figure 5) observed upon expression of MCLA-128 in stable CHO-DG44 BI-HEX[®] cells. Purity of the drug substance was high (> 98.5%).

Accelerated stability studies were used to analyze the formulated MCLA-128 protein. The stability data indicated that DEKK-containing MCLA-128 was

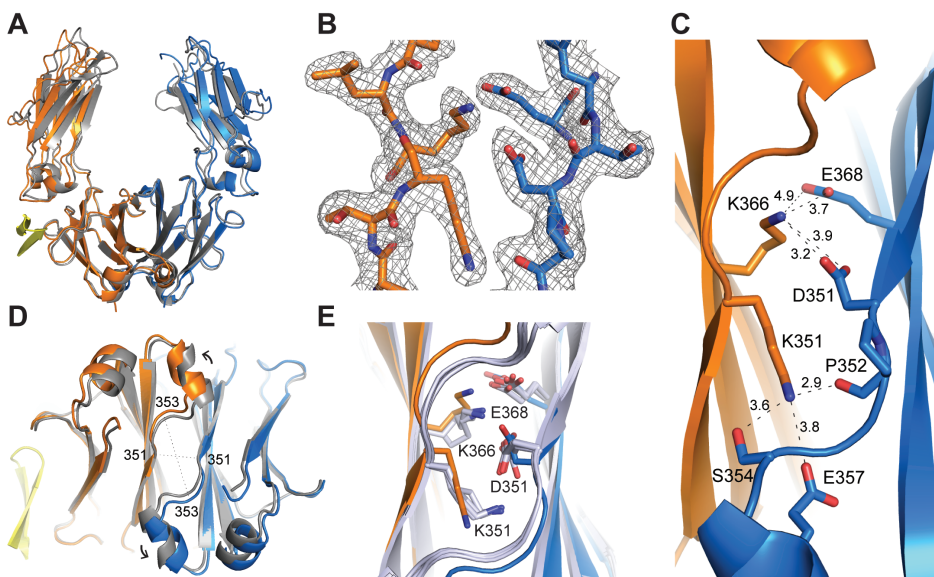


Figure 3. The crystal structure of the Fc region of DEKK at 2.3-Å resolution. A, Structural superposition of the DEKK and WT Fc regions (PDB # 1L6X (14)) based on CH3 domains. DEKK chain A (T366K,L351K) is colored orange, chain B (L351D,L368E) is blue and the Fc-III peptide is yellow; the WT structure is grey. B, Electron density ($2F_{\text{obs}} - F_{\text{calc}}$) at 1σ contour level of DEKK residues in chain A (orange) and in chain B (blue); these residues are annotated in 3C. C, View of the interactions within the CH3 interface of the engineered residues in DEKK (shown as sticks). The dashed lines indicate the distances between interacting atoms in Å. Color scheme as in (A). D, Bottom view of the CH3:CH3 dimerization interface of the superposed structures of the DEKK and WT Fc regions (PDB # 1L6X). The dashed lines measure the distances between residues 351(A)-(B) and 353(A)-(B) in both DEKK and WT as provided in the results section. The arrows indicate the conformational rearrangement of the helix consisting of residues 354–359 in DEKK compared to the same helix in the WT molecule. Color scheme as in (A). E, View of the CH3 interface of DEKK superimposed to the four best models generated by HADDOCK (light blue). Color scheme for DEKK as in (A).

stable for at least 24 months at a storage temperature of 5°C (Table S1 and S2). Initial signs of heterogeneity only started to show up in imaged capillary isoelectric focusing (iCE) after 6 months at 25°C, while the first out-of-specification result was only observed after 12 months of exposure to 25°C.

Discussion

The results of this study demonstrate that we could indeed design an Fc variant pair that enables efficient formation of IgG heterodimers while maintaining the stability of the native Fc region. We also show that this Fc variant pair provides an

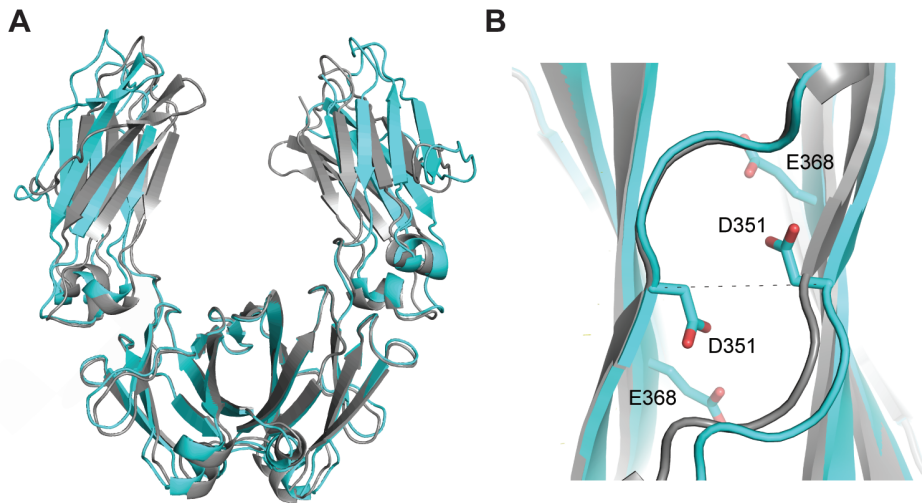


Figure 4. The crystal structure of the Fc region of DEDE at 2.2-Å resolution. A, Structural superposition of DEDE and WT Fc regions (PDB # 1L6X (14)), based on CH3 domains. DEDE is colored cyan; WT is grey. B, Zoomed-in bottom view of the CH3:CH3 dimerization interface of the superposed structures of DEDE and WT Fc regions (PDB # 1L6X), based on chain A. Mutated residues are shown as sticks. The dashed lines indicate the distance between residues 351(A)-(B) as provided in the results section.

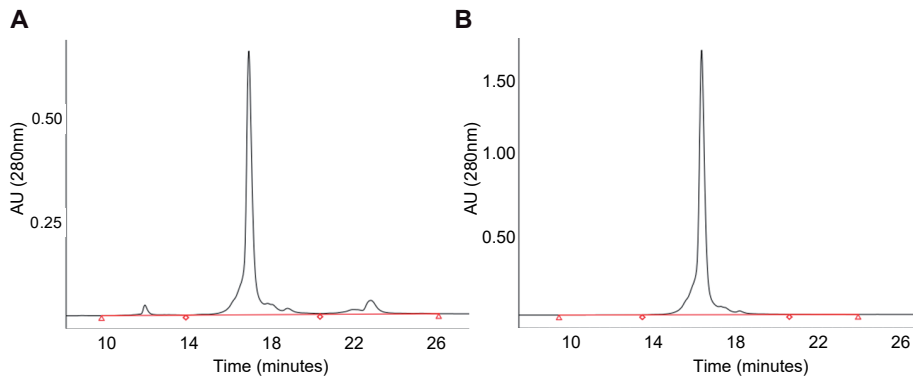


Figure 5. Cation exchange chromatography (CEX) of MCLA-128. CEX was used to remove product-related impurities from a protein A-purified sample of MCLA-128 produced using the DEKK Fc region pair. A, Analytical CEX chromatogram of the preparative CEX column load shows early eluting DEDE homodimers running at around 12 minutes, bispecific antibody MCLA-128 eluting between 14 and 20.5 minutes, and late eluting KK half-IgGs running at around 23 minutes. B, Analytical CEX chromatogram of the preparative CEX column eluate showing only bispecific antibody MCLA-128 demonstrating efficient removal of the DEDE and KK impurities. DEDE denotes the homodimer of the L351D,L368E Fc region variant, and KK denotes half-IgGs of the T366K,L351K Fc region variant.

Table 5. Crystallographic data collection and refinement statistics. Values in parentheses are for reflections in the highest resolution shell.

ASU is asymmetric unit; CC is correlation coefficient; r.m.s.d. is root mean square deviation. Rfree values are calculated based on 5% randomly selected reflections.

Data collection	DEKK	DEDE
Unit cell (Å, °)	a = 60.1 b = 65.4 c = 78.7 $\alpha = 90.0 \beta = 103.2 \gamma = 90.0$	a = 50.0 b = 147.0 c = 76.4 $\alpha = 90.0 \beta = 90.0 \gamma = 90.0$
Space group	P 1 21 1	C 2 2 21
Protein chains per ASU	2	1
Resolution (Å)	76.6–2.3 (2.4–2.3)	31.8–2.2 (2.3–2.2)
R _{merge} (%)	15.4 (53.1)	5.2 (25.0)
Completeness (%)	98.7 (95.4)	99.2 (98.4)
Total no. of reflections	74,091 (7,287)	48,553 (4,163)
No. unique reflections	26,379 (2,646)	14,188 (1,378)
Multiplicity	2.8 (2.9)	3.4 (3.3)
Mean I/σ(I)	3.6 (1.7)	15.9 (4.5)
CC _{1/2} (%)	97.2 (56.5)	99.8 (91.6)
Refinement		
R _{work} /R _{free} (%)	22.5/26.5	19.8/24.3
r.m.s.d. bonds (Å)	0.003	0.006
r.m.s.d. angles (°)	0.73	0.83
Mean B-factor (Å ²)	44.6 (27.6–77.9)	45.3 (13.0–119.9)
Ramachandran favoured (%)	99.3	99.0
Ramachandran outliers (%)	0	0
Rotamer outliers (%)	0	0
Protein Data Bank code	5NSC	5NSG

efficient platform for the generation of therapeutic bispecific antibodies in a human IgG₁ format. In the current study, experiments using charge introduction at the CH3 interface resulted in selecting residues L351 and T366 as candidates for further engineering; introduction of a positive charge at these positions resulted in impaired homodimerization of the IgG heavy chains. Furthermore, expression of an Fc variant pair consisting of substitutions L351D in one half of the CH3 interface and T366K in the other resulted in bispecific IgG levels in excess of 90%. Computational analysis was used to further engineer the CH3 domains. The DEKK Fc variant pair was designed to introduce novel electrostatic interactions at the core of the heterodimeric CH3 interface such that homodimer-favoring interactions are replaced by asymmetric ones.

The CH3 interface of the natural IgG Fc region is composed of a conserved hydrophobic core with charged residues at the rim of the interface. The crystal structure of DEKK confirms that K366 in chain A is engaged in electrostatic interactions with residues D351(B) and E368(B) engineered in the opposite chain (Figure 3C). Residue K351(A) is however involved in interactions that were not anticipated. Instead of interacting with D351(B) as predicted by the HADDOCK model, K351(A) adopts a different conformation and forms electrostatic interactions with P352(B), S354(B) and E357(B) (Figure 3E). This conformation likely causes a rearrangement of the C α -backbone that is accommodated by a shift of the helix at residues 354 to 359 (Figure 3D), a region of the protein also shown to have the greatest variability in previous heterodimeric Fc crystal structures (13). This movement allows the native contacts at the core of the CH3 interface to remain largely intact, which together with the novel interactions introduced in the DEKK Fc region may account for the stability of this molecule.

Structural analysis of the homodimer DEDE showed a widening in the distance between the β -sheets forming the interface core (Figure 4B). This observation correlates with the charge repulsion of the four negative charges introduced in the CH3 region and is in line with the experimental observation that DEDE homodimers are only present after overexpression of the L351D,L368E heavy chains. In contrast, homodimers containing Fc region substitutions L351K,T366K in both heavy chains are virtually absent after overexpression of this variant, and the resulting proteins are primarily present as half-IgGs (Figure 2C). Given the DEKK structure presented here, we hypothesize that the introduction of four lysines at the dimerization interface would cause substantial destabilization due to the long side chains causing both charge repulsion and steric hindrance. In contrast to transient productions that yield almost pure bispecific IgG (Figure 2), the stable CHO-DG44 BI-HEX[®] cells expressing MCLA-128 produce both the KK and DEDE molecules in minor amounts (Figure 5), which may result from suboptimal protein assembly in these cells (19). This figure also shows that these product-related impurities can be efficiently removed in the CEX polishing step that is routinely used in the purification of therapeutic IgGs.

DEKK was selected from a panel of variants tested for optimal performance under stress conditions. When subjected to conditions that are likely to induce unfolding and precipitation (freeze-thaw cycles, incubation at 50°C), and pharmacokinetic evaluation in mice, the behavior of the DEKK variant was found to be similar to that of natural IgG. Despite this similarity in terms of stability, the CH3 melting temperature of DEKK was only 69.5°C, which is lower than that reported for other Fc-engineered bispecific antibodies. For example, the CH3 melting temperature of ZW1 and EW-RVT -based antibodies is ~80°C, close to that of natural IgG. The

contribution of CH3 melting temperature to the overall stability of therapeutic IgGs is therefore not clear. We have used the DEKK substitutions to produce and purify the MCLA-128 bispecific antibody under GMP manufacturing conditions in Boehringer Ingelheim's CHO-DG44 BI-HEX[®] platform, resulting in gram/l fermentation yields. Standard IgG procedures were used to purify the protein. Purified bispecific IgG was formulated and subjected to long-term stability studies. These studies revealed the DEKK-containing MCLA-128 molecule to be highly stable. Only upon long-term exposure to 25°C significant heterogeneity of the MCLA-128 protein could be observed, ultimately resulting in diminished binding to one of the target antigens after 12 months. However, as still only very minimal IgG fragmentation could be observed by size exclusion chromatography at this time point (3%), this heterogeneity most likely reflects changes in the HER3 Fab domain only, and not the DEKK-containing Fc region of MCLA-128.

In summary, we provide an efficient platform for the generation of therapeutic bispecific antibodies in a human IgG₁ format.

Experimental Procedures

Several Fab regions were used in these studies. These Fabs were selected based on similar expression levels, proven stability and for differences in molecular mass to facilitate the nMS analyses. All residues at the homodimerization interface within the IgG₁ CH3 region as described in (11) were designed to individually or group-wise express a lysine (K, positive charge), or an aspartic acid (D, negative charge), see Table 1; Eu (20) numbering of residues was used throughout. A full-length cLC human IgG₁ specific for tetanus-toxoid (Fab MF1337 (3)) in expression vector MV1057 (21) was used to produce the proteins. The constructs were prepared at GeneArt (Regensburg, Germany) and transiently expressed in HEK293T cells. IgGs were quantified using Fortébio Octet technology and analyzed on a non-reducing SDS-PAGE gel, followed by Western blotting. Substitutions that impaired homodimer formation were identified by the presence of protein bands at ~74 kDa, corresponding to non-dimerized HC-LC complexes (half-IgG molecules).

This experiment revealed substitutions that impaired homodimer (AA) formation. We used published data (9,10,11) to identify residues in contact with these CH3 interface residues, and then designed and constructed charge pairs (AB) that were introduced into vector MV1057 as described above (see also Table 2). In this experiment we also included a cLC Fab (Fab MF1025) directed against thyroglobulin. Expression was as described above, except that the expression vectors containing the designed CH3 regions and directed against tetanus-toxoid

and thyroglobulin were mixed in a one-to-one ratio (each individual plasmid contained a cLC expression cassette). IgGs were purified using the small-scale purification procedure described below. Native mass spectrometry was used to detect the presence of homo- and heterodimers (AA, BB and AB), and half-IgG molecules (A and B), based on the molecular mass difference of the VH regions of MF1337 (13,703 Da) and MF1025 (12,472 Da). The data (Table 2) showed that one pair (T366K/L351D) resulted in high levels of bispecific antibody formation with low levels of contaminating homodimers.

The HADDOCK docking tool (7,8) and internal analysis were used to evaluate the effect of the proposed design changes *in silico* on the interaction between the CH3 domains of the bispecific IgG. As a structural model, we used a high-resolution crystal structure of the CH3 part of the IgG (PDB # 1L6X (14)). Design choices were introduced into this structure and evaluated using HADDOCK. The refined models were ranked according to the HADDOCK score, which is a weighted average of van der Waals energy, electrostatic energy, buried surface area, and desolvation energy. This HADDOCK score can be interpreted as an indication of affinity. HADDOCK refinement runs were performed for each designed variant pair, while assuming a rigid protein backbone and flexible amino acid residue side chains. HADDOCK scores were calculated for bispecific variant pairs (AB) as well as for homodimers (AA and BB). Preferred variants were selected based on low HADDOCK scores for the bispecific variants and high scores for the homodimer combinations (see Table 3), indicative of high and low affinities within the CH3 domain. HADDOCK-generated models were visualized using YASARA software (www.yasara.org), and analyzed to gain further insight into the results, and to guide design choices within the CH3 interface. The T366 and L351 residues were thus examined *in silico* by employing charged residues lysine, arginine, aspartic acid, and glutamic acid, and the HADDOCK scores for all resulting heterodimer and homodimer combinations calculated. Additional design changes were analyzed at positions Y349, S354, R355, and L368, with the aim of introducing complementary charge interactions across the heterodimer interface. This resulted in a set of 11 variant pairs for which HADDOCK predicted stable heterodimer formation in the absence of homodimer contamination.

These 11 variant Fc pairs were constructed, expressed, and purified according to the medium-scale purification procedure described below. The purified samples were analyzed in nMS to establish levels of heterodimers (AB), homodimers (AA, BB) and monomers (A, B) (Table 3).

Six Fc variant pairs with optimal heterodimer/homodimer ratios were expressed and purified using the medium-scale purification procedure described below. Samples were then subjected to stress conditions, and assayed as described below

(listed in Table 4). Differential scanning calorimetry (DSC) was used to measure the melting temperatures of the CH3 regions (full-length IgG and Fc-hinge proteins) and a pharmacokinetics evaluation in mice was used to estimate overall stability of the molecules. The results of these assays identified the Fc variant pair DEKK as the most promising platform for production of bispecific IgG.

To study the efficiency of heterodimer formation by the Fc variant pair DEKK, transient transfections were performed using skewed DNA ratios of the two vectors expressing each arm of the Fc variant pair (5:1 to 1:5). This was followed by purification using the medium-scale procedure described below, and nMS analysis to determine the relative amounts of the IgG species. This experiment was performed in duplicate using different combinations of VH genes in the context of the DEKK Fc variant pair (Figure 2). The different VH gene combinations used were MF1337xMF1122 and MF1337xMF2729 specific for tetanus-toxoid, fibrinogen and RSV-F protein respectively.

IgG expression constructs

Full-length cLC IgG₁ was prepared using MV1057-based expression vectors (21) modified with the design choices as described. Proteins containing only the IgG₁ hinge and Fc regions were used for crystallography and DSC experiments. These Fc-hinge proteins were produced using a truncated variant of MV1057 that has amino acid E216 as the first residue.

Protein production

Proteins were produced in HEK293T cells using FugeneHD transfection reagent according to the manufacturer's protocols or in Freestyle™ 293-F cells (Invitrogen) using polyethelenimine (PEI) with a PEI:DNA mass ratio of 2.5:1. Bispecific IgGs were transfected using a 1:1 DNA mass ratio unless stated otherwise.

IgG purification

Cell supernatants were purified at different scales. Small-scale protein A purification of IgGs was performed using PhyNexus tips according to the manufacturer's protocols, followed by neutralization of the acidic elution fraction using Tris. Medium-scale purification was performed using an ÄKTA Explorer 100 (GE Healthcare) equipped with HiTrap MabSelect Sure columns and HiTrap Desalting columns. After acidic elution from the MabSelect Sure columns, the proteins were directly desalted to PBS pH 7.4. Purification of Fc-hinge proteins for crystallography studies was carried out using batchwise incubation with MabSelectSure LX medium, followed by neutralization using Tris. In a next step, the proteins

were gel filtrated using a Superdex75 16/600 column (GE Healthcare) and concentrated using Vivaspin columns (Sartorius).

IgG quantification

IgGs (small-scale productions) were quantified using Fortébio Octet technology using Protein A sensors and human IgG (Sigma) was used for a standard curve. Medium and large-scale produced IgG were quantified by OD280 absorption.

SDS-PAGE/PageBlue staining

1–2 µg of protein was loaded on a NuPage 4–12% bis-tris gel (Invitrogen) in the presence or absence of reducing agent (Invitrogen). A protein marker was included on each gel. After running at 100–200V, the gel was stained using PageBlue protein staining solution (Fermentas) and subsequently destained using milliQ water.

SDS-PAGE/Western Blot

0.1–1 µg of protein was loaded on a NuPage 4–12% bis-tris gel (Invitrogen) in the presence or absence of reducing agent (Invitrogen). A pre-stained protein marker was included on each gel. After running at 100–200V, the gel was transferred to nitrocellulose and visualized using peroxidase-labeled anti-human Fc antibody followed by enhanced chemiluminescence (ECL) detection.

Differential scanning calorimetry (DSC)

DSC was used to measure the thermostability of the domains of the IgG described here. DSC experiments were performed on a MicroCal VP-DSC using Origin v7.0 (VPViewer and VPAnalyzer) software. The purified antibodies or Fc-hinge fragments were first dialyzed against a 10 mM phosphate, 150 mM NaCl buffer at pH 6.5. The samples were analyzed at a protein concentration of 0.25 mg/ml as determined by UV absorption. Scans ran from 50 to 95 °C with a scan rate of 1 °C/min, and were analyzed using GraphPad Prism 5.

Native mass spectrometry (nMS)

For nMS the IgGs were deglycosylated in order to create a single product with a distinct mass suitable for mass spectrometric analysis. 1 unit of N-glycosidase F (PNGase F; Roche Diagnostics, Mannheim, Germany) was incubated per 10 µg of IgG₁, overnight at 37°C in 0.1 M citrate buffer pH 3.0 / 1.0 M Tris-HCl pH 8.0. Buffer exchange using 10 kDa MWCO centrifugal filter columns (Millipore) was performed to remove glycan chains and change the buffer to 150 mM ammonium acetate pH 7.5. 3 µl of a 1 µM concentration of IgG were loaded

into gold-plated borosilicate capillaries made in house (using a Sutter *P*-97 puller [Sutter Instruments Co., Novato, CA, USA] and an Edwards Scancoat six sputter-coater [Edwards Laboratories, Milpitas, CA, USA]) for analysis on an LCT 1 mass spectrometer (Waters Corp., Milford, MA, USA), adjusted for optimal performance in high mass detection. A capillary voltage of 1,300 V was used and sampling cone voltage was 200 V. The source backing pressure was elevated in order to promote collisional cooling to approximately 7.5 mbar. Processing of the acquired spectra was performed using MassLynx 4.1 software (Waters Corp., Milford, MA, USA). Minimal smoothing was used, after which the spectra were centered. The mass of the species was calculated using each charge state in a series. The corresponding intensities of each charge state were assigned by MassLynx and summed. All analyses were repeated three times to calculate means. This approach allowed the relative quantification of all species in a sample. Note that the total amount of bivalent IgG species was set at 100% to allow a direct comparison between these molecules, while the amounts of the monovalent species, or half-IgGs, were calculated as a percentage relative to the bivalent molecules.

Fluorescence microscopy with Nile Red staining

Nile Red is an uncharged small (Mw 318.37 Da) molecular weight hydrophobic fluorescence probe that allows detection of very low levels of protein aggregates (22). The IgG samples were diluted to 0.2 mg/ml and filtered using 0.22 μ m PVDF sterile filters before applying the stress conditions. 0.2 μ l of 100 μ M Nile Red in ethanol was added to 10 μ l of the IgG samples just prior to measurements. The samples were introduced in a FastRead 102™ slide (Immune Systems, U.K.) and analyzed by counting particles in fluorescence microscopy using a Leica DM RXE microscope (Leica Microsystems GmbH, Wetzlar, Germany) equipped with a mercury lamp and a bandpass filter cube Leica N2.1 513 812 with an excitation filter BP515–560 nm (green light) and suppression filter LP 590 nm for specific excitation of Nile Red. The FastRead 102 slides display a square grid with a mesh size of 250 μ m. Particles were counted in 16 squares which correspond to 1 mm \times 1 mm and 0.1 μ l volume. The total number of particles was multiplied by ten to obtain the number of particles per microliter.

90° light-scatter spectroscopy

90° light-scattering spectra of IgG solutions are known to be very sensitive to small amounts of antibody aggregates in solutions (23). 90° light-scattering spectra of IgG solutions were measured using a FluoroMax-1 Spectrofluorometer (Horiba Scientific, U.K.) between 400 and 750 nm with excitation and emission monochromators moving synchronously. The IgG samples were diluted to 0.2 mg/ml, and filtered using 0.22 μ m PVDF sterile filters before applying the stress

conditions. 150 μ l of sample were added to a 1 cm x 2 mm black cuvette (Hellma 105–250-QS). The aggregation state of the IgG in the samples was determined by monitoring light scattering at 400 nm after subtraction of the background. The light-scattering intensity was expressed as count per seconds (cps).

1,8-ANS fluorescence spectroscopy

1-anilinonaphthalene-8-sulfonic acid (1,8-ANS) is an uncharged small (Mw 299.34 Da) hydrophobic fluorescent probe that is a sensitive indicator of protein folding and conformational changes, as well an indicator of antibody aggregation (24). The IgG samples were diluted to 0.2 mg/ml and filtered using 0.22 μ m PVDF sterile filters before applying the stress conditions. 150 μ l of sample were added to a 1 cm x 2 mm black cuvette (Hellma 105–250-QS); and 3.0 μ l of 2.5 mM 1,8-ANS in water were added on top (final concentration: 50 μ M 1,8-ANS). The sample was measured immediately after addition of 1,8-ANS. 1,8-ANS fluorescence emission was measured after excitation at 370 nm on a FluoroMax-1 Spectrofluorometer (Horiba Scientific, U.K.). The changes in 1,8-ANS fluorescence intensity and emission wavelength due to stress were determined.

X-ray crystallography

Prior to crystallization, the Fc-hinge construct of the DE Fc variant was modified to optimize asymmetric assembly of the DEKK Fc region into the crystal lattice. As described previously by Leaver-Fay *et al.* (13), this construct was mutated at positions M252E, I253A, and H435A to prevent binding of the DE chain to the Fc-III peptide (12) (DCAWHLGELVWCT, disulfide oxidized, ProteoGenix). The mutated DE construct and the Fc-hinge construct expressing the KK Fc region were expressed in 293FF cells in a one-to-one ratio, and purified according to the large-scale purification procedure described above. Purified Fc DEKK in 25 mM Tris pH 7.5 and 150 mM NaCl at a concentration of 12.3 mg/ml was mixed with 1 mM Fc-III peptide (13) dissolved in the same buffer. Protein of the DEDE homodimeric Fc variant was prepared by transfecting the Fc-hinge construct containing the DE design into 293FF cells followed by purification according to the large-scale purification procedure described above. The resulting protein was concentrated to 10 mg/ml in 25 mM Tris pH 7.5 and 150 mM NaCl. For initial crystallization trials, the protein solutions were screened using the vapor diffusion method in 96-well format plates (Corning) using commercially available screens: JCSG core suite (Qiagen), PEG/Ion (Hampton Research), and Wizard (Emerald BioSystems). The initial setup combined 0.15 μ l of protein with 0.15 μ l of mother liquor solution using a Phoenix robot (Art Robbins Instrument). Crystals appeared after two to three days in many conditions. Optimization screens were prepared in hanging-drop plates by varying concentration of precipitant solu-

tions and protein-mother liquor ratios at 18°C and 4°C. The best crystals for DEKK/Fc-III peptide were grown in 0.2 M sodium fluoride and 20% w/v PEG 3350, while the best crystals for DEDE were grown in acetate buffer pH 4.5, 0.2 M zinc acetate and 16% w/v PEG 3000. A protein:precipitant ratio of 1:1 and a temperature of 18°C was used in both cases. Crystals were transferred to a cryo-protectant solution containing mother liquor and 20% v/v glycerol prior to shock-cooling in liquid nitrogen. Diffraction data were collected at the European Synchrotron Research Facility (ESRF) at ID29 beamline for DEKK and at ID23–2 beamline for DEDE. Diffraction data were processed using IMOSLM (25) and AIMLESS (26) software. Structures were solved by molecular replacement in PHASER MR (27) software, using the published heterodimeric Fc complex with the Fc-III peptide (PDB # 5DK0 (13)) as a search model for DEKK, and an Fc wild-type structure (PDB # 4CDH (28)) for DEDE. The resulting solutions were refined using PHENIX (29) software, and model building was carried out using COOT (30) software. The structure figures were generated using PYMOL (<http://pymol.org>).

Pharmacokinetics

Pharmacokinetic characteristics of the bispecific IgGs were analyzed in non-target antigen-bearing female Balb/c mice of ~7 weeks of age after a single intravenous injection. Groups of 12 mice were dosed at 1 mg/kg; each group consisted of three subgroups of 4 mice and from each mouse 6 time points were sampled. Blood samples were collected pre-dose and 0.25, 1, 2, 4, 8, 24, 48, 96, 168, 268, and 336 hours after dosing. IgG levels in sera were established by ELISA (ZeptoMetrics, NY). Data were analyzed using SpectraMax software to establish C_{\max} ($\mu\text{g/ml}$), and α - and β -half-life (h).

Large scale fermentation and purification

MCLA-128 was produced at Boehringer Ingelheim Biopharmaceuticals (Biberach a.d. Riss, Germany) using their BI-HEX[®] mammalian IgG expression platform. MCLA-128 was expressed in Chinese Hamster Ovary (CHO) DG44 cells stably co-expressing the cLC, the different heavy chains, and the RMD enzyme (GDP-6-deoxy-D-lyxo-4-hexulose reductase), thereby yielding antibodies with a low level of fucose on their CH2-region-associated glycan structures. MCLA-128 drug substance was produced in a 2,000 l stainless steel bioreactor using a 14-day fed-batch process. The MCLA-128 protein was purified using a standard IgG manufacturing process involving protein A capture chromatography, a low-pH hold step for virus inactivation, anion exchange chromatography in flow through mode, and cation exchange chromatography (CEX). This last chromatography step was used to remove minor residual homodimer and half-IgG contamination. After a 20-nm virus filtration step,

MCLA-128 was concentrated and formulated at 20 mg/ml following ultrafiltration/diafiltration and addition of the final excipients. MCLA-128 drug product was filled in 6R type I glass vials at 20 mg/ml at a nominal fill volume of 5 ml.

Stability

To determine the shelf life of the MCLA-128 drug product, stability studies were performed according to the International Conference on Harmonization guidelines. Stability was analyzed at the proposed long-term storage temperature ($5^{\circ}\text{C} \pm 3^{\circ}\text{C}$) and under accelerated conditions ($25^{\circ}\text{C} \pm 2^{\circ}\text{C}$). The analytical procedures used are listed in Tables S1 and S2.

Acknowledgements

We are grateful to the European Synchrotron Radiation Facility (ESRF) for the provision of synchrotron radiation facilities, and to beamline scientists at the ESRF and the European Molecular Biology Laboratory for assistance. We thank Tim de Klijn for the useful discussions. Financial support was provided by the BioStruct-X (grant no. 283570) embedded in the European Union's Seventh Framework Programme (FP7/2007–2013).

Author contributions

CDN performed the crystallography experiments. LJAH performed cloning, HADDOCK modeling, and biophysical assays. EP conducted the stability assays. All three contributed to writing the paper. TA, PG, AB, and JdK were responsible for design of experiments, interpretation of results, and writing of the paper.

Accession numbers

The atomic coordinates and structures have been deposited in the Protein Data Bank (<http://www.pdb.org>) with PDB ID 5NSC and 5NSG.

References

1. Beck, A., Wurch, T., Bailly, C., and Corvaia, N. (2010) Strategies and challenges for the next generation of therapeutic antibodies. *Nat Rev Immunol.* **10**, 345–352
2. Kontermann, R. (2012) Dual targeting strategies with bispecific antibodies. *MABs.* **4**, 182–197
3. de Kruijf, J., Kramer, A., Visser, T., Clements, C., Nijhuis, R., Cox, F., van der Zande, V., Smit, R., Pinto, D., Throsby, M., and Logtenberg, T. (2009) Human immunoglobulin repertoires against tetanus toxoid contain a large and diverse fraction of high-affinity promiscuous VH genes. *J. Mol. Biol.* **387**, 548–558
4. Ha, J.-H., Kim, J.-E., and Kim, Y.-S. (2016) Immunoglobulin Fc heterodimer platform technology: from design to applications in therapeutic antibodies and proteins. *Front. Immunol.* **7**, 1–16
5. Spiess, C., Merchant, M., Huang, A., Zheng, Z., Yang, N.-Y. Y., Peng, J., Ellerman, D., Shatz, W., Reilly, D., Yansura, D. G., and Scheer, J. M. (2013) Bispecific antibodies with natural architecture produced by co-culture of bacteria expressing two distinct half-antibodies. *Nat. Biotechnol.* **31**, 753–758
6. Smith, E. J., Olson, K., Haber, L. J., Varghese, B., Duramad, P., Tustian, A. D., Oyejide, A., Kirshner, J. R., Canova, L., Menon, J., Principio, J., MacDonald, D., Kantrowitz, J., Papadopoulos, N., Stahl, N., Yancopoulos, G. D., Thurston, G., and Davis, S. (2015) A novel, native-format bispecific antibody triggering T-cell killing of B-cells is robustly active in mouse tumor models and cynomolgus monkeys. *Sci. Rep.* **5**, 17943
7. Dominguez, C., Boelens, R., and Bonvin, A. M. J. J. (2003) HADDOCK: a protein–protein docking approach based on biochemical or biophysical information. *J. Am. Chem. Soc.* **125**, 1731–1737
8. van Zundert, G. C. P., Rodrigues, J. P. G. L. M., Trellet, M., Schmitz, C., Kastiris, P. L., Karaca, E., Melquiond, A. S. J., van Dijk, M., de Vries, S. J., and Bonvin, A. M. J. J. (2016) The HADDOCK2.2 web server: user-friendly integrative modeling of biomolecular complexes. *J. Mol. Biol.* **428**, 720–725
9. Miller, S. (1990) Protein-protein recognition and the association of immunoglobulin constant domains. *J Mol Biol.* **216**, 965–973
10. Deisenhofer, J. (1981) Crystallographic refinement and atomic models of a human Fc fragment and its complex with fragment B of protein A from *Staphylococcus aureus* at 2.9- and 2.8-Å resolution. *Biochemistry.* **20**, 2361–2370
11. Gunasekaran, K., Pentony, M., Shen, M., Garrett, L., Forte, C., Woodward, A., Bin Ng, S., Born, T., Retter, M., Manchulenko, K., Sweet, H., Foltz, I. N., Wittekind, M., and Yan, W. (2010) Enhancing antibody Fc heterodimer formation through electrostatic steering effects: applications to bispecific molecules and monovalent IgG. *J Biol Chem.* **285**, 19637–19646
12. DeLano, W. L., Ultsch, M. H., de Vos, A. M., and Wells, J. A. (2000) Convergent solutions to binding at a protein-protein interface. *Science.* **287**, 1279–1283
13. Leaver-Fay, A., Froning, K. J., Atwell, S., Aldaz, H., Pustilnik, A., Lu, F., Huang, F., Yuan, R., Hassanal, S., Chamberlain, A. K., Fitchett, J. R., Demarest, S. J., and Kuhlman, B. (2016) Computationally designed bispecific antibodies using negative state repertoires. *Structure.* **24**, 641–651
14. Idusogie, E. E., Presta, L. G., Gazzano-Santoro, H., Totpal, K., Wong, P. Y., Ultsch, M., Meng, Y. G., and Mulkerrin, M. G. (2000) Mapping of the C1q binding site on rituxan, a chimeric antibody with a human IgG1 Fc. *J. Immunol.* **164**, 4178–4184
15. Sibéris, S., Ménez, R., Jorieux, S., de Romeuf, C., Bourel, D., Fridman, W. H., Ducancel, F., Stura, E. A., and Teillaud, J. L. (2012) Effect of zinc on human IgG1 and its FcγR interactions. *Immunol. Lett.* **143**, 60–69

16. Matsumiya, S., Yamaguchi, Y., Saito, J., Nagano, M., Sasakawa, H., Otaki, S., Satoh, M., Shitara, K., and Kato, K. (2007) Structural comparison of fucosylated and nonfucosylated Fc fragments of human immunoglobulin G1. *J. Mol. Biol.* **368**, 767–779
17. Saphire, E. O., Parren, P. W., Pantophlet, R., Zwick, M. B., Morris, G. M., Rudd, P. M., Dwek, R. A., Stanfield, R. L., Burton, D. R., and Wilson, I. A. (2001) Crystal structure of a neutralizing human IGG against HIV-1: a template for vaccine design. *Science* **293**, 1155–1159
18. Krissinel, E., and Henrick, K. (2007) Inference of macromolecular assemblies from crystalline state. *J. Mol. Biol.* **372**, 774–797
19. Mason, M., Sweeney, B., Cain, K., Stevens, P., and Sharfstein, S. T. (2012) Identifying bottlenecks in transient and stable production of recombinant monoclonal-antibody sequence variants in Chinese hamster ovary cells. *Biotechnol Prog.* **28**, 846–855
20. Kabat, E. A., Wu, T. T., Perry, H. M., Gottesman, K. S., and Foeller, C. (1991) Sequences of proteins of immunological interest. U.S. Public Health Service, National Institutes of Health, Bethesda, 5th Ed
21. De Kruif, J., Kramer, A., Nijhuis, R., Van Der Zande, V., Den Blanken, R., Clements, C., Visser, T., Keehnen, R., Den Hartog, M., Throsby, M., and Logtenberg, T. (2010) Generation of stable cell clones expressing mixtures of human antibodies. *Biotechnol Bioeng.* **106**, 741–750
22. Demeule, B., Gurny, R., and Arvinte, T. (2007) Detection and characterization of protein aggregates by fluorescence microscopy. *Int. J. Pharm.* **329**, 37–45
23. Demeule, B., Lawrence, M. J., Drake, A. F., Gurny, R., and Arvinte, T. (2007) Characterization of protein aggregation: The case of a therapeutic immunoglobulin. *Biochim. Biophys. Acta - Proteins Proteomics.* **1774**, 146–153
24. Demeule, B., Palais, C., Machaidze, G., Gurny, R., and Arvinte, T. (2009) New methods allowing the detection of protein aggregates. *MAbs.* **1**, 142–150
25. Battye, T. G., Kontogiannis, L., Johnson, O., Powell, H. R., and Leslie, A. G. (2011) iMOSFLM: a new graphical interface for diffraction-image processing with MOSFLM. *Acta Crystallogr. D Biol. Crystallogr.* **67**, 271–281
26. Evans, P. R. (2011) An introduction to data reduction: Space-group determination, scaling and intensity statistics. *Acta Crystallogr. Sect. D Biol. Crystallogr.* **67**, 282–292
27. McCoy, A. J., Grosse-Kunstleve, R. W., Adams, P. D., Winn, M. D., Storoni, L. C., and Read, R. J. (2007) Phaser crystallographic software. *J. Appl. Cryst.* **40**, 658–674
28. Silva-Martín, N., Bartual, S. G., Ramírez-Aportela, E., Chacón, P., Park, C. G., and Hermoso, J. A. (2014) Structural basis for selective recognition of endogenous and microbial polysaccharides by macrophage receptor SIGN-R1. *Structure.* **22**, 1595–1606
29. Adams, P. D., Afonine, P. V., Bunkóczy, G., Chen, V. B., Davis, I. W., Echols, N., Headd, J. J., Hung, L. W., Kapral, G. J., Grosse-Kunstleve, R. W., McCoy, A. J., Moriarty, N. W., Oeffner, R., Read, R. J., Richardson, D. C., Richardson, J. S., Terwilliger, T. C., and Zwart, P. H. (2010) PHENIX: A comprehensive Python-based system for macromolecular structure solution. *Acta Crystallogr. Sect. D Biol. Crystallogr.* **66**, 213–221
30. Emsley, P., Lohkamp, B., Scott, W. G., and Cowtan, K. (2010) Features and development of Coot. *Acta Crystallogr. Sect. D Biol. Crystallogr.* **66**, 486–501

Supplementary Tables

Table S1. Stability data for MCLA-128 at 5°C ± 3°C.

Lot E4775F03		0 months	1 month
Test	Acceptance criteria		
Appearance and Description			
Visible particles		Free from visible particles	Free from visible particles
General Tests			
pH	5.5–6.5	6.0	6.0
Osmolality (mOsm/kg)	270–330	288	287
Particulate contamination – sub-visible particles	≥ 10 µm: ≤ 6,000 particles/container ≥ 25 µm: ≤ 600 particles/container	≥ 10 µm: 123 ≥ 25 µm: 0	≥ 10 µm: 3 ≥ 25 µm: 0
Heterogeneity			
Imaged Capillary Isoelectric Focusing (iCE)	Report result %: Acid peak (APG) Main peak (MP) Basic peak (BPG)	APG: 27.7% MP: 71.6% BPG: 0.7%	APG: 25.8% MP: 73.7% BPG: 0.5%
Purity			
UP-Size exclusion chromatography (UP-SEC)	Monomer (M) ≥ 95.0% Report results in %: Aggregates (A), Fragments (F)	M: 99.2% A: 0.2% F: 0.6%	M: 98.9% A: 0.2% F: 0.8%
Capillary gel electrophoresis (CGE) – reduced	Sum of heavy and light chain ≥ 90.0%	98.2%	98.5%
Capillary gel electrophoresis (CGE) – non-reduced	Main peak ≥ 90.0%	97.6%	97.5%
Biological Activity			
Binding assay HER2, HER3, CD16 (Biacore)	HER2: 80–120% of development standard HER3: 80–120% of development standard CD16: 80–120% of development standard	HER2: 101% HER3: 100% CD16: 101%	HER2: 101% HER3: 100% CD16: 101%
Quantity			
Protein concentration by UV Scan (mg/mL)	18.0–22.0	19.6	19.7
Microbiological Purity			
Sterility**	No growth	Pass	n.a.

¹ < 1.8% = < LOQ for BPG

** Only assessed at 12 and 24-month time points.

n.a. = not applicable

2 months	3 months	6 months	9 months	12 months	18 months	24 months
Appearance and Description						
Free from visible particles	Free from visible particles	Free from visible particles	Free from visible particles	Free from visible particles	Free from visible particles	Free from visible particles
General Tests						
6.0	5.9	5.9	6.0	6.0	6.0	6.0
285	288	288	287	287	287	290
≥ 10 μm: 27	≥ 10 μm: 10	≥ 10 μm: 33 ≥ 25 μm: 0	≥ 10 μm: 10 ≥ 25 μm: 0	≥ 10 μm: 7 ≥ 25 μm: 0	≥ 10 μm: 13 ≥ 25 μm: 0	≥ 10 μm: 0 ≥ 25 μm: 0
Heterogeneity						
APG: 24.8%	APG: 25.1%	APG: 27.7%	APG: 26.9%	APG: 28.4%	APG: 27.3%	APG: 31.7%
MP: 74.6%	MP: 74.0%	MP: 71.7%	MP: 72.6%	MP: 71.0%	MP: 71.9%	MP: 67.4%
BPG: 0.5%	BPG: 0.9%	BPG: 0.6%	BPG: 0.5%	BPG: 0.6%	BPG: 0.8%	BPG ¹ : < 1.8%
Purity						
M: 99.1%	M: 99.0%	M: 98.8%	M: 98.8%	M: 98.8%	M: 98.8%	M: 98.6%
A: 0.2%	A: 0.3%	A: 0.3%	A: 0.3%	A: 0.3%	A: 0.3%	A: 0.4%
F: 0.6%	F: 0.7%	F: 0.9%	F: 0.8%	F: 0.9%	F: 0.9%	F: 1.0%
98.3%	98.4%	98.4%	98.2%	98.0%	98.4	98.3
97.2%	97.6%	97.7%	97.6%	97.4%	97.4	97.1
Biological Activity						
HER2: 101%	HER2: 100%	HER2: 101%	HER2: 101%	HER2: 100%	HER2: 100%	HER2: 100%
HER3: 99%	HER3: 99%	HER3: 99%	HER3: 99%	HER3: 97%	HER3: 100%	HER3: 100%
CD16: 101%	CD16: 101%	CD16: 101%	CD16: 101%	CD16: 100%	CD16: 96%	CD16: 94%
Quantity						
18.9	19.6	19.6	19.5	19.5	19.6	19.5
Microbiological Purity						
n.a.	n.a.	n.a.	n.a.	Pass	n.a.	Pass

Table S2. Stability data for MCLA-128 at 25°C ± 2°C.

MCLA-128 Lot E4775F03		
Test	Acceptance criteria	0 months
Appearance and Description		
Visible particles	Solution, essentially free from foreign particles, may contain few translucent, white to whitish product-related particles	Free from visible particles
General Tests		
pH	5.5–6.5	6.0
Osmolality (mOsm/kg)	270–330	288
Particulate contamination – sub-visible particles	≥ 10 µm: ≤ 6,000 particles/container ≥ 25 µm: ≤ 600 particles/container	≥ 10 µm: 123 ≥ 25 µm: 0
Heterogeneity		
Imaged Capillary Isoelectric Focusing (iCE)	Report result %: Acid peak (APG) Main peak (MP) Basic peak (BPG)	APG: 27.7% MP: 71.6% BPG: 0.7%
Purity		
UP-Size exclusion chromatography (UP-SEC)	Monomer (M) ≥ 95.0% Report results in %: Aggregates (A), Fragments (F)	M: 99.2% A: 0.2% F: 0.6%
Capillary gel electrophoresis (CGE) – reduced	Sum of heavy and light chain ≥ 90.0%	98.2%
Capillary gel electrophoresis (CGE) – non-reduced	Main peak ≥ 90.0%	97.6%
Biological Activity		
DBinding assay HER2, HER3, CD16 (Biacore)	HER2: 80–120% of development standard HER3: 80–120% of development standard CD16: 80–120% of development standard	HER2: 101% HER3: 100% CD16: 101%
Quantity		
Protein concentration by UV Scan (mg/mL)	18.0–22.0	19.6
Microbiological Purity		
Sterility	No growth	Pass

¹ < 1.8% = < LOQ for BPG

* Free from visible particles

n.a. = not applicable

1 month	2 months	3 months	6 months	9 months	12 months
Appearance and Description					
Free from visible particles	Free from visible particles	Free from visible particles	Free from visible particles	Free from visible particles	Free from visible particles
General Tests					
6.0	6.0	5.9	5.9	5.9	6.0
287	286	287	287	289	289
≥ 10 µm: 23 ≥ 25 µm: 0	≥ 10 µm: 27 ≥ 25 µm: 0	≥ 10 µm: 10 ≥ 25 µm: 0	≥ 10 µm: 13 ≥ 25 µm: 3	≥ 10 µm: 10 ≥ 25 µm: 3	≥ 10 µm: 230 ≥ 25 µm: 3
Heterogeneity					
APG: 28.0% MP: 71.4% BPG: 0.6%	APG: 32.0% MP: 67.3% BPG: 0.7%	APG: 31.8% MP: 67.3% BPG: 0.9%	APG: 37.9% MP: 61.5% BPG: 0.6%	APG: 47.4% MP: 52.0% BPG: 0.7%	APG: 54.6% MP: 44.9% BPG: 0.5%
Purity					
M: 98.8% A: 0.3% F: 1.0%	M: 98.8% A: 0.3% F: 1.0%	M: 98.0% A: 0.3% F: 1.7%	M: 97.6% A: 0.4% F: 2.0%	M: 96.9% A: 0.4% F: 2.6%	M: 96.3% A: 0.6% F: 3.2%
98.3%	98.2%	97.7%	96.8%	95.7%	94.7%
97.4%	96.6%	96.6%	95.9%	94.7%	93.5%
Biological Activity					
HER2: 101% HER3: 98% CD16: 101%	HER2: 100% HER3: 96% CD16: 100%	HER2: 100% HER3: 95% CD16: 100%	HER2: 99% HER3: 89% CD16: 98%	HER2: 98% HER3: 87% CD16: 97%	HER2: 96% HER3: 78% CD16: 95%
Quantity					
19.6	18.9	19.6	19.6	19.5	19.5
Microbiological Purity					
n.a.	n.a.	n.a.	n.a.	n.a.	n.a.

Tables S1 and S2. Stability data for MCLA-128 lot E4775F03 at $5^{\circ}\text{C} \pm 3^{\circ}\text{C}$ (Table S1) and at $25^{\circ}\text{C} \pm 2^{\circ}\text{C}$ (Table S2). These studies to define a shelf life for the MCLA-128 drug product were performed using analytical procedures according to International Conference on Harmonization guidelines (<http://www.ich.org/products/guidelines.html>).

CHAPTER 5

General discussion

Because of their central role in the functioning of multicellular organisms, cell receptors represent a key target of drug development efforts. In this thesis, different receptors have been functionally and structurally characterized using a broad range of biophysical techniques and cell based assays. This summarizing chapter discusses the implications and significance of the obtained results for the field of receptor biology.

Summary of insights on LRP1 structure prior to this thesis

The low-density lipoprotein receptor (LDLR) family is an evolutionary ancient family of cell surface receptors that perform a wide variety of physiological functions as transport proteins and as mediators in signal transduction cascades (1). Members of this protein family share similar structural characteristics, each consisting of three types of extracellular domains, namely complement-type cysteine-rich (CR) repeats, epidermal growth factor (EGF) -like repeats and YWTD six-bladed β -propellers that are combined in different arrangements. The major structural differences within the family are in the number of each domain type, leading to very different protein sizes. While LDLR has a molecular mass of 180 kDa, the herein studied LRP1 receptor is the largest member of the family and among the biggest monomeric proteins known with a molecular mass of roughly 600 kDa. LDLR contains only one cluster of CR repeats, whereas LRP1 contains four clusters of 2, 8, 10 and 11 CR repeats starting from the N-terminus. Each cluster of CR repeats is flanked by EGF-like repeats and YWTD six-bladed beta-propeller domains for a total of 61 domains forming the extracellular portion of LRP1. LRP1 has shown the ability to bind with high affinity a tremendous number of structurally and functionally different ligands, therefore it is considered a multiligand receptor (2). Similar to the other members of the family, the CR repeats of LRP1 have been found involved in ligand binding.

Structural studies of LDLR family members have focused on isolated CR or double CR modules using X-ray crystallography and NMR (3–7). These studies showed that the general folding of the CR domains of LRP1 is very conserved also compared to the CR repeats of the LDLR (8–12). Although the CR domains are all formed by approximately 40 amino acids and share a common fold containing three disulfide bonds and a highly conserved octahedral calcium binding pocket, the rest of their primary structure is very different. Since these domains are very small most of the side chains are exposed forming very different surface topographies and charge surface distributions.

These studies together with the structures of fragments of other LDLR family members bound to ligands (13–17) have helped revealing a common basic mode of binding of the CR repeats. The interaction is formed by salt bridges between

aspartic acid residues from the CR repeats and lysine residues from the ligand. The acidic residues are kept in place by the coordination to a calcium ion which creates a negatively charged binding pocket. The salt bridges are further stabilized by an hydrophobic interaction between an aromatic residue and the aliphatic portion of the lysine side chain (13). The CR repeats are connected by linkers of various lengths that allow adjustments of their mutual positions in order to form different binding pockets. However, the binding mode of CR repeats neither can explain the high LRP1 binding affinity of many ligands, nor it is able to explain the wide ligand binding versatility of LRP1. Thus, it was proposed that LRP1 binding must involve contributions from more than one domain (18).

To identify regions of LRP1 that are involved in ligand binding, soluble recombinant fragments of multiple adjacent CR repeats and LRP1 membrane-containing 'minireceptors' have been expressed in a variety of expression systems (*E.coli*, insect cells, eukaryotic cells) (19–25). These studies employing a range of techniques such as SPR, isothermal titration calorimetry, solid phase binding assays and fluorescence microscopy have led to the identification of multiple binding sites for different ligands, further confirming the hypothesis that LRP1 epitopes are constituted by a combination of different domains. However, discrepancies in measured equilibrium dissociation constant values and in describing which region binds to which ligand have gradually hinted towards a more complex ligand binding mechanism.

Earlier reports employing the full-length receptor have been carried out using LRP1 purified from human placenta (26) or from rat liver membrane extracts (27) by affinity chromatography. Alternatively, the soluble form of LRP1 was purified directly from plasma, since proteolytic cleavage of its β -chain from the α -chain occurs naturally in certain physiological conditions (28, 29). These protocols have been used for molecular and cellular studies but have not been able to produce large and pure enough amounts of protein required for structural investigations. In 1994 Delain *et al.* (30) analyzed LRP1 purified from human placenta membranes by negative stain electron spectroscopic imaging. The images revealed a very inhomogeneous sample of a flexible and elongated molecule. In our knowledge, this early work represents the only attempt to study the structure of LRP1 full-length prior to this thesis.

Overcoming the challenges in LRP1 expression

Although a lot is known about the individual domains of LDLR proteins, little structural information on LRP1 full-length was available at the beginning of this thesis project. The structure and binding mode of single CR repeats to certain

ligand domains had already been characterized, but the mechanism of action of LRP1 as a whole molecule was still not understood.

A molecule of the size of LRP1 with a very high content of disulfide bridges and glycosylation sites represents an extremely challenging protein to target for recombinant expression. In our initial attempts to express fragments of LRP1 in HEK cells we obtained poor expression levels and highly inhomogeneous sample due to improper disulfides formation (data not shown). These observations led us to believe that proper folding might require the presence of non-adjacent LRP1 domains. It has been shown that during the folding process of the LDLR non-native long-distance disulfide bonds and long range contacts between distant repeats form as transient intermediates, which are isomerized before the native structure is obtained (31). A similar process could likely be happening for LRP1, which has approximately five times more disulfide bonds than the LDLR.

Despite the initial unsuccessful attempts to express LRP1 fragments, we decided to focus our efforts on expressing the complete receptor ectodomain, based on the hypothesis that the presence of all the extracellular domains could ease the folding and secretion process. Furthermore, we believed that studying the entire LRP1 ectodomain was key to a proper understanding of its physiological behavior. Previous studies had reported the importance of the chaperone RAP for the folding of LRP1 and other LDLR family members (32,33). RAP binds to LRP1 with very high affinity and prevents premature binding of other ligands during the folding process (34). Even though the presence of RAP was not essential for secretion of LRP1 ectodomain, we took advantage of co-expressing LRP1 with RAP since it yielded higher protein amounts and it allowed us to obtain, in a relatively straightforward way, a highly stable secreted complex. As far as we know, this was the first time that LRP1 full-length ectodomain or any other monomeric protein of similar size was recombinantly expressed.

Having succeeded in expressing LRP1 and the LRP1:RAP complex, we investigated the binding stoichiometry of LRP1 and RAP. Despite there had been speculations that LRP1 could bind two RAP molecules before (34), other binding stoichiometries (21) had also been proposed leaving this question still unanswered. Our study gave unambiguous evidence that LRP1 harbors two RAP binding sites with different binding affinities. Furthermore, we could monitor the condition-dependent appearance of LRP1 monomer and LRP1:RAP complexes by employing native mass spectrometry. Native mass spectrometry analysis of glycosylated proteins is still considered very challenging due to the inherent heterogeneity of glycoproteins (35). However, combining dedicated expression strategies and high-resolution mass spectrometric instrumentation allowed us to unambiguously distinguish LRP1, LRP1:RAP 1:1 and LRP1:RAP 1:2 complexes.

To our knowledge, LRP1 is the most heavily glycosylated protein ever analyzed by native mass spectrometry,

Moreover, the LRP1 amounts obtained by taking advantage of DNA dilution and co-expression with RAP in transient HEK cells allowed us to perform more detailed biochemical and structural analyses. While higher resolution techniques, such as X-ray crystallography and cryo-EM, are not viable for a molecule as large and flexible as LRP1, we succeeded in studying the LRP1 conformation and ligand binding properties employing SPR, SAXS, cross-linking mass spectrometry and negative stain EM.

A model for pH-dependent binding and cargo release of LRP1

An important aspect of the ligand binding mode of LRP1 and other members of the family is that they dissociate from their ligand-cargo once in the endosomal compartments and are able to recycle back to the cell surface (36–39). Previous investigations identified two crucial factors triggering endosomal release of lipoproteins from LDLR and other members of the family: acidic pH (pH 5.5–6.5) and lower calcium concentration (2.5–10 μ M) within the endosome (40,41). The importance of each factor, however, is not completely understood. It appears they can both cause ligand release, though the release of LDL particles can also be driven by acidic pH only (36). Calcium binding studies employing single CR repeats of LRP1 (5) have shown that even though the calcium binding affinity diminishes at pH 5, it is still quite high, indicating the existence of additional pH-dependent mechanisms that account for the cargo release.

In the case of the LDLR, the basis of the pH-dependent cargo release mechanism was elucidated by domain deletion experiments (36,42) and by the X-ray structure of the LDLR ectodomain at pH 5.3 (43). The structure showed an intramolecular, calcium dependent interaction between two CR repeats and the beta-propeller domain that closely resembles the canonical ligand binding mode. These findings revealed that the release of the cargo is facilitated by a conformational change of the LDLR that brings the beta-propeller domain in close proximity to the ligand binding region. At neutral pH, instead, the LDLR adopts an open binding-active structure (44). Similarly, we discovered that low pH, rather than calcium concentration, seems to trigger an allosteric effect in the LRP1 conformation that allows for ligand release. In fact, our findings revealed that LRP1 releases RAP at pH < 6 and undergoes a pH-dependent conformational change from an elongated structure at neutral pH to a more compact conformation at acidic pH, and that this behaviour is reversible by means of reverting the pH. The ability to reversibly change conformation and bind again RAP, after release at pH < 6 and neutralization at pH 7.5, correlates well with the knowledge that in physi-

ological conditions, LRP1 is able to recycle to the cell surface for another round of ligand binding after releasing the cargo in the endosomal compartments (39). The conformational change was observed also when LRP1 was not bound to RAP, although in a lesser extent, emphasizing the importance of the environmental pH for LRP1 conformation. Our findings represent a significant advance in the understanding of LRP1 functional and structural behavior, highlighting the importance of complementary structural techniques to study challenging proteins that X-ray crystallography cannot address. However, a complete understanding of the role of this large and complex receptor is still not achieved. Technical improvements in structural methods, e.g. cryo-EM, might allow in the future for a high resolution 3D-structural investigation of LRP1.

Overall, we shed light on LRP1's structural and binding features discovering a pH-dependent conformational change that is consistent with previous findings on the LDLR, which motivates the speculation that that this mechanism could be adopted by several other members of the LDLR family and, perhaps, similar endocytic receptors. A more thorough understanding of the pH-dependent binding behavior of LRP1 might aid the development of new therapeutics aimed at interfering with the scavenging role of the receptor in certain pathological conditions, such as by blocking the uptake of factor VIII in hemophilia A patients.

Targeting of HER2 and HER3 receptors in cancer therapy

The receptor tyrosine kinase (RTK) family of HER receptors contribute to the ability of the cell to respond to environmental changes by binding extracellular growth factor ligands and promoting various signaling cascades within the cell (45). Abnormal activity of these receptors has been linked to multiple types of aggressive cancer (46). The HER2 receptor is present on the cell surface of a wide number of human cell types, but is often overexpressed in epithelial tumor cells, where it is associated with tumor invasion and metastasis (47). When dimerized with its main binding partner HER3, HER2 can activate the PI3K/Akt pathway that enhances tumor cell survival and proliferation (45). HER3 can form signaling-competent heterodimers after binding to one of its ligands, although HER2/HER3 oncogenic dimers in the absence of ligand have also been observed in tumors overexpressing HER2 (48).

There are two major classes of therapeutics targeting HER receptors: ectodomain-binding antibodies and tyrosine-kinase inhibitors (TKIs) (49). TKIs are small molecules that compete with ATP for the ATP binding site of the tyrosine-kinase domain, inhibiting its catalytic activity. Thus, TKIs are able to block intracellular interactions with protein adapters that transmit signals within the cell (50). Lapatinib is a dual anti-HER2/EGFR TKI (51,52) approved for the

treatment of breast cancer. Compared to TKIs, antibodies have the advantage of being intrinsically able to recruit immune effector cells to the tumor site through binding of the constant Fc domain of the antibody to Fc γ receptors on the effector cells' surface. The use of antibodies against the ectodomain of HER receptors was the first application of rational targeted therapy (47). Trastuzumab was the first monoclonal antibody (mAb) therapy to be approved for the treatment of HER2 positive breast cancer (53–55). Trastuzumab binds domain IV (56) of the extracellular portion of HER2 decreasing tumor cell proliferation (57). Trastuzumab's mode of action is not completely understood, but it involves downregulation of HER2 levels and HER2-associated signaling cascades together with recruitment of immune effector cells (58,59). Though trastuzumab is able to inhibit ligand independent HER2/HER3 activation, it was proven to be ineffective in blocking HER2/HER3 dimerization in the presence of ligand (48,60,61). Pertuzumab is another mAb targeting HER2 which prevents receptor dimerization by binding to domain II of HER2 (62,63). In this way, it is able to inhibit ligand-dependent HER2/HER3 dimerization and consequent activation of signaling cascades that mediate cancer proliferation and survival (62). The combination of trastuzumab and pertuzumab is a current standard treatment for HER2-positive metastatic breast cancer since it was shown to be more effective than the action of the single antibodies (64–66).

Although the targeting of individual HER receptors via TKIs or specific antibodies has revealed anti-tumor effects, a significant proportion of initially responsive tumors will eventually develop resistance (67,68). Many tumors develop resistance against HER2-targeted therapies due to upregulation of HER3 and consequent activation of compensatory signaling pathways, in particular the PI3K/Akt signaling network (69–72). The main HER3 ligand heregulin (HRG) is overexpressed in the majority of primary breast tumors (73) and it is often upregulated in HER2-overexpressing tumors as a consequence of HER2-targeted treatments (74,75). Targeting HER3 has become, therefore, an important strategy to overcome the acquired resistance of tumor cells to TKIs and targeted anti-HER2 agents (76). Several anti-HER3 monoclonal antibodies have been developed in the last decade and are currently under clinical trial (77, 78). The main strategies have focused on targeting HER3 ectodomain to prevent its ability to bind HRG and dimerize (79–82). However, antibodies targeting HER3 as a single agent have shown only limited clinical success, likely due to its relatively low abundance compared to EGFR and HER2 on tumor cells (76). Synergistic strategies that combine two or more mAbs engaging multiple non-overlapping sites of a receptor (e.g. trastuzumab + pertuzumab, trastuzumab + lapatinib) or distinct RTKs, have shown greater efficacy in several trials (76,83,84).

To overcome drug resistance in HER2-overexpressing tumors we aimed at developing a bispecific antibody (bAb) that could target HER2 and HER3 in the presence of high levels of HRG. Bispecific antibodies are a new therapeutic modality that is being actively investigated due to the ability to target different epitopes within one molecule, different molecules on the same cells, or different molecules on different cells, leading to enhanced and in some cases synergistic functionality (61,79,85,86). As described in Chapter 3, we selected PB4188 (MCLA-128) based on its ability to inhibit tumor growth better than the combination of trastuzumab and pertuzumab and a set of anti-HER3 mAbs. Importantly, PB4188 is able to suppress tumor growth even at very high HRG concentrations (> 10 nM), where combinations of trastuzumab and anti-HER3 monospecific antibodies and the previously published anti-HER2xHER3 bispecific antibody MM-111 (61) failed. Although PB4188 activity is observed in all the HER2-positive tumor cells, the highest activity was measured in cells expressing HER2 in high amounts. Since in most tumor cells HER3 levels are similar to normal tissues, while HER2 is overexpressed, the ability to target HER2 may represent a therapeutic advantage of PB4188 over mono-HER3 therapies. As previously suggested (61), we demonstrated that a molecule that is able to bind HER2 and consequently inhibit HRG-driven HER3 activation is more effective than monospecific anti-HER3 therapies or, as we have seen, combinations of anti-HER2 antibodies.

A problem often associated with antigen-selective cancer therapies is the side effects caused by off-site targeting due to the ubiquitous expression of RTKs. In breast cancer patients, cardiotoxicity is often observed following treatment with trastuzumab, alone or in combination with pertuzumab, since HER2 is also expressed in cardiomyocytes (87,88). PB4188 showed no cardiotoxicity due to its ability to target very specifically the HER2/HER3 associated signaling pathways. However, because of PB4188's high specificity, tumors may evolve alternative negative feedback loops and escape therapy, as seen before for other targeted treatments. To achieve a more durable response, or even the complete eradication of cancer, it may be required to harness the human immune response against cancer cells. Producing a self-sustaining systemic immunity that does not generate an unrestrained autoimmune inflammatory response is the goal of cancer immunotherapy (89,90). Therefore, a combination of tumor-targeting antibodies, such as PB4188, and immuno-modulatory molecules may represent the most promising approach to overcoming drug resistance and accomplish tumor suppression.

Structural studies of HER receptors

The ability of membrane receptors to transmit signals crucially depends on their structure and how it changes when binding a ligand. Multiple crystal structures of

extracellular regions and tyrosine kinase domains of HER receptors, in different activation states and in complex with inhibitory molecules, have helped to more accurately describe their functional behavior.

Obtaining the X-ray structures of the ectodomains of HER2 and HER3 in complex with the corresponding Fabs of PB4188 was key to confirm the locations of the epitopes and gain further insights into the molecular mechanism behind the activity of PB4188. In-cell binding experiments showed that the HER3-Fab binding event has a dissociation constant (K_D) 10-fold higher than that of the Fab binding to HER2. However, the binding of PB4188 appears to be driven by the HER2-Fab arm since it shows a very similar binding pattern to HER2 monovalent IgG. Moreover, the bispecific antibodies with a HER2-Fab arm targeting domain I performed significantly better in initial screenings than other bAbs targeting different HER2 domains, despite not showing any anti-tumor activity. Therefore, we concluded that the location of the HER2 epitope must play an important role for the enhanced activity of PB4188. The structure of the ectodomain of HER2 in complex with the Fab (MF3958) revealed that the epitope is located in a region of domain I that allows the Fab to localize right on top of HER2, at the most distal location from the membrane (considering the cell surface as the bottom). Altogether these observations led us to hypothesize that the binding to HER2 provides an advantageous site for the docking of PB4188 on the cell surface. The structure of HER3 ectodomain in complex with the Fab (MF3178) showed that the HER3 epitope is located in domain III, a region involved in ligand binding. The binding of PB4188 to HER3 is, therefore, incompatible with the active state of HER3 where a ligand is bound and domain III interacts with domain I. To have a more comprehensive understanding of PB4188 binding to HER2 and HER3 we conducted SAXS studies employing the full bispecific IgG and both receptors' ectodomains. In this way we could confirm that PB4188 is able to bind to both receptors in solution at the same time, with a paratope-to-paratope reach of ~ 140 Å which is in line with previously reported measures of such distance (91). However, the limitations of SAXS are intrinsic to the fact that is a solution method; therefore the findings do not necessarily correspond to a 'real situation' where the receptors are anchored to the cell membrane.

The findings of the crystal structures combined with the SAXS led us to propose that PB4188 might bind to HER2 in its monomeric or dimerized state, due to the fact that the location of the epitope does not interfere with the domains involved in the dimerization process. However, PB4188 cannot bind HER3 when engaged in a dimer, but likely locks HER3 in the inactive state. Further insights into PB4188's mechanism of action were obtained by employing a theoretical approach. Through the statistical-thermodynamic theory of the grand canoni-

cal ensemble we were able to describe the behavior of PB4188 binding to cells expressing HER3 and different levels of HER2 on their surface. From this model, it emerged that a higher number of HER2 receptors on the cell surface plays an important role in the enhanced activity of PB4188 at high ligand concentration, compared to bivalent anti-HER3 mAb. Combining these findings with the biological data, we concluded that PB4188's mechanism of action is connected to its ability to localize on tumor sites by docking on HER2 and to consequently bind HER3 with very high affinity, blocking its HRG binding site ('dock and block'). Eventually, we can conclude that PB4188's mechanism of action might have a high replication potential to enhance therapy selectivity in the treatment of complex diseases involving multiple cell surface receptors, such as other types of cancers and immune disorders.

It is important to note that none of the structural approaches described here take into account the fluidity of the cell membrane, a dynamic environment that influences receptors interactions. Structures of soluble ectodomains offer precious insights but still represent an incomplete view of the mechanisms of activation of full-length membrane receptors (92,93). Though many membrane proteins have been crystallized, type I transmembrane receptors are extremely challenging for crystallization due to the inherent flexibility and physicochemical properties of their transmembrane domain. To fully elucidate the complex relationship between receptor structure, conformational dynamics and function, studies of full-length receptors in their native environment are required. Advances of *in situ* structural techniques such as cryo-electron tomography (94) and solid state NMR (95) combined with cutting-edge cell biology approaches, may soon provide the fundamental link between structure, dynamics and function of these important membrane receptors and many others.

The future of bispecific antibodies

Multiple strategies for producing bispecific antibodies have been developed, resulting in more than 60 different formats (96) that can be categorized on whether they are based on the full IgG architecture or not (97,98). Full IgG bAbs contain the Fc region which present several advantages compared to fragment based formats. The Fc region facilitates the purification of bAbs, following standard IgG protocols, and makes them more stable and soluble. Furthermore, it allows antibodies to retain Fc-mediated effector functions and have longer serum half-lives (99,100). Promoting heterodimerization of the heavy chains from two different antibodies by introducing asymmetric mutations in the Fc region has been proven to be an effective approach for the design of full bispecific IgGs. Various strategies were developed during the past two decades that use steric or electrostatic steering

effects, or combinations thereof, to produce heterodimeric Fc designs (101–107). As of July 2016, seven heterodimeric-Fc based bAb constructs were being evaluated in clinical trials (100).

To generate a scaffold for the production of the bispecific antibody PB4188 (MCLA-128) we adopted a charge-introduction approach by substituting polar and hydrophobic residues into electrostatic ones at the core of the dimerization interface of the Fc region (Chapter 4). To identify the most promising mutations, a combination of docking, biological and structural validation was employed. This multi-scale approach allowed us to identify charge interactions that promoted the heterodimeric assembly of the two heavy chains, while disfavoring the corresponding homodimeric by-products. The structure of the resulting Fc molecule (DEKK), with substitutions L351D,L368E in one heavy chain and L351K,T366K in the other heavy chain, was investigated by X-ray crystallography, which provided a detailed view of the interactions at the dimerization interface. Interestingly, the structural models generated by HADDOCK (108) did not very accurately describe the actual structure as determined by X-ray crystallography. In fact, an unexpected conformation of the interactions at the CH3 interface led to a backbone shift of part of the Fc molecule (compared to wild type Fc). HADDOCK did not predict such a shift because we opted to keep the C α -backbone fixed in order to save computational time. This refinement mode allowed optimization of the side chain positions only, an approach similar to many other modeling protocols. These observations illustrate the importance of structural validation, even for a seemingly easy-to-model case such as the Fc region, where many related structures are available in the Protein Data Bank. Due to the fairly dynamic nature of proteins, even mutations predicted to destabilize a by-product may be accommodated by small conformational changes. In fact, although DEKK showed very favorable stability and pharmacodynamic properties, some homodimeric impurities for one of its by-products could be observed in supernatants derived from stable producer cell lines. Variable purity is a common issue in heterodimeric Fc engineering (100). By investigating the crystal structure of the homodimeric Fc by-product DEDE (L351D,L368E in both chains) we observed an enlarged distance across the CH3 β -sheet core of the dimerization interface, indicating some structural instability. However, many of the native interactions were still able to form.

Although homodimeric impurities can be separated by ion-exchange chromatography, this decreases the yields of the bispecific IgG. Therefore, it might be desirable to improve the purity of the bispecific production process. In the case of DEKK, this could be achieved by identifying additional mutations that could further destabilize the DEDE homodimer. A fairly straightforward way to do so would be to use the crystal structures obtained as starting models in

HADDOCK and use an option that does not keep the C α -backbone fixed. Although HADDOCK did not accurately predict the actual three-dimensional structure of DEKK, the stability of the molecule and of its homodimeric by-product DEDE was quite accurately described. We calculated the HADDOCK scores using the crystal structures of DEKK and DEDE and compared them with the HADDOCK energy predictions generated earlier. Interestingly, the scores of the structures obtained by X-ray crystallography correlated quite well with the HADDOCK predictions, confirming that HADDOCK is a valuable tool for the prediction of molecular stability despite the approximations it makes (Table 1). Of course, other modeling tools are also available, such as a recently published strategy where negative designs were taken into account in an iterative multi-state approach (109).

An impressive number of different formats for bispecific antibodies have been developed, with many now approved for therapeutic use or undergoing clinical trials (110). This may be due, to some extent, to the fact that antibody engineering has shown an enormous potential due to its versatility of applications (110). The IgG molecule can function as a frame made of modular blocks that can be assembled and modified easily, creating almost infinite possibilities. The existence of so many scaffolds can be seen as an advantage, since there is a wide range of different applications bispecific antibodies can address. Bispecific antibodies are not only being developed for cancer therapy, but also for diagnostic purposes or the treatment of chronic inflammatory diseases, autoimmunity, neurodegeneration, bleeding disorders and infections (110). Even when considering only cancer therapy, bispecific antibodies with different molecular properties are required for addressing antigens with different sizes, arrangements and surface densities (as seen in Chapter 3). It is therefore evident that one size will not fit all.

Table 1. HADDOCK calculated energy predictions. HADDOCK scores of Fc WT, DEKK and DEDE model predictions and of DEKK and DEDE determined X-ray structures.

	WT	DEKK prediction	DEDE prediction	DEKK X-ray structure	DEDE X-ray structure
HADDOCK score	-208.2 +/-3.2	-243.9 +/-1.2	-185.1 +/-2.6	-204.7 +/-4.8	-152.2 +/-5.2
Cluster size	20	20	20	20	20
RMSD from the overall lowest-energy structure (Å)	0.3 +/-0.2	0.3 +/- 0.2	0.3 +/-0.2	0.3 +/-0.1	0.3 +/-0.2
van der Waals energy (kcal/mol)	-62.8 +/--3.6	-58.1 +/--2.3	-66.7 +/--9.8	-61.9 +/--5.6	-58.2 +/--2.9
Electrostatic energy (kcal/mol)	-773.0 +/--51.7	-1010.9 +/-30.4	-575.5 +/--86.2	-718.5 +/--73.6	-469.7 +/--27.4
Desolvation energy (kcal/mol)	9.2 +/--5.3	16.4 +/--3.9	-3.3 +/--5.1	0.9 +/--7.7	0.0 +/--7.7
BSA (Å ²)	2505.8 +/--14.5	2480.0 +/--26.1	2401.6 +/--52.2	2318.2 +/--27.4	2112.5 +/--30.3

References

1. Willnow, T. E., Nykjaer, A., and Herz, J. (1999) Lipoprotein receptors: new roles for ancient proteins. *Nat. Cell Biol.* **1**, E157–E162
2. Herz, J., and Strickland, D. K. (2001) LRP: a multifunctional scavenger and signaling receptor. *J Clin Invest.* **108**, 779–784
3. Huang, W., Dolmer, K., and Gettins, P. G. W. (1998) NMR solution structure of complement-like repeat CR8 from the NMR solution structure of complement-like repeat CR8 from the low density lipoprotein receptor-related protein. *J. Biol. Chem.* **274**, 14130–14136
4. Dolmer, K., Huang, W., and Gettins, P. G. W. (2000) NMR solution structure of complement-like repeat CR3 from the low density lipoprotein receptor-related protein: evidence for specific binding to the receptor binding domain of human alpha-2-macroglobulin. *J. Biol. Chem.* **275**, 3264–3269
5. Simonovic, M., Dolmer, K., Huang, W., Strickland, D. K., Volz, K., and Gettins, P. G. W. (2001) Calcium coordination and pH dependence of the calcium affinity of ligand-binding repeat CR7 from the LRP. Comparison with related domains from the LRP and the LDL receptor. *Biochemistry.* **40**, 15127–15134
6. Jensen, G. A., Andersen, O. M., Bonvin, A. M. J. J., Bjerrum-Bohr, I., Etzerodt, M., Thøgersen, H. C., O’Shea, C., Poulsen, F. M., and Kragelund, B. B. (2006) Binding site structure of one LRP–RAP complex: implications for a common ligand–receptor binding motif. *J. Mol. Biol.* **362**, 700–716
7. Guttman, M., Prieto, J. H., Handel, T. M., Domaille, P. J., and Komives, E. A. (2010) Structure of the minimal interface between ApoE and LRP. *J. Mol. Biol.* **398**, 306–319
8. Daly, N. L., Scanlon, M. J., Djordjevic, J. T., Kroon, P. A., and Smith, R. (1995) Three-dimensional structure of a cysteine-rich repeat from the low-density lipoprotein receptor. *Proc. Natl. Acad. Sci. USA.* **92**, 6334–6338
9. Fass, D., Blacklow, S., Kim, P. S., and Berger, J. M. (1997) Molecular basis of familial hypercholesterolaemia from structure of LDL receptor module. *Nature.* **388**, 691–693
10. Daly, N. L., Djordjevic, J. T., Kroon, P. A., and Smith, R. (1995) Three-dimensional structure of the second cysteine-rich repeat from the human low-density lipoprotein receptor. *Biochemistry.* **34**, 14474–14481
11. Kurniawan, N. D., Atkins, A. R., Bieri, S., Brown, C. J., Brereton, I. M., Kroon, P. A., and Smith, R. (2000) NMR structure of a concatemer of the first and second ligand-binding modules of the human low-density lipoprotein receptor. *Protein Sci.* **9**, 1282–1293
12. North, C. L., and Blacklow, S. C. (2000) Solution structure of the sixth LDL-A module of the LDL receptor. *Biochemistry.* **39**, 2564–2571
13. Fisher, C., Beglova, N., and Blacklow, S. C. (2006) Structure of an LDLR–RAP complex reveals a general mode for ligand recognition by lipoprotein receptors. *Mol. Cell.* **22**, 277–283
14. Verdaguer, N., Fita, I., Reithmayer, M., Moser, R., and Blaas, D. (2004) X-ray structure of a minor group human rhinovirus bound to a fragment of its cellular receptor protein. *Nat. Struct. Mol. Biol.* **11**, 429–434
15. Yasui, N., Nogi, T., Kitao, T., Nakano, Y., Hattori, M., and Takagi, J. (2007) Structure of a receptor-binding fragment of reelin and mutational analysis reveal a recognition mechanism similar to endocytic receptors. *Proc. Natl. Acad. Sci. USA.* **104**, 9988–9993
16. Dagil, R., O’Shea, C., Nykjær, A., Bonvin, A. M. J. J., and Kragelund, B. B. (2013) Gentamicin binds to the megalin receptor as a competitive inhibitor using the common ligand binding motif of complement type repeats. *J. Biol. Chem.* **288**, 4424–4435
17. Lee, C.-J., De Biasio, A., and Beglova, N. (2010) Mode of interaction between beta-2GPI and lipoprotein receptors suggests mutually exclusive binding of beta-2GPI to the receptors and anionic phospholipids. *Structure.* **18**, 366–376

18. Strickland, D. K., Au, D. T., Cunfer, P., and Muratoglu, S. C. (2014) Low-density lipoprotein receptor-related protein-1 role in regulation of vascular integrity. *Arter. Thromb Vasc Biol.* **34**, 487–499
19. Bu, G., and Rennke, S. (1996) Receptor-associated protein is a folding chaperone for low density lipoprotein receptor-related protein. *J. Biol. Chem.* **271**, 22218–22224
20. Horn, I. R., van den Berg, B. M. M., van der Meijden, P. Z., Pannekoek, H., and van Zonneveld, A.-J. (1997) Molecular analysis of ligand binding to the second cluster of complement-type repeats of the low density lipoprotein receptor-related protein. *J. Biol. Chem.* **272**, 13608–13613
21. Neels, J. G., van den Berg, B. M. M., Lookene, A., Olivecrona, G., Pannekoek, H., and van Zonneveld, A.-J. (1999) The second and fourth cluster of class A cysteine-rich repeats of the low density lipoprotein receptor-related protein share ligand-binding properties. *J. Biol. Chem.* **274**, 31305–31311
22. Obermoeller-McCormick, L. M., Li, Y., Osaka, H., FitzGerald, D. J., Schwartz, A. L., and Bu, G. (2000) Dissection of receptor folding and ligand-binding property with functional minireceptors of LDL receptor-related protein. *J. Cell Sci.* **114**, 899–908
23. Croy, J. E., Shin, W. D., Knauer, M. F., Knauer, D. J., and Komives, E. A. (2003) All three LDL receptor homology regions of the LDL receptor-related protein bind multiple ligands. *Biochemistry.* **42**, 13049–13057
24. Mikhailenko, I., Battey, F. D., Migliorini, M., Ruiz, J. F., Argraves, K., Moayeri, M., and Strickland, D. K. (2001) Recognition of alpha2-macroglobulin by the low density lipoprotein receptor-related protein requires the cooperation of two ligand binding cluster regions. *J. Biol. Chem.* **276**, 39484–39491
25. Meijer, A. B., Rohlena, J., van der Zwaan, C., van Zonneveld, A.-J., Boertjes, R. C., Lenting, P. J., and Mertens, K. (2007) Functional duplication of ligand-binding domains within low-density lipoprotein receptor-related protein for interaction with receptor associated protein , alpha-2-macroglobulin , factor IXa and factor VIII. *Biochim. Biophys. Acta.* **1774**, 714–722
26. Ashcom, J. D., Tiller, S. E., Dickerson, K., Cravens, J. L., Argraves, W. S., and D.K., S. (1990) The Human alpha-2-macroglobulin receptor: identification of a 420-kD cell surface glycoprotein specific for the activated conformation of alpha-2-macroglobulin. *J. Cell Biol.* **110**, 1041–1048
27. Moestrup, S. K., and Gliemann, J. (1989) Purification of the rat hepatic alpha-2-macroglobulin receptor as an approximately 440-kDa single chain protein. *J. Biol. Chem.* **264**, 15574–15577
28. Quinn, K. A., Grimsley, P. G., Dai, Y.-P., Tapner, M., Chesterman, C. N., and Owensby, D. A. (1997) Soluble low density lipoprotein receptor-related protein (LRP) circulates in human plasma. *J. Biol. Chem.* **272**, 23946–23951
29. Gaultier, A., Arandjelovic, S., Li, X., Janes, J., Dragojlovic, N., Zhou, G. P., Dolkas, J., Myers, R. R., Gonias, S. L., and Campana, W. M. (2008) A shed form of LDL receptor-related protein-1 regulates peripheral nerve injury and neuropathic pain in rodents. *J. Clin. Invest.* **118**, 161–172
30. Delain, E., Barray, M., Pochon, F., Gliemann, J., and Moestrup, S. K. (1994) Electron microscopic visualization of the human alpha-2-macroglobulin receptor and its interaction with alpha-2-macroglobulin/chymotrypsin complex. *Ann. N. Y. Acad. Sci.* **737**, 202–211
31. Jansens, A., van Duijn, E., and Braakman, I. (2002) Coordinated nonvectorial folding in a newly synthesized multidomain protein. *Science (80-.).* **298**, 2401–2403
32. Battey, F. D., Gafvels, M. E., FitzGerald, D. J., Argraves, W. S., Chappell, D. A., Strauss, J. F., and Strickland, D. K. (1994) The 39-kDa receptor-associated protein regulates ligand binding by the very low density lipoprotein receptor. *J. Biol. Chem.* **269**, 23268–23273

33. Kounnas, M. Z., Argraves, W. S., and Strickland, D. K. (1992) The 39-kDa receptor-associated protein interacts with two members of the low density lipoprotein receptor family, alpha-2-macroglobulin receptor and glycoprotein 330. *J. Biol. Chem.* **267**, 21162–21166
34. Williams, S. E., Ashcom, J. D., Argraves, W. S., and Strickland, D. K. (1992) A novel mechanism for controlling the activity of alpha-2-macroglobulin receptor/low density lipoprotein receptor-related protein. *J. Biol. Chem.* **267**, 9035–9040
35. Wang, G., de Jong, R. N., van den Bremer, E. T. J., Parren, P. W. H. I., and Heck, A. J. R. (2017) Enhancing accuracy in molecular weight determination of highly heterogeneously glycosylated proteins by native tandem mass spectrometry. *Anal. Chem.* **89**, 4793–4797
36. Davis, C. G., Goldstein, J. L., Südhof, T. C., Anderson, R. G. W., Russell, D. W., and Brown, M. S. (1987) Acid-dependent ligand dissociation and recycling of LDL receptor mediated by growth factor homology region. *Nature.* **326**, 760–765
37. Chen, W.-J., Goldstein, J. L., and Brown, M. S. (1990) NPXY, a sequence often found in cytoplasmic tails, is required for coated pit-mediated internalization of the low density lipoprotein receptor. *J. Biol. Chem.* **265**, 3116–3123
38. Czekay, R.-P., Orlando, R. A., Woodward, L., Lundstrom, M., and Farquhar, M. G. (1997) Endocytic trafficking of megalin/RAP complexes: dissociation of the complexes in the late endosomes. *Mol. Biol. Cell.* **8**, 517–532
39. Laatsch, A., Panteli, M., Sornsakrin, M., Hoffzimmer, B., Grewal, T., and Heeren, J. (2012) Low density lipoprotein receptor-related protein 1 dependent endosomal trapping and recycling of apolipoprotein E. *PLoS One.* **7**, e29385
40. Dirlam-Schatz, K. A., and Attie, A. D. (1998) Calcium induces a conformational change in the ligand binding domain of the low density lipoprotein receptor. *J. Lipid Res.* **39**, 402–411
41. Zhao, Z., and Michaely, P. (2009) The role of calcium in lipoprotein release by the low-density lipoprotein receptor. *Biochemistry.* **48**, 7313–7324
42. Beglova, N., Jeon, H., Fisher, C., and Blacklow, S. C. (2004) Cooperation between fixed and low pH-inducible interfaces controls lipoprotein release by the LDL receptor. *Mol. Cell.* **16**, 281–292
43. Rudenko, G., Henry, L., Henderson, K., Ichtchenko, K., Brown, M. S., Goldstein, J. L., and Deisenhofer, J. (2002) Structure of the LDL receptor extracellular domain at endosomal pH. *Science (80-)*. **298**, 2353–2358
44. Jeon, H., and Shipley, G. G. (2000) Vesicle-reconstituted low density lipoprotein receptor: visualization by cryoelectron microscopy. *J. Biol. Chem.* **275**, 30458–30464
45. Yarden, Y. (2001) The EGFR family and its ligands in human cancer: signalling mechanisms and therapeutic opportunities. *Eur. J. Cancer.* **37**, S3–S8
46. Zaczek, A., Brandt, B., and Bielawski, K. P. (2005) The diverse signaling network of EGFR , HER2 , HER3 and HER4 tyrosine kinase receptors. *Histol Histopathol.* **20**, 1005–1015
47. Zhang, H., Berezov, A., Wang, Q., Zhang, G., Drebin, J., Murali, R., and Greene, M. I. (2007) ErbB receptors: from oncogenes to targeted cancer therapies. *J. Clin. Invest.* **117**, 2051–2058
48. Junttila, T. T., Akita, R. W., Parsons, K., Fields, C., Phillips, G. D. L., Friedman, L. S., Sam-path, D., and Sliwkowski, M. X. (2009) Ligand-independent HER2/HER3/PI3K complex is disrupted by trastuzumab and is effectively inhibited by the PI3K inhibitor GDC-0941. *Cancer Cell.* **15**, 429–440
49. Hynes, N. E., and Lane, H. A. (2005) ERBB receptors and cancer: the complexity of targeted inhibitors. *Nat. Rev.* **5**, 341–354
50. Levitzki, A., and Mishani, E. (2006) Tyrophostins and other tyrosine kinase inhibitors. *Annu. Rev. Biochem.* **75**, 93–109
51. Spector, N. L., Xia, W., Burris III, H., Hurwitz, H., Dees, E. C., Dowlati, A., O’Neil, B., Overmoyer, B., Marcom, P. K., Blackwell, K. L., Smith, D. A., Koch, K. M., Stead, A.,

- Mangum, S., Ellis, M. J., Liu, L., Man, A. K., Bremer, T. M., Harris, J., and Bacus, S. (2005) Study of the biologic effects of Lapatinib, a reversible inhibitor of ErbB1 and ErbB2 tyrosine kinases, on tumor growth and survival pathways in patients with advanced malignancies. *J. Clin. Oncol.* **23**, 2502–2512
52. Xia, W., Mullin, R. J., Keith, B. R., Liu, L.-H., Ma, H., Rusnak, D. W., Owens, G., Alligood, K. J., and Spector, N. L. (2002) Anti-tumor activity of GW572016: a dual tyrosine kinase inhibitor blocks EGF activation of EGFR/erbB2 and downstream Erk1/2 and AKT pathways. *Oncogene.* **21**, 6255–6263
 53. Drebin, J. A., Link, V. C., and Greene, M. I. (1988) Monoclonal antibodies reactive with distinct domains of the neu oncogene-encoded p185 molecule exert synergistic anti-tumor effects in vivo. *Oncogene.* **2**, 273–277
 54. Carter, P., Presta, L., Gorman, C. M., Ridgway, J. B. B., Henner, D., Wong, W. L. T., Rowlandf, A. M., Kotts, C., Carvert, M. E., and Shepard, H. M. (1992) Humanization of an anti-p185HER2 antibody for human cancer therapy. *Proc. Natl. Acad. Sci. USA.* **89**, 4285–4289
 55. Cobleigh, M. A., Vogel, C. L., Tripathy, D., Robert, N. J., Scholl, S., Fehrenbacher, L., Wolter, J. M., Paton, V., Shak, S., Lieberman, G., and Slamon, D. J. (1999) Multinational study of the efficacy and safety of humanized anti-HER2 monoclonal antibody in women who have HER2-overexpressing metastatic breast cancer that has progressed after chemotherapy for metastatic disease. *J. Clin. Oncol.* **17**, 2639–2648
 56. Cho, H.-S., Mason, K., Ramyar, K. X., Stanley, A. M., Gabelli, S. B., Dennery Jr, D. W., and Leahy, D. (2003) Structure of the extracellular region of HER2 alone and in complex with the Herceptin Fab. *Nature.* **421**, 756–759
 57. Izumi, Y., Xu, L., di Tomaso, E., Fukumura, D., and Jain, R. K. (2002) Herceptin acts as an anti-angiogenic cocktail. *Nature.* **416**, 279–280
 58. Hudziak, R. M., Lewis, G. D., Winget, M., Fendly, B. M., Shepard, H. M., and Ullrich, A. (1989) p185HER2 monoclonal antibody has antiproliferative effects in vitro and sensitizes human breast tumor cells to tumor necrosis factor. *Mol. Cell. Biol.* **9**, 1165–1172
 59. Lane, H. A., Beuvink, I., Motoyama, A. B., Daly, J. M., Neve, R. M., and Hynes, N. E. (2000) ErbB2 potentiates breast tumor proliferation through modulation of p27Kip1-Cdk2 complex formation: receptor overexpression does not determine growth dependency. *Mol. Cell. Biol.* **20**, 3210–3223
 60. Wehrman, T. S., Raab, W. J., Casipit, C. L., Doyonnas, R., Pomerantz, J. H., and Blau, H. M. (2006) A system for quantifying dynamic protein interactions defines a role for Herceptin in modulating ErbB2 interactions. *Proc. Natl. Acad. Sci. USA.* **103**, 19063–19068
 61. McDonagh, C. F., Huhlov, A., Harms, B. D., Adams, S., Paragas, V., Oyama, S., Zhang, B., Luus, L., Overland, R., Nguyen, S., Gu, J., Kohli, N., Wallace, M., Feldhaus, M. J., Kudla, A. J., Schoeberl, B., and Nielsen, U. B. (2012) Antitumor activity of a novel bispecific antibody that targets the ErbB2/ErbB3 oncogenic unit and inhibits heregulin-induced activation of ErbB3. *Mol. Cancer Ther.* **11**, 582–593
 62. Agus, D. B., Akita, R. W., Fox, W. D., Lewis, G. D., Higgins, B., Pisacane, P. I., Lofgren, J. A., Tindell, C., Evans, D. P., Maiese, K., Scher, H. I., and Sliwkowski, M. X. (2002) Targeting ligand-activated ErbB2 signaling inhibits breast and prostate tumor growth. *Cancer Cell.* **2**, 127–137
 63. Franklin, M. C., Carey, K. D., Vajdos, F. F., Leahy, D. J., de Vos, A. M., and Sliwkowski, M. X. (2004) Insights into ErbB signaling from the structure of the ErbB2-pertuzumab complex. *Cancer Cell.* **5**, 317–328
 64. Nahta, R., Hung, M.-C., and Esteva, F. J. (2004) The HER-2-targeting antibodies trastuzumab and pertuzumab synergistically inhibit the survival of breast cancer cells. *Cancer Res.* **64**, 2343–2346

65. Scheuer, W., Friess, T., Burtscher, H., Bossenmaier, B., Endl, J., and Hasmann, M. (2009) Strongly enhanced antitumor activity of trastuzumab and pertuzumab combination treatment on HER2-positive human xenograft tumor models. *Cancer Res.* **69**, 9330–9337
66. Baselga, J., Gelmon, K. A., Verma, S., Wardley, A., Conte, P., Miles, D., Bianchi, G., J., C., McNally, V. A., Ross, G. A., Fumoleau, P., and Gianni, L. (2010) Phase II trial of pertuzumab and trastuzumab in patients with human epidermal growth factor receptor 2–positive metastatic breast cancer that progressed during prior trastuzumab therapy. *J. Clin. Oncol.* **28**, 1138–1144
67. Nahta, R., Yu, D., Hung, M.-C., Hortobagyi, G. N., and Esteva, F. J. (2006) Mechanisms of disease: understanding resistance to HER2-targeted therapy in human breast cancer. *Nat. Clin. Pract.* **3**, 269–280
68. Malm, M., Frejd, F. Y., Ståhl, S., Löfblom, J., Malm, M., Frejd, F. Y., Ståhl, S., Löfblom, J., Malm, M., Frejd, F. Y., and Löfblom, J. (2016) Targeting HER3 using mono- and bispecific antibodies or alternative scaffolds. *MAbs.* **8**, 1195–1209
69. Hutcheson, I. R., Knowlden, J. M., Hiscox, S. E., Barrow, D., Gee, J. M. W., Robertson, J. F., Ellis, I. O., and Nicholson, R. I. (2007) Heregulin beta1 drives gefitinib-resistant growth and invasion in tamoxifen-resistant MCF-7 breast cancer cells. *Breast Cancer Res.* **9**, :R50
70. Ritter, C. A., Perez-Torres, M., Rinehart, C., Guix, M., Dugger, T., Engelman, J. A., and Arteaga, C. L. (2007) Human breast cancer cells selected for resistance to trastuzumab in vivo overexpress epidermal growth factor receptor and ErbB ligands and remain dependent on the ErbB receptor network. *Clin. Cancer Res.* **13**, 4909–4920
71. Motoyama, A. B., Hynes, N. E., and Lane, H. A. (2002) The efficacy of ErbB receptor-targeted anticancer therapeutics is influenced by the availability of epidermal growth factor-related peptides. *Cancer Res.* **62**, 3151–3158
72. Sergina, N. V., Rausch, M., Wang, D., Blair, J., Hann, B., Shokat, K. M., and Moasser, M. M. (2007) Escape from HER-family tyrosine kinase inhibitor therapy by the kinase-inactive HER3. *Nature.* **445**, 437–441
73. Revillion, F., Lhotellier, V., Hornez, L., Bonnetterre, J., and Peyrat, J.-P. (2008) ErbB/HER ligands in human breast cancer, and relationships with their receptors , the bio-pathological features and prognosis. *Ann. Oncol.* **19**, 73–80
74. Li, Q., Ahmed, S., and Loeb, J. A. (2004) Development of an autocrine neuregulin signaling loop with malignant transformation of human breast epithelial cells. *Cancer Res.* **64**, 7078–7085
75. Wilson, T. R., Fridlyand, J., Yan, Y., Penuel, E., Burton, L., Chan, E., Peng, J., Lin, E., Wang, Y., Sosman, J., Ribas, A., Li, J., Moffat, J., Sutherland, D. P., Koeppen, H., Merchant, M., Neve, R., Settleman, J., and Settleman, J. (2012) Widespread potential growth-factor-driven resistance to anticancer kinase inhibitors. *Nature.* **487**, 505–509
76. Gala, K., and Chandarlapaty, S. (2014) Molecular pathways: HER3 targeted therapy. *Clin. Cancer Res.* **20**, 1410–1417
77. Gaborit, N., Lindzen, M., and Yarden, Y. (2016) Emerging anti-cancer antibodies and combination therapies targeting HER3/ERBB3. *Hum. Vaccin. Immunother.* **12**, 576–592
78. Shi, F., Telesco, S. E., Liu, Y., Radhakrishnan, R., and Lemmon, M. A. (2010) ErbB3/HER3 intracellular domain is competent to bind ATP and catalyze autophosphorylation. *Proc. Natl. Acad. Sci. USA.* **107**, 7692–7697
79. Schaefer, G., Haber, L., Crocker, L. M., Shia, S., Shao, L., Dowbenko, D., Totpal, K., Wong, A., Lee, C. V., Stawicki, S., Clark, R., Fields, C., Phillips, G. D. L., Prell, R. A., Danilenko, D. M., Franke, Y., Stephan, J.-P., Hwang, J., Wu, Y., Bostrom, J., Sliwkowski, M. X., Fuh, G., and Eigenbrot, C. (2011) Article A two-in-one antibody against HER3 and EGFR has superior inhibitory activity compared with monospecific antibodies. *Cancer Cell.* **20**, 472–486

80. Garner, A. P., Bialucha, C. U., Sprague, E. R., Garrett, J. T., Sheng, Q., Li, S., Sineshchekova, O., Saxena, P., Sutton, C. R., Chen, D., Chen, Y., Wang, H., Liang, J., Das, R., Mosher, R., Gu, J., Huang, A., Haubst, N., Zehetmeier, C., Haberl, M., Elis, W., Kunz, C., Heidt, A. B., Herlihy, K., Murtie, J., Schuller, A., Arteaga, C. L., Sellers, W. R., and Ettenberg, S. A. (2013) An antibody that locks HER3 in the inactive conformation inhibits tumor growth driven by HER2 or neuregulin. *Cancer Res.* **73**, 6024–6036
81. Mirschberger, C., Schiller, C. B., Schräml, M., Dimoudis, N., Gerdes, C., Reiff, U., Lifke, V., Hoelzlwimmer, G., and Kolm, I. RG7116 , a novel therapeutic antibody that binds to HER3 in the inactive state , potently blocks HER3 signaling , and is optimized for immune cell effector activation
82. Lee, S., Greenlee, E. B., Amick, J. R., Ligon, G. F., Lillquist, J. S., Natoli, E. J., Hadari, Y., Alvarado, D., and Schlessinger, J. (2015) Inhibition of ErbB3 by a monoclonal antibody that locks the extracellular domain in an inactive configuration. *Proc. Natl. Acad. Sci. USA.* **112**, 13225–13230
83. Carvalho, S., Levi-Schaffer, F., Sela, M., and Yarden, Y. (2016) Immunotherapy of cancer: from monoclonal to oligoclonal cocktails of anti-cancer antibodies: IUPHAR Review 18. *Br. J. Pharmacol.* **173**, 1407–1424
84. Konecny, G. E., Pegram, M. D., Venkatesan, N., Finn, R., Yang, G., Rahmeh, M., Untch, M., Ruskak, D. W., Spehar, G., Mullin, R. J., Keith, B. R., Gilmer, T. M., Berger, M., Podratz, K. C., and Slamon, D. J. (2006) Activity of the dual kinase inhibitor lapatinib (GW572016) against HER-2-overexpressing and trastuzumab-treated breast cancer cells. *Cancer Res.* **66**, 1630–1640
85. Kontermann, R. E., and Brinkmann, U. (2015) Bispecific antibodies. *Drug Discov. Today.* **20**, 838–847
86. Robinson, M., Hodge, K., Horak, E., Sundberg, A., Russeva, M., Shaller, C. C., von Mehren, M., Shchavezleva, I., Simmons, H., Marks, J., and Adams, G. (2008) Targeting ErbB2 and ErbB3 with a bispecific single-chain Fv enhances targeting selectivity and induces a therapeutic effect in vitro. *Br. J. Cancer.* **99**, 1415–1425
87. Ewer, M. S., and Ewer, S. M. (2010) Cardiotoxicity of anticancer treatments: what the cardiologist needs to know. *Nat. Rev. Cardiol.* **7**, 564–575
88. Pugatsch, T., Abedat, S., Lotan, C., and Beerli, R. (2006) Anti-erbB2 treatment induces cardiotoxicity by interfering with cell survival pathways. *Breast Cancer Res.* **8**, :R35
89. Chen, D. S., and Mellman, I. (2013) Oncology meets immunology: the cancer-immunity cycle. *Immunity.* **39**, 1–10
90. Spitzer, M. H., Carmi, Y., Reticker-Flynn, N. E., Kwek, S. S., Madhireddy, D., Martins, M. M., Gherardini, P. F., Prestwood, T. R., Chabon, J., Bendall, S. C., Fong, L., Nolan, G. P., and Engleman, E. G. (2017) Systemic immunity is required for effective cancer immunotherapy. *Cell.* **168**, 1–16
91. Zhu, P., Liu, J., Bess Jr, J., Chertova, E., Lifson, J. D., Grise, H., Ofek, G. A., Taylor, K. A., and Roux, K. H. (2006) Distribution and three-dimensional structure of AIDS virus envelope spikes. *Nature.* **441**, 847–852
92. Valley, C. C., Lewis, A. K., and Sachs, J. N. (2017) Piecing it together: unraveling the elusive structure-function relationship in single-pass membrane receptors. *Biochim. Biophys. Acta.* 10.1016/j.bbamem.2017.01.016
93. Kovacs, E., Zorn, J. A., Huang, Y., Barros, T., and Kuriyan, J. (2015) A structural perspective on the regulation of the epidermal growth factor receptor. *Annu. Rev. Biochem.* **84**, 739–764
94. Pfeffer, S., Woellhaf, M. W., Herrmann, J. M., and Forster, F. (2015) Organization of the mitochondrial translation machinery studied in situ by cryoelectron tomography. *Nat. Commun.* **6**, 6019

95. Kaplan, M., Narasimhan, S., De Heus, C., Mance, D., van Doorn, S., Houben, K., Popov-Celeketic, D., Damman, R., Katrukha, E. A., Jain, P., Geerts, W. J. C., Heck, A. J. R., Folkers, G. E., Kapitein, L. C., Lemeer, S., van Bergen, P. M. P., and Baldus, M. (2016) EGFR dynamics change during activation in native membranes as revealed by NMR. *Cell*. **167**, 1–11
96. Spiess, C., Merchant, M., Huang, A., Zheng, Z., Yang, N.-Y., Peng, J., Ellerman, D., Shatz, W., Reilly, D., Yansura, D. G., and Scheer, J. M. (2013) Bispecific antibodies with natural architecture produced by co-culture of bacteria expressing two distinct half-antibodies. *Nat. Biotechnol.* **31**, 753–758
97. Fan, G., Wang, Z., Hao, M., and Li, J. (2015) Bispecific antibodies and their applications. *J. Hematol. Oncol.* **8**, :130
98. Kontermann, R. (2012) Dual targeting strategies with bispecific antibodies. *MAbs*. **4**, 182–197
99. Spiess, C., Zhai, Q., and Carter, P. J. (2015) Alternative molecular formats and therapeutic applications for bispecific antibodies. *Mol. Immunol.* **67**, 95–106
100. Ha, J.-H., Kim, J.-E., and Kim, Y. S. (2016) Immunoglobulin Fc heterodimer platform technology: from design to applications in therapeutic antibodies and proteins. *Front. Immunol.* **7**, :394
101. Atwell, S., Ridgway, J. B. B., Wells, J. A., and Carter, P. (1997) Stable heterodimers from remodeling the domain interface of a homodimer using a phage display library. *J. Mol. Biol.* **270**, 26–35
102. Ridgway, J. B. B., Presta, L. G., and Carter, P. (1996) “Knobs-into-holes” engineering of antibody CH3 domains for heavy chain heterodimerization. *Protein Eng.* **9**, 617–621
103. Moore, G. L., Bautista, C., Pong, E., Nguyen, D.-H. T., Jacinto, J., Eivazi, A., Muchhal, U. S., Karki, S., Chu, S. Y., and Lazar, G. A. (2011) A novel bispecific antibody format enables simultaneous bivalent and monovalent co-engagement of distinct target antigens. *MAbs*. **3**, 546–557
104. Von Kreudenstein, T. S., Lario, P. I., and Dixit, S. B. (2014) Protein engineering and the use of molecular modeling and simulation: the case of heterodimeric Fc engineering. *Methods*. **65**, 77–94
105. Gunasekaran, K., Pentony, M., Shen, M., Garrett, L., Forte, C., Woodward, A., Ng, S. Bin, Born, T., Retter, M., Manchulenko, K., Sweet, H., Foltz, I. N., Wittekind, M., and Yan, W. (2010) Enhancing antibody Fc heterodimer formation through electrostatic steering effects. *J. Biol. Chem.* **285**, 19637–19646
106. Choi, H.-J., Seok, S.-H., Kim, Y.-J., Seo, M.-D., and Kim, Y.-S. (2015) Crystal structures of immunoglobulin Fc heterodimers reveal the molecular basis for heterodimer formation. *Mol. Immunol.* **65**, 377–383
107. Choi, H.-J., Kim, Y.-J., Lee, S., and Kim, Y.-S. (2013) A heterodimeric Fc-based bispecific antibody simultaneously targeting VEGFR-2 and Met exhibits potent antitumor activity. *Mol. Cancer Ther.* **12**, 2748–2760
108. van Zundert, G. C. P., Rodrigues, J. P. G. L. M., Trellet, M., Schmitz, C., Kastiris, P. L., Karaca, A. S. J., Melquiond, A. S. J., van Dijk, M., de Vries, S. J., and Bonvin, A. M. J. J. (2016) The HADDOCK2 .2 web server: user-friendly integrative modeling of biomolecular complexes. *J. Mol. Biol.* **428**, 720–725
109. Leaver-Fay, A., Froning, K. J., Atwell, S., Aldaz, H., Pustilnik, A., Lu, F., Huang, F., Yuan, R., Hassanali, S., Chamberlain, A. K., Fitchett, J. R., Demarest, S. J., and Kuhlman, B. (2016) Computationally designed bispecific antibodies using negative state repertoires. *Structure*. **24**, 641–651
110. Brinkmann, U., and Kontermann, R. E. (2017) The making of bispecific antibodies. *MAbs*. **9**, 182–212

APPENDIX

Summary

Nederlandse samenvatting

List of publications

Curriculum vitae

Acknowledgements

Summary

Proteins are the building blocks of life and are involved in nearly all cell functions. They are composed of 20 amino acids which combine in different sequences, resulting in unique three-dimensional structures. The functioning of a protein strongly depends on its structural features. The elucidation of protein structures is of great importance for the understanding of disease triggering mechanisms and for the development of new drugs. In this thesis, different biophysical and biochemical techniques are employed to gain insights into the structural and functional features of three proteins belonging to two important cell surface receptor families. Cell surface receptors represent the checkpoints of the cell: they sense the cellular environment and send specific messages to the inside of the cell via interaction with other molecules. If a specific message fails to be delivered or, on the contrary, is overly transmitted, the balanced functioning of the cell is disturbed and disease may arise. Therefore, cell surface receptors are among the number one targets for rational drug design. Chapter 1 briefly presents the main classes of human cell surface receptors and the main subjects of this study: low density lipoprotein (LDL) receptor-related protein 1 (LRP1) and human epidermal growth factor receptor 2 (HER2) and 3 (HER3).

Chapter 2 focuses on LRP1, the largest member of the LDL receptor family. LRP1 is known to interact with numerous binding partners, fulfilling many biological tasks besides its main role as a scavenger. LRP1 is a challenging protein for structural investigation due to its composition and very large size. Its extracellular region contains 61 domains that are highly glycosylated and rich in cysteines. Small-angle X-ray scattering (SAXS) and negative stain electron microscopy (EM) were combined with surface plasmon resonance (SPR), native and crosslink mass spectrometry (MS) to elucidate LRP1's binding behavior and structural features. This synergistic approach made it possible to obtain the first structural characterization of the entire extracellular region of LRP1. LRP1 binding properties and role as endocytic receptor were investigated using the chaperone receptor-associated protein (RAP) as model ligand. We observed that LRP1 can reversibly bind RAP at neutral pH and release it at pH lower than 6, which corresponds to the pH environment of the endosomal compartments. The conformation of the ectodomain of LRP1 was shown to be pH-dependent, with an elongated but not fully extended form at pH 7.5, and a more compact one at pH < 6. These results shed light on the importance of the pH environment, which contributes to the cargo release mechanism in LRP1's endocytic cycle. A similar behavior had previously been observed for the LDL receptor, which suggests that it could characterize a broader number of endocytic receptors.

Chapter 3 describes the identification and development of a novel bispecific full-length antibody (PB4188 or MCLA-128) targeting the receptor tyrosine kinases HER2 and HER3. These receptors normally regulate cell proliferation and survival by binding to growth factors, which trigger the activation of different signaling pathways. When their activity is dysregulated, due to mutations or overexpression of the receptors or of their ligands, cancer may develop. HER2 and HER3 can form heterodimers which, in the presence of the HER3 ligand heregulin (HRG), can transmit strong survival signals, allowing tumors to become more invasive and often resistant to anticancer therapies. Bispecific antibodies are a novel class of bio-pharmaceuticals that combine two different antigen binding sites in a single molecule. By recognizing multiple targets, bispecific antibodies have the potential to exert a more potent and durable action compared to monospecific antibodies and other therapeutic agents. PB4188 was identified through an unbiased screening and by adopting different *in vitro* and *in vivo* assays as activity readouts. This bispecific antibody targets HER2 and HER3 in a highly selective manner and strongly inhibits the HRG-driven activation of the PI3K/Akt downstream pathway, which usually is the main cause for the development of drug resistance in tumors where HER2 is overexpressed. By combining biological data with X-ray crystallography and statistical modeling we could elucidate the mechanism of action of this novel molecule. PB4188 is able to target cancer cells by binding to HER2, which is usually more amplified than HER3, and consequently bind HER3 in an epitope that overlaps with the ligand binding pocket. In this way, PB4188 inhibits HRG binding and activation of the HRG/HER3-associated signaling events. This novel ‘dock and block’ strategy could be more broadly adopted for the development of other bispecific antibodies targeting multiple receptors involved in cancers and other pathologies.

In chapter 4 the engineering efforts behind the development of the bispecific antibody MCLA-128 are presented. Bispecific antibodies can be produced by means of different strategies. However, issues regarding the production, the stability and their pharmacokinetic properties may arise, hindering the successful development of a drug candidate. For MCLA-128 a common light chain strategy was adopted to overcome the problem related to the mispairing of the heavy and light chains. Furthermore, we introduced asymmetric mutations in the CH3 domains of the Fc region of the IgG to promote the heterodimeric assembly of two different antibody heavy chains. In order to identify the most promising mutations, *in vitro* assays, computational docking and X-ray crystallography were employed. By combining these approaches we could develop a very stable bispecific antibody that is based on the architecture of a natural IgG and can be produced with high purity.

Appendix

Overall, different applications of structural investigation are presented in this thesis, illustrating the potential of structural biology to complement biochemical and pharmaceutical research in order to help the quest for new drugs and the understanding of their mechanism of action at the atomic level.

Nederlandse Samenvatting

Proteïnen zijn de bouwstenen van het leven en zijn betrokken bij zowat alle cel-functies. Ze zijn samengesteld uit 20 aminozuren, die in verschillende sequenties gecombineerd worden, wat resulteert in unieke driedimensionale structuren. De werking van een proteïne is sterk afhankelijk van haar structurele kenmerken: proteïnen met gelijkaardige vouwdomeinen vervullen vaak een vergelijkbare biologische rol. Het ophelderden van de structuur van proteïnen is van groot belang voor het begrijpen van de mechanismen die bepaalde ziekten veroorzaken en voor de ontwikkeling van nieuwe geneesmiddelen. In deze thesis worden verschillende biofysische en biochemische technieken gebruikt om inzicht te verwerven in de structurele en functionele kenmerken van drie proteïnen uit twee belangrijke families van celoppervlakreceptoren. Deze receptoren zijn de ‘checkpoints’ van de cel: ze nemen de celomgeving waar en sturen door interactie met andere moleculen specifieke boodschappen naar de binnenkant van de cel. Als een bepaalde boodschap niet wordt afgeleverd, of in tegendeel bovenmatig wordt verzonden, raakt de gebalanceerde werking van de cel verstoord, wat tot ziekte kan leiden. De receptoren van het celoppervlak zijn daarom bij de belangrijkste doelwitten van rationeel ontworpen geneesmiddelen. Hoofdstuk 1 introduceert kort de voornaamste klassen van menselijke celoppervlakreceptoren en de proteïnen waar deze studie op focust: low density lipoprotein (LDL) receptor-related protein 1 (LRP1) en human epidermal growth factor receptor 2 (HER2) en 3 (HER3).

Hoofdstuk 2 focust op LRP1, het grootste lid van de LDL-receptorfamilie. Het is bekend dat LRP1, naast zijn rol als opruimer, verschillende andere biologische taken vervult, en daarvoor interageert met tal van bindingspartners. Onderzoek naar de structuur van LRP1 wordt bemoeilijkt door zijn samenstelling en erg grote afmetingen. De extracellulaire regio bevat 61 sterk geglycosyleerde en cysteïne-rijke domeinen. Small-angle X-ray scattering (SAXS) en electronenmicroscopie (EM) met negatieve kleuring werden gecombineerd met surface plasmon resonance (SPR) en massaspectrometrie (MS) om het bindingsgedrag en de structurele kenmerken van LRP1 te achterhalen. Deze synergistische aanpak leidde tot de eerste structurele karakterisatie van de volledige extracellulaire regio van LRP1. Ook de bindingskenmerken en de rol van LRP1 als endocytosereceptor werden onderzocht. Het chaperonne-eiwit receptor-associated protein (RAP) werd daarbij als modelligand gebruikt. We stelden vast dat LRP1 RAP omkeerbaar kan binden bij neutrale pH en de ligand weer loslaat bij een pH lager dan 6, wat overeenstemt met de pH-omgeving van de endosomale compartimenten. De conformatie van het ectodomein van LRP1 bleek pH-afhankelijk, met een langere doch niet volledig uitgestrekte conformatie bij pH 7,5, en een meer compacte vorm bij pH

lager dan 6. Deze resultaten werpen licht op het belang van de pH-omgeving, die bijdraagt tot het mechanisme waarvolgens LRP1 tijdens de endocytische cyclus haar lading weer loslaat. Vergelijkbaar gedrag werd eerder beschreven voor de LDL-receptor, wat suggereert dat het mogelijk karakteristiek is voor meerdere endocytosereceptoren.

Hoofdstuk 3 beschrijft de identificatie en ontwikkeling van een nieuw bispecifiek antilichaam (PB4188 of MCLA128) dat de receptortyrosinekinases HER2 en HER3 kan binden. Deze receptoren reguleren onder normale omstandigheden de proliferatie en overleving van cellen. Ze binden daartoe groeifactoren die verschillende signalisatiepaden activeren. Wanneer hun activiteit ontregeld raakt, tengevolge van mutaties of de overexpressie van de receptoren of hun liganden, kan kanker ontstaan. In aanwezigheid van de HER3-ligand hereguline (HRG) sturen heterodimeren van HER2 en HER3 sterke overlevingsignalen door. Tumoren worden daardoor invasiever en bouwen vaak ook resistentie op tegen bepaalde kankerbehandelingen. Bispecifieke antilichamen zijn een nieuwe klasse van biofarmaceutica die twee verschillende antigen-bindingsplaatsen combineren in één enkele molecule. Omdat ze meerdere doelwitten herkennen, zijn bispecifieke antilichamen mogelijk effectiever en duurzamer dan monospecifieke antilichamen en andere therapeutische middelen. PB4188 werd geïdentificeerd via een onbevooroordeelde screening en met behulp van verschillende analyses van de activiteit *in vitro* en *in vivo*. Het bispecifieke antilichaam bindt HER2 en HER3 op hoogst selectieve wijze en onderdrukt sterk de activatie van het PI3K/Akt-signalisatiepad door HRG, die vaak verantwoordelijk is voor het ontstaan van resistentie in tumoren waarin bovenmatig veel HER2 wordt aangemaakt. De combinatie van biologische gegevens met Röntgen-kristallografie en statistische modellering onthulde het werkingsmechanisme van deze nieuwe molecule met optimale therapeutische eigenschappen. PB4188 viseert kankercellen door zich te binden aan HER2, dat doorgaans algemener is dan HER3, en bindt vervolgens HER3 in een epitootop die overlapt met de ligandbindingsplaats. Op deze manier verhindert PB4188 de binding van HRG en activatie van de met HRG/HER3 geassocieerde signalisatie. Deze nieuwe 'dock and block' ('bind en blokkeer')-strategie zou breder kunnen worden toegepast voor de ontwikkeling van bispecifieke antilichamen die zich richten op meerdere receptoren betrokken bij kankers of andere aandoeningen.

Hoofdstuk 4 biedt een overzicht van het ontwikkelingsproces van het bispecifieke antilichaam MCLA-128. Bispecifieke antilichamen kunnen volgens verschillende strategieën geproduceerd worden. Problemen met betrekking tot productie, stabiliteit en farmacokinetiek kunnen de succesvolle ontwikkeling van een kandidaatgeneesmiddel hinderen. Een 'gemeenschappelijke lichte keten'-strategie voorkwam verkeerde combinaties van zware en lichte ketens. Daarnaast werden in

de CH3-domeinen van de Fc-regio van het immunoglobuline G (IgG) asymmetrische mutaties aangebracht om de heterodimerisatie van de twee verschillende zware ketens te bevorderen. Om de meest veelbelovende mutaties te identificeren werd gebruik gemaakt van *in vitro*-methoden, computationele 'docking tools' en Röntgen-kristallografie. De combinatie van deze strategieën maakte de ontwikkeling mogelijk van een erg stabiel bispecifiek antilichaam, dat gebaseerd is op de architectuur van een natuurlijk IgG en met hoge zuiverheid geproduceerd kan worden.

Deze thesis beschrijft verschillende toepassingen van structureel onderzoek en illustreert het potentieel van structurele biologie om een bijdrage te leveren aan biochemisch en farmaceutisch onderzoek, in de zoektocht naar nieuwe geneesmiddelen en een beter begrip van hun werkingsmechanisme op atomair niveau.

List of publications

De Nardis, C., Lösösl, P., van den Biggelaar, M., Madoori, P. K., Leloup, N., Mertens, K., Heck, A. J., and Gros, P. (2017) Recombinant expression of the full-length ectodomain of LDL receptor-related protein 1 (LRP1) unravels pH dependent conformational changes and the stoichiometry of binding with receptor-associated protein (RAP). *J Biol Chem.* **292**, 912–924

De Nardis, C., Hendriks, L. J. A., Poirier, E., Arvinte, T., Gros, P., Bakker, A. B. H., and de Kruif, J. (2017) A new approach for generating bispecific antibodies based on a common light chain format and the stable architecture of human immunoglobulin G1. *J Biol Chem.* 2017, doi: 10.1074/jbc.M117.793497

Geuijen, C., **De Nardis**, C., Maussang, D., Rovers, E., Gallenne, T., Hendriks, L. J. A., Visser, T., Nijhuis, R., Logtenberg, T., de Kruif, J., Gros, P., and Throsby, M. (2017) Application of unbiased combinatorial screening to generate a bispecific IgG1 that selectively and potently inhibits HER3 signaling via HER2-guided ligand blockade. *Submitted*

Curriculum vitae

I was born on January 1st, 1989 in Rome, Italy, where I grew up. After obtaining my high school diploma from Convitto Nazionale Vittorio Emanuele II, I enrolled in 2007 in the Chemistry Bachelor program at La Sapienza University of Rome. In 2010, I obtained my BSc degree in Chemistry (110/110 *cum laude*). Consequently, I continued my studies at La Sapienza and followed the Master of Science program in Chemistry of Biological Systems, which I concluded in 2012 (110/110 *cum laude*). My thesis project, entitled 'Structural studies of proteins involved in bacterial biofilm formation', was performed during a 9-month internship at the Department of Biochemistry under the supervision of prof. dr. Francesca Cutruzzolá and dr. Giorgio Giardina. During my master I have attended, as part of the Erasmus Program, a semester of lectures of the master track Drug Innovation at the Universiteit van Amsterdam (UvA). In 2012, I moved back to The Netherlands to start a PhD project with prof. dr. Piet Gros in the Crystal & Structural Chemistry group at the Bijvoet Center for Biomolecular Research of Utrecht University, with a focus on structural studies of receptor-ligand interactions. This project was part of the ManiFold Marie Curie Innovative Doctoral Programme on protein folding and assembly. The results of this project are presented in this thesis. During my PhD I also collaborated with Merus, an Utrecht-based immunoncology company that develops novel bispecific antibody therapeutics. Together we have investigated how one of their bispecific antibodies works at the atomic level. The results of this collaboration are described in this thesis. Currently, I am working as a scientific writer at Merus.

Acknowledgements

My PhD has been an incredible journey. Like all the unforgettable journeys it has had some obstacles. Without all the people mentioned here I would probably not have made it through. Thank you!

Piet. It all started with a short project description on a protein called LRP1 for the ManiFold grant. The main reason I wanted to join your group, however, was because it looked like the right place to learn more about structural biology. And so it was. Over the course of the more than 4 years I have spent in K&S I have learned an awful lot. Your scientific integrity and intellectual curiosity have provided a strong guidance, teaching me how good scientific research should always be done. Besides science, you have also taught me how to deal with the Dutch and their directness. Thank you for the important lesson on saying 'no' to the boss. Thank you for assigning me the Merus projects at a difficult point in my PhD and for your understanding when I had doubts. Finally, thank you for giving me trust and freedom during the writing process.

I would like to thank all the members of the committee and the collaborators, who have also taught me a lot during these years. Stefan, thank you for writing the ManiFold grant. Without you I would probably not have moved to this country that I have learned to like so much. Thank you for the kindness that you have always shown, by welcoming us in your house the first year and by spending time to answer my questions on Hsp70 and LRP1. Ineke, thank you for the meetings to discuss the role of chaperones in LRP1 folding and for the suggestions you have always been keen to give. Koen, I remember when I presented my project in your office just a few months after the start of my PhD and you showed the contagious enthusiasm that has always characterized our following meetings. Thanks to you and Maartje for believing in the LRP1 project, it is also because of your help that it has brought about such a nice publication. Alexander, I am glad we have had the chance to collaborate at the end of my PhD. Thank you for your kindness and openness. Jan Voorberg, thank you for accepting to be in my reading committee and for the very nice words on my thesis. Ton, your work has been very important for the realization of a big part of this thesis. I am glad you accepted to be part of my defense committee. Thank you all for taking time to read my thesis.

Mark, John, Cecile. Thank you for trusting me to work with you on the MCLA-128 projects and for your unwavering support. I have really enjoyed meeting with you to discuss the data and to write up what have become two wonderful publications. I am very grateful that our collaboration could continue at Merus. Linda, your openness, warmth and scientific knowledge have been a big help and made working with you a real pleasure (it still is!). David, your friendliness,

professionalism and excellent Dutch-speaking skills are inspiring. I am glad you became my supervisor. You have already taught me a lot in these few months and I am looking forward to learn more from you.

It is now time to thank one of the most solid pillars during my PhD (dis) adventures: the K&S group. It has been wonderful to be your colleague during these 4.5 years! Deniz, your friendly ways struck me from the very first time I have talked to you. I am so glad of everything we have been able to share. Thank you for being such a lively and charming friend, I really like how you defuse any sort of situation into something fun. Teşekkürler! Hedwich, you have been a great office mate and a point of reference for so many questions on ‘how to do things’ in and out of the lab. Thank you for all the help. I appreciated our serious but also frivolous conversations about all sorts of topics and I am glad we could often share our worries and hopes about the future. Revina, you are incredibly sweet and incredibly strong at the same time, I don’t know how you do that but it is truly special. Thank you so much for being a good listener and source of advice. You have helped me a lot during the tough times. Vivi, it was great to have someone to talk Italian to in the lab, even though you have often tried to answer me in Dutch! I admire your determination to learn Dutch and your artistic side. Dimphna, thank you for bringing a fresher view on things in K&S. Your easy-going attitude mixes so well with your scientific curiosity that I am sure you will get to that professor position one day! Tim, the most fortunate outcome of the Fc ER project was that I got to know you better. I really enjoyed our time in Lisbon, Grenoble and early morning coffees. Thank you for helping me with my million questions on Linux (and everything else), for teaching me Mathematica and, most importantly, for making fun of me from time to time :). My last year would have not been quite the same without you! Remco, you have been a positive presence in the lab and a great help when needed. I’ve always liked your sense of style and your openness to the world. Thank you for introducing me to Dutch music, in particular Frescu and Jeugd van Tegenwoordig ;). Thanks to you and Matti for driving me around in Brittany, it was a lot of fun even if we were always the last ones to arrive! Matti, I have always appreciated how you combine the rigor of a scientist with the fantasy of a musician. It was fun to hear you speaking Italian at random moments in the lab. We both know that JBC is one of the most awesome journals no matter what they say! Louris, you are a kind, warm-hearted person. You have been always very generous in helping me in the lab and I have always enjoyed our chats and swims at the Krommerijn (and your awesome rhubarb cake!). XG, I love your curiosity and unexpected jokes. I’ve had a lot of fun with you at the synchrotron! Thank you for the help in solving structures. Peng, you have been a great colleague and friend since the very beginning of my PhD. I have

enjoyed talking to you about everything, from science to gossip to food. Thank you for teaching me how to collect data and solve structures, and for giving me always honest advice. Pramod, your help was crucial at the beginning of my PhD. Thank you for being a generous and friendly guidance. Federico, it was great to find some *italianità* since the early start of my PhD. Your coaching in pretty much anything in the lab has been essential. Your wit, humor and great cooking skills have made the time we shared at K&S even more pleasurable. Wout, I am glad you joined N809 with your easygoing and cheerful attitude. It was fun to party in ACU and I will never forget your awesome Clockwork Orange outfit (I hope you have watched the movie by now)! Ramon, I have definitely forgiven the fact that you 'hit' me once ;). You are a lot of fun and - as I have recently found out - also a great dancer! Matthieu and Lucas, aka 'the Frenchies', thanks for refreshing the international atmosphere in the group. Matthieu, talking to you has always been very enjoyable and listening to you playing the piano is a real pleasure. Lucas, it has been fun talking to you about random stuff and I love your dance moves. Nick, your dry humor is quite irresistible. Thank you for the help with structure-related questions. The group will certainly benefit a lot from your presence. Take good care of the Pymol page! Noortje, thank you for your support and friendly attitude, you have helped me a lot in this last year. Laura, Robert, it was great to share time with you too! :)

Moreover, I would like to thank the rest of the K&S group. Bert, Eric, thank you for your guidance and ever-helpful attitude towards solving scientific puzzles. I have learned a lot from you. Joke, you are the K&S guardian angel. Thank you for taking excellent care of the lab and of all of us with efficiency and gentleness. Arie, thank you for teaching me more on crystallization, fishing and measuring crystals. Loes, thank you for helping with SAXS, you have always been very kind and available. Martin, thank you for the help with difficult datasets and crystallography questions, and for your hospitality in the Black Forest. Toine, thank you for teaching me how to properly manage data and helping with Linux problems.

Now I would like to thank my dearest friends in Utrecht and beloved paranympths: Nadia and Martina. It all started with the three of us interviewing for the ManiFold positions. From then you have become a constant presence in my life. I could not even imagine how my PhD could have been without you two. You have been patient ears for my worries, welcoming shoulders for my tears and joyful eyes for my successes. Thank you so much! Nadia, we have tuned our relation to find the perfect chord. Your solid personality has helped me to stay grounded when things felt shaky. Thanks to you I discovered yoga, which aided me a lot during these PhD years. I have always enjoyed our conversations, shared interests (and frustrations) on conscious lifestyles, and learned a lot from you. How you manage

to do all the things you do and so well is still a mystery to me, but I feel deeply inspired by it! Martina, your kind heart is a blessing for who has the luck to be your friend. Being your housemate (and husband!) has been a fun and enriching experience, you taught me important lessons, such as that I should be grateful for what I have and worry less. I admire your curious and free-minded attitude, always willing to learn new things and engage with the world. Your amazing voice will always make me cry!

And now my favorite Germans of all times and co-members of the ‘Fantastic Four’ awesome group: Jonas and Philip. You guys are incredibly different but both so charming and adorable, if I may quote someone :). Jonas, thank you for the whiskey tastings, past-midnight chats, extravaganza nights in ACU, German-style lasagnas, music experiences, shared green-minded attitude... and much more! Thank you just for being an amazing friend, I have enjoyed so much spending time with you. I hope you will stick around for a while longer! Philip, your open-mindedness and willingness to engage in conversations on many different topics made talking to you always a pleasure. I really admire how prepared and to-the-point you can be, while always making everybody feel at ease. You have been a supportive friend and generous collaborator, your thorough attitude has been helpful and inspiring. Thank you so much. I hope we will keep in touch!

I would also like to thank the rest of the ManiFold gang. Tania, you are a really positive and warm person. I am glad I had a (second) chance to get to know you better in this last year :). Anna, your outspoken Greek ways made me laugh a lot during our first year. More recently I learned to appreciate your determination and sense of organization, probably because in this regard we have a lot in common :). Yang, thank you for your sweetness and sense of humor. I will never forget your smile. I hope to see you and Suri again sometime in the future. Saran, you have a visionary and generous spirit. Thank you and Sakthi for the excellent food and interesting conversations. I wish you both all the best! Daniel, thank you for the support during my first year. Ivan, thank you for your gentle ways and fluent Italian chats. I had a lot of fun with all of you guys!

Among my other friends here in The Netherlands, I would like to thank you, Benedetta. I find your intelligence, sweetness and style truly unique and enchanting. Thank you for all the interesting conversations that always led to one beer too many :). Parricia, you have been my first friend in The Netherlands and one of the most awesome ones. Thank you for being always welcoming, supportive and fun. I am so glad we are still in touch despite the kilometers in between us!

E ora i miei angeli custodi di sempre: Martina e Alessia. Marti, sono immensamente grata che la nostra amicizia abbia saputo superare le prove del tempo (28 anni!) e si sia evoluta rimanendo, però, in fondo sempre la stessa. Grazie per il

supporto che mi hai sempre dimostrato. Non potrei mai fare a meno delle nostre stimolanti conversazioni; con te mi sentirò sempre un po' a casa, perchè in fondo tu sei come una sorella per me. Ale, da quando ci misero in banco insieme il primo anno di liceo non ci siamo più separate. Sono felice che siamo rimaste unite nonostante la lontananza e abbiamo continuato a collezionare bellissimi ricordi, come il viaggio in California, uno dei viaggi più belli che abbia mai fatto. Grazie per la tua sincera e generosa amicizia, su cui ho sempre sentito di poter contare.

Grazie a tutti i miei amici di Roma che non hanno mai smesso di mostrarmi affetto nonostante i tanti anni che vivo lontano. Edo, grazie per l'amicizia e il sostegno che mi hai sempre dimostrato. Barbara, Emilia, grazie per la vostra energica e affettuosa presenza, nonchè contagiosa ironia. Fabri, grazie per essere venuto a trovarmi a Utrecht; parlare con te è sempre un piacere. Grazie anche a Claudia e Rosa per aver reso i nostri incontri una piacevole e immancabile caratteristica delle mie visite a Roma.

Grazie Giorgio, per avermi guidato nei primi passi verso la ricerca, ma anche per essere stato un ottimo ascoltatore e consigliere nei momenti di difficoltà. Nonostante gli anni passati, sei e rimarrai una importante figura di riferimento e fonte di ispirazione.

Grazie mamma. Grazie papà. Siete stati le colonne portanti durante questi anni di studio. Grazie per aver sempre creduto in me e per avermi fornito tutti gli strumenti - psicologici, emozionali e materiali - per realizzare la vita che desidero. Sono molto felice del rapporto aperto che abbiamo costruito, basato su una sincera e affettuosa comunicazione. Il vostro infinito amore è la coperta che mi fa sentire calda e protetta ogni notte; anche se lontani siete sempre qui con me. Non potrò mai esservi grata abbastanza. Vi voglio bene!

Tim. We met at a turning point of my life and since then things have never been the same. It feels like before I had been wearing dark glasses all the time to protect my eyes, but with you I have started seeing the bright colors of the world without any hurt. You are a great companion and source of support. What we have is truly magic. Thank you for all you do. I love you.